New Biosensors for Metabolic Imaging

A thesis submitted to the National University of Ireland, Cork

In fulfilment of the requirements for the degree of

Doctor of Philosophy by

Neil O'Donnell

School of Biochemistry and Cell biology

National University of Ireland, Cork

2018

Head of School: Prof. Rosemary O'Connor

Supervisor: Dr. Ruslan Dmitriev

Second Supervisor: Prof. Dmitri Papkovsky

Table of Contents

In memory of my Grandfather

Michael O’Donnell

1939 - 2018

Declaration

This thesis has not been submitted in whole or part to this or any other university for any degree, and is, unless otherwise stated, the original work of the author.

_____ October 2018

Neil O'Donnell

Abstract

Tissue engineering is a multi-disciplinary field that involves three-dimensional cell and tissue models, live cell microscopy and related imaging modalities, along with fluorescence and phosphorescence-based biosensors. These technologies can work together in developing biologically relevant 3D tissue models for the modelling of complex physiological and diseased states. One of the main challenges facing such models is the lack of non-invasive strategies for quantitative real time monitoring of cellular and tissue physiology, metabolism and viability, that are compatible with live cell microscopy. This thesis presents the design and development of new biosensor, scaffold and nanoparticle materials, with the aim of facilitating quantitative metabolic imaging in cell and tissue culture, via fluorescence lifetime microscopy and phosphorescence lifetime microscopy.

Thus, we have developed protein-based biosensor probes, sensitive to pH and calcium in intensity and fluorescence lifetime modalities for the labelling of cellulose scaffold materials, producing a hybrid scaffold material for tissue engineering applications. This was done by genetically engineering of recombinant proteins expressing the cellulose-binding domain (CBD) CenA protein, derived from the fungus *C. fimi*, fused to pH-sensitive enhanced cyan fluorescent protein (ECFP) and enhanced yellow fluorescent protein (EYFP), forming CBD-ECFP and CBD-EYFP biosensors, respectively. A third biosensor was also developed with CBD and the genetically encoded calcium indicator known as circularly permutated EGFP (cpEGFP)/M13/Calmodulin (CaM) fusion protein (GCaMP2) forming CBD-GCaMP2. For all three CBD constructs we observed responses in fluorescence intensity to changes in calcium for GCaMP2 and pH for both CBD-ECFP and CBD-EYFP, achieving efficient and stable labelling of various cellulose scaffolds including nanofibrillar, GrowDex, bacterial cellulose and decellularised plant materials. CBD-ECFP labelled GrowDex produced a biosensor scaffold material capable of supporting the growth of 3D cultured human colon cancer cells HCT116, with the ability to measure real-time changes in extracellular pH. The developed labelling strategy allows for the design of biosensor scaffold materials with potential multi-parametric fluorescence lifetime microscopy modalities, which can be used to achieve the controlled production of 3D tissue models with measurable pH and metabolic gradients.

Intracellular metabolic imaging is currently dominated by synthetic nanoparticle constructs that suffer from suboptimal intracellular staining, along with high toxicity and immunogenicity. Here we developed several self-assembling protein nanoparticle constructs based on viral like particle, elastin like polypeptide-cowpea chlorotic mottle virus capsid protein (ELP-CP) and protein nanocage ferritin. Such constructs hold promise due to their biological nature making them more biocompatible and biodegradable, thereby reducing toxic and immunogenic effects. Such self-assembling protein nanoparticles are also amenable to multiple strategies of functionalisation such as metallochelate coupling, genetic engineering, chemical modification, and encapsulation.

We evaluated metallochelate coupling to design intracellular O_2-sensitive biosensors, where oligohistidine-tagged recombinant proteins are bound to nitrilotriacetate (NTA) or iminodiacetic acid (IDA) groups on dyes and small molecules. The NTA or IDA groups form a complex with transition metal ions such as: Zn^{2+}, Ni^{2}+, Co^{2+}, or Cu^{2+}. This complex then co-ordinates to histidine amino acids on the recombinant protein. We successfully produced ratiometric phosphorescent probes from enhanced green fluorescent protein (EGFP), enhanced monomeric blue fluorescent protein 2 (mTagBFP2) and *Discosoma* red fluorescent protein (DsRed express) coupled to tetracarboxylic platinum (II)-coproporphyrin I (PtCP) PtCP-NTA. Such complexes can be used for ratiometric-based measurements of O_2, where fluorescent proteins (FPs) can be used as O_2-insensitive references. Most notably we demonstrated the first example of a phosphorescent O_2-senstive viral like particle (VLP) structure, ELPCP-H_6-PtCP and in comparing to commercial O_2-sensitive probe MitoXpress, we observed higher phosphorescence brightness, similar lifetime responses and increased sensitivity in response to O_2. The potential to couple a range of FPs or self-assembling protein nanoparticles to O_2 sensitive phosphorescent dyes demonstrates that metallochelate coupling is a highly attractive strategy in the design of new intracellular O_2 sensors.

Using genetic engineering and encapsulation strategies we successful produced both pH and O_2-sensitive ferritin nanoparticles. Genetic engineering enabled the expression of multiple cell targeting and penetrating peptides, such as bactenecin 7 and α-enolase, along with fluorescent proteins EGFP or ECFP, without affecting spectral properties of the fluorescent proteins or ferritin self-assembly. Genetic engineered ECFP-FTN construct demonstrated pH sensitivity in fluorescence intensity and lifetime across a physiological range of pH, potentially allowing for applications in fluorescence lifetime microscopy-based measurements of intracellular pH. Through the strategy of pH dependent disassembly and reassembly encapsulation of phosphorescent O_2 sensitive probe Pt-Glc, we successfully produced O_2-sensitive horse ferritin-based (hoFTN) nanoparticles. The resulting hoFTN-Pt-Glc displayed a higher phosphorescence intensity signal than free Pt-Glc, possibly due to the concentrated number of Pt-Glc molecules in close proximity within the ferritin structure, and demonstrated responses to oxygenation, increasing phosphorescence intensity when deoxygenated. However, in characterisation of hoFTN-Pt-Glc with MEF cells we observed poor intracellular staining confined to endosomes, similar to free Pt-Glc. These results showed that encapsulation here does not improve intracellular staining or phosphorescence lifetime responses. Despite poor characterisation of ferritin constructs in HCT116 and MEF cell lines, the strategies evaluated here show promise and demonstrate an interchangeable approach to functionalising self-assembling protein nanoparticles and fluorescent proteins for applications in fluorescence lifetime microscopy and phosphorescence lifetime microscopy-based quantitative and ratiometric live cell imaging

List of abbreviations

2D – Two dimensional

2PLSM – Two-photon excited laser-scanning microscopy

3D – Three dimensional

BC – Bacterial cellulose

BCECF – 2',7'-Bis-(2-Carboxyethyl)-5-(and-6)-Carboxyfluorescein, Acetoxymethyl Ester

BFP – Blue fluorescent protein

BHQ-3 – Black hole quencher 3

BME – Basement membrane

BMi – Bone mimicking

BphP – Bacterial phytochromes

BSA - Bovine serum albumin

Ca^{2+} – Calcium

CBD – Carbohydrate binding domain

CBM – Carbohydrate binding module

CCMV – Cowpea chlorotic mottle virus

CFP – Cyan fluorescent protein

CNC – Cellulose nanocrystals

CPMV – Cowpea mosaic virus

CuAAC – Cu-catalyzed azide-alkyne cycloaddition

DNA- Deoxyribonucleic acid

DsRed – *Discosoma* Red

ECM – Extracellular matrix

EDC – 1-Ethyl-3-(3-dimethylaminopropyl)carbodiimide

EGF – Epidermal growth factor

EGFR – Epidermal growth factor receptor

ELP – Elastin like polypeptide

EPR – Electron paramagnetic resonance

FACS – Fluorescence-activated cell sorting

FAD – Flavin adenine dinucleotide

FCCP – Carbonyl cyanide-4-(trifluoromethoxy)phenylhydrazone

FITC – Fluorescein isothiocyanate

FLIM – Fluorescence lifetime imaging microscopy

FMN – Flavin mononucleotide

FP – Fluorescent protein

FPALM – Fluorescence photoactivation localization microscopy

FPF – Fluorescent protein fusion

FR- Folate Receptor

FRET – Forster resonance energy transfer

FTN – Ferritin

FTNH – Ferritin heavy chain

FTNL – Ferritin light chain

GECI – Genetically encoded calcium indicator

GFP – Green fluorescent protein

GI – Gastrointestinal

HA – Haemagglutinin

HEPES – 4-(2-hydroxyethyl)-1-piperazineethanesulfonic acid

hPSC – Human pluripotent stem cells

IDA – Iminodiacetic acid

IPTG – Isopropyl β-D-1-thiogalactopyranoside

LED – Light-emitting diode

LMA – Low melting agarose

LSCM – Laser scanning confocal microscope

MCTS – Multi-cellular tumor spheroids

MiniSOG – Mini singlet oxygen generator

MMPs – Matrix metalloproteinases

MoNaLISA - Molecular nanoscale live imaging with sectioning ability

NADH – Nicotinamide adenine dinucleotide

NFC – Nanofibril cellulose

NHS-ester – N-hydroxysuccinimide ester

NIRS – Near infrared spectroscopy

NTA – Nitrilotriacetate

PCL – Polycaprolactone

PDLLA – Poly-D, L-lactide

PDMS – Polydimethylsiloxane

PEG – Polyethylene glycol

PGA – Polyglycolic acid

PLA – Polylactic acid

PLIM – Phosphorescence lifetime imaging microscopy

PLLA – Poly-L-lactide

PtCP- tetracarboxylic platinum (II)-coproporphyrin I

Pt-Gal – Pt (II)-tetrakis(pentafluorophenyl)porphine - tetra (thiogalactose)

Pt-Glc – Pt (II)-tetrakis(pentafluorophenyl)porphine - tetra (thioglucose)

PtTFPP – Pt (II)-tetrakis(pentafluorophenyl)porphine

PVX – Potato virus X

Q.Y – Quantum yield

RNA – Ribonucleic acid

ROS – Reactive oxygen species

RSFP – Reversibly photoswtichable fluorescent proteins

RT – Room temperature

$SCO^{2-/-}$ – Lacking, *SCO_2* cytochrome C oxidase assembly protein

SIM – Structured illumination microscopy

smURFP – Small ultra-red fluorescent protein

STED – Stimulated emission depletion

STORM- Stochastic optical reconstruction microscopy

TCSPC – Time-correlated single photon counting

TfR – Human transferrin receptor

TMRM – Tetramethylrhodamine, methyl ester

TMV – Tobacco mosaic virus

VLP – Viral like particle

VNP – Viral nanoparticle

YFP – Yellow fluorescent protein

Chapter 1: Literature review- 3D tissue models and biosensor materials for tissue engineering

1.1 Introduction

Tissue engineering is the development of biologically relevant tissues outside of the human body for clinical use, combined with the understanding of the complex physiological characteristics and processes of living tissues. It is a multi-disciplinary field that encompasses 3D cell and tissue-based scaffold and non-scaffold-based models, live cell microscopy and imaging modalities, along with fluorescence and phosphorescence-based biosensors. All these disciplines work together to drive the development of biologically relevant 3D tissue models, which can be monitored in real time for modelling complex physiological and non- physiological diseased states. Tissue engineered 3D models are currently used in studying stem cell growth and transplantation, personalised medicine, and the modelling of various disease states (i.e. cancer) along with the development of therapies for their treatment. For such engineered tissues to be physiologically relevant, real time monitoring and optimisation of their extracellular and intracellular gradients (e.g. O_2, Ca^{2+}, pH, and temperature) must be applied. Therefore, the development of imaging modalities and biosensors compatible with live cell imaging of 3D tissue models is key for the advancement of the field of tissue engineering. Here, I will discuss the state of various 3D tissue models, imaging modalities, and biosensor materials applied for tissue engineering, and the future directions and possibilities that are being explored.

1.2 Three-dimensional tissue models

Several cell-cell and cell-extracellular matrix (ECM) interactions establish a communication network that maintains physiological characteristics of a living tissue. These include structural tensile strength, cellular polarity, adhesion, differentiation, migration and proliferation [1]. *In vitro* cell cultures that establish these physiological interactions can mimic real *in vivo* tissues much more closely than two-dimensional (2D) cultures. Cell flattening occurring in conventional 2D culture results in abnormal alterations in cytoskeleton, gene expression, nuclear shape, cellular proliferation and differentiation, and susceptibility to drug therapies [2], all of which are significantly different from those seen in 3D. Currently, 3D tissue models are used in stem cell therapies as a support matrix for the growth and transplantation of *in vitro* systems that closely mimic *in vivo* morphology. Such models are applied in both cell physiology and drug therapy studies. Such models are also useful for studying cancer biology, in which we can model cancer growth and develop cancer therapies [3, 4]**.** 3D tissue models can be categorised into two main groups, scaffold-based and scaffold-free systems, examples of such types can be seen in Figure 1.1, below.

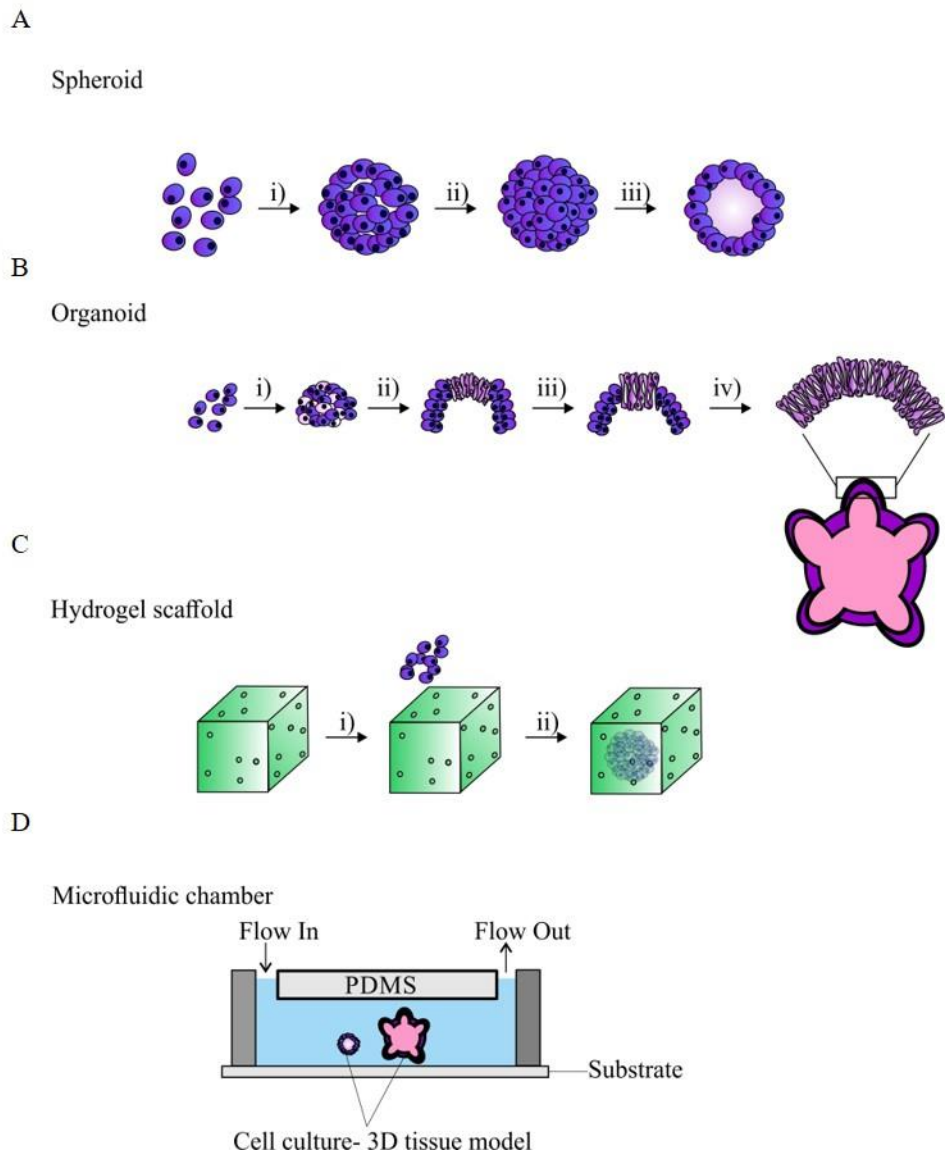

Figure 1.1. Examples of 3D tissue models. (A) Cells can aggregate together forming spheroids (i), then polarize (ii), and differentiate (iii). (B) In organoid system, stem cells differentiate (i) and self-organize by processes of cell sorting (ii) and lineage commitment (iii) into fully developed structures possessing many features of real tissue (iv). (C) Hydrogel and related scaffold structures provide structured and rigid 3D environment for cells and aggregates growing within. (D) Microfluidic chamber allows culturing the 3D tissue model under the controlled flow.

1.2.1. Scaffold-free 3D tissue models

Scaffold-free models utilise the ability of cells to synthesise their own ECM, or naturally produce it within live tissue. They include spheroids [5], organoids [6], tissue explants [7, 8], artificial tissue [9] and xenografts [10].

The most common type of scaffold-free model are spheroids (Fig 1.1 A), which are produced via assembly of mono- or multi-cell type-consisting spherical shape aggregates, typically of 50-500 μm

size [5]. Spheroids can be produced in several ways, such as liquid overlay technique [11], hanging drop technique [12], microwell arrays via micropatterned wells [13] or by bio-printing [14]**.** Cells within the spheroid can re-establish mutual contacts and re-create specific microenvironments (e.g. O_2, pH and metabolite diffusion gradients), therefore, reproducing cellular morphology *in vivo.* For cancer cell spheroids, often referred as multi-cellular tumor spheroids (MCTS), four phenotype classifications have been proposed: round, mass, grape-like, and stellate phenotype [15], [16], [17]. The round-type spheroid is characterised by strong cell–cell adhesion, with regularly organised nuclei. The mass-type spheroids are also spherical in shape but are much larger and possess disorganised nuclei. The grape-like type spheroids have grape-like morphology forming loose clusters, with weak cell-cell interactions. The stellate-type spheroids are invasive, possessing stellate projections that migrate chains of cells into the ECM. The phenotype of tumor spheroids is dependent on gene and protein expression profiles of the cell lines [15] and signals from tumor microenvironment [16]. Due to heterogeneity of conditions and gradients of metabolites, nutrients, metabolic waste and soluble factors (e.g. growth factors, chemokines, cytokines) spheroids are often comprised of cells in various stages of the cell cycle [18]. Radial structure of MCTS results in radial differences in gene and protein expression, cell regulation and drug metabolism. These gradients and cellular heterogeneity within the spheroid culture closely resemble *in vivo* tumors [19]. Applications of MCTS to study cell metabolism, have shown similar increased glycolysis and lactate production, and Warburg effect of metabolic switching seen as in tumors *in vivo* [20, 21]. Culturing MCTS with stromal and immune cells allows for the study of host-tumor and microenvironment interactions that play key roles in cellular regulation, angiogenesis, and invasiveness of tumors [22-24]. Therefore, MCTS are useful tools in studying tumor biology and drug treatments. Spheroids can also be cultured from mesenchymal stem cells (MSCs), which display anti-inflammatory responses, angiogenesis, and tissue regeneration with improved cell survival after transplantation [25-27], all of which are not seen in 2D cell cultures of MSCs. MSC spheroids possess an elongated exterior morphology and a spherical interior morphology, with small rounded MSCs are prone to differentiation into the adipogenic lineage, whereas large, elongated spheroids differentiate into the osteogenic lineage [28]. MSCs spheroids are applied in a range of preclinical animal studies such as: bone and cartilage regeneration with bone marrow MSCs and synovial MSCs [29, 30], regeneration in liver and kidney tissues with umblival cord MSCs and adipose tissue MSCs [31, 32], and wound healing in dermal wounds with adipose MSCs [33]. Overall MSC spheroids show high potential in tissue engineering for regenerative medicine, however a greater understanding of molecular signaling within the MSCs needs to be explored, along with better methodologies for clinical applications. Spheroid cultures have been successfully imaged via number of modalities including light sheet microscopy [34], confocal fluorescence and phosphorescence microscopy [35, 36] and two-photon microscopy [37].

Organoids are cultured organ-specific 3D cellular clusters produced from primary tissue, embryonic stem cells or induced pluripotent stem cells (Fig 1.1 B). In contrast to spheroids, they contain different cell types, are capable of self-renewal, organization via self-sorting, and, to some extent, possess functionality seen the tissues they are derived from *in vivo* [38]. Organoids produced to date include: intestinal [39], kidney [40], brain [41], retinal [42], stomach [43], lung [44], inner ear [45], skin [46], and liver-like tissues known as liver buds, all produced using progenitor stem cell types or induced pluripotent stem cells [47]. Despite being a more physiological 3D tissue model than spheroids, amenable to established experimental techniques, and disease modeling, organoids still lack proper vascularization and blood supply. However, these issues can be overcome by co-culturing with additional cell types (e.g. stroma and immune cells), by perfusion and microfluidic approaches to generate concentration gradients of growth and signaling factors [48] and to mimic blood flow through the tissue [49]. In recent years efforts to produce more physiological relevant organoids by bioengineering have been made. A human intestinal tissue model with functioning enteric nervous system was developed from human PSC derived neural crest cells and human intestinal organoids. Enteric nervous system is responsible for gastrointestinal (GI) motility, secretion, blow flow, permeability, and fluid exchange, with its function frequently lost in many GI diseases. The development of this intestinal organoid model with enteric nervous system function allowed for the study of motility disorders of the GI tract such as Hirschsprung's disease which is caused by defective enteric neuron development [50].

The development of patient-derived organoids has the potential for a more stable and physiological model closely mirroring disease states and cancer histology's they are derived from, along with drug screening and discovery; due to the minimizing of culture induced genetic drift. Research using organoids generated from biopsied primary human pancreatic adenocarcinoma maintained the tumour differentiation status, histology, and patient-specific physiologic changes including: hypoxia, oxygen consumption, epigenetic marks, and differential sensitivity to Enhancer of zeste homolog 2 inhibition [51]**.** Organoids are also compatible with standard confocal and two-photon excited fluorescence microscopies, which have been applied to study chromosome segregation by genetically encoded fluorescent proteins (FPs) [52], analyse proliferating cells by fluorescence lifetime imaging microscopy (FLIM) [53] and responses to drug treatments [54].

1.2.2 Scaffold-based tissue models

Scaffolds are designed to encourage adhesion, proliferation, differentiation, and migration of cells seeded and grown within. They provide mechanical strength, porosity, efficient exchange of gases, nutrients, and metabolites. Frequently used hydrogels represent water-rich 3D networks of hydrophilic cross-linked polymers, that closely mimic the ECM with mechanics of soft tissues, supporting transport of metabolites and waste, and cell adhesion [55]. Hydrogels are represented by natural (e.g. cellulose,

collagen, chitosan) and synthetic materials (e.g. polyethylene glycol) [56]. Scaffolds can also be produced from synthetic polymers such as polycaprolactone [57], polylactic acid [58], polystyrene [59] or others [60].

Collagen is a fibrous protein, comprised of a right-handed bundle of three parallel, left-handed polyproline II-type helices, providing structural support to body tissues [61]. Collagen hydrogels are primarily comprised of type I collagen, derived from pepsin- or acid-solubilized form, frequently sourced from rat tail tendon. The hydrogel is formed by increasing temperature and pH, which induces collagen fibril assembly in presence of culture media or cells [62]. Collagen hydrogel scaffolds have been used to mimic the 3D tumour microenvironment, demonstrating co-existence of multiple cell types in cancer development [63], particularly in breast cancer, in which collagen is the main component of the breast stroma. Here in breast tissues, collagen affects morphology and the phenotype of the breast epithelium, and its variation in density has been linked to onset of breast cancer [64]. Dense collagen type 1 3D scaffolds were used to mimic high collagen densities seen in breast epithelium, the dense collagen scaffold was observed to have a strong interaction with prolactin resulting in tumorigenic conversion of T47D cells into an invasive malignant phenotype [65]. Further studies showed that dense collagen type 1 scaffolds have regulatory effects on 17β-estradiol (E2) and prolactin interactions, increasing growth, invasion and modification of the collagen matrix in estrogen receptor alpha breast cancers [66]. Collagen concentration and elasticity also affects the 3D culture of ovarian follicles, with differences observed in cell survival, follicle growth and development, sex hormone production, and oocyte maturation; with changes in collagen type 1 elasticity and concentration [67]. This study Highlights the importance of collagen as a 3D scaffold matrix and its overall compositional effects on 3D cell culture. Therefore, special care should be taken when using collagen in 3D cell culture as it is susceptible to reorganization via interactions with cells, thus the scaffold can lose its orientation and have detrimental effects on cellular behavior.

Matrigel is a cocktail of ECM proteins extracted from Englebreth-Holm-Swarm epithelial tumors in mice, where they form a basement membrane (BME). The BME is an important ECM in epithelial and endothelial tissues where it supports tissue integrity, acting as a barrier to cells and molecules, separating different tissue types thereby maintaining tissue specificity, and acts as a transducer for various growth factors and enzymes [68]. Matrigel primarily consists of BME-derived components laminin, collagen IV, entactin, and heparin sulfate proteoglycan. These provide structural and signaling functions seen in the BME. Matrigel forms a hydrogel at 24-37 °C and is frequently used 3D scaffold [69], for example, in 3D tumor cell culture where it helps to create microenvironment for cancer ‘stem-like’ cells, influencing miRNA expression involved in cell regulation, adhesion and migration [70, 71]. Matrigel is also widely applied in morphological and developmental studies of non-malignant cell lines, such as breast and prostate epithelia, with and without microfluidics [72], as well as intestinal epithelia

in combination with organoid culture [73]. There are several limitations of Matrigel based on its composition, (decreased collagen-I and hyaluronan), batch-to-batch variability, and strict storage conditions. Matrigel is non-human in origin and therefore its composition does not accurately mimic the human tumour microenvironment, this affects its translational potential and its use in tissue engineering. Thus, further research is needed towards the development of hybrid matrices that can improve or replace Matrigel [74], and one such alternative is Myogel, which is derived from human uterus benign leiomyoma tumors. Experiments comparing Matrigel with Myogel on its own or combined with low melting agarose (LMA), showed that both Mygogel and Myogel-LMA out preformed Matrigel in *in-vitro* transwell invasion and capillary formation assays [75]. Overall myogel more closely mimics the human tumour microenvironment of solid cancers in terms of gene and protein expression, invasion and migration. The price of Myogel is also much lower than that of Matrigel and avoids the need to sacrifice thousands of mice for production, therefore, the translational potential of Myogel for tissue engineering is high with the possibility of culturing tumour tissue from patients.

Cellulose is an ideal scaffold material as it mimics the mechanical properties of the ECM, as well as being both biocompatible and biodegradable. Its backbone consists of glucose units connected by β-glycosidic linkages, arranged into a highly organized fibrillar structure. The inter and intra-chain hydrogen bonding restricts flexibility, and therefore provides rigidity to the polymer. The cellulose structures used as 3D scaffold materials are known as nanocellulose, which refers to extracts or processed cellulose materials with nano-size dimensions. Nanocellulose can be divided into three groups according to their morphology and method of production: cellulose nanocrystals (CNC), nanofibril cellulose (NFC) and bacterial cellulose (BC) [76]. Nanocellulose has found applications in tissue engineering, photonics, biosensing and biomaterials research [77], being utilised as scaffold materials [76, 78, 79] for cartilage tissue regeneration [80], bone tissue[81], differentiating endothelial cells [82] and others.

NFCs are comprised of cellulose nanofibers derived from raw cellulose material via enzymatic hydrolysis and mechanical shearing processes, which result in delamination of the fiber wall and fibrillation into nanoscale network of cellulose fibers [83]. NFC hydrogels have been utilized as 3D tissue culture scaffolds due to their rigid, porous and tunable structure, finding uses in research of human pluripotent stem cells (hPSC) [84] and liver progenitor cells [85]. BC is produced by microorganisms extracellularly, predominantly by *Gluconacetobacter xylinus*. BC is synthesised by protruding glucose chains from the bacterial pores, which combine forming fibrils which aggregate, forming cellulose nanofibers [86]. These nanofibers are well spaced, forming a large surface area in which a large volume of water can be stored, and extensive hydrogen bonding between the nanofibers gives BC a high mechanical strength. These properties make BC very attractive for applications as scaffolds in tissue replacement, with uses in tissue engineering of cartilage, where it has been shown to support the

proliferation and ingrowth of chondrocytes [87, 88]. BC has recently found applications in tissue engineered blood vessels, with one such study using tubular implants of BC for the replacement of carotid arteries in sheep where it provided a scaffold for the attachment of vascular smooth muscle cells. However, a low patency rate of only 67% was achieved, well below the 97% patency rate accepted for clinical studies [89]. Decellularised plant materials are a recently developed type of cellulose scaffold that provide a pre-vascularized scaffold for tissue engineering applications, taking advantage of similarities in the vasculature of plant and animal tissues. decellularised is carried out by treatment with hexane to remove the waxy hydrophobic layer from the outside of the plant, and bleach to remove the plant cellular component. It has been shown that decellularised spinach leaves when re-cellularized with human endothelial cells, displayed contractile function and calcium flux [90].

Cellulose-derived scaffolds can be modified by a wide range of processes for cell adhesion and biocompatibility such as: (i) Chemically, with polyethyleneglycole, thiols and other oligo- and polymers [91]. (ii) With the use of proteins with cellulose-binding domains [76, 92]. Or (iii) biosynthetically [93]. The same can be applied for biosensing applications via modifications with: nanocrystals, [94], FRET-based enzyme-based biosensing, for analysis of proteolytic activity in wound fluids and gold nanoparticles immobilised via antibodies [95]. To date, some of the practical biosensing applications for cellulose represent biomass conversion and immobilisation [96], multi-colour labelling [97, 98] and biomarker sensing in the alimentary tract of daphnia [99].

Major synthetic polymers used for scaffold-based tissue models come from the polyester family of hydrophobic homopolymers; Polylactic acid (PLA), Polyglycolic acid (PGA) and, Polycaprolactone (PCL).

Polylactic acid (PLA) is a semi-crystalline hydrophobic polymer composed of lactide monomer subunits. PLA is synthesized by ring-opening polymerisation (ROP) of a lactide monomer [100], and is degraded by hydrolysis of its ester groups, in which its substituent monomers are naturally metabolized yielding CO2 and water [101]. Lactide is a chiral molecule and therefore exists in two optically active isomers: L and D-lactide. Depending on what lactide isomer is used in the ROP reaction three times of PLA can be synthesized: Poly- D- lactide (PDLA) is formed from D-Lactide monomers, Poly- L – lactide (PLLA) is formed from L-Lactide monomers and Poly- D,L- Lactide (PDLLA) is a racemic mixture of both D and L isomers. PDLA contains amorphous regions and as a result PDLA and PDLLA degrade at a faster rate than PLLA. PLA polymers have applications in drug delivery [102-104], implantable medical devices [105] and 3D cell culture scaffolds [58].

Polyglycolic acid (PGA) is a semi crystalline hydrophobic polymer composed of glycolide monomer subunits. PGA is synthesized by ROP of glycolic acid, catalyzed by tin(II) 2-ethylhexanoate ($Sn(Oct)_2$) [106], and like PLA, is degraded by hydrolysis of its ester groups. PGA degrades faster than PLA due to it being less hydrophobic than PLA, which possesses a methyl instead of a hydroxyl group. PGA polymers have found applications in 3D cell culture and tissue engineering scaffolds [107-109]

Applications of PGA on its own are limited to the short term due to its fast degradation rate, and clinical applications of PGA are as a co-polymer with PLA, known as poly(lactic-co-glycolic acid) (PLGA) [110] or with other biological components, such as collagen [111] and hyaluronic acid [112].

Polycaprolactone (PCL) is a semi crystalline hydrophobic polyester, and is synthesized largely by the ROP of an ε-caprolactone [113]. Because its hydrophobicity it degrades slower than other polymer scaffolds, such as PLA and PGA. Therefore, PCL has advantages in long term applications, such as drug delivery [114] due to controlled release of its cargo, implantable medical devices such as bone grafts, and has found applications in 3D cell culture scaffolds [57].

Both PLA and PGA are biodegradable and bioresorbable as the polymers are broken down into naturally occurring lactic and glycolic acid respectively. However, the acidic by-products can acidify the local environment altering cellular behavior and survival [115, 116] as well as causing inflammatory complications [117, 118]. There is conflicting research and studies in the literature as to the biocompatibility of PLA and PGA, in terms of their immunogenicity and toxicity, with several studies supporting an acceptable biocompatibility, whilst others have shown systemic or local reactions due to acidic by-products. Synthetic materials unlike natural ones, lack intrinsic cellular adhesion sites and possess low cellular differentiation potential. Therefore, they must be modified for improved cellular adhesion and differentiation. Problems also arise in *in vivo* applications with a loss of homogeneity in cellular populations, due to the scaffold interior being difficult for cells to access.

1.2.3 'Hybrid' scaffold materials

In hybrid scaffold materials sensing dyes, peptides and cell adhesion molecules are attached to a 3D scaffold material, in which the cells or tissue are cultured [59, 119, 120]. The scaffolds attached to sensor dyes are of particular intertest as they can be used for multi-parametric imaging of 3D tissue models, for example, hybrid phosphorescent O_2-sensing scaffolds were proposed for range of cell-based models, including tumor spheroids and brain slices [59]. Here, the commercial polystyrene-based scaffold Alvetex™ was impregnated with a phosphorescent O_2-sensitive dye Pt(II)-tetrakis(pentafluorophenyl)porphine (PtTFPP), and optimised for live cell fluorescence microscopy and imaging of O_2 distribution in cultured cells. Results showed the scaffold allowed for the measurement of cellular: oxygenation, respiration, viability, and responses to drug treatment, all at various depths within the scaffold, allowing for control of cellular environment and their conditions. In such scaffolds, cells and tissues do not need to be stained, as their functional status is analyzed indirectly, via extracellular gradients. Similarly, scaffolds based on other materials and for analysis of other physiologically important biomolecules (e.g. Ca^{2+}) can be developed. Hybrid scaffolds allow for the real time monitoring of cell or tissues environment along with its extracellular influence on its environment in response to drug treatments and hypoxic conditions. Such scaffolds would potentially

allow the development of more translational relevant engineered tissue models as well as a more accurate and comprehensive study of cellular processes and drug treatments.

1.2.4. Microfluidics in 3D tissue models

The use of microfluidics allows for the precise control of fluid flow and mass exchange in micrometer-size structures, such as channels and chambers. In 3D tissue models it can provide spatial and temporal control for co-cultures of multiple cell types, fluid flow and sheer stress (e.g. perfusion of circulating vasculature and immune cells) and biomolecule gradients [121]. A 3D vascularised organotypic microfluidic assay was developed to study breast cancer metastases, mimicking human breast cancer cell extravasation into a bone mimicking (BMi) microenvironment, generated with osteo-differentiated primary human bone marrow-derived mesenchymal stem cells, through perfusable human microvascular networks composed of endothelial and mural-like cells. Results showed that extravasation rates were significantly different with BMi microenvironment to the unconditioned or myoblast containing microenvironment [122]. This research demonstrates the power of microfluidics in the development of a physiological model for breast cancer metastases and drug screening.
Microfluidic systems are prepared mainly by process known as 'soft lithography' [123], [124], using optically clear and O_2-permeable polydimethylsiloxane (PDMS), which is compatible with live cell fluorescence imaging [125], however PDMS is autofluorescent [126] which can affect imaging.
'Organ-on-a-chip' technology combines microfluidics with 3D tissue cultures of spheroids or organoids to mimic tissue and organ physiology *in vivo* [123]. Organ-on-chips have been reported for a range of organs including: liver [14, 127], intestine [128, 129], lung [130, 131], heart [132, 133], kidney [134, 135], vasculature [136-138], and blood brain barrier [139]. Such models have been applied in disease modeling [140], drug screening and toxicity testing [141]. However, it is unclear to what degree organ-on-chips can model real *in vivo* tissue. Cell seeding and growth in microfluidic channels limits the size of produced tissue models and exposes cells to various types of stresses, such as temporary hypoxia or anoxia [142, 143].

1.2.5. Future of 3D tissue models

Ensuring the reproducibility and physiological relevance of the different 3D models is of paramount importance. The goal of 3D tissue models is the development of a tissue model that can mimic tissue architecture and cellular microenvironments, down to the microscopic detail. Different approaches separately or in combination, can help to tackle these issues faced such as: microfluidics, bioprinting, high-resolution live cell imaging, and hybrid scaffold materials. The use of microfluidics can help model blood flow and shear stress experienced by cells, and bioprinting allows patterning (3D printing) of biological materials including cells, biomolecules and biomaterials, to produce tissue-mimicking

constructs. The technology has been already used in transplantation [144], printing of 3D heterogeneous hydrogel structures [145] for research in regenerative medicine [146, 147], and drug screening [148], [149]. 3D bioprinting of biological materials is based on three strategies: Laser [150], Droplet [151], and extrusion [152] printing. Droplet bioprinting is the earliest bioprinting technique, in which droplets are used to encapsulate cells and nonliving materials for printing layer by layer on a substrate. The use of droplet printers has seen a rise in popularity in recent years due to relatively low costs, high precision, and the ability to print multiple cell types with a high viability post printing, along with other nonliving materials such as hydrogels. However, this technique is not without its drawbacks as it is not compatible with printing high viscosity materials or high cell densities. This in turn affects the mechanical strength of the resulting structures and more so, the production of a fully functional and physiological 3D construct [153, 154]. In laser bioprinting, cells and nonliving materials are excited by laser beam focused on a laser absorbing ribbon, which collects the 3D construct on a substrate facing the ribbon. Laser bioprinting is nozzle-less system and therefore avoids the problems associated with high viscosity bio inks and cell densities faced by the inkjet bioprinting technique. However, the laser printer itself is costly and it cannot print large constructs due to the limited width of the laser beam [155], this has affected the potential clinical translation of the technique. Extrusion bioprinting uses an ejector system in co-ordination with an automated three axis stage, to deposit cells or nonliving materials on a substrate. The technique allows for printing high viscosity materials, along with cells possessing high density and viability [156]. The continuous dispensing of the bio-ink instead of a droplet allows for higher spatial control in comparison to the inkjet technique, however this can result in sheer stress induced damage of cells [157]. Moreover, the constructs produced are of a clinically relevant size with correct anatomical shape [158]. Therefore, with an affordable price and more clinically relevant constructs than laser bioprinting, as well as a higher viscosity of bio-ink with higher cell densities compared to inkjet printing; Extrusion bioprinting appears to be the most advantageous technique at present.

However, despite advances in bioprinting techniques, the methodology of bioprinting requires figuring out what to print to re-create a physiologically relevant tissue. For example, the gradients of O_2, pH, metabolites and waste products experienced by cells must be known or predictable. Such components can be analysed via multi-parametric live cell imaging (i.e. two-photon excited, confocal, light-sheet and FLIM-PLIM microscopies) and other minimally invasive techniques. Imaging approaches can be ultimately integrated in the design of scaffolds and tissue models, in order to achieve the desired and controllable functional properties of engineered tissue, such as variability or morphology [59, 159, 160].

1.3 Live cell microscopy and different imaging modalities

Tissue and cell samples are traditionally assessed by destructive methods such as histology or immunofluorescence of fixed and sectioned samples, tissue disintegration, flow cytometry, cell lysis,

along with the extraction of RNA, DNA, proteins, and metabolites with subsequent assays via: western blotting, PCR, genetic sequencing, microarrays, ELISA, immunohistochemistry, and mass spectrometry. Destructive methods assess the cellular processes as end points, without real time dynamic monitoring, and often the sample is used up and lost during the analysis process. However, methods like optical imaging, Raman spectroscopy, electron spin resonance, and micro-optical coherence tomography [161], provide real time analysis of tissue and cell samples on a cellular scale. Optical live cell imaging is a noninvasive study of cells in their natural environment, using fluorescence or phosphorescence-based probes to provide analysis of the sample at a cell or organelle level. Fluorescence or phosphorescence-based probes can be attached to small molecules, nanoparticles or genetically encoded protein constructs, for the targeting of specific cell types and organelles. The intensity or lifetime of the fluorescent or phosphorescent light emitted is used to provide information on biomarkers of disease, cellular function or local environment [162]. Figure. 1.2 shows Jablonski diagram of energy transitions in luminescent molecules and the processes of fluorescence and phosphorescence.

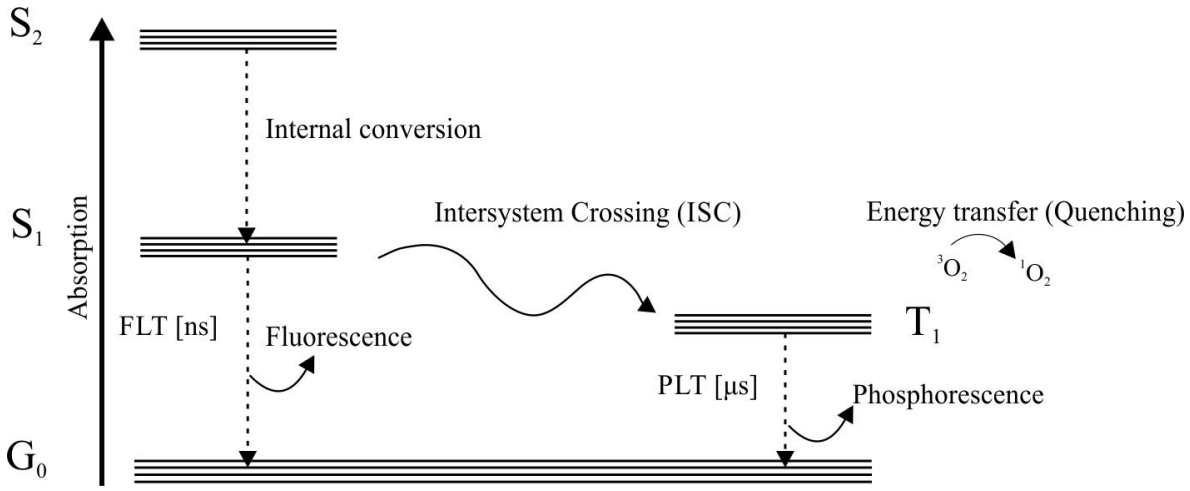

Figure 1.2. Jablonski diagram. After absorption of a photon of light, luminescent molecule gets excited into high energy staye S_1, S_2. Fluorescent molecules return to the ground state G_0, emitting light within ps-ns time interval. Some compounds transition to triplet state(s) via the process of intersystem crossing. Emission from T_1 is a spin forbidden process, which occurs at µs-ms scale. Transfer of energy to donors or quenchers (e.g. paramagnetic O_2 molecule) shorten the emission (phosphorescence lifetime, PLT).

The fluorescent reporter is illuminated with a photon of light exciting a chromophore to a higher energy state. The chromophore can emit fluorescence (10^{-12} - 10^{-9} s) and return to the ground (G_0) state. Due to dissipation of energy, emission occurs at a longer wavelength, in a process known as a Stokes' shift. Some luminescent structures undergo energy transitions much slower and emit light after 10^{-8} - 10^{-3} s,

this is known as phosphorescence. The average time, which the chromophore spends in the excited state before emitting light, is called fluorescence or phosphorescence lifetime. Specific brightness of a chromophore is determined by its molar absorptivity, quantum yield and photostability. Chemical modifications, encapsulation in nanoparticles, shielding by chemical or polypeptide structures, can be used to improve brightness. Some dyes show sensitivity in fluorescence or phosphorescence due to protonation, interaction with other molecules (e.g. ions), quenchers (e.g. O_2), viscosity and temperature [163], altering luminescent emission intensity and lifetime, therefore, these sensitivities can be used to design various probes and biosensors. The fluorescence Stokes' shift allows efficient separation of the emitted light from high-energy excitation and therefore, only allows for the detection of the fluorescent reporter of interest via intensity-based imaging. Fluorescence and phosphorescence imaging can be carried out using different instruments, including widefield and laser scanning confocal microscopes (LSCM), two-photon excited microscope, macroscopic animal imager, super-resolution and other imaging devices.

1.3.1 Platforms for intensity-based measurements

In widefield fluorescence microscopy, a parallel beam of light is produced by single-wavelength light-emitting diodes (LEDs) or mercury lamps. This wavelength of light illuminates and excites the selected fluorophore within the sample, and through the use of optical filters, only the selected emitted wavelength of fluorescence light is collected. Widefield fluorescence microscopy can achieve quality resolution, contrast, sensitivity, and fast acquisition speeds, however, this mode is only suitable for relatively thin samples, up to 50 µm thick and has limited applicability for 3D imaging.

In LSCM a laser beam of excitation light is passed through a pinhole aperture in the optical plane, focusing the light on a specific region of the sample, thereby minimising the problems of photo-bleaching and phototoxicity. The emitted light is channeled to light sensing detectors via the pinhole aperture, rejecting the out of focus light and increasing spatial resolution. The excitation light from the laser beam and its corresponding detection point are scanned across the sample via dichroic mirrors and the image is constructed. The main limitation of LCSM is the limited light penetration depth across the sample, due to light scattering and diffraction, achieving depths of 100-200 µm, however, long wavelength emitting dyes and probes can help improve light penetration depth. Other approaches that complement the LCSM, are light-sheet microscopy [164] and two-photon excited laser-scanning microscopy (2PLSM) [165].

2PLSM is a non-linear optical microscopy process, developed for improved light penetration across thick biological samples [165]. The setup of 2PLSM is similar to the confocal microscope except it uses a laser with ultra-short pulse duration (10^{-15} s), and epi-detection pathway, in which all the light collected by the objective is guided to the detector in order to capture as much of the scattered photons as possible [165]. 2PLSM utilises fluorescence excitation by the process of 'two photon' absorption, in

which two photons of near-infrared light simultaneously excite a fluorophore to achieve higher energy state, sufficient for fluorescence or phosphorescence imaging in the visible range [166]. 2PLSM provides improved resolution with thicker samples up to ~500 μm or more, and minimises photobleaching and photodamage, as the fluorescence excitation is limited to a narrow area of the sample [167]. However, 2PLSM does not improve spatial resolution compared to confocal microscopy [168] and can cause more substantial photodamage in thin samples [169].

A powerful solution to improve light penetration depth and minimise the photodamage is to selectively illuminate a single focal plane, optically sectioning the sample. One such modality that utilises optical sectioning is light sheet fluorescence microscopy (LSFM). The principle of LSFM is that an illuminating sheet of light in X-Y plane is passed through the side of the sample, overlapping the focal plane, perpendicular to the excitation light. LSFM is carried out by selective plane illumination microscope (SPIM) [170]. Due to a thin plane of the sample being exposed to light at a single time, there is a decrease in scattered out of focus light, thereby improving resolution, while photodamage is confined to the thin illuminated section, along with increased acquisition speeds compared to single point scanning measurements [164]. A 3D image of the sample can be generated by passing the light sheet through the sample, forming image stacks [171]. LSFM has been used to image 3D cell culture samples, such as human mammary spheroids MCF10A (50-150 μm thick) expressing histone 2B (H2B) coupled to photoactivatable monomeric cherry (PAmCherry) FP, known as H2B-PAmCherry [172], microfluidic co-culture of human umbilical vein endothelial cells (HUVECs) with hepatocellular carcinoma cells (HepG2) [173] and others. LSFM reduces phototoxic damage and allows for long-term observations of thick 3D cell culture models, with high spatial resolution. SPIM can be bought commercially (e.g. ZEISS Lightsheet Z.1) or can be built by the users themselves (OpenSPIM [174]) allowing them to tailor the setup to their requirements, such as combinations with FLIM and PLIM.

Super resolution microscopy is a collection of imaging methodologies, aimed at achieving imaging resolutions below the diffraction limit. These methods include SIM, STORM, PALM and others [175]. Structured illumination microscopy (SIM**)** is based on fluorescence microcopy, with conventional fluorophores, however, it uses non-uniform illumination of light in the form of a sinusoidal grid, with images taken at three phase shifts for three different grid orientations. The final image is made up of 9 images, with resolution increased two fold compared to widefield fluorescence microscopy [176]. SIM can be applied in three dimensions (3D-SIM) to improve resolution by using three beams of interfering light, generating a pattern along the axial (Z) direction and the lateral (X and Y) directions [177]. Stochastic optical reconstruction microscopy (STORM), is another super-resolution technique that produces a fluorescence image from the localisation of specially designed organic fluorophores and FPs that are switched on and off using light of different wavelengths in a series of imaging cycles. In each cycle, only certain fluorophores are switched on, allowing for their positions to be determined with high accuracy, through repeating the cycle and constructing an overall image [178]. STORM was first

demonstrated with Cy3-Cy5 pair of cyanine dyes [178] but since then have been optimized for other switchable fluorophores in direct STORM (dSTORM) [179]. Fluorescence Photoactivation Localization Microscopy (FPALM) uses light-inducible fluorophores to control the number of visible fluorophores by separating the optically active from the inactive. The sample is illuminated with two different wavelengths, one for readout and other for photoactivation. The photoactivated fluorophores become active when illuminated, subsequently localized and inactivated after period via photobleaching, the cycle is repeated for other photoactivated fluorophores present in sample, thereby constructing the image of the sample [180]. Stimulated emission depletion (STED) microscopy uses selective deactivation of fluorophores to create a fluorescence-based image, thereby minimising the area of illumination at the focal point, enhancing the resolution. STED utilizes a laser beam to excite the fluorophores and once excited, the fluorescence emission can be suppressed via stimulated emission using a depletion beam (STED beam), which suppresses the fluorophores back into the ground state. Ultimately the excitation and STED beam are scanned across the sample forming a sub-diffraction image [181].

Originally designed for fixed tissues prepared in unique way, super resolution microscopy methods are becoming optimised for analysis of live and thick 3D samples, such as 3D tissue models. 2PLSM has been combined with STED to improve image resolution, achieving live imaging of neuronal morphology up to 300-μm deep in living brain tissue [182].

Measuring fluorescence or phosphorescence intensity using above-mentioned instruments allows for labeling, localization, tracking and semi-quantitative measurements in live cells and 3D tissue models. Ratiometric detection is based on the use of dyes or biosensors able to be excited or emitting in response to environmental parameter (e.g. O_2, pH or Ca^{2+}) [183]. Using calibration, the ratiometric response allows for quantitative measurements, however, reliance on different wavelengths has its drawbacks. Normally ratiometric biosensors display spectrally well separated 'reference' and 'sensing' wavelengths, however, with thick and heterogeneous samples these will be absorbed and scattered by tissue differently, depending on the measurement depth. This means that ratiometric calibration will not be valid across the whole sample in 3D due to differences in thickness and heterogeneity of the full sample, thereby questioning the overall applicability of the approach. A number of other methods have been proposed for intensity-based measurements, with measurements of fluorescence or phosphorescence lifetimes among the most advanced.

1.3.2 Measurement of fluorescence and phosphorescence lifetimes

In recent years methods utilising fluorescence lifetime imaging microscopy (FLIM) and phosphorescence lifetime imaging microscopy (PLIM) have become popular. FLIM and PLIM scanners

can be implemented with most microscopy platforms, including LSCM, widefield microscopy, 2PLSM, super resolution and light-sheet microscopy. FLIM and PLIM expand the use of available reporters, which can be distinguished not only by their spectral properties, but also by the luminescence lifetime [184], providing quantitative readouts for pH, ions, O_2 and other parameters.

The key advantage of fluorescence *lifetime* imaging over fluorescence *intensity* imaging is that fluorescence lifetime is an intrinsic property of the fluorophore, independent upon the method of measurement, therefore, results are largely independent from fluorophore concentration, and imaging is not affected by light scattering, photobleaching, and variations in excitation light [163]. The fluorescence lifetime of the fluorophore depends on its energetically unstable state, making it susceptible to quenching via differences in polarity [185], pH, temperature [36], ion concentration, protein interactions and other factors. The shortening of lifetime via quenching-induced conformational changes provides information on the molecular environment of the fluorophore, and allows for the quantitative differentiation between populations of quenched and unquenched fluorophores, in the form of simplified calibration relationships [163]. PLIM shows a number of similar applications, largely including measurement of O_2 and temperature [186, 187]. The limitation of PLIM is that is a slower process than FLIM, however, it provides the possibility of time-gated detection, allowing to effectively filter out the sample background autofluorescence, which is indispensable in analysis of some tissue types, e.g. GI tract.

A number of experimental approaches have been developed for FLIM and PLIM, including frequency and time domain-based readout, with variations such as time-correlated single photon counting (TCSPC) using fast-gated image intensifiers [188, 189]. In TCSPC, the luminescent molecules are excited by a pulsed laser source with a high repetition rate. Photons emitted by the sample are detected and the times associated with them are measured, thereby constructing a decay curve. This method provides high detection sensitivity, accurate lifetime measurements and, when combined with LSCM and 2PLSM, it allows optical sectioning of the sample. TCSPC is also compatible with PLIM, allowing fast acquisition times, shorter than 1 minute. FLIM and PLIM constantly illuminating the sample constantly. Instead they illuminate via combination of very short pulses, in the 10^{-12} s range. This minimizes the degree of photodamage than in conventional widefield or laser-scanning microscopies. Systems such as TCSPC also rely on highly efficient photon counting detectors, allowing using lower laser power intensities. These are the main advantages of the methodology, making it highly suitable for analysis of 3D tissue models.

1.4 Probes for live cell multi-parametric imaging of 3D tissue models

Imaging of 3D cell and tissue models requires high depth penetration of light, fast imaging speed, and the use of non-destructive intensity of excitation light. High depth penetration of light is needed to

image the thick 3D samples, avoiding light scattering reducing the resolution of the image. The depth penetration of light depends on: the ability to image the fluorophore or phosphor via microscopy techniques and its physical properties such as its spectra, along with the homogeneous distribution of the probe within the sample. Fast image acquisition speeds and low intensity of excitation light are needed to prevent and limit photobleaching and phototoxicity, which can lead to loss of luminophore function and toxic effects on the live samples. Photobleaching and phototoxicity occur due to energy emitted by excited luminophores, which is not limited to the form of fluorescence or phosphorescence emission of light, for example, this dissipated energy can cause reactions with O_2, producing reactive oxygen species (ROS) [190, 191]. The quenching of phosphorescence also produces singlet oxygen, however, this process causes minimal sample damage with modern O_2 probes [187].

The probes and fluorescent dyes needed for multi-parametric imaging of 3D tissue models can be adapted from traditional intensity-based measurements and advanced FLIM and PLIM applications. In theory everything is compatible with 3D tissue models, but the practical challenge is the ability to efficiently stain the 3D tissue model in a reasonably short period of time. Small molecules and nanoparticles used can display very poor distribution across the sample or stain only particular cell types, with most nanoparticles also displaying poor staining in formed 3D tissue models. The use of genetically encoded biosensors is mainly limited to use of transgenic models and is challenging for transient transfection. Multi-parametric analysis can be also complemented by classical immunofluorescence, however, antibodies are bulky molecules that require either prolonged staining protocols or laborious sectioning of the samples.

The development of luminescence lifetime probes can potentially solve the challenges involved in live cell imaging of 3D tissue models. Lifetime imaging is independent of fluorophore concentration and is therefore unaffected by light scattering, in relation to sample thickness and phototoxicity [163]. A wide array of FPs [192, 193] and nanoparticles [194] have been utilized in FLIM [163, 195] and PLIM [196] for live cell imaging. In Table. 1.1, the usability of a wide range of probes for multi-parametric imaging of 3D tissue is highlighted.

Table 1.1. Probes and biosensors with useful properties for multi-parametric quantitative imaging of 3D tissue models (Table modified from [197])

Measured parameter	**Description of probe(s)**	**Spectral properties, FLIM/ PLIM-compatible (?)**	**3D tissue models tested. Comments. References**
Autofluorescence 'metabolic' imaging	Endogenous NAD(P)H, FAD	340 nm exc. (700-740 nm two-photon)/ 460 nm em. FLIM (1-6 ns) FAD: 450 nm exc./ 520 nm em.	Tumor spheroids and 'organoids' [198-200].
Cytosolic NADH-NAD^+ ratio	Genetically encoded biosensor	488 nm exc. (800 nm two-photon)/ 525 nm em. FLIM (1.87-2.6 ns)	Needs transfection. More selective and brighter than autofluorescence imaging.

	Peredox		Tested on live brain slices (*ex vivo*) [201].
Redox/ ROS	Genetically encoded reduction-oxidation-sensitive green fluorescent protein 1 (roGFP1)	488 nm exc. (740-950 nm two-photon)/ 525 nm em. Ratiometric, FLIM (2.46 ns)	Needs transfection. Moderate responses in fluorescence lifetime (but better in ratiometric intensity mode) to changes in redox ratio. Tested on live brain slices (*ex vivo*)[202].
Molecular oxygen (O_2)	Nanoparticles: PA2, NanO2/ MM2, SI/SII	405 nm exc. (740-780 nm two-photon)/ 650-660 nm em. PLIM (20-70 μs) SII-series: 470 and 632 nm exc./ 770 nm em. PLIM (10-40 μs).	Neurospheres, brain slices, tumor spheroids. Most bright, photostable and reliable calibration but typically need 'continuous staining' procedure [35, 203].
Molecular oxygen (O_2)	Small molecule probes Pt-Glc, Pt-Gal	One-photon excited, 405 nm exc./ 650 nm em. PLIM (20-57 μs)	Tested in neurospheres, brain slices, tumor spheroids, *ex vivo* colon, bladder and intestinal tissues. Pt-Glc displays some tissue-specificity in calibration. More efficient tissue staining than with nanoparticles [196, 204-209].
Molecular oxygen (O_2)	Porous polymer-based O_2-sensitive scaffolds for 3D culture	405, 540 nm exc./ 650 nm em. PLIM (20-55 μs).	Tested with tumor spheroids (HCT116, PC12) and live brain slices. Allow monitoring of pericellular O_2 in 3D culture grown within polymer scaffold [59, 210].
Intracellular temperature	Nanoparticles	546 nm exc./ 585 nm em. FLIM (2.4-2.7 ns)	Tumor spheroids [211].
pH	Genetically encoded fluorescent proteins	pHRed: 440 nm exc. (860 nm two-photon)/ 610 nm em. FLIM (1.7-2.1 ns) ECFP: 440 nm exc./ 512 nm em.) FLIM (1.8-2.8 ns)	Need transfection. Not tested with 3D tissue models. Some are visible only under two-photon excitation [212, 213].
pH	Nanoparticles	546 nm exc./ 600 nm em. FLIM (3.7-4.7 ns).	Tested with rat primary neurospheres. Localize in lysosomes [214].
pH	BCECF and other small molecule dyes	Green-red fluorescence. FLIM.	Concentration and cell-type dependent responses, low photostability [214]. Tested with cockroach salivary duct tissue [215].
Ca^{2+}	Small molecule probes Oregon Green BAPTA-1 (OGB-1) and others	OGB-1: 488 nm exc./ 510 nm em. FLIM (0.6-3.9 ns)	Live brain slices [216-218].

Ca^{2+}	Genetically encoded biosensor Cerulean	432 nm exc./ 530 nm em. FLIM (0.8-2.4 ns).	Needs transfection or transgenic animals. Live brain slices. Preferred use in two-photon excited mode [219, 220].
Lactate/ glycolysis	Genetically encoded ratiometric sensors	430 nm exc./ 485 and 535 nm em. (ratiometric) Not tested in FLIM.	Needs transfection. Live brain slices [221, 222].
Labeling of proliferating cells	Cell-permeable dye (Hoechst 33342) quenched by BrdU	405 nm exc./ 440 nm em. FLIM (1.3-2.2 ns)	Tumor spheroids and intestinal organoids. Needs comparison between BrdU (+/-) cells in the experimental model. Can be adapted to other dyes staining nuclei [53].
Viscosity	Small molecule probes (BODIPY-based rotors)	488 nm exc. (800 nm two-photon)/ 515 nm em. FLIM (1-3 ns).	Tumor spheroids. Concentration-dependent calibration complicates data interpretation for 3D tissue models [223].
K^{+}	Nanoparticles (BODIPY-based K+ -sensitive fluoroionophore FI3 encapsulated in cationic polymer RL100 nanoparticles)	640 nm exc./660 nm em. FLIM (3.5-4.5 ns).	Tumour spheroids, neurospheres, intestinal organoids, and *ex vivo* organotypic rat brain slices [224]

1.4.1 Fluorophores

Endogenous fluorophores are fluorescent biomolecules present naturally within a sample and contributes to cell and tissue autofluorescence. This autofluorescence is normally caused by fluorophores such as: aromatic amino acids, reduced nicotinamide adenine dinucleotide (NADH) and flavin adenine dinucleotide (FAD). FLIM of endogenous fluorophores and their expression profiles provides information on the metabolic and functional state of the sample, which can be used to differentiate healthy tissue from diseased. The main advantage of endogenous fluorophores is that no specific labeling is required. However, the fluorescence signals are often weak and non-specific due to limitations in light penetration and low expression of the fluorophores. Furthermore their interactions with cellular components and proteins is also very complex, which results in multi-exponential decays, which in turn affects the interpretation of measured fluorescence lifetimes. Due to short excitation wavelengths of endogenous fluorophores, for example near-UV in the case of NADH, two-photon excited imaging must be employed. In comparison to *state-of-the-art* approaches to analyze the balance of cell energy production pathways [225, 226], metabolic imaging with NAD(P)H does not provide

direct information on oxidative phosphorylation, glycolysis and Krebs cycle fluxes and therefore, can be viewed as supplementary parameter in analysis of cell metabolism.

Exogenous fluorophores and phosphors address the above limitations associated with endogenous fluorophores, such as signal weakness and low specificity. Exogenous fluorophores and phosphors have a large diversity in wavelength and lifetime range, and in their production. For example, they can be: proteins, bioconjugates, or nanoparticles etc. The luminescence lifetime of fluorophores is frequently sensitive to changes in their microenvironment, including self-aggregation, interaction with lipids, proteins, their molecular rotation etc. Therefore, responsive FLIM probes can be designed in a way that changes in their luminescent lifetimes will be a function of their environment, allowing for the measurement of quantitative responses to a wide range of potential analytes.

The main directions in the design of FLIM and PLIM probes are; (i) the optimization of their sensing properties such as spectral, brightness, photostability, specificity and the maximal response to the measured parameter, to achieve reliable calibration; (ii) the design of optimal delivery features such as cell permeability, and intracellular or tissue localization. The probe ideally should not interfere with cell physiology or the process it is tasked to analyze, for example, a probe directed for analysis of O_2 should have no effects on oxygen consumption rate, cell mitochondrial function, and energy production pathways. Probes are frequently present in form of simple dyes, small molecule conjugates, FPs, supramolecular conjugates or nanoparticles. From this list, nanoparticles often display the best overall sensing features, including reliable calibration, however, their bio-delivery often represents a complicated task due the complex nature of interactions between nanoparticles and biological components such as extracellular microenvironment, cellular membrane and subcellular environment [227]. In contrast, small molecule dyes can stain 3D tissue models very easily, but their calibration is strongly concentration-dependent. This is somewhat due to the unpredictable behavior inside the cells and the presence of multiple heterogeneous cell layers in 3D tissue model.

pH gradients play important roles in cellular processes such as proliferation, senescence, and apoptosis, endo- and exocytosis (i.e. secretory pathway), intracellular transport, contraction of muscle cells, and regulation of ion influxes. pH is tightly regulated within mammalian cells, with their organelles each requiring a different range of pH for their respective functions. For example, in the cytosol pH values around 7 are needed for the proper function of organelles, acidic pH of 4-5 in lysosomes for degradation of proteins, and alkaline pH of 7.5-8.0 in mitochondria for oxidative phosphorylation. Pathologic conditions can alter significantly intracellular and extracellular pH via perturbing effects on ion homeostasis, therefore pH is an important biomarker for disease states, such as cancer and neurological disorders. Changes in intracellular pH can be measured via number of dyes 2',7'-Bis-(2-Carboxyethyl)-5-(and-6)-Carboxyfluorescein, Acetoxymethyl Ester (BCECF), FPs and nanoparticles. While FLIM is preferred readout, there are only few suitable probes (i.e. nanoparticles and FPs) with lifetime ranges over physiological pH (Table 1.1). Cellular and tissue temperatures are tightly regulated via adaptive thermogenesis pathways within a narrow temperature range [228-230].

Temperature affects important processes, such as biomolecule diffusion, energy production in mitochondria, and enzyme function. Elevated temperatures activate the heat shock pathway, in which heat shock proteins (HSP) are expressed to stabilize and refold damaged proteins or to insure the correct folding of newly produced proteins. Temperature regulation is also important in the imaging and treatments of diseases [231], such as cancer [232], and can be an important biomarker. Similarly, the viscosity of cytoplasm and other intracellular organelles can be a key factor in drug diffusion, especially in 3D engineered cells and tissues. Viscosity can be measured by fluorescent probes called molecular rotors, also sensitive in fluorescence lifetime domain. Several fluorescent T-sensitive and viscosity probes for intracellular measurements were designed but only few of them have been tested with 3D tissue models.

The detection of molecular oxygen (O_2) is a well-developed and important area of research, due to the physiological importance of oxygen and its influences on growth, differentiation and functions of cells within 3D cell and tissue models [187]. Intracellular phosphorescence based O_2 sensors have been the basis of small molecule, nanoparticle and solid-state sensors and probes, that contribute efficient tissue staining, calibration and brightness with a broad compatibility with various imaging platforms. The phosphorescent O_2 probes often display mono-exponential decay, large Stokes' shift and µs-range of phosphorescence lifetimes. These parameters make them compatible for multiplexing with virtually any other biosensors, and therefore, are often superior to FLIM-based probes to other analytes. O_2 probes help in studies of hypoxia-dependent cell responses, direct analysis of mitochondrial function, cell and tissue viability, intracellular and extracellular gradients and have become popular tools in analysis of various 3D tissue models such as spheroids, cellular aggregates, *ex vivo* tissues, and organoids. A number of tested probes and sensor materials have been applied in the literature, with some of them demonstrating multi-parametric imaging of O_2 [36, 53, 59, 203, 207, 233, 234].

Cellular metabolism and bioenergetics are key to proper cell function, and its dysregulation is a biomarker of disease. Metabolism can be imaged and measured via genetically constructed FPs such as Peredox, which measures NADH/NAD^+ ratio. The shift in redox potential and production of reactive oxygen species (ROS) are indicators of oxidative stress which can adversely affect mitochondrial biogenetics and overall cell function, which have been successfully imaged by HyPer3, TriPer, and roGFP1 [202, 235, 236]. A drawback of these proteins is that they suffer from low response to FLIM and from cross sensitivity with pH, therefore requiring transfection or use in transgenic animals, however, they still perform better than endogenous fluorophores.

The new development of FLIM and PLIM in multi-parametric imaging has generated new applications and probes. Our group has discovered that the process of BrdU-dependent fluorescence quenching of nuclear-labeling dye, Hoechst 33342, reveals strong response in fluorescence lifetime and can be employed for labeling of proliferating cells in live culture [53]. The degree of quenching depends on the cell type and staining conditions such as the concentration of BrdU and Hoechst, as well as the incubation time. This methodology can potentially be applied for drug-induced effects on the duration

of cell cycle, identification and discrimination of proliferating cells in complex tissue models. Hoechst dye is two-photon excitable and similar type of quenching effects can be observed for other nuclear stains, e.g. SiR-Hoechst [237].

1.4.2 Fluorescent proteins

Fluorescent proteins (FPs) are applied as non-invasive probes for the study of biological models, with applications in the study of protein tracking, expression, and protein-protein interactions. Most FPs are based on the original green FP (avGFP) discovered in 1960, from the *Aequorea Victoria* jellyfish. This original avGFP has been genetically engineered to produce a wide array of FPs such as: blue (BFP), cyan (CFP), and yellow (YFP) FPs. Later on saw the development of red (RFPs), which were discovered from the coral *Discosoma* (DSRed), yielding orange (OFP), far-red FPs, and infrared FPs. Prototypical FPs based on avGFP and DsRed are ~25 kDa in size and contain three conserved amino acid residues responsible for chromophore formation. The FP structure consists of a rigid β-barrel comprised of 11 β-sheets around a central α-helix. The α-helix contains the three conserved amino acids, Ser^{65}, Tyr^{66}, and Gly^{67}, which are responsible for chromophore formation. Formation of the chromophore is a three-step reaction and starts with cyclisation via the nucleophilic attack of the amine group on Gly^{67}, to the carbonyl carbon of the Ser^{65}. The carbonyl carbon of the Ser^{65} is dehydrated, forming an imidazolin-5-one heterocyclic ring intermediate. Tyr^{66} is then oxidized by molecular oxygen, forming a Cα−Cβ double bond of the Try^{66} aromatic ring to the imidazoline. The bond formation results in the production of a 4-(p-hydroxybenzylidene)-imidazolidin-5-one conjugated ring system, conferring visible fluorescence to the FPs.

1.4.2.1 Expansion of fluorescent protein colour palette

The initial expansion of the FP colour palette from avGFP was pioneered by the Tisen group and its many collaborators. Mutation of Trp^{66} to His^{66} to increase wtGFP brightness resulted in the production of a blue fluorescing protein (BFP) [238]. When exploring the use of BFP as FRET pair with avGFP, both a UV and a blue emission band were discovered in the spectra of avGFP. The removal of the UV band via mutation of the Ser^{65} to Thr^{65} resulted in a 5-fold increase of the blue band, increasing the brightness of avGFP [239]. A second mutation of Phe^{64} to Leu^{64} resulted in the increase of optimal folding and the maturation temperature of the chromophore, from 28°C to 37°C. This double mutation of avGFP was seen as a breakthrough, as it allowed the use of GFP at mammalian cell temperatures of ~37°C and increased its fluorescent brightness [240]. The double mutant avGFP is currently marketed as enhanced green fluorescent protein (EGFP) . A further two FPs were engineered with mutation at Thr^{203} to Tyr^{203}, which yielded yellow fluorescent protein (YFP) [241], and a mutation at Tyr^{66} to Trp^{66}

produced cyan fluorescent protein (CFP) [242]. The first red fluorescent protein (RFP) was isolated from the Anthozoa species of coral *Discosoma nummiforme,* known as DsRed. It formed a stable tetramer, sharing structural similarities to monomer avGFP. The chromophore of DsRed is similar to that of avGFP, except for the presence of a second Cα−Cβ double bond, which results in a shift to red fluorescence emission. However, DsRed's tetramer conformation results in aggregation when used as a protein tag, perturbing protein functions and localisations. Therefore, a monomeric variant of DsRed was needed in order to solve the issues of dimerisation. A monomeric red FP (mRFP) [243] was designed by altering the newly designed, rapidly maturing variant of DsRed [244]. mRFP was then used as the basis of FPs in the 'Fruit series' mFruits. Here, groups have mutated mRFP to exhibit maximum wavelengths from 560 nm to 610 nm, with FPs named after fruits that resemble their emission colours.

Non-prototypical FPs not based on avGFP or DSRed are derived from vertebrates or prokaryotes. Non-prototypical FPs derived from bacterial phytochromes (BphPs) extend FPs colour palette into the far-red spectrum of light (710-850 nm) and into the infrared spectrum of light (800-1000 nm). Their development is crucial to the development of infrared FPs, as prototypical infrared FPs have yet to be discovered in nature or in laboratory. BphPs based FPs use biliverdin (BV) produced by heme oxygenase 1 (HO-1) to produce their fluorescence light. The best example of a BpHp based FP is the small Ultra Red Fluorescent Protein (smURFP), derived from cyanobacterial phycobiliprotein. smURFP is very photostable and is the one of the brightest far red, non-prototypical FP to date, with intrinsic fluorescence comparable to EGFP [245]. An example of a non-prototypical FP derived from vertebrates is the FP UnaG, derived from the eel species *Anguilla japonica.* It produces O_2 independent green fluorescence, induced by a noncovalent ligand known as bilirubin (a reduction product of BV) [246]. UnaG possesses several advantages over prototypical avGFPs due to their smaller size in the case of genetic fusions for protein studies, and secondly because of its ability to fluoresce in hypoxic conditions. The development of non-prototypical FPs will provide new avenues for the expansion and improvement of FPs. Other types of non-prototypical FPs are those based on the binding of flavin mononucleotide (FMN) to produce fluorescent light. One such FP is Mini Singlet Oxygen Generator (MiniSOG), which is engineered from Arabidopsis phototropin 2. MiniSOG generates singlet oxygen when illuminated by blue light for electron microscopy imaging applications [247]. Prototypical FP developments have also been aided by the genetic engineering of proteins from prokaryotes. HyPer is a hydrogen peroxide (H_2O_2) detector based on circularly permuted YFP (cpYFP) inserted into a prokaryotic regulatory domain sensitive to H_2O_2, known as OxyR [248]. Mutation of Cys^{199} to Ser^{199} renders HyPer insensitive to H_2O_2, but perseveres its sensitivity to pH, forming the ratiometric pH probe SypHer [249].

Recent efforts of FP expansion include the development of red and far-red (710-850nm) FPs. This push in development is due to the longer wavelength of red an far-red light, which results in higher light penetration depth and reduced phototoxicity. Therefore, red and far-red FPs are highly beneficial for

applications in tissue and whole animal imaging. A comparative study of prototypical far red FPs, including E2-Crimson, eqFP650, eqFP670, Katusha, Katusha2S, mNeptune, mKate, mKate2, and mCardinal, determined Katusha2S to be the best overall far-red FP for whole body imaging applications [250], with Katusha2S possessing the highest fluorescence brightness and signal-to-noise ratio in tissue and whole-body staining. However, due to its tandem dimer conformation, its application in protein studies was hindered, thereby making monomeric proteins like mKate2 more advantageous for applications in protein studies [251]. Recently a new monomeric RFP mScarlet has been developed, displaying record brightness and quantum yield (Q.Y), out-preforming mKate2 in fusion tag applications [252].

The development of infrared FPs has come from the engineering of BphPs derived from the bacterium *Deinococcus radiodurans* known as IFP1.4 [253], and subsequently iRFPs from bacterium *Rhodopseudomonas palustris* [254]. These two infrared FPs have served as the basis of the development of a range of infrared FPs: IFP2.0, iRFP670, iRFP682, iRFP702 and iRFP720 [255, 256]. However, the series of iRFPs are dimeric, and, as a result, cannot be used for genetic fusion tags. Recently, monomeric miRFP670, along with miRFP703, have been developed, which display increased brightness and efficient binding of BV in mammalian cells. The monomeric conformation and increased brightness allows for applications in cellular and *in vivo* imaging, with the visualisation of protein dynamics, RNA interactions and signalling cascades [257, 258].

Table 1.2 Fluorescent proteins with useful properties for live cell imaging.

Spectra class	Name	Exc./Em.	Extinction coefficient ($M^{-1}cm^{-1}$)	Q.Y	Comments and References
Infrared	IFP2.0	690nm/711nm	86,000	0.08	[255]
Infrared	miRFP670v1	642nm/670nm	71,300	0.12	[257, 258]
Infrared	miRFP703	674nm/703nm	90,900	0.08	[257, 258]
Far-red	smURFP	642nm/670nm	180,000	0.18	[245]
Far-red	mKate2	587nm/631nm	63,000	0.39	[251]
Far-red	Katusha2S	588nm/633nm	67,000	0.44	[250]
Red	DsRed express	554nm/586nm	30,100	0.42	[244]
Red	mCardinal	604nm/659nm	87,000	0.19	[259]
Red	mNeptune2.5	599nm/643nm	95,000	0.24	[259]
Red	FusionRed	580nm/608	94,500	0.19	[260]
Red	rsFusionRed2	580nm/607nm	35,500	0.12	Reversable photoswtichable

					fluorescent protein (RPFP) λoff to on 400-510nm λon to off 592nm [261]
Red	rsCherry	572nm/610nm	80,000	0.02	RPFP λoff to on 550nm λon to off 450nm [262]
Red	rsTagRFP	567nm/585nm			RPFP λoff to on 440nm λon to off 567nm [263] FRET with EYFP [264]
Red	mCherry	587nm/610nm	72,000	0.22	[265]
Red	mScarlet	569nm/594nm	100,000	0.7	[252]
Red	mRuby3	558nm/592nm	128,000	0.45	[266] FRET with mClover3
Orange	mOrange2	549nm/565nm	58,000	0.6	[267]
Yellow	EYFP	514nm/527nm	83,000	0.61	[268]
Yellow	mVenus	515nm/528nm	92,000	0.57	[269]
Yellow	mCitrine	516nm/528nm	69,000	0.72	[270]
Green	EGFP	488nm/507nm	56,000	0.6	[240]
Green	mNeonGreen	506nm/517nm	116,000	0.8	[271]
Green	mClover3	506nm/518nm	109,000	0.78	[266]
Green	Dronpa	503nm/518nm	95,000	0.85	RPFP λoff to on 488nm λon to off 405nm [272]
Cyan	ECFP	434nm/477nm	26,000	0.4	[212, 273]
Cyan	mTurquoise2	434nm/474nm	30,000	0.93	[274] FRET with mNeonGreen [275] and mVenus

Blue	EBFP2	383nm/448nm	32,000	0.56	[276]
Blue	mTagBFP2	399nm/454nm	50,600	0.64	[277]

1.4.2.2 Factors affecting the selection of fluorescent proteins for imaging applications

Each FP spectral class has its own set of advantages and disadvantages depending on the imaging application and conditions used [278, 279]. For example, RFPs are more suitable to imaging thicker samples due to their longer emission and excitation wavelengths, compared to BFPs which possess shorter wavelengths, resulting in high levels of phototoxic damage to the sample. However, a drawback of RFPs is that they are not as bright as other FPs due to their longer emission and excitation wavelengths. To determine what FPs are suitable for an experiment or imaging application, its intrinsic properties must be considered, along with the experimental parameters, such as: brightness, photostability, environmental sensitivities, chromophore maturation, and oligomerization**.**

Theoretical luminescence brightness is calculated by multiplying the extinction coefficient by its Q.Y. The extinction coefficient is defined as the capacity of the FP to absorb the excitation light of the specific wavelength required, and therefore, a higher extinction coefficient results in a greater amount of light absorbance. In the case of Q.Y, it is the ratio of the number of photons emitted as fluorescence to the number of excitation photons absorbed. Therefore, a high Q.Y results in a higher number of excited photons for emission as fluorescent light. Together, a high extinction coefficient and Q.Y confers high brightness to the FP, which is desirable to achieve a high fluorescence signal and to differentiate between any background fluorescence. However, in many commercially marketed FPs, brightness comparisons between FPs are made qualitatively, without giving details on the extinction coefficient or the Q.Y. It is therefore very important to ascertain these two parameters to truly determine a FP's brightness.

For longer experiments, a key property to consider is a FP's photostability, as multiple cycles of excitation and emission light can irreversibly deactivate and photobleach the FP, thereby diminishing its fluorescence over time. However, the selection of an FP simply based on its theoretical photostability is problematic, due to the absence of a clearly defined methodology to characterise this parameter [280]. Another factor to consider is the different intrinsic properties of each FP, (i.e. wavelength and the intensity of light needed for excitation), causing variations in photostability, even within the same spectral class.

A FP's fluorescence intensity and lifetime can be sensitive to its environment. The most common environmental factors that affect the properties of FPs are solvent polarity, pH and the presence of extrinsic quenchers (i.e. ions). Solvent polarity and viscosity can cause changes in the difference between excitation and emission spectra peaks (known as Stokes shifts, named after George G. Stokes).

Most FPs are sensitive to pH, with each FP possessing a specific pKa value of pH at which its fluorescence brightness is quenched by one half. Effects of pH should be considered if the FP is being targeted to the acidic organelles of the cell, like the lumen or lysosomes. Within such acid organelles, low acidic pH responsive FPs (i.e. with a low pKa value) should be avoided, if the goal is not to quantify changes in pH. GFP and its derivatives CFP and YFP are responsive to changes in pH, which can be quantified from responses in their fluorescence intensities and lifetimes. pH affects fluorescence by protonating the electron-rich chromophore, reducing the absorption of excitation [281]. Several cationic and anionic ions can quench the fluorescence of FPs, with YFP being particularly sensitive to Cl^- ions [282]. Therefore, a FP's sensitivities to pH, ion and polarity changes that affect FP's fluorescence intensities and lifetimes can be used to quantitatively measure these factors [283].

The maturation time of a FP is the time it takes for the FP to efficiently fold and mature its chromophore structure for optimal fluorescence brightness. In the case of time-sensitive experiments that require quick responses, a short maturation time is needed. Temperature and O_2 levels are known to affect maturation times, with many FPs requiring different conditions for optimal maturation. In the literature, contrasting maturation times are given. This is due to the absence of a single standardised procedure for the determination of maturation times. For example, EGFP maturation time is 14 minutes at 37°C, and this is widely reported to be its optimal conditions. However, one study found that EGFP matured in 8 minutes at 29°C, in direct conflict with studies reporting that 37°C was optimal [284]. O_2 is key in the formation of the FP chromophore, where it oxidises the Tyr^{66} residue. Therefore, under hypoxic conditions, the chromophore does not mature, resulting in a correctly folded FP that is not fluorescent [285]. However, there are some types of FP that can mature independent of O_2. For example, the O_2-independent FP UnaG is derived from the Unagi eel [246], with applications in hypoxic imaging [286].

Many FPs exist in different oligomer states, with the majority forming monomers, and a few forming dimers and tetramers. Oligomerisation is problematic for applications in FP fusions (FPFs), where oligomerisation can affect the protein of interest's function. It also can affect Forster resonance energy transfer (FRET), as oligomerisation can give false positive FRET responses [273]. Therefore, it is important to make sure FPs are monomeric in such applications. However, this isn't always straight forward, as many FPs commercially marketed as monomeric have been known to form dimers [287]. Some FPs are prone to form affinity oligomers in high concentrations, in close proximity, and when fused to oligomeric proteins.

1.4.2.3 Fluorescent proteins as imaging tools

Protein interactions, along with intracellular and extracellular metabolite gradients, serve as the basis of cell signalling and cellular processes. To visualise such signalling pathways and processes,

fluorophores such as FPs have been applied in the imaging tool known as FRET. FRET was described by Theodor Forster [288], and is a fluorescence tool in which an excited donor fluorophore transfers its energy non-radiatively to a neighbouring acceptor fluorophore, resulting in the acceptor emitting increased fluorescence [289]. FRET is a distance dependent process with a range of 1–10 nm between the two FPs and is used in visualising proximity changes in the donor and acceptor FPs. As a result, FRET can be applied to the study of protein-protein interactions, as well as changes in protein conformation, ion concentrations, and enzyme activity [290, 291]. FPs are the most commonly used fluorophores in FRET applications, as they can be genetically attached to proteins and domains of interest easily for live cell imaging in both intra and intermolecular measurements. In the case of intramolecular measurements, the FRET pair are on the same molecule, and in intermolecular, the FRET pair are on different molecules. For two FPs to be successful FRET pairs, their spectra must overlap so that the donor FP's emission can excite the acceptor FP. The first successful and most popular FRET pair is CFP – YFP [292], which have been used in the detection of Ca^{2+} concentrations [293] and the direct detection of integrin interactions [294]. However, the FRET pair of CFP – YFP suffers from photobleaching of the YFP acceptor and spectral cross talk, due to the closeness of the two FP's spectra. GFP – RFP FRET pairs possess greater spectra separation and have been developed to overcome issues with cross talk. However, due to the use of RFPs, they suffer from low brightness with weak FRET emission. Despite this, they have found applications in FLIM-FRET imaging. FLIM is the most accurate method of measuring FRET and the least prone to cross talk, as it only considers the donor fluorescence emission. The presence of FRET can quench the donor FP's fluorescence lifetime and, in turn, the amount of quenching by FRET can be quantified by measuring the shortening of the fluorescence lifetime of the donor FP. This is known as FLIM-FRET imaging. This technique has been applied to the quantitative analysis of 3D tissue models, for example, in studying the signalling pathways of CaMKII and RhoA in live brain slices [295] and in the activation of apoptosis in tumour spheroids [296]. However, when applying FLIM-FRET, special attention must be given to selecting FRET pairs that are not sensitive to environmental factors that may affect their fluorescence lifetimes, such as pH [212], viscosity [223], and temperature [36].

FPs have also been developed for applications in super resolution imaging, known as reversibly photoswtichable fluorescent proteins (RSFPs), which switch between on and off states in response to certain wavelengths of light [297]. For example, in the RSFPs of GFP, this process involves a change in the isomerisation and protonation states. along with conformational changes in the chromophore [298]. The *cis*-conformation is fluorescent, whereas the *trans*- is dark [299, 300]. RSFPs have found applications in protein tracking [301] and interactions [264] as well as in super-resolution imaging [261]. The advantages of using RSFPs is that they allow for the reduced quantity and duration of excitation light. This, therefore, limits the phototoxicity of the sample and reduces photobleaching of the fluorophore. The on-off switching also allows for extended imaging times, with applications in

super resolution imaging. However, the bulk of current and established RSFPs are based on GFP and use a UV- blue wavelength excitation light, which is highly phototoxic. Therefore, there is a need for the development of red RSFPs. Current red RSFPs, like rsCherry [298] and TagRFP [264], still use blue light to switch on the FP. The development of the orange-green wavelength excitation light, red RSFPs, has recently come from a study in which monomeric FusionRed was mutated to produce 3 new variants: rsFusionRed 1-3. All three possessed higher brightness, with rsFusionRed 2 and 3 exhibiting the fastest on-off switching of red RSFP to date. Most importantly, all three could be switched on using green excitation light [261]. The faster switching time and green light on-switching allowed for shorter, more frequent acquisition times in super resolution imaging with Molecular Nanoscale Live Imaging with Sectioning Ability (MoNaLISA) [302].

The continued expansion and improvement of FPs, particularly into the far red and infra-red spectrum, drives FP development for applications in FLIM-FRET and super resolution imaging, allowing for the live cell imaging of protein interactions and activities, as well as metabolic gradients. However, despite the advances discussed, the original EGFP, EYFP and ECFP are still the most popular FPs used to date, due to an unwillingness to utilise the newer, reportedly more suitable FPs stemming from doubts regarding the legitimacy of the improved FPs. Commercially marketed FPs are also relatively expensive, with many researchers depending on the generosity of other research groups developing FPs.

1.5 Self-assembling protein nanoparticles

Self-assembling protein nanoparticles is the term used to describe nanoparticles derived from protein nanocages, which are formed through the self-assembly of their capsid or subunit proteins. They act as robust cages, 20-100 nm in size, with well-defined topology, providing interior, exterior, and subunit locations for genetic and chemical modification with small molecules and sensor dyes. They possess many advantages that make them suitable for use as vaccines [303], drug delivery and imaging probes [304], such as: (i) low toxicity to cell and tissue models due to their biological nature, (ii) intrinsic self-assembly, (iii) high potential for modifications on exterior or interior of the structure, (iv) chemically and environmentally stable, natural cell penetrating activity, and (v) they are compatible with bacterial production. Their self-assembly process is driven by non-covalent interactions between the individual subunits, which can include: hydrophobic, electrostatic, and hydrogen bonds, as well as van der walls interactions [305, 306]. The types of self-assembling protein nanoparticles discussed here are viral like particles (VLPs) and ferritin derived protein nanocages.

1.5.1 Viral nanotechnology

Viral nanotechnology combines the disciplines of virology, chemistry, physics, physiology, pharmacology, and materials science, with the aim of developing viral nanoparticles (VNPs) and VLPs as a platform for the generation of functional materials [307]. VLPs are derived from viral proteins that lack viral genetic material, rendering them non-infectious; whereas VNPs contain viral genetic material. Here I will be discussing VLPs, as the lack of infectious genetic material makes them more advantageous for nanoparticle applications in drug delivery and imaging probes.

The most commonly used viral types for VLPs are icosahedron shaped, which possess a polyhedron structure with 20 triangular faces, organized in a 5:3:2 symmetry. According to Caspar and Klug's theory [308], the icosahedral virus is described as a spherically truncated icosahedron, made up of capsid subunits, resembling pentagons and hexagons. A triangulation number (T number) is used to describe the relations between the number of pentagons and hexagons, and thus explain their quasi symmetry in the capsid shell. The T-number is calculated by assuming that the viral organisation is a flat sheet of hexamers. Here, the relative position of the hexamers can be indexed along the axis, denoted by h and k, and related by a 60° rotation. The mathematical relation is given in the following formula;

Equation. 1.1 $T = h^2 + hk + k^2$

with h and k being any positive integer or zero. T numbers can thus only adopt positive integer values. The size of the capsid is proportional to the T number, so a larger T number results in a larger capsid [309]. Icosahedral viruses, most commonly utilised as VLPs, are the plant viruses: Cowpea chlorotic mottle virus (CCMV), and Cowpea mosaic virus (CPMV); along with the bacteriophages: MS2, and Qβ [310-313].

VLPs can be genetically engineered to alter the structural properties of the viral capsid allowing for functionalisation, expressing various targeting peptides, FPs, antibodies, drugs, amino acids, and purification tags etc. Oligo-histidine tags can be inserted via genetic engineering to viral protein subunits for metallochelate coupling via nitrilotriacetate (NTA), resulting in the attachment of O_2-sensitive Pt-porphyrin phosphorescent dyes to VLP structure [314]. Amino acids with reactive side chains, such as lysine, cysteine, aspartate, and glutamate for bioconjugation chemistry, can be genetically introduced via molecular cloning, if not already present on the capsid surface. Lysine can be modified through a reaction at their nucleophilic primary amine groups ($-NH_2$), with the N-hydroxysuccinimide-esters (NHS-esters) [315]. Cysteine can be modified by conjugate addition to Michael acceptors, the most common of which are maleimide groups. The thiol group of the cysteine amino acid side chain reacts specifically with an electrophilic maleimide group at a pH between 6.5 to 7.5, thereby conjugating maleimide reagent and its attached peptide to the VLP [316]. Carboxylic amino acids, aspartate and glutamate, can be functionalised by activating carboxylic acid groups with 1-ethyl-

3-(3-dimethylaminopropyl)carbodiimide (EDC), which can then react with NHS to form an NHS-ester group [317, 318]. The NHS-ester group can now be conjugated to a specific ligand, expressing a primary amine for conjugation. The interior of the viral capsid can be utilised for the encapsulation of cargo molecules within the viral structure. There are three main methodologies for encapsualtion: (i) encapsulation via self-assembly, (ii) infusion, or (iii) mineralisation. VLPs can be disassembled into their protein capsid subunits which are then mixed with the cargo molecules of interest and reassembled. Retention within the cavity can be achieved via covalent attachment to amino acids or through genetic engineering to the VLP C- or N- terminus for interior expression [319, 320], or via non-covalent interactions with nucleic acids of VNPs with positively charged small molecules [313, 321]. Encapsulation can be carried out by gating mechanisms in which changes in pH or metal ion concentration trigger structural transitions. The small molecules are infused into the swollen open form of the VLP, and are then trapped within the interior when the VLP is in closed form [322]. This is achieved by altering buffer conditions, i.e. pH or ion, inducing conformational changes. VLPs can act as templates for constrained material synthesis, a process that mimics biomineralisation [323]. Here, the VLPs are exposed to metallic or other inorganic precursors which diffuse into the capsid pores and become nucleated by the amino acids in the interior, leading to the synthesis of inorganic nanocrystals.

VLPs represent a smart platform allowing for multiplexation with a wide array of targeting moieties, in conjunction with imaging and therapeutic agents for precise targeted delivery. This targeting delivery, combined with a wide biodistribution and low toxicity, make VLPs ideal for biomedical applications in drug delivery and imaging. The ideal imaging probe should possess optimised pharmacokinetics (in terms of the balance in penetration or accumulation and clearance timing), low toxicity, biodistribution (in terms of cells and tissues targeted), and high brightness. VLPs can potentially address these issues, as they tend to be cleared from the body much quicker than synthetic nanomaterials [324, 325]. Along with the addition of targeting moieties, VLPs can be altered to be cell and tissue specific, improving pharmacokinetics and biodistribution [326]. VLPs derived from bacteriophages and plant viruses possess low toxicity to human cells and tissues, due to the lack of infectious viral DNA. VLP positioning and localisation can be traced when attached to FPs and fluorophore dyes, allowing for the real-time visualisation of their pharmacokinetics and biodistribution [327]. It is important to find a balance between cell and tissue penetration and clearance of the VLPs, with longer circulation times allowing for higher specificity and accumulation. This, however, can induce toxic effects or cause background interference in imaging. On the other hand, shorter circulation times can result in lower specificity and accumulation, which can cause problems in imaging brightness and cell specific delivery of drugs and other agents.

VLPs have been used in a wide array of imaging modalities such as: optical live cell imaging, magnetic resonance imaging (MRI), and positron emission imaging (PET). Optical live cell imaging is a non-

invasive study of cells in their natural environment, using fluorescence-based probes. Below I have given examples of the different types of VLP structures that have been used to date in such applications.

Rod-shaped plant viruses

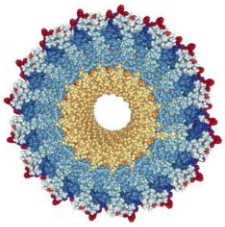

TMV

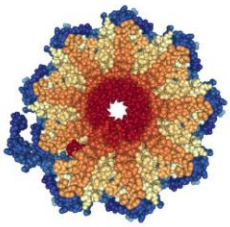

PVX

Bacteriophages

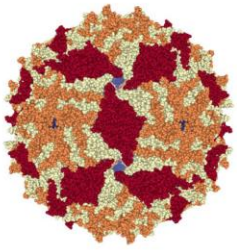

MS2

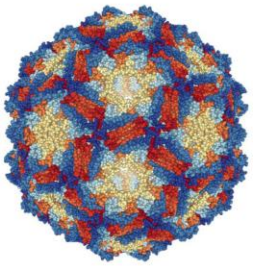

QB

Icosahedral plant viruses

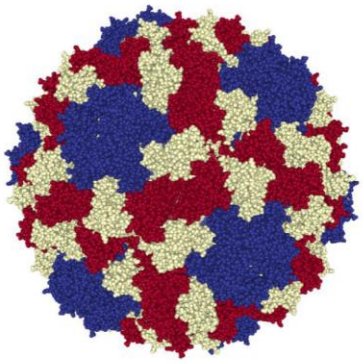

CCMV

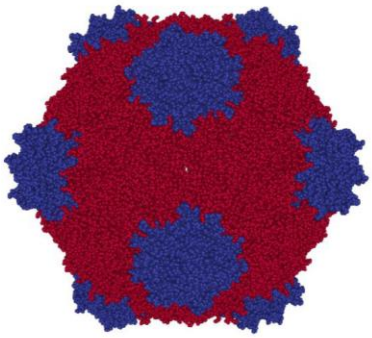

CPMV

Figure 1.3. CryoEM reconstruction images of the three types of viruses most commonly applied as VLPs. Rod shaped viruses (images for Rod shaped viruses orientated face on too see hollow tubular structure): Tobacco mosaic virus (TMV), dimensions of 18nm by 300 nm composed of 2130 protein subunits, and Potato virus X (PVX) 13nm by 515nm, composed of 1270 protein subunits. Bacteriophages: MS2 outer diameter of 27 nm and an inner diameter of 15 nm comprised of 180 capsid subunits, and Qβ outer diameter of 28 nm and an inner diameter of 21 nm comprised of 180 capsid subunits. Icosahedral plant viruses: Cowpea chlorotic mottle virus

(CCMV) outer diameter of 28nm and an inner diameter of 18nm comprised of 180 capsid subunits, and Cowpea mosaic virus (CPMV) comprised of 180 capsid subunits, with an out diameter of 30nm and an inner of 22nm. The figures/data were obtained from VIPERdb (http://viperdb.scripps.edu) VIPERdb2: an enhanced and web API enabled relational database for structural virology [328].

1.5.1.1 Rod-shaped plant viruses

Tobacco mosaic virus (TMV) is a rod-shaped plant virus, comprised of a straight tubular shaped capsid with dimensions of 18nm by 300 nm and is made up of 2130 protein subunits. TMV has been utilised in a number optical imaging applications**.** In one such study TMV's capsids were conjugated via isothiocyanate coupling to BF3-NCS, a two photon-excitable blue fluorescence dye for imaging of the brain vasculature in mice models. Though the VLP showed strong fluorescence brightness it was seen to block blood perfusion in small brain vessels, possibly due to the VLP's large size and high degree of aggregation [329]. Overall the TMV-BF3 VLP shows promise for two-photon deep tissue imaging, but optimisation of size and further studies in biodistribution and pharmacokinetics are needed. A second type of a rod-shaped plant virus is the Potato virus X (PVX), which possess a filamentous rod-shaped strucutre with dimensions of 13nm by 515nm, composed of 1270 protein subunits. PVX has been utilised in the development of fluorescently labeled VLPs for optical imaging. PVX has been bioconjugated to Alexa Fluor 647 succinimidyl ester via lysine amino acids, and peptide ligand GE11 for epidermal growth factor receptor (EGFR) targeting, via maleimide addition to cysteine amino acids. The filamentous VLP produced showed successful targeting and imaging of $EGFR^{+}$ cell lines possessing the GE11 peptide [330]. However, some nonspecific targeting was observed due to the VLP's posttive surface charge. This nonspecific targeting cab be resolved by shielding the positive charge of the PVX via PEGylation. This shielding optimisation which has been seen to increase PVX circulation times and reduce uptake into immune cells (such as macrophages) [331]. PVX has also been genetically engineered to express mCherry or GFP, with mCherry-PVX showing uptake and staining of human HT-29 colon cancer cells and solid tumour xenografts in mice [332].

1.5.1.2 Bacteriophages

MS2 is an icosahedral bacteriophage virus comprised of 180 capsid subunits with an outer diameter of 27 nm and an inner of 15 nm. VLPs of MS2 can be produced in *E. coli* and has been utilised as a scaffold for delivery of cargos such as: RNA and DNA, drugs, antibodies, and enzymes. MS2 VLPs delivery abilities have been examined through the use of dual modification with: 180 polyethylene glycol (PEG) chains via bioconjugation of lysine residue bioconjugation with NHS-esters; and interior attachment of 50 -70 fluorescent *p*-nitroaniline dye molecules via bioconjugation with Tyr^{85} residues through

diazonium coupling, mimicking a drug cargo. The exterior PEGylation achieved yielded a 90% reduction in antibody binding of the capsid surface, and the interior modification demonstrated high potential for the containment of drug molecules [333]. MS2 has been shown to deliver a variety of cargos into cells, due to encapsulation in its interior cavity and relative ease of modifications to its exterior surface. MS2 expressing targeting peptide SP94 for human hepatocellular carcinoma (HCC) cells, and fluorescent dyes for co-localisation (Alexa Fluor 532, 488 and 555), successfully transported quantum dot nanoparticles, chemotherapeutic drugs (doxorubicin, cisplatin with 5-flurouracil), and siRNA cocktail for anti-cyclin. MS2 carrying doxorubicin, cisplatin, and 5-fluorouracil selectively killed the HCC cell line, Hep3B, at drug concentrations below 1 nM, and those containing the siRNA cocktail for anti-cyclin induced growth arrest and apoptosis of Hep3B at siRNA concentrations below 150 pM [334]. This study demonstrated both the multivalent potential of MS2, and its capacity for storage and transportation of a variety of cargos for applications in cancer chemotherapeutics. The biodistribution and pharmacokinetics of MS2 VLPs has been examined using internal ^{64}Cu isotope labelling of mice xenograft models. MS2 and MS2-PEG both displayed similar biodistribution, with MS2-PEG displaying less uptake in the spleen due to shielding via PEG chains. Significant amounts of both constructs were found in circulation in the blood 24 hours after administration [335]. The ability to avoid immune system clearance is highly advantageous, as it allows for a higher dosage to reach the VLPs targeted tissues. Further studies attached anti-EGFR antibodies to exterior of ^{64}Cu isotope labelled MS2 VLPs to examine biodistribution in breast cancer models. Results showed binding of the EGFR receptor for over 2 days, along with long circulation times and moderate tumour uptake. However, the attachment of tumour targeting antibodies did not result in an increase in tumour uptake, this is possibly as a result of leakage from the solid tumour [312]. Therefore, MS2 VLPs have been shown to possess suboptimal targeting and uptake in solid tumours. A second type of bacteriophage is Qβ, an icosahedral shaped virus comprised of 180 capsid subunits with an outer diameter of 28 nm and an inner of 21 nm. Qβ is closely related to MS2 but it is structurally more stable due presence of internal disulfide bonds linking the subunits. Qβ has been utilised in applications for cargo delivery, in one study they were attached to carbohydrate binding ligand CD22, for specific targeting of cells expressing CD22, via Cu-catalyzed azide-alkyne cycloaddition (CuAAC) chemistry. The VLPs were then loaded internally with super folder GFP (sfGFP) genetically attached to Rev tagged cargo enzyme which in turn tethers to the α-Rev aptamer for attachment to the Qβ capsid [313], The Qβ VLPs displayed specific uptake into CD22 expressing Chinese hamster ovary (CHO) cells, visualized by sfGFP fluorescence. Qβ has also been genetically engineered to display epidermal growth factor (EGF) on the exterior of the capsid proteins, for cell specific targeting of EGF receptors on human epidermoid carcinoma A431 cells, and were also attached to Alexa Fluor 488 via CuAAC chemistry for localisation. These functionalised VLPs induced autophosphorylation of the EGF receptor and apoptosis of A431 cells [336]. The above studies highlight the potential of Qβ VLPs to transport cargo cell specifically and also demonstrate the application of multiple functionalisation strategies applicable to Qβ. The biodistribution and

pharmacokinetics of Qβ VLPs has been examined using internal Gd^{3+} ion labelling via CuAAC chemistry in mice models. Gd^{3+} labelled Qβ VLPs were found to accumulate heavily in the liver, with most VLPs cleared 5 hours after intravenous injection. The surface charge of Gd^{3+} labelled Qβ VLPs was altered in order to determine if surface charge affects the pharmacokinetics of Qβ. As a result the VLPs surface charge was neutralised with acylation of surface-exposed amine groups, resulting in shorter circulation times. When the amine groups were then subsequently restored the circulation times increased, therefore, the ability to alter surface charge can help in altering the pharmacokinetics of Qβ [337]. This effect of surface charge is seen in a number of other VLPs, in which VLPs are altered to possess negative surface charges, resulting in shorter circulation times: CCMV [338], CPMV [339] and TMV [327], Qβ [336] and MS2 [312].

1.5.1.3 Icosahedral plant viruses

Cowpea chlorotic mottle virus (CCMV) is an icosahedral plant virus comprised of 180 capsid subunits, with an outter diameter of 28nm and an inner diameter of 18nm. The CCMV viral capsid is dynamic, existing in fluctuation and possess pores on its surface, which allow for the diffusion of small molecules across the capsid, into and out of the interior of the VLPs [340]. Various cargos have been introduced into the CCMV structure. For example, Doxorubicin (Dox) which has been successfully encapsulated within CCMV VLPs expressing either, carboxyfluorescein succinimidyl ester or Alexa Fluor 610 NHS ester (AF610) for localisation, along with folic acid (FA) as targeting peptide. The VLPs showed specific targeting and uptake into the folate receptor (FR) positive cell line MCF7, in comparison to FR negative cell lines HepG2 and HEK. The VLP's cargo of Dox was released slowly over time from the cellular lysosomes [311]. An aggregate of the ligand 1,4,7,10-tetraaza-1-(1-carboxymethylundecane)-4,7,10-triacetic acid cyclododecane (DOTAC10) was used to complex Gd^{3+} or Photodynamic therapy (PDT) photosensitiser Zn^{+2} phthalocyanine (ZnPc) dye, which formed paramagnetic aggregates for encapsulation into the CCMV VLPs via pH induced self-assembly. The use of the DOTAC10 ligand resulted in reduced undesired aggregation of ZnPc, and lead to a higher loading of Gd^{3+} into the VLPs [341]. The interior of viral capsids are positively charged, and therefore favor the encapsulation of negatively charged molecules. One such strategy to facilitate the encapsulation of positively charged molecules has been the incorporation of noncovalent anchors, such as coiled-coil linkers. Here, capsid proteins and target molecules have been genetically engineered to express coiled-coil motifs, which dimerise forming a heterodimeric coiled-coil, allowing for the controlled attachment and encapsulation of the target molecule within the assembled capsid. CCMV capsid proteins have been genetically engineered to express a heterodimeric coiled coil, attached to the enzyme *Pseudozyma antartica* lipase B (PalB) to facilitate enzymatic activity studies. The coiled coil allowed for the control of PalB enzyme encapsulation within the CCMV VLPs. The encapsulated PalB had a higher activity compared to that

of the free form PalB, due to encapsulation within the CCMV VLPs localising PalB enzyme into a concentrated area, rather than diffused within the sample. It was subsequently observed that due to only one substrate molecule being encapsulated at one time, there was no change in the reaction velocity when increasing the number of PalB enzymes encapsulated. Therefore, it was not necessary to encapsulate more than one PalB enzyme at a time [342]. This coiled coil linker strategy was also applied for the encapsulation of EGFP [343], thereby demonstrating an advantageous method of controlled encapsulation of cargos into VLPs, as well as the potential of co-encapsulation of different enzyme types within the VLPs. The subunits of the cowpea chlorotic mottle virus (CCMV) have also been genetically altered via fusion to the thermally responsive elastin like polypeptide (ELP) allowing for self-assembly via two different mechanisms. The first mechanism is a pH induced assembly via the CCMV part of the VLP subunits, yielding 28 nm sized VLPs, whilst the second mechanism is a temperature induced assembly via the ELP part of the VLP subunits, yielding 18nm sized VLPs [344]. Here the ELP contains repeating pentapeptides of Val-Pro-Gly-X-Gly, with X any natural amino acid except proline, that are switchable from an extended water-soluble state to a collapsed hydrophobic state in response to increases in temperature [345] Further research with the ELP-CP VLPs demonstrated a third pathway via metal ion induced assembly yielding VLPs of 20nm in size, encapsulating His_6-tagged GFP within the CCMV-ELP interior [346]. Cowpea mosaic virus (CPMV) is an icosahedral plant virus comprised of 180 capsid subunits, with an outer diameter of 30nm and an inner diameter of 22nm. CPMV VLPs have been extensively used in cell and tissue specific delivery of cargo molecules for imaging and cancer therapeutics, where CPMV VLPs were used as a scaffold for a multiplexing strategy in the design of vascular endothelial growth factor receptor 1 (VEGFR-1) targeting VLPs. Two peptides were attached to the CPMV via hydrazone ligation chemistry: F56f targeting peptide for VEGFR-1 targeting, as well as a fluorescent PEG chain for localisation and shielding, PEG-500f. The application of hydrazone ligation chemistry allowed for the controlled sequential attachment of peptides to the VLPs, generating multifunctional VLPs, that displayed cell specific targeting of VEGFR-1 expressing EA.hy926 endothelial cells, as well as specific targeting to human colorectal adenocarcinoma (ATCC HTB-38) tumour in a xenograft mouse model [310]. The cytoskeletal protein, vimentin has been shown to interact with CPMV, with studies demonstrating CPMV-vimentin mediated uptake in vascular endothelial [347], tumour [348], and inflammatory responsive immune cells [349]. CPMV-vimentin has been successfully infused with a range of cargo molecules; Dox, 4′,6-diamidino-2-phenylindole (DAPI), propidium iodide (PI), acridine orange (AO), and proflavine (PF), all of which were retained via interaction with the encapsulated RNA molecule in the interior of the CPMV capsid. The resulting VLPs were subsequently bioconjugated to Alexa Fluor 555 via NHS to lysine residues for VLP localisation. Cargo delivery was demonstrated via panel of cancer cells, cervical (HeLa), prostate (PC-3), and colon (HT-29), and was observed that the CPMV VLPs enter via vimentin mediated uptake and once inside they are degraded by the endolysosomes, releasing their cargo allowing for imaging or chemotherapeutic induced cell death [350]. The above

CPMV VLP construct demonstrated the power of infusion and RNA retention as a functionalisation strategy in the development of VLPs in cell targeted drug and imaging delivery applications. CPMV has also been utilised in vascular imaging, where the VLPs were bioconjugated to Alexa Fluor 555 (AF55) via NHS coupling to lysine's on the exterior of its surface. The VLP construct here displayed higher brightness per particle than other vasculature probes and dyes tested and were able to image vasculature and blood flow in live mouse and chick embryos to a depth of 500 µm, where they remained in the endothelial cells for at least 72 hours. In subsequent research the VLPs allowed for the visualisation of human fibrosarcoma-mediated tumor angiogenesis, potentially providing a real time imaging map of angiogenesis [351]. CPMV VLPs have been observed to be potential drug carriers to central nervous systems damaged by neurodegenerative disorders or infectious diseases. CPMV VLPs bioconjugated to Alexa Fluor 555 via NHS coupling to surface lysine residues, demonstrated uptake into mice with neurotropic mouse hepatitis virus (MHV). In healthy mice, the VLPs localised to the brain blood barrier (BBB) endothelial cells; whereas in MHV infected mice the VLPs moved from the BBB, and localised to the brain tissues and lesions on the brain [352]. This study demonstrates the potential of CPMV VLPs for the delivery of neurological drugs across the BBB to the CNS for the treatment of neurological and infectious diseases. The biodistribution and pharmacokinetics of CPMV VLPs has been examined by labelling with Gd^{3+} or Tb^{3+} ions. Research in mice models found that the labelled VLPs were cleared from the plasma within 20 minutes of injection, with the majority of the labelled VLPs localising to the liver which remained present for 48 hours after injection [339]. However, when the labelled VLPs were orally introduced to mice, a different biodistribution is observed in spleen, kidney, liver, lung, stomach, small intestine, lymph nodes, brain, and bone marrow [353]. The difference in biodistribution could be down to the fact that uptake is via the intestinal epithelia, rather than into the vasculature circulation. Previous studies noted immune response to CPMV VLPs, but this was overcome through the addition of PEG chains [354].

1.5.1.4 Factors affecting VLP design and applications

When selecting and designing VLPs certain factors must be considered such as: shape, size, charge, and surface peptide expression (i.e. shielding agents and targeting peptides). The optimal VLP construct is one that can avoid immune cell clearance by phagocytosis thereby elongating its long circulation time, and along with cell and tissue specific delivery, avoid non-specific interactions with other cells and tissues. VLP's shape affects clearance by phagocytosis and targeted uptake, where it has been shown that elongated VLPs are able to avoid clearance by immune cell phagocytosis as they achieve a large contact angle with the macrophage cells reducing internalisation, in contrast to spherical NPs. It has been also shown that elongated NPs have increased efficiency of transport across the cell plasma membrane due to a greater contact area. This is evident for PVX which, due to its filamentous rod shape

avoids macrophage internalisation, thereby increasing the dosage of VLPs for tumour uptake [330]. Size also plays a role in attachment and uptake to targeted cells and tissues, with ideal VLP size radius ~ 30 to 50nm for cell endocytosis. Although larger VLPs possess a larger surface area for peptide attachment and cargo loading into their interior, they also encounter problems in hydrodynamic stress and shear forces, thereby compromising attachment to the target cells or tissues. As a result, a compromise in size is needed between surface area affecting loading potential, and avoiding problems in attachment. Charge of the VLPs is a key factor to be considered in relation to cell interactions and pharmacokinetics, with positively charged VLPs being observed to bind mammalian cells more efficiently than negatively charged VLPs due to the negative charge of plasma cell membrane. Positively charged VLPS are also able to avoid aggregation issues and penetrate tumour tissue more effectively [355], as seen in the attachment of positively charged polyarginine groups to CPMV VLPs, resulting in a superior uptake into HCC cells compared to plain CPMV VLPs. Positive surface charge also correlates to a longer circulation time in relation to pharmacokinetics as evident from observing the plasma circulation times of negatively charged CCMV VLPs with a half-life of ~15 minutes [338], compared to that of positively charged Qβ VLPs with a half-life of ~3 hours [337]. The choice of peptides expressed on VLPs can augment pharmacokinetics and targeting, with PEG chains which shield VLPs to reduce non-target cell uptake and aid in evading the immune system for increased circulation time. PEG chains alter the composition of the protein corona that is formed around the VLPs, therefore proteins used for immune system recognition are no longer present. This along with a hydrophobic barrier confer a stealth like quality to the VLPs [356, 357]. The increase circulation times is thought to result in increased accumulation in targets, such as tumours due to the increased amount of VLPs and incidence of contact with its target. However, drawbacks to the usage of PEG have been observed, and its usage should be considered. PEG is thought to be inert biologically and has FDA approval, However evidence has emerged of PEG causing hypersensitivity reaction after a second dosage, mediated by the production of anti-PEG antibodies by the innate immune system, resulting in accelerated blood clearance. However, since the response is by the innate immune system and not the complement, no immune memory is established. Therefore, it has been observed that spacing out dosages by over 7 days resulted in the decrease of anti-PEG antibodies [358]. Another down side of shielding to avoid immune system clearance, is the inhibition of uptake to the target cells or tissues due to the hydrophobic PEG groups [359]. Strategies to remove the PEG chains before uptake, thereby shielding the VLPs till they come into contact with their intended target, have included the utilisation of linkers that can be removed via cleavage with enzymes. For example, enzymes secreted by tumours such as Cathepsin and Matrix metalloproteinases (MMPs) [360], or by low pH [361] present in vesicles associated with uptake (i.e endolysosomes). Cell and tissue specific targeting peptides for receptors over expressed in the cases of disease can be used to minimise nonspecific uptake, and target the VLP to specific cell types and tissues. The targeting potential of VLPs is supported by a high volume of

evidence in the literature, discussing various strategies for attachment of targeting peptides and their applications [362, 363].

1.5.2 Ferritin

Ferritin is a major iron storage protein found in most living organisms including, mammals [364], bacteria [365], and plants [366]. Mammalian ferritin is composed of 24 subunits of either 21 kDa ferritin heavy (FTNH) or 19 kDa ferritin light (FTNL) chains [367], with the ratio of the different chains varying between different tissues. The primary role of FTNH is the binding and oxidisation of Fe^{2+} to Fe^{3+}, whereas FTNL carries out iron nucleation and storage of the Fe^{3+} inside the protein shell. The fully assembled ferritin folds into a spherical cage like structure, 450k Da in size with an internal cavity of 8 nm and an external size of 12 nm [368]. The internal cavity allows for the oxidation of toxic Fe^{2+} to Fe^{3+} via FTNH oxidisation, and subsequent storage of up to 4500 atoms of Fe^{3+} [367]. The primary role of ferritin is iron storage and its transport to and from cells via receptor mediated endocytosis. Ferritins bind to a variety of mammalian cell types [369-375], However, in human cells the only type of receptor identified for ferritin is the human transferrin receptor-1 (TfR-1) and TfR-2, which binds to FTNH and transferrin [376-378]. Therefore, Ferritin's intrinsic ability to cross plasma cell membrane into cytosol of cells via receptor mediated endocytosis with ferritin receptors such as TfR-1 and TfR-2 in human cells, and T cell immunoglobulin and mucin domain containing 2 (TIM-2) [369, 370] and scavenger receptor class A, member 5 (Scara5) [379] in murine cells makes it advantageous for biomedical applications. Due to ferritin's interactions with such receptors, there is a debate about whether it is the attached peptides directing delivery, or the intrinsic targeting property of the ferritin nanoparticle. This issue complicates studies investigating targeting peptide expressing ferritin nanoparticles, in that experiments should ideally be carried out to compare peptide expressing and 'plain' ferritin nanoparticles loading in cell models. For example, this could be investigated by labelling the two ferritin nanoparticles with different coloured fluorescent molecules to observe cellular uptake via imaging or fluorescence-activated cell sorting (FACS) analysis.

Ferritin can be functionalised via genetic engineering or chemically at its exterior to express a wide array of proteins such as: targeting peptides [380], fluorescent and dye molecules [381], and antibodies [382, 383]; and ferritin's interior cavity also allows for the encapsulation of drugs and imaging agents [384, 385]. Chemical modifications involve attaching targeting peptides, dye or fluorescent molecules to the outside of the ferritin structure via amino acid side chains such a lysine, cysteine, aspartate, and glutamate; present on the exterior of the structure (see section 1.5.1). These amino acids can be modified with fluorescent molecules such as: Fluorescein isocyanate (FITC) [386-388] via isocyanate coupling and Alexa Fluor 488 [389] attached via NHS-ester chemistry, with the attachment of fluorescent

molecules enabling for the visualisation of the nanoparticle's pharmacokinetics and biodistribution. FRET pair fluorescent molecules have also been attached to ferritin, in the case of Alexa Fluor 350 and 430 [390]. This enables applications in the monitoring of protein-protein interactions and conformational changes within the ferritin nanoparticles. Other functional groups have been attached by chemical modification are monosaccharides derivatives for cell surface lectin targeting, where mannose and galactose derivatives were attached via maleimide chemistry to cystine residues of the ferritin structure [391]. Ferritin nanoparticles have also been PEGylated via maleimide [392] or EDC [393] chemistry, as previously stated PEG chains can shield protein nanoparticles to reduce non-target cell uptake and aid in evading the immune system for increased circulation time. Genetic engineering involves the design of recombinant ferritin protein nanoparticles with DNA encoding for protein and peptide sequences, such engineering has resulted in the expression of targeting peptides [380] and antigens [382, 383]. Both the C and N- terminal of the FTNH subunit sequence can be engineered to express recombinant proteins sequences of interest. When engineering at the N terminal, the protein is expressed externally; for the C-terminal, expression is internal, however, there are conflicting reports in the literature that demonstrate genetic linkage of recombinant proteins to the C-terminus results in the ferritin nanoparticles expressing the engineered C- terminus externally when ferritin is fully assembled [383, 394].

One of the more promising and advantageous structural characteristic of ferritin nanoparticles is the internal cavity's ability to encapsulate metal-based compounds such as drugs and imaging agents. These compounds can be encapsulated within the ferritin cavity via pH dependent assembly process, in which at low pH the ferritin is disassembled into its 24 subunit parts, then subsequently reassembled as pH is increased back to neutral. Compounds containing metal groups are chelated by same amino acid groups of the ferritin structure that bind Fe^{2+} for oxidation to Fe^{3+}. However, nonmetal containing drug compounds suffer from diffusion of the ferritin interior via its hydrophilic channels due to weak electrostatic interactions with the internal ferritin binding sites. This issue can be overcome by complexing the drug molecule of choice with various transition metal ions such as Cu^{2+} [395] or by the addition of charged molecules such as poly- L- aspartic acid [396]. X ray crystallography studies have determined the binding sites of platinum (Pt) within the ferritin cavity at His^{136} and Lys^{68}, His^{105}, Cys^{90}, and Cys^{102} on FTNH [397]. This shows that Pt based compounds are bound within the ferritin cavity, and not simply trapped by encapsulation.

1.5.2.1 Ferritin nanoparticle applications

Ferritin nanoparticles have been successfully applied in optical imaging applications due to its ability to act as a scaffold for conjugations of various dye molecules and targeting peptides to its exterior

surface, and encapsulation within its interior cavity. Taking advantage of ferritin's pH dependent structure, hybrid ferritin photoactivatable nanoparticles, expressing both near infrared dye molecule Cy5.5 and its quencher BHQ-3 (black hole quencher 3) have been developed. When the nanoparticles encounter tumour MMPs the cleavable peptide sequence attaching Cy5.5 to the ferritin nanoparticle is cleaved, thereby releasing Cy5.5 molecules from the ferritin nanoparticles and away from the BHQ-3 quencher, activating Cy5.5 fluorescence activity [398]. The same concept was applied in the development of ferritin nanoparticles expressing Cy5.5 and targeting peptide Arginine-Glycine-Aspartic (RGD) [380]. RGD is a cell adhesion motif, with a high and specific affinity for αvβ3 integrins, which are over-expressed in tumour neovasculature. When injected into U87MG tumour mice, the nanoparticles successfully accumulated at tumour sites, directed by the RGD peptide [398]. A similar ferritin nanoparticle structure was developed genetically expressing RGD peptide and a bioconjugated Cy5.5 mono NHS ester, this nanoparticle was used for evaluating imaging of inflammation and angiogenesis in experimental carotid and abdominal aortic aneurysm (AAA) disease. When comparing signal strength of Cyc5.5 in RGD-FTN to that of control ferritin with no RGD, it was found that RGD-FTN possessed a higher signal strength in diseased carotids and AAAs. Histology results also showed RGD-FTN co-localised with macrophages in carotids and both macrophages and neoangiogenesis in AAA lesions. Therefore, showing that RGD-Ftn enhances vascular molecular imaging for both vascular inflammation and angiogenesis [399].

Ferritin has also found applications in medical imaging with magnetic resonance imaging (MRI) agents, due to its ability to sequester heavy atoms and heavy atom complexes, in particular iron oxides already present within the ferritin core possess superparamagnetic characteristics ideal for MRI. Research using breast cancer cell line MCF-7 which overexpresses the ferritin receptor Scara5, and apoferritin loaded with MRI contrast agent Gd-HPDO3A, along with anti-cancer drug curcumin, were effective in selectively treating MCF-7 cancer cells, visualised with the MRI agent Gd-HPDO3A [400].

Due to ferritin's ability to encapsulate and bind compounds containing metal groups, or those complexed to transition metals and charged accessory molecules [396], in addition to modification with targeting peptides for specific cell targeting, ferritin is an ideal nanoparticle for applications in drug delivery. Ferritin expressing RGD peptide was encapsulated with anti-cancer drug doxorubicin (precomplexed to transition metal Cu^{2+} to enable efficient loading of into ferritin), displayed improved pharmacokinetics when compared to free doxorubicin. This improvement in pharmacokinetics is due to the RGD- FTN nanoparticles facilitating increased uptake into targeted tumour cells [380]. Anticancer drug, cis-platin has been successfully encapsulated within ferritin's cavity via pH dependent assembly. Here ferritin nanoparticles containing cis-platin and conjugated to monoclonal antibodies (mAb) Ep1 for targeting human melanoma specific antigen CSPG4, by a heterobifunctional crosslinker showed specificity for melanoma cells expressing CSPG4 antigen, with similar results seen in xenograft mice models with pre-established palpable melanoma [401].

The ability to genetically engineer ferritin to express multiple antigens on the surface make it a useful nanoparticle in application of vaccine development. Vaccine for influenza virus was developed by genetically engineering ferritin derived from *Helicobacter pylori*, to express influenza viral haemagglutinin (HA) antigens (HA-FTN) [382], and was subsequently evaluated in mice and ferret models. In mice models the HA-FTN nanoparticle vaccine caused the production of neutralising antibodies for the HA variants. The ferritin vaccine showed increased effect compared to that of the commercial influenza vaccine and elicited no immune responses to the bacterial derived ferritin. Subsequent research showed that HA-FTN treated mice and ferrets exposed to lethal dose of highly pathogenic H5 2004 VN virus, survived [402]. However, despite positive results to date no ferritin nanoparticle vaccines have been approved for clinical use, unlike VLPs in case of HPV and hepatitis vaccinations.

The ability to alter ferritin at the external surface via chemical and genetic modifications, and cargo loading of the internal cavity generates nanoparticles with high potential in applications such as drug delivery, optical and medical imaging, as well as vaccine development. Genetic and chemical modifications of ferritin subunits allow spatial control and determination of the ratio of functional groups on fully assembled 24 subunit ferritin nanoparticles. The mixing of two sets of ferritin subunits with different mofications attached (i.e. one set of subunits with a fluorescent dye and another set expressing a targeting peptide), then subsequently inducing assembly allows for the design of multiplexed protein nanoparticles with controlled expression of functional groups. The capacity to encapsulate and coordinate drug and imaging agents within the ferritin structure is ferritin's most advantageous feature. This is due to the high number of drug or imaging agents that can be encapsulated within ferritin nanoparticles for targeted delivery, which is in stark contrast to administering a larger quantity of free drug or imaging compounds without targeted delivery.

Despite advantages these advantages the application of ferritin nanoparticles in vivo is currently limited. This is due to issues regarding pharmacokinetics and immunogenicity. With the use of human ferritin, it would be obvious to think that as it exists naturally in the body already, immune responses would be negligible. However, in practice, denaturation of the ferritin nanoparticle could expose immunogenic epitopes on its surface, as well as interactions with various biological interfaces in the body covering ferritin in epitopes for immune system response. Genetic and chemical modifications can also be immunogenic, for example in the immune response PEGylation, in which antibodies are produced in response to the presence of PEG chains [403]. Efforts to design recombinant ferritin nanoparticles with efficient cell specific targeting and loading can offset many of these issues raised.

1.6 Conclusion

Tissue engineering is a multi-disciplinary field that encompasses 3D cell and tissue-based scaffold and non-scaffold-based models, live cell microscopy and imaging modalities, along with fluorescence and phosphorescence-based biosensors. All of these disciplines work together to drive the development of biologically relevant 3D tissue models, which can be monitored in real time for the modelling of complex physiological and non- physiological diseased states. For such engineered tissues to be physiologically relevant, real time monitoring and optimisation of their extracellular and intracellular gradients (e.g. O_2, Ca^{2+}, pH, and temperature) must be applied. Therefore, the development of imaging modalities and biosensors compatible with live cell imaging of 3D tissue models is key. To date a large volume of imaging modalities and biosensors have been applied to monitor cell-cell interactions, disease biomarkers and metabolite gradients. Moving forward, the development of scaffold materials, imaging probes and modalities that are compatible and complement each other in a fully interdisciplinary approach are key in obtaining physiologically relevant tissue engineered models.

Chapter 2: Materials and Methods

2.1 Materials

All oligonucleotides were synthesised by Sigma-Aldrich (Dublin, Ireland), and all synthesised genetic constructs were from Genscript (Piscataway, NJ, USA) unless stated otherwise. Plasmid DNA encoding for EGFP with N-terminal His_6-tag in pQE-30 (Qiagen, UK) was donated by Dr. I. Okkelman (University College Cork, Ireland). Plasmid DNA encoding TagBFP2 with N-terminal His_6-tag in pQE-30 was purchased from Evrogen (Moscow, Russia). pET-15b vector encoding for N terminal His_6-tag, H_6-ELPCP was donated by Prof. Jan C. M. Van Hest (Radboud University, Netherlands). Plasmid DNA encoding for GCaMP2-pRSET B was donated by Prof. Holger Sondermann (Cornell University, USA).Plasmid DNA encoding ECFP in pProEx HTA was provided by Prof. M. Erard (Universite Paris Sud, France). Antarctic Phosphatase, restriction enzymes *XmaI BamHI, HindIII-HF, Kpn I, SmaI* and, T4 DNA polymerase were from New England Biolabs (Brennan & Co, Dublin, Ireland), T4 DNA Ligase, 2X PCR buffer, Wizard MiniPreps Plasmid DNA purification and SV Gel Clean-up kits were from Promega (MyBio, Ireland). Lysozyme, LB broth, protease inhibitor cocktail, CellLytic B and all the other reagents were from Sigma-Aldrich (Dublin, Ireland). Tetramethylrhodamine metyl ester (TMRM), Bis-Benzimide Hoechst 33342, Calcein Green AM, Carbonyl cyanide-4-(trifluoromethoxy)phenylhydrazone (FCCP), and oligomycin were from Sigma-Aldrich (Dublin, Ireland). O_2-sensitive phosphorescent probe Pt-Glc was synthesised as described before [196] and O_2-sensitive phosphorescent probe PtCP-NTA was synthesised as described in [314], pH-Xtra and MitoXpress -Xtra phosphorescent probes were from Luxcel Biosciences (Little Island, Cork). Bicinchoninic acid (BCA) protein assay kit was from Thermofisher (Dublin, Ireland). 0.1-1.4 mg/ml protein standards and Bradford Reagent were from Sigma-Aldrich (Dublin, Ireland). GrowDex scaffolds were from UPM Biochemicals (Helsinki, Finland). Bacterial cellulose spheres were produced and donated by Dr. Peter Timashev (Institute for Regenerative Medicine, I.M. Sechenov First Moscow State University, Moscow, Russian Federation). Fresh plant materials (celery 'stems' petioles *Apium graveolens*, potato tubers *Solanum tuberosum*, and carrot tubers *Daucus carota subsp. sativus*) were purchased from local vendors (Tesco and Lidl, Cork, Ireland). Horse spleen derived ferritin was from Sigma-Aldrich (Dublin, Ireland). 15 µ-slide III 3D perfusion chamber slides were from Ibidi GmbH (Martinsried, Germany), 96 and 8 well plates, 35 mm^2 dishes and all sterile cell culture plasticware were from Sarstedt (Wexford, Ireland). 35 mm^2 Dishes with 14 mm uncoated glass coverslip were from MatTek (Ashland, MA, USA). All chemicals (HPLC or spectrophotometric grade) unless otherwise stated were from Sigma-Aldrich (Dublin, Ireland).

2.2 Methods

2.2.1 Cell Culture

Human colon cancer HCT116 cells and mouse embryonic fibroblasts (MEFs) were obtained from American Tissue Culture Collections (ATCC, Manassas, VA, USA). A mutant cell line, HCT116 $SCO_2^{-/-}$, which is deficient in synthesis of cytochrome c oxidase SCO2, the assembly unit for complex IV of the ETC, were donated by P. M. Hwang (NIH, Bethesda, USA). MEF cells were cultured in Dulbecco's Modified Eagle's medium (DMEM) with 10 % fetal bovine serum (FBS), 10 mM 4-(2-hydroxyethyl)-1-piperazineethanesulfonic acid (HEPES) (pH 7.2), 2 mM L-glutamine (L-Gln), 100 U/ml penicillin /100 μg/ml streptomycin (P/S). HCT116 and HCT116 SCO2-/- cells were cultured in McCoys 5A medium supplemented with 10% FBS, 10 mM HEPES, pH 7.2, 2 mM Glutamine, 2 mM penicillin-streptomycin. All cells were grown in a humidified atmosphere of 5 % CO2 and 95 % air at 37°C unless otherwise stated. For experiments in 96 well plates and 8 well microscope dishes, all wells were coated with 0.01% collagen IV or collagen IV: poly-D-lysine (0.07mg/mL: 0.03mg/mL) for glass bottom-based dishes to help collagen IV attachment, 24 hours before cell seeding. The 0.01% collagen IV or collagen IV: poly-D-lysine were removed from the wells and washed 3-4 times in PBS, then allowed to dry, ready for cell seeding. All cell types and cell seeding numbers are displayed in Table 2.1.

Table 2.1. Cell seeding densities

Cells	96 well (cells per well)	8 well (cells per well)	35 mm^2 dish (cells per dish)
MEF cells	30,000	30,000	90,000
HCT116	30,000	100,000	200,000
HCT116 $SCO_2^{-/-}$	30,000	100,000	200,000

2.2.2 Cell based assays

2.2.2.1 Oxygen consumption rate (OCR)

OCR was measured using a phosphorescent O_2-sensitive probe, MitoXpress (Aligent). Cells were grown and treated as above (Section 2.2.1Cell culture). The cell culture media was then replaced with 100 μl of air-equilibrated medium, containing 200 nM MitoXpress probe. The wells were covered in 150 μl pre-warmed mineral oil, providing an O_2-impermeable seal. The plate was analysed on a TR-F reader Victor 2 (PerkinElmer Life Sciences) pre-set at 37°C and measured at atmospheric O_2. Each sample was measured every 3-5 min for over 1 hour. Two intensity values were taken at delay times of

30 and 70 μs with a gate time of 100 μs. Intensity signals were converted into phosphorescence lifetime (τ) values using the following calculation:

Equation 2.1. $\tau = \frac{(t_2 - t_1)}{Ln(\frac{F_1}{F_2})}$

where F_1, F_2 are TR-F intensity signals at delay times t_1 and t_2. Initial rates of cell deoxygenation were calculated as nmole/min per 10^6 cells. Average O_2 levels were calculated and OCR was calculated using O_2 consumed by cells in 1 min per 1 mg of total soluble protein.

2.2.2.2 Extracellular acidification (ECA) assay

Cells were seeded on 96 well plates coated with 0.01 % collagen IV and grown for 24 hours (unless stated otherwise). The cells were then washed with 150 μl un-buffered DMEM supplemented with 1 mM sodium pyruvate, 10 mM glucose and 2 mM L-glutamine. The cells were then incubated under CO_2 free conditions at 37°C for 2-2.5 hours. The medium was then replaced with buffered DMEM containing 10 mM HEPES, 1 mM sodium pyruvate, 10 mM glucose and 2 mM L-glutamine. The plate was then placed back into the CO_2 free incubator for 30 min – 1 hour. After incubation of 3 hours under CO_2-free conditions, the medium was changed to 100 μl buffered DMEM, containing 1 μM pH-Xtra probe (Aligent). For measurements of lactate-ECA (L-ECA) the plate was read on a TR-F reader Victor 2 (PerkinElmer Life Sciences) pre-set at 37ºC and measured at 20.9 %, 4 % , 3 % or 1 % atmospheric O_2. To measure Total-ECA (T-ECA) a layer of 150 μl of pre-warmed to 37°C heavy mineral oil was added to seal the plate after the addition of the pH-Xtra probe, before starting the analysis. The plate was read for at least 1 hour using 340 ± 35 nm excitation and 615 ± 8.5 nm emission, two intensity signals were measured at delay times of 100 and 300 μs with a measurement window of 30 μs. Intensity values were converted into probe fluorescence life-time using Equation 2.1. ECA is then expressed as a function of pH/[H^+] versus time, using a calibration curve of fluorescence lifetime values from a range of pH-buffered standards.

2.2.2.3 Cellular ATP assay

Total cellular ATP levels were measured using CellTiter-Glo assay (Promega). Cells were grown on 96 well plates, and ratio of 1:1 of CellTiter-Glo reagent to media was added to each well to lyse the cells. The plate was shaken for 2 min and each sample was transferred into a white 96 well plate and read on Victor 2 plate reader under standard luminescence settings. Protein concentrations were assessed using

BCA protein assay kit. Data was then corrected to protein content for each sample (BCA assay is described below in 2.2.2.4).

2.2.2.4 Bicinchoninic acid (BCA) protein assay

Protein concentrations were measured using BCA assay kit (Thermo Fisher Scientific) as per the manufacturer's instructions, on a 96 well plate and analysed on Victor 2 plate reader. Sample proteins for measurement and BCA standards (2000, 1500, 1000, 750, 500, 250, 125, 25, 0 µ/mL) were added to the plate. The working reagent was then added to all samples and standards. The plate was incubated at 37°C for 30 minutes and absorbance measured at 562nm. Protein concentrations were calculated using Beer Lambert law.

2.2.2.5 Bradford Protein assay

Protein concentrations were measured using Bradford assay (Sigma) as per manufactures instructions, on a 96 well plate and analysed on Victor 2 plate reader. 5µL of the sample proteins for measurement and BSA standards (Sigma) (1.5, 1, 0.5, 0.25 and 0 mg/mL) were added to the plate. 250µL of Bradford reagent was then added to each of the samples and standards. Protein concentrations were calculated using Beer Lambert law.

2.2.3 Molecular cloning

All oligonucleotide primer sequences used, and construct sequences constructed are displayed in Table 2.3 and 2.4 respectively.

Table 2.3 Oligonucleotide sequences 5' – 3'

Name	Sequence Forward (F) and Reverse (R)
QES-B (pGe30)	R- 5'GTTCTGAGGTCATTACTGG
S2F (pGe30)	F- 5'CGGATAACAATTTCACACAG
DsRed	F- 5′AGTCGGTACCATGGCCTCCTCCGAGGACGTC R- 5'AGTCGGTACCCAGGAACAGGTGGTGGCGGCC

EGFP	F- 5’TCTAGATCCGGTAGATCCC R- 5’GTGAGCAAGGGCGAGGAGCTG
GCaMP2	F- 5’AGTCGGTACCGGTACAGGTGGTTCTGGTGGTATGGCTAGCATGACTGGT R- 5’GATCGGTACCCTTCGCTGTCATCATTTGTA
ECFP	F- 5’GATCGGTACCGGTACAGGTGGTTCTGGTGGTGTGAGCAAGGGCGAGGA R- 5’GATCGGTACCTCTAGATCCGGTAGATCCT
EYFP	R- 5’GATCGGTACCCTTGTACAGCTCGTCCATGCCGA
CBD_{cenA}	F- 5’CGTGGGGCTGGTCGTCGGCAC R- 5’GCTCCCGGCTGCCGCGTCGAC
h-FTNH	F- 5’GCTTTCATTATCACTGTCTCC R- 5’ATGACGACCGCGTCCACCTCG
ENL-BAC	F- 5’TGACGGATCCTCTTCTATGGACATCGTTCTGCGTGCTCCGCTGATGGGTCCAAGG R- 5’GATCGGTACCCCCAGGCCGTGGGAATGGCAATGGCCTTGGACCCATCAGCGGAGCA

Table 2.3. Construct sequences 5’ to 3’.

Name	Sequence	Vector
EGFP	GGATCCCCAAGGCCATTGCCATTCCCACGGCCTGGGGGTACCCATCACCATCACCATCAC CATGGTACCGGTCCCGGGGTGAGCAAGGGCGAGGAGCTGTTCACCGGGGTGGTGCCCAT CCTGGTCGAGCTGGACGGCGACGTAAACGGCCACAAGTTCAGCGTGTCCGGCGAGGGCG AGGGCGATGCCACCTACGGCAAGCTGACCCTGAAGTTCATCTGCACCACCGGCAAGCTG CCCGTGCCCTGGCCCACCCTCGTGACCACCCTGACCTACGGCGTGCAGTGCTTCAGCCGC TACCCCGACCACATGAAGCAGCACGACTTCTTCAAGTCCGCCATGCCCGAAGGCTACGT CCAGGAGCGCACCATCTTCTTCAAGGACGACGGCAACTACAAGACCCGCGCCGAGGTGA AGTTCGAGGGCGACACCCTGGTGAACCGCATCGAGCTGAAGGGCATCGACTTCAAGGAG GACGGCAACATCCTGGGGCACAAGCTGGAGTACAACTACAACAGCCACAACGTCTATAT CATGGCCGACAAGCAGAAGAACGGCATCAAGGTGAACTTCAAGATCCGCCACAACATCG AGGACGGCAGCGTGCAGCTCGCCGACCACTACCAGCAGAACACCCCCATCGGCGACGGC CCCGTGCTGCTGCCCGACAACCACTACCTGAGCACCCAGTCCGCCCTGAGCAAAGACCC CAACGAGAAGCGCGATCACATGGTCCTGCTGGAGTTCGTGACCGCCGCCGGGATCACTC TCGGCATGGACGAGCTGTACAAGTCCGGACTCAGATCTCGAGCTCAAGCCTCGAATTCT GCAGTCGACGGTACTGCGGGTCCGGGATCTACCGGATCTAGACCCGGGGGTGGCGGTTC TGGTGGCGGCACCGGTGGCGGTTCTGGTGGCAAAAAGGAATTCGAGTGCGTGTACGGTG ATACCATGGTCGAAACGGAGGACGGTAAGATTAAAATCGAAGATCTGTACAAACGCCTT GCCTAAGCTT	pQE-30
TagBFP2	CACGTTAAGGGATTTTGGTCATGACTAGTGCTTGGATTCTCACCAATAAAAAACGCCCGG CGGCAACCGAGCGTTCTGAACAAATCCAGATGGAGTTCTGAGGTCATTACTGGATCTATC AACAGGAGTCCAAGCGAGCTCGTAAACTTGGTCTGACAGTTACCAATGCTTAATCAGTG AGGCACCTATCTCAGCGATCTGTCTATTTCGTTCATCCATAGTTGCCTGACTCCCCGTCGT GTAGATAACTACGATACGGGAGGGCTTACCATCTGGCCCCAGTGCTGCAATGATACCGC GAGACCCACGCTCACCGGCTCCAGATTTATCAGCAATAAACCAGCCAGCCGGAAGGGCC	

	GAGCGCAGAAGTGGTCCTGCAACTTTATCCGCCTCCATCCAGTCTATTAATTGTTGCCGG GAAGCTAGAGTAAGTAGTTCGCCAGTTAATAGTTTGCGCAACGTTGTTGCCATTGCTACA GGCATCGTGGTGTCACGCTCGTCGTTTGGTATGGCTTCATTCAGCTCCGGTTCCCAACGA TCAAGGCGAGTTACATGATCCCCCATGTTGTGCAAAAAAGCGGTTAGCTCCTTCGGTCCT CCGATCGTTGTCAGAAGTAAGTTGGCCGCAGTGTTATCACTCATGGTTATGGCAGCACTG CATAATTCTCTTACTGTCATGCCATCCGTAAGATGCTTTTCTGTGACTGGTGAGTACTCAA CCAAGTCATTCTGAGAATAGTGTATGCGGCGACCGAGTTGCTCTTGCCCGGCGTCAATAC GGGATAATACCGCGCCACATAGCAGAACTTTAAAAGTGCTCATCATTGGAAAACGTTCT TCGGGGCGAAAACTCTCAAGGATCTTACCGCTGTTGAGATCCAGTTCGATGTAACCCACT CGTGCACCCAACTGATCTTCAGCATCTTTTACTTTCACCAGCGTTTCTGGGTGAGCAAAA ACAGGAAGGCAAAATGCCGCAAAAAAGGGAATAAGGGCGACACGGAAATGTTGAATAC TCATACTCTTCCTTTTTCAATATTATTGAAGCATTTATCAGGGTTATTGTCTCATGAGCGG ATACATATTTGAATGTATTTAGAAAAATAAACAAATAGGGGTTCCGCGCACATTTCCCCG AAAAGTGCCACCTGACGTCTAAGAAACCATTATTATCATGACATTAACCTATAAAAATA GGCGTATCACGAGGCCCTTTCGTCTTCACCTCGAGAATTGTGAGCGGATAACAATTGACA TTGTGAGCGGATAACAAGATACTGAGCACATCAGCAGGACGCACTGACCGAATTCAGAG AAAGAGGAGAAATACTAGATGAGCGAACTGATCAAAGAGAACATGCACATGAAGCTGT ACATGGAAGGCACCGTTGACAACCACCACTTTAAGTGCACGTCTGAGGGTGAGGGTAAG CCGTACGAAGGCACCCAAACCATGCGTATCAAAGTTGTGGAGGGCGGTCCACTGCCGTT CGCTTTTGACATTCTGGCGACCAGCTTCCTGTACGGTTCCAAAACGTTCATTAACCATAC TCAGGGCATTCCGGATTTCTTCAAACAGAGCTTTCCGGAAGGTTTCACCTGGGAGCGTGT CACCACGTATGAAGATGGTGGTGTGTTGACCGCCACCCAAGATACCTCCCTGCAAGATG GCTGTCTGATCTATAACGTGAAAATTCGTGGCGTCAACTTTACGAGCAATGGTCCGGTGA TGCAGAAGAAAACCCTGGGTTGGGAGGCGTTTACGGAAACCCTGTATCCGGCCGATGGT GGCCTGGAGGGCCGTAACGACATGGCACTGAAGCTGGTTGGTGGCAGCCATTTGATCGC AAATGCCAAGACGACGTACCGCAGCAAGAAACCGGCGAAAAATCTGAAGATGCCGGGT GTTTACTATGTCGACTACCGTCTGGAACGCATTAAAGAAGCGAATAATGAGACTTACGT GGAGCAGCACGAGGTTGCAGTCGCGCGCTATTGCGACTTGCCTAGCAAGCTGGGTCATA AACTGAATTAATAAGCTTAGTTAGTTAGCTCTAGAGGCATCAAATAAAACGAAAGGCTC AGTCGAAAGACTGGGCCTTTCGTTTTATCTGTTGTTTGTCGGTGAACGCTCTCCTGAGTA GGACAAATCCGCCGCCCTAGACCTAGGCGTTCGGCTGCGGCGAGCGGTATCAGCTCACT CAAAGGCG	
DsRed	GGCCTGCTGCGCGGCCGCCATCAGGGCGTGCATGCGCTGCAGGGCGCGCATGGCGGCCT GCGCGAACGCCCGCGCGTGCGCGATCGCGGCCGCGGCCGCGGCCCGCCGCTGCGCGGCC ATCCGGATCGCCAGGCGGAAGGCGATCAGGGCCGCCCGCCGGCGCTGCGCCTGGGCCAT CCGGTGCCGCCGGTGCCGGTGCGCCTGCAGGGCGTGCGCGAAGCGCCGGCGGATATTCC GGATTATAAAAAACTGAGCTTTCCGGAAGGCTTTAAATGGGAACGCGTGATGAACTTTG AAGATGGCGGCGTGGTGACCGTGACCCAGGATAGCAGCCTGCAGGATGGCAGCTTTATT TATAAAGTGAAATTTATTGGCGTGAACTTTCCGAGCGATGGCCCGGTGATGCAGAAAAA AACCATGGGCTGGGAAGCGAGCACCGAACGCCTGTATCCGCGCGATGGCGTGCTGAAAG GCGAAATTCATAAAGCGCTGAAACTGAAAGATGGCGGCCATTATCTGGTGGAATTTAAA AGCATTTATATGGCGAAAAAACCGGTGCAGCTGCCGGGCTATTATTATGTGGATAGCAA ACTGGATATTACCAGCCATAACGAAGATTATACCATTGTGGAACAGTATGAACGCGCGG AAGGCCGCCATCATCTGTTTCTG	pQE-30
H_6-ELPCP	GTTCCGGGCGTCGGTGTTCCTGGATTAGGTGTTCCAGGTGTAGGTGTTCCAGGACTCGGT GTTCCTGGTGTAGGTGTTCCTGGTTTAGGTGTTCCAGGTGGCGGTGTTCCTGGTGTGGGA GTTCCTGGTTTAGGTCTCGAGGTGGTCCAACCTGTTATTGTAGAACCCATCGCTTCAGGC CAAGGCAAGGCTATTAAAGCATGGACCGGTTACAGCGTATCGAAGTGGACCGCCTCTTG TGCGGCTGCCGAAGCTAAAGTAACCTCGGCTATAACTATCTCTCTCCCTAATGAGCTATC GTCCGAAAGGAACAAGCAGCTCAAGGTAGGTAGAGTTTTATTATGGCTTGGGTTGCTTCC	pQE-16

	CAGTGTTAGTGGCACAGTGAAATCCTGTGTTACAGAGACGCAGACTACTGCTGCTGCCTC CTTTCAGGTGGCATTAGCTGTGGCCGACAACTCGAAAGATGTTGTCGCTGCTATGTACCC CGAGGCGTTTAAGGGTATAACCCTTGAACAACTCACCGCGGATTTAACGATCTACTTGTA CAGCAGTGCGGCTCTCACTGAGGGCGACGTCATCGTGCATTTGGAGGTTGAGCATGTCA GACCTACGTTTGACGACTCTTTCACTCCGGTGTAT	
ELPCP-H_6	ATGAGAGGATCCGTTCCGGGCGTCGGTGTTCCTGGATTAGGTGTTCCAGGTGTAGGTGTT CCAGGACTCGGTGTTCCTGGTGTAGGTGTTCCTGGTTTAGGTGTTCCAGGTGGCGGTGTT CCTGGTGTGGGAGTTCCTGGTTTAGGTCTCGAGGTGGTCCAACCTGTTATTGTAGAACCC ATCGCTTCAGGCCAAGGCAAGGCTATTAAAGCATGGACCGGTTACAGCGTATCGAAGTG GACCGCCTCTTGTGCGGCTGCCGAAGCTAAAGTAACCTCGGCTATAACTATCTCTCTCCC TAATGAGCTATCGTCCGAAAGGAACAAGCAGCTCAAGGTAGGTAGAGTTTTATTATGGC TTGGGTTGCTTCCCAGTGTTAGTGGCACAGTGAAATCCTGTGTTACAGAGACGCAGACTA CTGCTGCTGCCTCCTTTCAGGTGGCATTAGCTGTGGCCGACAACTCGAAAGATGTTGTCG CTGCTATGTACCCCGAGGCGTTTAAGGGTATAACCCTTGAACAACTCACCGCGGATTTAA CGATCTACTTGTACAGCAGTGCGGCTCTCACTGAGGGCGACGTCATCGTGCATTTGGAGG TTGAGCATGTCAGACCTACGTTTGACGACTCTTTCACTCCGGTGTATGGTGGCGGTAGAT CTCATCACCATCACCATCACTAA	pQE-16
BN7-His7-EGFP-linker-FTNH	GGTACCGTAGTCGCCGCGCGCGTCGTGTTATAGGTACGACGAGGTACCCATCACCATCA CCATCACCATGGTACCGGTGGCAGATCTAGGCCATCTAGGACCCGGGCGCCACGGCAGC TGACGTCTTAAGCTTCGGACTCGAGCTCTAGACTCAGGCCTGAACATGTCGAGCAGGTAC GGCTCTCACTAGGGCCGCCGCCAGTGCTTGAGGTCGTCCTGGTACACTAGCGCGAAGAG CAACCCCAGAAACGAGTCCCGCCTGACCCACGAGTCCATCACCAACAGCCCGTCGTCGT GCCCCGGCAGCGGCTACCCCCACAAGACGACCATCACCAGCCGCTCGACGTGCGACGGC AGGAGCTACAACACCGCCTAGAACTTCAACCGGAACTACGGCAAGAAGACGAACAGCC GCCACTATATCTGCAACACCGACTACATCAACATGAGGTCGAACACGGGGTCCTACAAC GGCAGGAGGAACTTCAGCTACGGGAAGTCGAGCTACGCCAAGTGGTCCCACAGCGGGA GCTTGAAGTGGAGCCGCGCCCAGAACATCAACGGCAGCAGGAACTTCTTCTACCACGCG AGGACCTGCATCGGAAGCCCGTACCGCCTGAACTTCTTCAGCACGACGAAGTACACCAG CCCCATCGCCGACTTCGTGACGTGCGGGGTCCAGTCCCACCAGTGCTCCCACCCGGTCCC GTGCCCGTCGAACGGCCACCACGTCTACTTGAAGTCCCAGTCGAACGGCATCCACCGTA GCGGGAGCGGGAGCGGCCTGTGCGACTTGAACACCGGCAAATGCAGCGGCAGGTCGAG CTGGTCCTACCCGTGGTGGGGCCACTTGTCGAGGAGCGGGAACGAGTGCCCGGGGGTGG CGGTTCTGGTGGCGGCACCGGTGGCGGTTCTGGTGGCATGACGACCGCGTCCACCTCGC AGGTGCGCCAGAACTACCACCAGGACTCAGAGGCCGCCATCAACCGCCAGATCAACCTG GAGCTCTACGCCTCCTACGTTTACCTGTCCATGTCTTACTACTTTGACCGCGATGATGTGG CTTTGAAGAACTTTGCCAAATACTTTCTTCACCAATCTCATGAGGAGAGGGAACATGCTG AGAAACTGATGAAGCTGCAGAACCAACGAGGTGGCCGAATCTTCCTTCAGGATATCAAG AAACCAGACTGTGATGACTGGGAGAGCGGGCTGAATGCAATGGAGTGTGCATTACATTT GGAAAAAAATGTGAATCAGTCACTACTGGAACTGCACAAACTGGCCACTGACAAAAATG ACCCCCATTTGTGTGACTTCATTGAGACACATTACCTGAATGAGCAGGTGAAAGCCATCA AAGAATTGGGTGACCACGTGACCAACTTGCGCAAGATGGGAGCGCCCGAATCTGGCTTG GCGGAATATCTCTTTGACAAG CACACCCTGGGAGACAGTGATAATGAAAGCTAAGCTT	pQE-30
BN7-EGFP-linker-FTNH	GGTACCGTAGTCGCCGCGCGCGTCGTGTTATAGGTACGACGAGGTACCGGTACCGGTGG CAGATCTAGGCCATCTAGGACCCGGGCGCCACGGCAGCTGACGTCTTAAGCTTCGGACT CGAGCTCTAGACTCAGGCCTGAACATGTCGAGCAGGTACGGCTCTCACTAGGGCCGCCG CCAGTGCTTGAGGTCGTCCTGGTACACTAGCGCGAAGAGCAACCCCAGAAACGAGTCCC GCCTGACCCACGAGTCCATCACCAACAGCCCGTCGTCGTGCCCCGGCAGCGGCTACCCC CACAAGACGACCATCACCAGCCGCTCGACGTGCGACGGCAGGAGCTACAACACCGCCTA GAACTTCAACCGGAACTACGGCAAGAAGACGAACAGCCGCCACTATATCTGCAACACCG	pQE-30

	ACTACATCAACATGAGGTCGAACACGGGGTCCTACAACGGCAGGAGGAACTTCAGCTAC GGGAAGTCGAGCTACGCCAAGTGGTCCCACAGCGGGAGCTTGAAGTGGAGCCGCGCCCA GAACATCAACGGCAGCAGGAACTTCTTCTACCACGCGAGGACCTGCATCGGAAGCCCGT ACCGCCTGAACTTCTTCAGCACGACGAAGTACACCAGCCCCATCGCCGACTTCGTGACGT GCGGGGTCCAGTCCCACCAGTGCTCCCACCCGGTCCCGTGCCCGTCGAACGGCCACCAC GTCTACTTGAA GTCCCAGTCGAACGGCATCCACCGTAGCGGGAGCGGGAGCGGCCTGTGCGACTTGAACA CCGGCAAATGCAGCGGCAGGTCGAGCTGGTCCTACCCGTGGTGGGGCCACTTGTCGAGG AGCGGGAACGAGTGCCCGGGGGTGGCGGTTCTGGTGGCGGCACCGGTGGCGGTTCTGGT GGCATGACGACCGCGTCCACCTCGCAGGTGCGCCAGAACTACCACCAGGACTCAGAGGC CGCCATCAACCGCCAGATCAACCTGGAGCTCTACGCCTCCTACGTTTACCTGTCCATGTC TTACTACTTTGACCGCGATGATGTGGCTTTGAAGAACTTTGCCAAATACTTTCTTCACCA ATCTCATGAGGAGAGGGAACATGCTGAGAAACTGATGAAGCTGCAGAACCAACGAGGT GGCCGAATCTTCCTTCAGGATATCAAGAAACCAGACTGTGATGACTGGGAGAGCGGGCT GAATGCAATGGAGTGTGCATTACATTTGGAAAAAAATGTGAATCAGTCACTACTGGAAC TGCACAAACTGGCCACTGACAAAAATGACCCCCATTTGTGTGACTTCATTGAGACACATT ACCTGAATGAGCAGGTGAAAGCCATCAAAGAATTGGGTGACCACGTGACCAACTTGCGC AAGATGGGAGCGCCCGAATCTGGCTTGGCGGAATATCTCTTTGACAAGCACACCCTGGG AGACAGTGATAATGAAAGCTAAGCTT	
ENL-BN7-EGFP-linker-FTNH	GGTACCGTAGTCGCCGCGCGCGTCGTGTTATAGGTACGACGAGGTACCGGTACCGGTGG CAGATCTAGGCCATCTAGGACCCGGGCGCCACGGCAGCTGACGTCTTAAGCTTCGGACT CGAGCTCTAGACTCAGGCCTGAACATGTCGAGCAGGTACGGCTCTCACTAGGGCCGCCG CCAGTGCTTGAGGTCGTCCTGGTACACTAGCGCGAAGAGCAACCCCAGAAACGAGTCCC GCCTGACCCACGAGTCCATCACCAACAGCCCGTCGTCGTGCCCCGGCAGCGGCTACCCC CACAAGACGACCATCACCAGCCGCTCGACGTGCGACGGCAGGAGCTACAACACCGCCTA GAACTTCAACCGGAACTACGGCAAGAAGACGAACAGCCGCCACTATATCTGCAACACCG ACTACATCAACATGAGGTCGAACACGGGGTCCTACAACGGCAGGAGGAACTTCAGCTAC GGGAAGTCGAGCTACGCCAAGTGGTCCCACAGCGGGAGCTTGAAGTGGAGCCGCGCCCA GAACATCAACGGCAGCAGGAACTTCTTCTACCACGCGAGGACCTGCATCGGAAGCCCGT ACCGCCTGAACTTCTTCAGCACGACGAAGTACACCAGCCCCATCGCCGACTTCGTGACGT GCGGGGTCCAGTCCCACCAGTGCTCCCACCCGGTCCCGTGCCCGTCGAACGGCCACCAC GTCTACTTGAA GTCCCAGTCGAACGGCATCCACCGTAGCGGGAGCGGGAGCGGCCTGTGCGACTTGAACA CCGGCAAATGCAGCGGCAGGTCGAGCTGGTCCTACCCGTGGTGGGGCCACTTGTCGAGG AGCGGGAACGAGTGCCCGGGGGTGGCGGTTCTGGTGGCGGCACCGGTGGCGGTTCTGGT GGCATGACGACCGCGTCCACCTCGCAGGTGCGCCAGAACTACCACCAGGACTCAGAGGC CGCCATCAACCGCCAGATCAACCTGGAGCTCTACGCCTCCTACGTTTACCTGTCCATGTC TTACTACTTTGACCGCGATGATGTGGCTTTGAAGAACTTTGCCAAATACTTTCTTCACCA ATCTCATGAGGAGAGGGAACATGCTGAGAAACTGATGAAGCTGCAGAACCAACGAGGT GGCCGAATCTTCCTTCAGGATATCAAGAAACCAGACTGTGATGACTGGGAGAGCGGGCT GAATGCAATGGAGTGTGCATTACATTTGGAAAAAAATGTGAATCAGTCACTACTGGAAC TGCACAAACTGGCCACTGACAAAAATGACCCCCATTTGTGTGACTTCATTGAGACACATT ACCTGAATGAGCAGGTGAAAGCCATCAAAGAATTGGGTGACCACGTGACCAACTTGCGC AAGATGGGAGCGCCCGAATCTGGCTTGGCGGAATATCTCTTTGACAAGCACACCCTGGG AGACAGTGATAATGAAAGCTAAGCTT	pQE-30
CBD_{CenA}	GCTCCCGGCTGCCGCGTCGACTACGCCGTCACCAACCAGTGGCCCGGCGGCTTCGGCGC CAACGTCACGATCACCAACCTCGGCGACCCCGTCTCGTCGTGGAAGCTCGACTGGACCT ACACCGCAGGCCAGCGCATCCAGCAGCTGTGGAACGGCACCGCGTCGACCAACGGCGGC CAGGTCTCCGTCACCAGCCTGCCCTGGAACGGCAGCATCCCGACCGGCGGCACGGCGTC	pUC-57

	GTTCGGGTTCAACGGCTCGTGGGCCGGGTCCAACCCGACGCCGGCGTCGTTCTCGCTCAA CGGCACCACCTGCACGGGCACCGTGCCGACGACCAGCCCCACGGGTACC	
CBD-ECFP	GCTCCCGGCTGCCGCGTCGACTACGCCGTCACCAACCAGTGGCCCGGCGGCTTCGGCGC CAACGTCACGATCACCAACCTCGGCGACCCCGTCTCGTCGTGGAAGCTCGACTGGACCT ACACCGCAGGCCAGCGCATCCAGCAGCTGTGGAACGGCACCGCGTCGACCAACGGCGGC CAGGTCTCCGTCACCAGCCTGCCCTGGAACGGCAGCATCCCGACCGGCGGCACGGCGTC GTTCGGGTTCAACGGCTCGTGGGCCGGGTCCAACCCGACGCCGGCGTCGTTCTCGCTCAA CGGCACCACCTGCACGGGCACCGTGCCGACGACCAGCCCCACGGGTACCGGTACAGGTG GTTCTGGTGGTGTGAGCAAGGGCGAGGAGCTGTTCACCGGGGTGGTGCCCATCCTGGTC GAGCTGGACGGCGACGTAAACGGCCACAAGTTCAGCGTGTCCGGCGAGGGCGAGGGCG ATGCCACCTACGGCAAGCTGACCCTGAAGTTCATCTGCACCACCGGCAAGCTGCCCGTG CCCTGGCCCACCCTCGTGACCACCCTGACCTGGGGCGTGCAGTGCTTCAGCCGCTACCCC GACCACATGAAGCAGCACGACTTCTTCAAGTCCGCCATGCCCGAAGGCTACGTCCAGGA GCGCACCATCTTCTTCAAGGACGACGGCAACTACAAGACCCGCGCCGAGGTGAAGTTCG AGGGCGACACCCTGGTGAACCGCATCGAGCTGAAGGGCATCGACTTCAAGGAGGACGG CAACATCCTGGGGCACAAGCTGGAGTACAACTACATCAGCCACAACGTCTATATCACCG CCGACAAGCAGAAGAACGGCATCAAGGCCAACTTCAAGATCCGCCACAACATCGAGGA CGGCAGCGTGCAGCTCGCCGACCACTACCAGCAGAACACCCCCATCGGCGACGGCCCCG TGCTGCTGCCCGACAACCACTACCTGAGCACCCAGTCCGCCCTGAGCAAAGACCCCAAC GAGAAGCGCGATCACATGGTCCTGCTGGAGTTCGTGACCGCCGCCGGGATCACTCTCGG CATGGACGAGCTGTACAAGTCCGGACTCAGATCTCGAGCTCAGGCTTCGAATTCTGCAGT CGACGGCACCGCGGGCCCAGGATCTACCGGATCTAGAGGTACC	pQE-30
CBD-GCaMP2	GCTCCCGGCTGCCGCGTCGACTACGCCGTCACCAACCAGTGGCCCGGCGGCTTCGGCGC CAACGTCACGATCACCAACCTCGGCGACCCCGTCTCGTCGTGGAAGCTCGACTGGACCT ACACCGCAGGCCAGCGCATCCAGCAGCTGTGGAACGGCACCGCGTCGACCAACGGCGGC CAGGTCTCCTCACCAGCCTGCCCTGGAACGGCAGCATCCCGACCGGCGGCACGGCGTCG TTCGGGTTCAACGGCTCGTGGGCCGGGTCCAACCCGACGCCGGCGTCGTTCTCGCTCAAC GGCACCACCTGCACGGGCACCGTGCCGACGACCAGCCCCACGGGTACCGGTACAGGTGG TTCTGGTGGTATGGCTAGCATGACTGGTGGACAGCAAATGGGTCGGGATCTGTACGACG ATGACGATAAGGATCTCGCCACCATGGTCGACTCATCACGTCGTAAGTGGAATAAGACA GGTCACGCAGTCAGAGCTATAGGTCGGCTGAGCTCACTCGAGAACGTCTATATCATGGC CGACAAGCAGAAGAACGGCATCAAGGCGAACTTCAAGATCCGCCACAACATCGAGGAC GGCGGCGTGCAGCTCGCCTACCACTACCAGCAGAACACCCCCATCGGCGACGGCCCCGT GCTGCTGCCCGACAACCACTACCTGAGCACCCAGTCCAAACTTTCGAAAGACCCCAACG AGAAGCGCGATCACATGGTCCTGCTGGAGTTCGTGACCGCCGCCGGGATCACTCTCGGC ATGGACGAGCTGTACAAGGGCGGCACCGGAGGGAGCATGGTGAGCAAGGGCGAGGAGC TGTTCACCGGGGTGGTGCCCATCCTGGTCGAGCTGGACGGCGACGTAAACGGCCACAAG TTCAGCGTGTCCGGCGAGGGTGAGGGCGATGCCACCTACGGCAAGCTGACCCTGAAGTT CATCTGCACCACCGGCAAGCTGCCCGTGCCCTGGCCCACCCTCGTGACCACCCTGACCTA CGGCGTGCAGTGCTTCAGCCGCTACCCCGACCACATGAAGCAGCACGACTTCTTCAAGTC CGCCATGCCCGAAGGCTACATCCAGGAGCGCACCATCTTCTTCAAGGACGACGGCAACT ACAAGACCCGCGCCGAGGTGAAGTTCGAGGGCGACACCCTGGTGAACCGCATCGAGCTG AAGGGCATCGACTTCAAGGAGGACGGCAACATCCTGGGGCACAAGCTGGAGTACAACA CGCGTGACCAACTGACTGAAGAGCAGATCGCAGAATTTAAAGAGGCTTTCTCCCTATTTG ACAAGGACGGGGATGGGACAATAACAACCAAGGAGCTGGGGACGGTGATGCGGTCTCT GGGGCAGAACCCCACAGAAGCAGAGCTGCAGGACATGATCAATGAAGTAGATGCCGAC GGTAATGGCACAATCGACTTCCCTGAGTTCCTGACAATGATGGCAAGAAAAATGAAAGA CACAGACAGTGAAGAAGAAATTAGAGAAGCGTTCCGTGTGTTTGATAAGGATGGCAATG GCTACATCAGTGCAGCAGAGCTTCGCCACGTGATGACAAACCTTGGAGAGAAGTTAACA	pQE-30

	GATGAAGAGGTTGATGAAATGATCAGGGAAGCAGACATCGATGGGGATGGTCAGGTAA ACTACGAAGAGTTTGTACAAATGATGACAGCGAAGGGTACC	
ECFP	GGTACAGGTGGTTCTGGTGGTATGGCTAGCATGACTGGTGGACAGCAAATGGGTCGGGA TCTGTACGACGATGACGATAAGGATCTCGCCACCATGGTCGACTCATCACGTCGTAAGTG GAATAAGACAGGTCACGCAGTCAGAGCTATAGGTCGGCTGAGCTCACTCGAGAACGTCT ATATCATGGCCGACAAGCAGAAGAACGGCATCAAGGCGAACTTCAAGATCCGCCACAAC ATCGAGGACGGCGGCGTGCAGCTCGCCTACCACTACCAGCAGAACACCCCCATCGGCGA CGGCCCCGTGCTGCTGCCCGACAACCACTACCTGAGCACCCAGTCCAAACTTTCGAAAG ACCCCAACGAGAAGCGCGATCACATGGTCCTGCTGGAGTTCGTGACCGCCGCCGGGATC ACTCTCGGCATGGACGAGCTGTACAAGGGCGGCACCGGAGGGAGCATGGTGAGCAAGG GCGAGGAGCTGTTCACCGGGGTGGTGCCCATCCTGGTCGAGCTGGACGGCGACGTAAAC GGCCACAAGTTCAGCGTGTCCGGCGAGGGTGAGGGCGATGCCACCTACGGCAAGCTGAC CCTGAAGTTCATCTGCACCACCGGCAAGCTGCCCGTGCCCTGGCCCACCCTCGTGACCAC CCTGACCTACGGCGTGCAGTGCTTCAGCCGCTACCCCGACCACATGAAGCAGCACGACT TCTTCAAGTCCGCCATGCCCGAAGGCTACATCCAGGAGCGCACCATCTTCTTCAAGGACG ACGGCAACTACAAGACCCGCGCCGAGGTGAAGTTCGAGGGCGACACCCTGGTGAACCGC ATCGAGCTGAAGGGCATCGACTTCAAGGAGGACGGCAACATCCTGGGGCACAAGCTGG AGTACAACACGCGTGACCAACTGACTGAAGAGCAGATCGCAGAATTTAAAGAGGCTTTC TCCCTATTTGACAAGGACGGGGATGGGACAATAACAACCAAGGAGCTGGGGACGGTGAT GCGGTCTCTGGGGCAGAACCCCACAGAAGCAGAGCTGCAGGACATGATCAATGAAGTA GATGCCGACGGTAATGGCACAATCGACTTCCCTGAGTTCCTGACAATGATGGCAAGAAA AATGAAAGACACAGACAGTGAAGAAGAAATTAGAGAAGCGTTCCGTGTGTTTGATAAG GATGGCAATGGCTACATCAGTGCAGCAGAGCTTCGCCACGTGATGACAAACCTTGGAGA GAAGTTAACAGATGAAGAGGTTGATGAAATGATCAGGGAAGCAGACATCGATGGGGAT GGTCAGGTAAACTACGAAGAGTTTGTACAAATGATGACAGCGAAGGGTACC	pQE-30
gCaMP2	ATGGCTAGCATGACTGGTGGACAGCAAATGGGTCGGGATCTGTACGACGATGACGATAA GGATCTCGCCACCATGGTCGACTCATCACGTCGTAAGTGGAATAAGACAGGTCACGCAG TCAGAGCTATAGGTCGGCTGAGCTCACTCGAGAACGTCTATATCATGGCCGACAAGCAG AAGAACGGCATCAAGGCGAACTTCAAGATCCGCCACAACATCGAGGACGGCGGCGTGC AGCTCGCCTACCACTACCAGCAGAACACCCCCATCGGCGACGGCCCCGTGCTGCTGCCC GACAACCACTACCTGAGCACCCAGTCCAAACTTTCGAAAGACCCCAACGAGAAGCGCGA TCACATGGTCCTGCTGGAGTTCGTGACCGCCGCCGGGATCACTCTCGGCATGGACGAGCT GTACAAGGGCGGCACCGGAGGGAGCATGGTGAGCAAGGGCGAGGAGCTGTTCACCGGG GTGGTGCCCATCCTGGTCGAGCTGGACGGCGACGTAAACGGCCACAAGTTCAGCGTGTC CGGCGAGGGTGAGGGCGATGCCACCTACGGCAAGCTGACCCTGAAGTTCATCTGCACCA CCGGCAAGCTGCCCGTGCCCTGGCCCACCCTCGTGACCACCCTGACCTACGGCGTGCAGT GCTTCAGCCGCTACCCCGACCACATGAAGCAGCACGACTTCTTCAAGTCCGCCATGCCCG AAGGCTACATCCAGGAGCGCACCATCTTCTTCAAGGACGACGGCAACTACAAGACCCGC GCCGAGGTGAAGTTCGAGGGCGACACCCTGGTGAACCGCATCGAGCTGAAGGGCATCGA CTTCAAGGAGGACGGCAACATCCTGGGGCACAAGCTGGAGTACAACACGCGTGACCAAC TGACTGAAGAGCAGATCGCAGAATTTAAAGAGGCTTTCTCCCTATTTGACAAGGACGGG GATGGGACAATAACAACCAAGGAGCTGGGGACGGTGATGCGGTCTCTGGGGCAGAACC CCACAGAAGCAGAGCTGCAGGACATGATCAATGAAGTAGATGCCGACGGTAATGGCAC AATCGACTTCCCTGAGTTCCTGACAATGATGGCAAGAAAAATGAAAGACACAGACAGTG AAGAAGAAATTAGAGAAGCGTTCCGTGTGTTTGATAAGGATGGCAATGGCTACATCAGT GCAGCAGAGCTTCGCCACGTGATGACAAACCTTGGAGAGAAGTTAACAGATGAAGAGGT TGATGAAATGATCAGGGAAGCAGACATCGATGGGGATGGTCAGGTAAACTACGAAGAG TTTGTACAAATGATGACAGCGAAGCCCGGG	pQE-30

2.2.3.1 Fluorescent proteins

Vector encoding for EGFP with N-terminal His_6-tag in pQE-30 (Qiagen, UK) was donated by Dr. I. Okkelman (University College Cork, Ireland). Plasmid DNA encoding TagBFP2 with N-terminal His_6-tag in pQE-30 was purchased from Evrogen (Moscow, Russia). Sequence encoding for DsRed was synthesised from DsRed-Express-N1 vector as a template via PCR using 5′- 5′-AGTCGGTACCATGGCCTCCTCCGAGGACGTC (forward) and AGTCGGTACCCAGG AACAGGTGGTGGCGGCC (reverse) primers. The resulting sequence was subcloned into pQE-30 vector via KpnI site (Table 1). All constructs were transformed into *E. coli* SG13009 (Qiagen) cells. All the produced expression constructs were verified by sequencing (GATC Biotech AG).

2.2.3.2 ELPCP Constructs

pET-15b vector encoding for N terminal His_6-tag, H_6-ELPCP was donated by Prof. Jan C. M. Van Hest (Radboud University, Netherlands) (Table 1). C terminal His-tag ELPCP-H_6 sequence was synthesised from H_6-ELPCP vector via PCR using CCMV-F (5′-TAGCGGATCCGTTCCGGGCGTCGGTGTTCCT) and CCMV-R (GATCAGATCTACCGCCACCATACACCGGAGT) primers. The resulting sequence was subcloned into pQE-16 vector via *BamHI* and *BglII* sites. Both constructs were transformed into *E. coli* BL21 (DE3) cells. All the produced expression constructs were verified by sequencing (GATC Biotech AG).

2.2.3.3 EGFP- Human heavy chain ferritin (FTNH) Constructs

Construct 1 (BN7-His7-EGFP-linker-FTNH) was composed of heavy chain human ferritin (FTNH) with C-terminally attached to the N-terminal of EGFP via short linker sequence, to aid protein folding of EGFP (CCCGGGGGTGGCGGTTCTGGTGGCGGCACCGGTGGCGGTTCTGGTGGC) with C terminal His_7 tag for purification via Ni^{2+}-NTA affinity chromatography, attached to cell penetrating peptide bactenecin 7 (BN7). Construct 2 (BN7-EGFP-linker-FTNH) did not include His_7 purification tag. Sequences were synthesised by Genscript (Piscataway, NJ, USA) and supplied in pUC-57 plasmids which were treated with restriction enzymes *BamHI* and *HindIII* to remove the sequences. The sequences were then subcloned into pGe30 vectors and transformed into *E. coli* SG13009 (Qiagen) cells. All the produced expression constructs were verified by sequencing (GATC Biotech AG).

2.2.3.4 ECFP- Human heavy chain ferritin (FTNH) Construct

Sequence obtained by restriction digest with *XmaI* to remove EGFP from FTNH-EGFP-BN7 Construct 1. ECFP, synthesised by Genscript (Piscataway, NJ, USA) in pUC-57, was treated with *XmaI* and inserted into the digested construct 1 sequence, in place of the removed EGFP. The construct was then treated with *BamHI* to allow insertion of ENL cell targeting peptide sequence treated with *BamHI* between the pGe30 plasmid and BN7 sequence. pQE-30 vectors were re-ligated and transformed into *E. coli* SG13009 (Qiagen) cells. All the produced expression constructs were verified by sequencing (GATC Biotech AG).

2.2.3.5 CBD-ECFP, CBD-EYFP and CBD-GCaMP2

Sequence encoding for N-terminal CBD-CenA fragment (Ala32 -Thr137) was designed with BamHI, KpnI and SmaI restriction digest sites, and synthesised by Genscript (Piscataway, NJ, USA) in pUC-57 plasmid (See Table 1). The sequence was subcloned in frame with human ferritin sequence in pQE-30 plasmid. The human ferritin sequence was removed via restriction digestion with SmaI and HindIII enzymes, followed by treatment with T4 DNA polymerase and self-ligation, producing CBDΔ(FTN) plasmid DNA (See Table 1). ECFP, EYFP and GCaMP2 coding sequences were synthesised by Genscript (Piscataway, NJ, USA and supplied in pUC-57 plasmids (See Table 1). Polymerase chain reaction (PCR) was carried out with plasmid DNA as template and primers introducing KpnI restriction site and cloned in CBDΔ(FTN) plasmid DNA, digested with KpnI, pre-treated with Antarctic Phosphatase, ligated and transformed in *E. coli* SG13009 (Qiagen) cells, producing CBD-ECFP, CBD-EYFP and CBD-gCaMP2 (Table 1). CBD-fusions were produced with GTGGSGG linker between CBD and FP. All the produced expression constructs were verified by sequencing (GATC Biotech AG).

2.2.4 Bacterial protein production and purification

2.2.4.1 mTagBFP, EGFP, DsRed and ECFP fluorescent proteins

mTagBFP, EGFP, DsRed, and ECFP proteins were produced in *E. coli* SG13009 cells, and grown in LB medium, with Ampicillin (100 μg/mL) and Kanamycin (25 μg/mL), untill OD600 of 0.4−0.5 was reached (37 °C). Cells were induced with 0.25 mM Isopropyl β-D-1-thiogalactopyranoside (IPTG) overnight at room temperature harvested and stored as pellets at -80°C. Protein purification was carried out via lysing the bacterial pellets in “PCL” buffer (50 mM NaH_2PO_4, 0.3 M NaCl, 10 mM imidazole,

pH 8 (>5 volumes per mg of wet weight) with 1× Cell Lytic B (Sigma C8740), 0.25−1 mg/mL Lysozyme, 1× protease inhibitor cocktail (Sigma P2714), incubation on ice for 0.5 h, passing the extract through the needle (23 1/4 G, 5 times), and centrifugation (15 000g, 15 min, 4 C). Cleared extracts were applied on Ni^{2+}-NTA resin (Sigma P6611) in gravity-flow columns, which were washed with PCL buffer and then eluted with PCL buffer supplemented with 250 mM Imidazole. Eluted proteins were dialysed against PCL buffer without imidazole or another buffer (8 kDa MWCO BioDesignDialysis Tubing™ Fisher Scientific, RT, 2× 1 hour), concentrations were then quantified using Bradford assay.

2.2.4.2 ELPCP

H_6-ELPCP and ELPCP-H_6 were produced in *E. coli* BL21 (DE3) cells and purified according to the method described by authors [344] with minor modifications to the procedure. The bacterial pellets were lysed in 50 mM NaH_2PO_4, 10 mM Imidazole, 1.3 M NaCl, pH 8, (>5 volumes per mg of wet weight) with 1× CellLytic B (Sigma C8740), 0.25−1 mg/mL Lysozyme, 1× protease inhibitor cocktail (Sigma P2714) 10 μg/mL DNase, 10 μg/mL RNase A, incubation on ice for 0.5 h, passing the extract through the needle (23 1/4 G, 5 times), and centrifugation (15 000g, 15 min, 4 C). Cleared extracts were applied on Ni^{2+}-NTA resin (Sigma P6611) in gravity-flow columns, which were washed with lysis buffer containing 20 mM imidazole, and then eluted with the same buffer containing 250 mM imidazole. To produce ELPCP dimers, the purified proteins were dialysed against 'capsid' buffer (50 mM Tris, pH 7.5, 500 mM NaCl, 10 mM $MgCl_2$, 1mM EDTA) (8 kDa MWCO, 1 h, RT), then against the same buffer without EDTA. To produce VLPs, dimers were further dialysed against 'assembly' buffer (50 mM CH_3COONa, pH 5, 500 mM NaCl, 10 mM MgCl2). The dimers and assembled VLPs were stored at 4 °C. Purity and molecular weight of proteins were assessed by SDS-PAGE and concentrations by Bradford assay.

2.2.4.3 EGFP and ECFP- Human heavy chain ferritin (FTNH) Constructs

All FTNH constructs were produced in E. coli SG13009 cells, and grown in LB medium, with Ampicillin (100 μg/mL) and Kanamycin (25 μg/mL), till OD600 of 0.4−0.5 was reached (37 °C). Cells were induced with 0.25 mM IPTG overnight at room temperature, harvested and stored as pellets at -80°C. Protein purification was carried out via lysing the bacterial pellets in 'MiniSOG' buffer (0.2 M NaCl, 30 mM NaH2PO4, 2 mM Tris-HCl, pH 8.3, with 1× Cell Lytic B (Sigma C8740), 0.25−1 mg/mL Lysozyme, 1× protease inhibitor cocktail (Sigma P2714), incubation on ice for 30 minutes, passing the extract through the needle (23 1/4 G, 5 times), and centrifugation (15 000 g, 15 min, 4 C). Cleared extracts were applied on Ni^{2+}-NTA resin (Sigma P6611) in gravity-flow columns, which were washed

with MiniSOG buffer. Then the proteins were eluted with MiniSOG buffer supplemented with 250 mM Imidazole. Eluted proteins were dialysed against PBS (8 kDa MWCO, RT, 2× 1 h). Protein concentrations were quantified using Bradford assay and their purity was confirmed by SDS-PAGE.

2.2.4.4 CBD-ECFP and CBD-GCaMP2

Both CBD-ECFP and CBD-GCaMP2 were produced in E. coli SG13009 cells, and grown in LB medium, with Ampicillin (100 μg/mL) and Kanamycin (25 μg/mL), till OD600 of 0.4−0.5 was reached (37 °C). Cells were induced with 0.25 mM IPTG overnight at room temperature, harvested and stored as pellets at -80°C. Protein purification was carried out via lysing the bacterial pellets in 'MiniSOG' buffer (0.2 M NaCl, 30 mM NaH_2PO_4, 2 mM Tris-HCl, pH 8.3, with 1× CellLytic B (Sigma C8740), 0.25−1 mg/mL Lysozyme, 1× protease inhibitor cocktail (Sigma P2714), incubation on ice for 30 minutes, passing the extract through the needle (23 1/4 G, 5 times), and centrifugation (15 000g, 15 min, 4 C). Cleared extracts were applied on Ni^{2+}-NTA resin (Sigma P6611) in gravity-flow columns, which were washed with MiniSOG buffer. Then the proteins were eluted with MiniSOG buffer supplemented with 250 mM Imidazole. Eluted proteins were dialysed against PBS (8 kDa MWCO, RT, 2× 1 h). Protein concentrations were quantified using Bradford assay and their purity was confirmed by SDS-PAGE.

2.2.5 Metallochelate coupling of PtCP-NTA to proteins

5 mM of fluorescent proteins in PCL buffer were mixed with 1.5 to 2 x molar excess of PtCP-NTA, 0.5 mM ZnSO4, and 0.1% Triton X100, in final volume of 500 μL. With the Negative control containing 1 mM EDTA-Na. Samples were incubated for 1 hour at room temperature, protected from light on rotary shaker. The solutions were desalted on PD MiniTrap G25 (GE Healthcare, Buckinghamshire, UK) columns against PBS. Coupling efficiency was assessed by UV−vis spectrophotometry measured absorbance and molar extinction coefficent ε(PtCP) = 72,000 M^{-1} cm^{-1} (380 nm), through Beer Lambert Law in equation 2.2.

Equation 2.2: $Concentration\ of\ dye = \frac{A\ X\ Dilution\ Factor}{\varepsilon}$

Where, A is the absorbance of PtCP-NTA and ε it's molar extinction coefficient both at 380 nm. The concentration of the dye was then used to determine the coupling efficiency of fluorescent proteins to the dye PtCP in equation 2.3

Equation 2.3: $\frac{[Concentration\ of\ dye]}{[Concentration\ of\ protein]}\ X\ 100$

2.5mM dimer forms of ELPCP (N- or C-terminal His_6) protein in capsid buffer was mixed with 7.5nmol of PtCP-NTA, 0.5mM ZnSO4, and 0.1% Triton X100, in final volume of 500µL. With the Negative control containing 1 mM EDTA-Na. The samples were treated in the same manner as above. The VLPs were assembled after coupling via dialysis against Assembly buffer at room temperature, cleared by centrifugation (10 000g, 10 min) and analysed spectrally and by dynamic light scattering (DLS) for size distribution for VLPs. Coupling efficncy of ELPCP to PtCP-NTA was calculated using equation 2.2 and 2.3 as above for fluorescent proteins to PtCP-NTA

2.2.5 Bioconjugation of fluorescein isocyanate (FITC) and Alexa Fluor 488 to horse ferritin

4 nmoles of recombinant or horse spleen-derived ferritin protein were mixed 72 x molar excess (288 nmoles) of fluorescein isocyanate (FITC) or Alexa Fluor 488 (ThermoFisher Scientific) and 0.2M sodium bicarbonate (pH 9), in final volume of 45 0µL. The reaction was carried out over 8 hours at 4°C, protected from light on rotary shaker. The reaction was stopped by the addition of 50mM NH_2Cl. The solutions were desalted on PD MiniTrap G25 columns against PBS. Coupling efficiencies were assessed by UV−vis spectrophotometry using ε(FITC) = 75,000 (488 nm) M−1 cm−1 and ε (Alexa Fluor 488) = 71,000 (488nm) M−1 cm−1. Nanoparticle sizes were analysed by DLS by size distribution.

2.2.6 Encapsulation of Pt-Glc in horse ferritin

1 nmoles of recombinant or horse spleen derived ferritin protein (Sigma) were disassembled by decreasing the pH of the solution to pH 2 via addition of 150 µL 0.2M HCl and incubating at room temperature for 2 hours. The pH was increased to pH 6 via dialysis against 0.2 M Tris, 0.5 M NaCl pH 6 buffer and incubated at room temperature for 1 hour. 32 x molar excess of Pt-Glc (32 nmoles) was added to the solution and the pH of the solution was increased to pH 9 via dialysis against 0.2M Tris, 0.5M NaCl pH 9 buffer and incubated at room temperature overnight. The solutions were desalted on PD MiniTrap G25 columns against PBS. Encapsulation efficiency was assessed by UV−vis spectrophotometry using ε(PtGlc) = 75,000 (395 nm) and nanoparticle sizes were analysed by DLS by size distribution.

2.2.7 Cellulose-based hybrid scaffolds for FLIM

2.2.7.1 Cellulose scaffold preparations

GrowDex hydrogel (UPM) was diluted from 1.5% to 0.5% for experimental work with phenol red-free DMEM supplemented with 10 mM glucose, 1 mM sodium pyruvate, 2 mM L-glutamine for FLIM measurements or cell culture media and equal volume Matrigel, if imaging on upright microscope to prevent shaking or the scaffold. BC spheres were produced and provided by Dr. Peter Timashev (Institute for Regenerative Medicine, I.M. Sechenov First Moscow State University, Moscow, Russian Federation). The spheres were cut into small sections for experimental work. Decellularisation of plant tissues was adapted from the method of [212]. Spinach leaves were cut with 5 mm diameter puncher and the petioles of the celery stems were cut into ~1 mm thick sections. They were then pre-treated with hexane, washed with PBS and incubated in 10% SDS for 4 days, then in a solution of 10% sodium hypochlorite / 0.1% Triton X100 for 48 hours, and finally in deionised water for 48 hours with gentle rocking at room temperature. Decellularised tissues were stored at 4 °C for 2 weeks in the presence of 0.05% sodium azide or were sterilised by immersing in 70% ethanol and sequential washing in sterile Hanks' Balanced Salt Solution for cell-based experiments. For imaging on an upright microscope, GrowDex and decellularised plant materials were embedded in Matrigel, at 50% scaffold: 50% Matrigel by volume.

2.2.7.2 Scaffold labelling and fluorescence lifetime measurements

Cellulose scaffold labelling of BC and GrowDex with CBD-ECFP and CBD-GCaMP2 was optimised to be 5µM with 30-minute incubation. For decellularised celery, carrot and potato incubated with 5µM CBD-EYFP with 30-minute incubation for optimal brightness and labelling efficiency in fluorescence microscopy. Solution-based fluorescence lifetime measurements for CBD-ECFP labelled Growdex were carried out on Fluorolog-3 (Horiba) Spectrofluorometer at range of pH values using buffer solutions, adapted from [212] based on 270 mM KCl, 4 mM CaCl2, 2 mM MgCl2, 40 mM Sucrose and 10% fetal bovine serum (FBS) and supplemented with either 20 mM MES (pH 5.8-6), 20 mM MOPS (pH 6.4-7.2), or 20 mM HEPES-Na (pH 7.6-8). Extracellular acidification (ECA) was measured on Victor2 TR-F microplate reader as described in [404]

2.2.7.3 Cell culture with cellulose scaffolds

Human colon cancer HCT116 wild-type (WT) and $SCO_2^{-/-}$ cells were grown in McCoy 5A medium supplemented with 10% FBS, 10 mM HEPES, pH 7.2, 2 mM Glutamine, 2 mM penicillin-streptomycin

essentially as described before in [36]. For microscopy, 200,000 cells were mixed with 0.5% GrowDex and embedded in 50 µL Matrigel in the centre of 35 mm TC Petri dish, grown for 2-3 days then stained with 5µM CBD-ECFP and analysed. For ECA assay, cells were seeded on collagen IV pre-coated 96-well plate (30,000 per well) and grown for 2 days before analysis.

2.2.7.4 Fluorescence microscopy and FLIM of CBD-tagged proteins

Optimisation of staining with CBD-tagged proteins, stability and assessment of cell growth were performed on Axiovert 200 inverted fluorescence PLIM microscope [404] equipped with T/O2 control and LED excitation sources (390, 470 and 590 nm). CBD-tagged proteins were excited using 470 nm LED with emission collected at 510-560 nm, using 10x/0.3 or oil-immersion 40x/1.3 Plan Neofluar objectives. FLIM was performed on Axio Examiner Z1 upright laser-scanning FLIM-PLIM microscope [36] equipped with 5x/0.25 Fluar, 20x/1.0 W-Plan and 63x/1.0 W-Plan Apochromat dipping objectives, integrated T and Z-axis controls, DCS-120 confocal TCSPC scanner, photon counting detectors and SPC Image software (Becker & Hickl GmbH). TMRM was excited using 405 nm BDL-SMNI pulsed diode laser with emission collected at 565-605 nm. CBD-GCaMP2 was excited using 488 nm BDL-SMNI pulsed diode laser (emission collected at 512-536 nm), CBD-ECFP was excited using 447 nm BDL-SMT pulsed diode laser (emission collected at 512-536 nm). Calibration of pH sensitivity of fluorescence lifetimes was carried out in buffer solutions from [36] based on 135 mM KCl, 2 mM $CaCl_2$, 1 mM $MgCl_2$, 20 mM Sucrose and 10% FBS and supplemented with either 10 mM MES (pH 5.8-6), 10 mM MOPS (pH 6.4-7.2), or 10 mM HEPES-Na (pH 7.6-8). Cell stimulations were carried out using 1 µM Carbonyl cyanide-4-(trifluoromethoxy)phenylhydrazone (FCCP) and 10 µM oligomycin or with equal amounts of DMSO (mock) with cells in phenol red-free DMEM supplemented with 10 mM glucose, 1 mM sodium pyruvate, and 2 mM L-glutamine (no HEPES).

2.2.8 Ferritin constructs

2.2.8.1 Cell culture and characterisation of ferritin constructs

All ferritin nanoparticle size measurements were carried out by Dynamic Light Scattering (DLS) with Zetasizer Nano ZS 4 mW 633nm He-He Laser. Mouse embryonic fibroblasts (MEFs) were grown in Dulbecco's Modified Eagle's medium (DMEM) supplemented with 10% fetal bovine serium (FBS) as described before [36]. For microscopy, 90,000 cells were seeded at the centre of a collagen IV: PDL coated 35 mm glass bottom dish (MatTek) and grown for 2-3 days or 30,000 cells were seeded per well on a collagen IV: PDL coated 8 well microscope insert plate. For hoFTN encapsulated PtGlc

experiments the MEF cells on the were then stained with 2.5µM FITC-hoFTN PtGlc (concentration of encapsulated PtGlc) or with 2.5µM Pt-Glc for 1 hour, with 1µM calcein counter stain for 30 minutes prior to analysis via confocal microscopy. Or stained with 2.5µM FITC-hoFTN PtGlc (concentration of encapsulated PtGlc) or with 2.5µM Pt-Glc for 20 hours with 1µM calcein counter stain for 30 minutes prior to analysis via confocal and fluorescence microscopy. For EGFP -FTNH constructs and Alexa Fluor 488-hoFTN experiments the MEF cells on the 8 well microscope insert plate were incubated with 0.2 µM of EGFP -FTNH constructs 1 or 2 (concentration of FTNH) or 0.2 µM Alexa Fluor 488- hoFTN (concentration of hoFTN) for 16 hours, and counterstained with 0.2 nM TMRM for 30 minutes prior to measurements via fluorescence microscopy.

2.2.8.2 Fluorescence microscopy imaging of ferritin constructs

Optimisation of staining and cell growth were performed on an Axiovert 200 inverted fluorescence PLIM microscope [404] equipped with T/O2 control and LED excitation sources (390, 470 and 590 nm).

For EGFP -FTNH constructs and Alexa Fluor 488-hoFTN imaging was carried out with the above Axiovert 200 inverted fluorescence PLIM microscope [404]. EGFP and Alexa Fluor 488 were imaged with 470 nm LED excitation, with emission collected at 510-650 nm. While TMRM was imaged with 590 nm LED excitation, with emission collected 600- 650 nm. Image collected using 10x/0.3 or 40x/1.3 EC Plan Neofluar objectives. Confocal high powered imaging of ferritin constructs was carried out with Axio Examiner Z1 upright laser-scanning FLIM-PLIM microscope [36] equipped with 5x/0.25 Fluar, 20x/1.0 W-Plan and 63x/1.0 W-Plan Apochromat dipping objectives, integrated T and Z-axis controls, DCS-120 confocal TCSPC scanner, photon counting detectors and SPCImage software (Becker & Hickl GmbH). Ferritin constructs of FITC-hoFTN PtGlc excited using 488 nm tuneable fianium laser for FITC and calcein with emission collected at 510-560 nm and BDL-SMC picosecond 405 nm laser (Becker & Hickl GmbH) for Pt-Glc with emission collected at 635-675 nm using 10x/0.3 or oil-immersion 63x Plan Neofluar objectives. All cellular stains used for microscopy measurements are listed in Table 2.2

Table 2.2. Cellular stains for microscopy measurements

Probe	**Concentration**	**Function**	**Staining procedure**	**Excitation, emission (nm)**
TMRM	20 nM	Stains mitochondria	Add 20nM to sample, 30 minutes before measurement	543nm, 555-600nm

Hoechst 33342	1 µM	Stains nucleic acid	Add 1µM to sample, 30 minutes before measurement	350nm, 461-600nm
Calcein	1 µM	Stains whole cell for cell viability	Add 1µM to sample, 30 minutes before measurement	495nm, 515-600nm

2.2.9 Spectroscopy

Absorption spectra were measured on 8453-diode array spectrophotometer (Agilent), fluorescence spectra were measured on LS50B (PerkinElmer) spectrometer in PBS, pH 7.4, as described previously [314].

2.2.10 Data assessment of CBD-ECFP GrowDex scaffolds FLIM response and cell culture

Fluorescence intensity images exported from widefield (ImSpectror Pro software, LaVision) or TCSPC-FLIM (SPCImage software, Becker & Hickl) microscopes were used as is or assembled as 3D stacks in SVI Huygens Pro 17.0 software (Scientific Volume Imaging BV, Netherlands). For quantification of cell and scaffold staining efficiency and stability, fluorescence intensity images were analysed in ImageJ software (Fiji.sc). Data are presented here are as average values with standard deviation shown as error bars. The experiments were performed in triplicate with the data presented as averaged values from independently chosen regions of interest (ROI). For statistical significance, data were evaluated using independent t-test, with confidence levels P=0.05 and P=0.005, indicated with asterisks in figures. The fluorescence lifetime decays were fitted directly in SPCImage software (Becker & Hickl) using tail-enhanced mono-exponential or double-exponential fitting functions to achieve χ^2 < 1.5. For pH calibration, the fluorescence lifetime distribution histograms (produced in SPCImage with optimised fitting function, three independent replicates per each pH point) were exported in Origin 6.0 software (Microcal Inc., USA), fitted with Cauchy-Lorentz distribution function to identify mean values and fitted for corresponding pH values using Sigmoid function in Origin 6.0. The following relationship was obtained for CBD-ECFP (447 nm exc.):

Equation 2.4: $\tau = \frac{2133}{1+e^{-1.42*(pH-4.89)}}$

where τ is in ps. For conversion of measured fluorescence lifetime values in pH, a simplified polynomial relationship was used:

Equation 2.5: $pH = 16.48 - 0.0141 * \tau + 4.56 * 10^{-6} * \tau^2$

where τ is in ps.

2.2.11 Dynamic light scattering

All nanoparticle construct sizes were determined using dynamic light scattering (DLS) on Zetasizer NANO ZS equipped with 4 mW 633 nm laser (Malvern Instruments). DLS technique measures nanoparticle size through the concept of the Brownian law of motion of nanoparticles in a liquid medium. The nanoparticles undergoing Brownian cause fluctuations in scattered light intensity, where smaller nanoparticles cause faster fluctuations in light intensity than larger ones. The DLS calculates nanoparticle size from the velocity of the Brownian motion, which is defined by the translational diffusion coefficient (D), which can be converted to nanoparticle size by using the Stokes-Einstein equation [405].

Equation 2.6: $d_H = \frac{kT}{3\pi\eta D}$

Where, d_H is the hydrodynamic diameter of the nanoparticles, k the Boltzmann's constant, T the absolute temperature, η the viscosity of the liquid medium, and D the diffusion constant.

Chapter 3: Evaluation of Metallochelate coupling for the design of new intracellular O_2 probes.

3.1 Introduction

3.1.1 Phosphorescent oxygen sensitive probes

Molecular oxygen is one of the key molecules for life in both prokaryotic and eukaryotic organisms including plants and human cells alike [406]. Oxygenation and supply of molecular oxygen (O_2) within cells and tissues is of significant importance, with the dysregulation of O_2 supply and oxygenation affecting major cellular functions, such as: proliferation, differentiation, apoptosis, energy production, cell signalling pathways and enzymatic reactions [225, 407-410]. O_2 is an important marker of cell viability, metabolism, and normal physiological behaviour of cells [38, 411, 412]. There are several methodologies and techniques to measure physiological O_2 gradients in cell and tissue models such as indirect staining with antibodies, hypoxia markers or FPs [413-415], as well as electron paramagnetic resonance (EPR), microelectrodes, and near infrared spectroscopy (NIRS) oximetry [416-418]. However, the techniques listed do not allow for direct, non-invasive measurements of O_2 gradients. Quenched-phosphorescence O_2 detection is a technique that does allow for such measurements, along with the analysis of O_2 in respiring cells with stable calibration, subcellular resolution and multiplexing potential [35, 419]. The technique utilises the ability of molecular O_2 to quench photoluminescent signals. The luminophore in the triplet state undergoes quenching via collisional interactions with O_2. The O_2 molecule accepts energy from the luminophore-excited triplet state, thereby reducing phosphorescence signal intensity and lifetime. This measurement is O_2 concentration dependent, allowing for calculation of O_2 concentration via the Stern Volmer equation (1.1), in which the relationship of phosphorescence lifetime (τ) and intensity (I) is utilised.

Equation 3.1 $\frac{I_0}{I} = \frac{\tau_0}{\tau} = 1 + K_{s-v}[O_2] = 1 + K_q\tau_0[O_2]$

Where, I_0 and τ_0 are unquenched intensity and lifetime at zero O_2 respectively. K_{s-v} is the stern volmer quenching constant. K_q is the biomolecular quenching rate constant which depends on the environment of the reporter dye, temperature, and sterical factors. Luminescence lifetime is the average amount of time a luminophore remains in an excited state before the emission of energy as a photon of light. Lifetime measurements are highly suited for luminescence quenching measurements of O_2 compared to intensity based measurements, as its response is independent of dye concentration used. Phosphorescence lifetimes of O_2 sensitive dyes (i.e. Pt porphyrins) are in the longer microsecond range compared to fluorescence lifetime of FPs, which are in the nanosecond range. The longer lifetime range allows for easier and more reliable measurements. The above equation (1.1) can be rewritten as follows;

Equation 3.2 $[O_2] = (\tau_0 - \tau)/(\tau K_{s-v})$

The Stern-Volmer equation (1.2) is only applied to homogeneous populations that produce a linear Stern-Volmer relationship. However, in practical applications, many populations possess a heterogeneous population, resulting in a nonlinear Stern-Volmer relationship. This can be overcome using a two-site model (also known as Demas model) equation (1.3) [420].

Equation 3.3 $\frac{I_0}{I} = 1/(\frac{f_{(\alpha 1)}}{(1+K_{sv1}[Q])}) + (\frac{f_{(\alpha 2)}}{(1+K_{sv2}[Q])})$

Where, $f_{(\alpha 1)}$ and $f_{(\alpha 2)}$ are the two fractional contributions of the total luminescence emissions at two sites, and K_{sv1} and K_{sv2} are their respective quenching constants [421].

Many photoluminescent O_2-sensitive materials are composed of synthetic indicator dyes, such as macrocyclic complexes of heavy metal ions Pd, Pt, Ru, and Ir. These complexes are known as metalloporphyrins. Among them, the Pt(II) and Pd(II)-porphyrins are the most popular dyes used as they possess strong phosphorescence signals with high molar absorption coefficients for high absorbance of light and large Stokes' shifts, reducing interference and quenching between absorbance and emission. When comparing the two, Pt(II)-porphyrins possess lifetimes in the range of 20 to 100 µs and are used for measurements within the physiological range of O_2 0-200 µM, whereas Pd(II)-porphyrins possess lifetimes in range of 400- 1000µs and are used for measurements at <50µM of O_2 [419]. As a result, Pt(II)-porphyrins are preferred over Pd(II)-porphyrins as they possess shorter emission times and are quenched less at conventionally used 21% O_2. This decreases the acquisition times needed, making them more practical to use.

The most popular of the Pt(II)-porphyrins are modified derivatives of platinum tetrakis(pentafuorophenyl)porphyrin (PtTFPP) and Pt(II) coproporphyrin I (PtCP). This is due to their brightness, photostability and relatively low cost. However, initially, they suffered from poor cellular delivery due to their high hydrophobicity resulting in self-aggregation and nonspecific binding to cells and proteins. It wasn't until these issues were addressed that they became widely used. To improve intracellular delivery, the dyes can be functionalised to hydrophilic groups via click chemistry to reduce hydrophobicity. PtTFPP has been functionalised with four monosaccharides thio-glucose (Pt-Glc) and thio-galactose (Pt-Gal) [196]. The monosaccharides confer probe hydrophilicity and cell permeability without compromising O_2 sensitivity or probe brightness. In order to improve intracellular delivery and staining, PtCP has been conjugated to hydrophilic macromolecular carriers or cell targeting peptides. PtCP expressing an isothiocyanate reactive group was conjugated to bovine serum albumin (BSA) via isothiocyanate coupling, marketed as MitoXpress by Luxcel [422]. MitoXpress is applied in the quantitative assessment of intracellular O_2 concentration and cellular oxygenation [423]. PtCP has also been conjugated to positively charged TAT derived peptides [424], in which the conjugates displayed well defined intracellular staining, which was more uniform than that of the MitoXpress and other carrier based probes, allowing for the study of both intracellular O_2 levels and the monitoring of changes

in cell respiration in live cells [425]. Conjugation of PtCP to bactenecin 7 peptide fragment (BN7) [426] resulted in development of O_2 sensitive probe that successfully displayed intracellular staining and displayed responses to changes in cell respiration, similar to that of the TAT conjugated probes in PC12 cells [427].

The PtTFPP dyes have also displayed improved intracellular staining by incorporating the dye inside polymers. Incorporation of PtTFPP into cationic polymer Eudragit RL-100, known as NanO2, has resulted in the development of probes suited for lifetime-based time resolved fluorescence (TR-F) detection and PLIM imaging of O_2 [428]. The positive charge on the RL-100 polymer increases cell permeability, localising to lysosomes and endosomes. NanO2 displays suitability for measurements of phosphorescence lifetime in cell oxygenation upon metabolic treatments [423]. However, in neurosphere models, it displayed aggregation [429]. This issue has been addressed by the conjugation of negatively charged PMMA-AA/PtTFPP, which demonstrated improved intracellular staining in neural cell models of live cell brain slices and neurospehre spheroid cultures [430]. Research that conjugated blue fluorescent polymer polyfluorene to meso-Tetrakis(pentafluorophenyl)porphyrinato]platinum(ii) (PtF20TPP), developed O_2-sensitive phosphorescent nanoparticles with ratiometric FRET functionality [431]. This research inspired improvements to the RL-100 NanO2 PtTFPP nanoparticles via the addition of a polyfluorene polymer. Again, this polymer serves as a FRET antenna to improve brightness and confer the ability to carry out two photon excitation and ratiometric intensity-based detection. This probe was named MM2 [35].

Despite advances in intracellular O_2 sensors, only a certain number of probes and dyes achieve optimal intracellular staining and cell targeting. The inability to stain a diverse range of cell types and tissue models currently hinders their usage, due to their need for long impractical staining times. The development of intracellular O_2 sensors with antenna dyes for FRET measurements, although a significant breakthrough, is limited by the range of suitable antenna dyes for successful application. Efforts to reduce the hydrophobicity and to add charged nanoparticles for intracellular delivery have reached a plateau, in that their height of their success has been realised.

Therefore, the development of new structures is significant, such as conjugation to self-assembling nanoparticles that allow for the attachment for multiple dye molecules, targeting groups and protective groups (i.e. PEG). However, the development of such constructs is needed for regenerative medicine, where the measurement of O_2 is of vital importance in the study of drug and metabolic responses in advanced tissue models such as spheroids and organoids. Here we have evaluated metallochelate coupling of Pt(II)-porphyrin dyes to self-assembling protein nanoparticles, and a range of FPs, as a viable strategy in the development of multiplexed imaging platforms and ratiometric sensors.

3.1.2 Fluorescent proteins for live cell imaging

FPs are a homologous class of proteins that absorb light and re-emit it at a longer wavelength as fluorescence, like that of fluorescent molecules. In the case of FPs, this ability is derived from a sequence of 3 amino acids that form the chromophore. The first FP to be derived and characterised was green fluorescent protein (GFP), from the *Aequorea Victoria* jellyfish. Through protein mutation of the GFP chromophore structure, blue (BFP), yellow (YFP), cyan (CFP) FPs were discovered along with red (RFP), derived from *Discosoma nummiforme* (DSRed). Since this initial work, FP colour palette and properties has been expanded. To determine which FP is suitable for an experiment or imaging application, its intrinsic properties must be considered along with the experimental parameters, such as: brightness, photostability, environment, chromophore maturation, and oligomerisation.

FPs are applied in live cell fluorescence imaging for the study of biological models. Here, they are used to study cellular processes and dynamics, allowing for the visualisation of small molecules, ions, proteins, nucleic acids, and biochemical reactions. Some FPs display sensitivities to pH, ion and polarity changes, affecting their fluorescence intensities and lifetimes, which allow for the quantitative measurements of these factors [283]. The development of photoactivatable FPs [297] has allowed for the analysis of protein tracking [301] and interactions [264], as well as applications in super-resolution imaging [261].

FPs are applied in live cell imaging through the use of FP fusions (FPFs) for the visualisation of gene expression in target cells or via conjugation with nanoparticles, proteins (e.g. antibodies, self-assembling protein nanoparticles), or genetic material for cell delivery [432]. FPFs are plasmid vectors that contain FP encoding genes at either the N or C terminal of the protein of interest. The placement of the FP gene is dependent on the FP being used and the experimental aims. Issues regarding the positioning of the FP must be considered with regards to the placement of the FP gene at the correct terminal, so as not to block targeting domains for specific sub-cellular localisation. Enough space must also be given for FP to fully fold into its tertiary structural conformation. Once designed, the FPF plasmid is transfected into the target cells via lipofection [433] . In the cell, the promoter expression is induced, causing the FPF genes to be transcribed and translated into proteins, thereby allowing for the study of protein expression and localisation in cellular organelles [252, 434, 435]. However, FPFs are not without their downfalls. FPs can potentially interfere with the structure or function of the protein to which they are fused, by oligmersing and aggregating in high concentrations, or when in close proximity to each other. Alternative methods of attaching FPs or small molecule fluorophores to scaffolds like nanoparticles, peptides or other carriers have been explored for live cell imaging [332, 436, 437]. The advantages of coupling to nanoparticles allows for the control over the number and ratio of attached FPs or small molecule fluorophores, which can reduce issues with oligomerisation and aggregation, as well as the attachment of various targeting peptides for intracellular delivery.

3.1.3 Metallochelate coupling

An alternative strategy to FPF genetic constructs in probing cells and tissues for visualisation of cells and protein dynamics is the use of chelating FPs to oligo- histidine tags on the surfaces of nanoparticles or proteins of interest. This strategy is known as metallochelate coupling (also referred to as metal histidine coordination in literature). Oligo-histidine sequences are capable of coordinating transition metal ions (Zn^{2+}, Ni^{2+}, Co^{2+}, or Cu^{2+}) which are chelated partly by nitrilotriacetic acid (NTA) and iminodiacetic acid (IDA) chelating groups. His tags can be inserted into the N or C terminus of recombinant protein for purification via affinity chromatography, in which NTA- Ni^{2} selectively binds to recombinant His-tagged proteins. This coordination can also be used for labelling strategies of attaching His- tagged recombinant proteins to NTA or IDA expressing groups such as fluorophores, organic and synthetic dyes [438, 439]. The most commonly used transition metal for coordination is Ni^{2+}. However, the drawback of using NTA- Ni^{2+} is that Ni^{2+} is a heavy metal therefore, it can be both toxic to cells and quench the fluorescence of its attached fluorophore. An alternative is Zn^{2+} which occurs naturally in biological systems and is not a quencher of fluorescence [440].

The labelling of proteins of interest with small molecule-based fluorescent probes via metallochelate coupling is viewed to be an alternative to FPF genetic constructs, many of which fail to cross the plasma cell membrane. Therefore, they have been only used successfully for proteins on the plasma cell membrane. The probe consists of NTA-Ni2+ group for binding and a fluorophore for visualisation. The probe is then added to the cell culture. Here, it binds to the expressed protein of interest that contains the specific peptide for binding. These probes selectively bind to oligo-histidine tagged proteins of interest, thereby allowing for their characterisation (i.e. localisation). Recent work has been centred on the development of probes for intracellular cell staining. A synthetic fluorescent probe consisting of Ni^{2+}-NTA group and fluorophore based on coumarin derivative, along with a arylazide moiety (AC) known as Ni^{2+}-NTA-AC was developed for live cell imaging of the His-tagged recombinant DNA repair protein, Xeroderma pigmentosum group A (XPA122) [441]. The probe was specifically designed with reduced negative charge to be intracellular and was successful in the staining of HeLa cells and specifically complexed to the transfected His-tagged XPA122 protein. When compared to the FPF genetic construct of His-RFP-His-XPA122, it was found that localisation was distributed evenly throughout the cell, suggesting that RFP affects protein localisation. However, one significant drawback of the probe was that it was observed to bind to histidine rich proteins in cell, resulting in lower sensitivity. Cell penetrating peptide transactivator of transcription (TAT) was coordinated to fluorescently labelled carrier complex containing three NTA groups via its His_6-tag [442]. The TAT penetrating peptide transports the tris-NTA complex across the plasma cell membrane into the cell, where it preferentially binds to the recombinant His_{10}-tagged protein of interest and releases the His_6-tagged TAT peptide. The probe was evaluated with HeLa and C2C12 cells for the specific binding of

His_{10} tagged antigen translocation complex (TAP) in the cellular ER and for the DNA-silencing complex methyl CpG-binding protein 2 (MeCP2) in the nucleus. Site specific staining of both recombinant proteins was observed, like that of the FPF genetic constructs: TAP1-mVenus-His_{10} and MeCP2-GFP- His_{10}. These are examples of such small molecule probes that can stain intracellularly specific His-tagged proteins of interest, without perturbing protein folding or localisation, providing a possible alternative to FPF genetic constructs.

From evidence that supported metallochelate coupling's ability to attach oligo-histidine tagged proteins to NTA expressing molecules, we hypothesised that it could be a viable strategy (Fig 3.1 A) in the coupling of protein-based nanoparticles and FPs to O_2-sensitive dyes labelled with NTA, such as PtCP-NTA (Fig 3.1 B). The use of metallochelate coupling to attach FP to PtCP-NTA would facilitate the design of an O_2-sensitive probe with fluorescence-based localisation and ratiometric-based measurements of O_2, where FP can be used as an O_2-insensitive reference (i.e. like that of MM2 and polyfluorene). Here we selected FPs over organic fluorescent dyes due to the need for genetic expression of the oligo-histidine tag on FPs for metallochelate coupling. This combined with the ability to attach different coloured FPs allows for the detection and optimisation of FRET between the PtCP-NTA. In the case of protein based nanoparticles, we selected ELPCP, a viral-like particle composed of elastin like polypeptide (ELP) and cowpea chlorotic mottle virus (CCMV) protein capsid [443]. This dual structure results in two different self-assembly mechanisms within the one VLP. ELP thermal induced assembly in which subunits of ELPCP are dialyzed against a pH7.5 1.3M NaCl buffer at 35°C for 15 minutes. This resulted in the production of 18nm sized VLPs, comprised of 90 subunits. The second mechanism is via CCMV pH induced assembly. Here the ELPCP subunits are dialysed against pH 7.5 buffers which induces dimerization of the subunits. Then they are dialysed against pH 5 buffers which results in the production of assembled 28nm VLPs comprised of 180 subunits. We used the pH induced assembly pathway, as the conditions were compatible with those of metallochelate coupling and generated more ELPCP subunits for coupling of PtCP-NTA, thereby increasing the potential phosphorescence brightness of the construct.

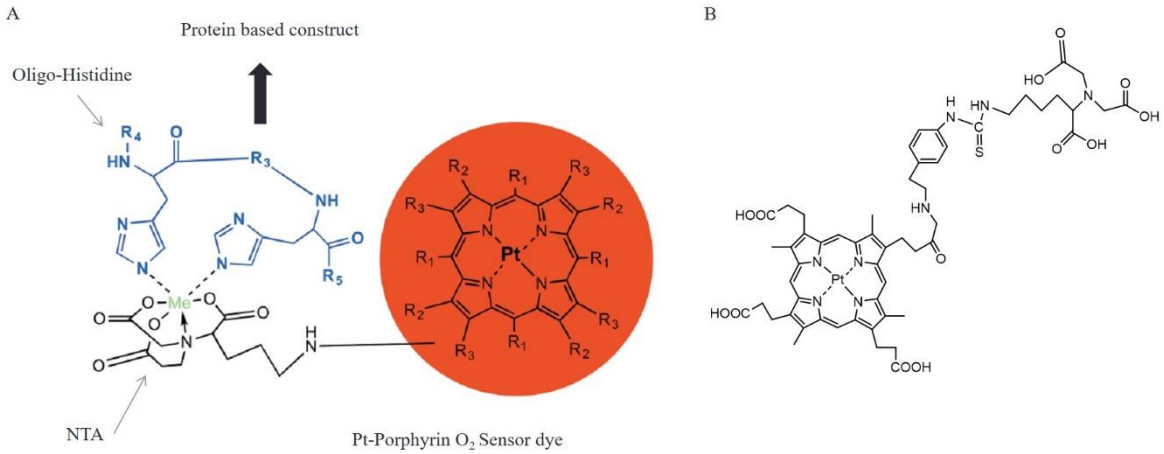

Figure 3.1. Schematic of metallochelate coupling strategy and structure of PtCP-NTA. (A) Oligo-histidine sequences on our protein-based constructs coordinate transition metal ions (Zn^{2+}, Ni^{2+}, Co^{2+}, or Cu^{2+}), which are chelated partly by nitrilotriacetic acid (NTA) chelating groups on Pt-Porphyrin O_2 sensor dye (i.e. PtCP-NTA). Thereby coupling protein-based constructs to O_2 sensitive dyes labelled with an NTA group. (B) Structure of Pt-Porphyrin O_2 sensor dye, PtCP-NTA

3.2 Aims

Here, we aim to evaluate metallochelate coupling as a viable strategy to couple PtCP-NTA phosphorescent O_2-sensitive dye to His_6-tagged FPs and VLP subunits of ELPCP, with the goal of developing O_2-sensitive complexes for live cell imaging.

3.3 Results

3.3.1 Optimisation of fluorescent protein production

First, we evaluated several monomeric FPs for applications in metallochelate coupling. From the literature of FPs, we selected FPs with high brightness and high expression in *E.coli* bacterial protein production system, along with a high degree of solubility. For optimisation of production and purification conditions we selected EGFP, DsRed express, and TagBFP. We cloned all three into pQE-30 His_6-tagged expression vector and transfected them into SG13009 strain *E.coli* cells supplied by Qiagen. This is due to the SG13009 strain‘s optimal pREP4 plasmid expression regulation over the pQE-30 expression vector. With EGFP, following growth at 37°C until OD_{600}= ~0.4, we used the following induction conditions: 72 hours at 4°C, 16 hours at room temperature, and 4 hours at 37°C. With different concentrations (of inducer of expression) IPTG at 1 mM, 0.5 mM, or 0.25 mM to induce expression. From sodium dodecyl sulfate–polyacrylamide gel electrophoresis (SDS-PAGE) analysis

and visualisation of EGFP's fluorescent spectra, we found the optimal production conditions to be 16 hours at room temperature, with 0.25 mM IPTG induction (Fig 3.2).

.

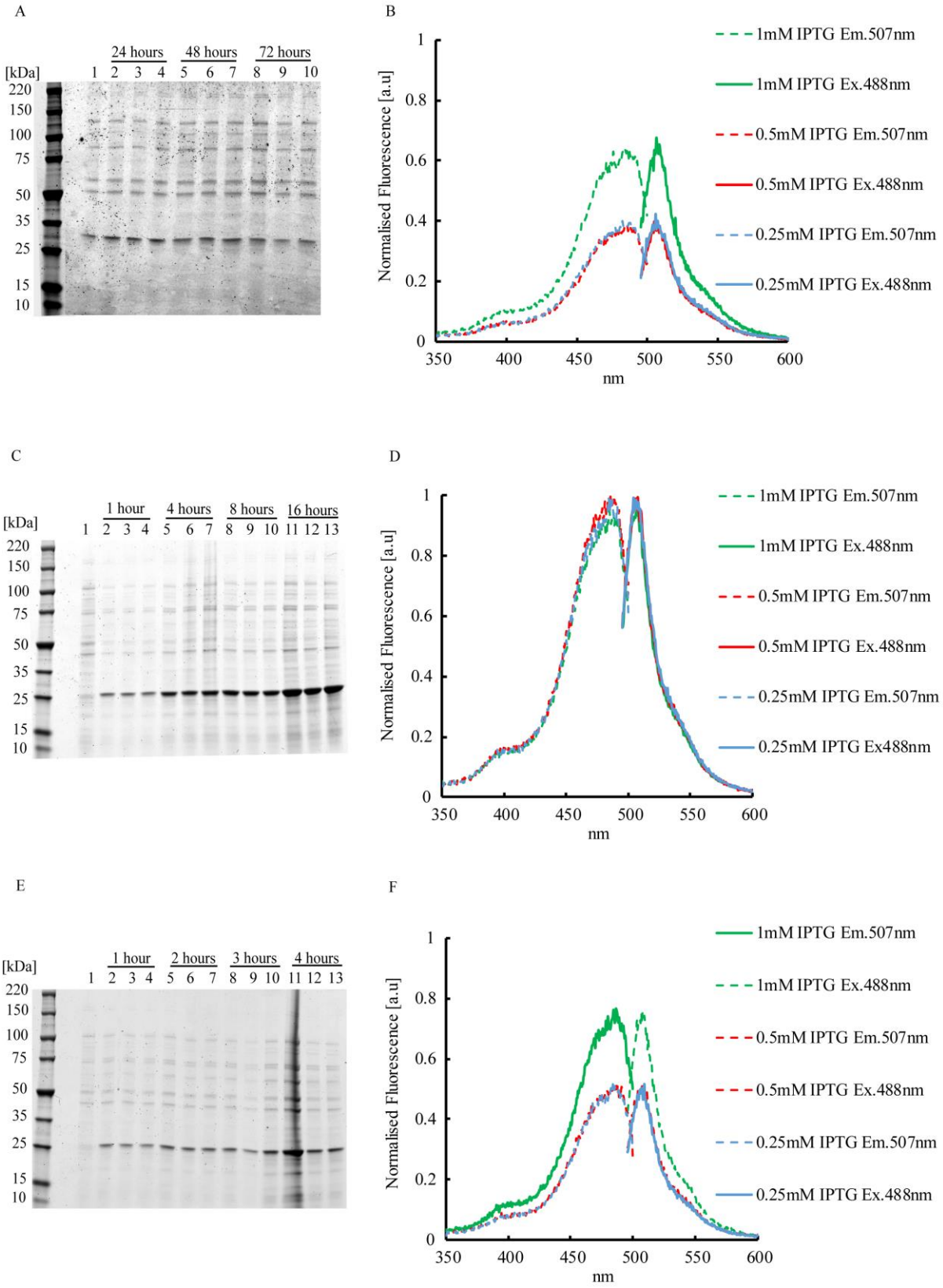

Figure 3.2. Optimisation of EGFP protein production. (A, C, and E) Bacterial IPTG induced EGFP protein samples and uninduced samples, ran on SDS-PAGE 4-10 % gel and analysed via Coomassie staining. With lane 1 loaded with uninduced samples and 1 mM, 0.5 mM and 0.25 mM IPTG induced samples respectively for each time point. With expected size of EGFP ~27kDa (A) 4°C for 72 hours, (C) Room temperature for 16 hours, (E)

37°C for 4 hours. (B, D, and F) Fluorescence excitation (Em. 507 nm) and emission (Exc. 488 nm) spectra of EGFP (B) 4°C for 72 hours, (D) Room temperature for 16 hours, (F) 37°C for 4 hours.

We then subsequently used the optimal room temperature for 16 hours with 0.25mM IPTG production conditions for EGFP, in the production of DsRed and TagBFP2 (Fig 3.3).

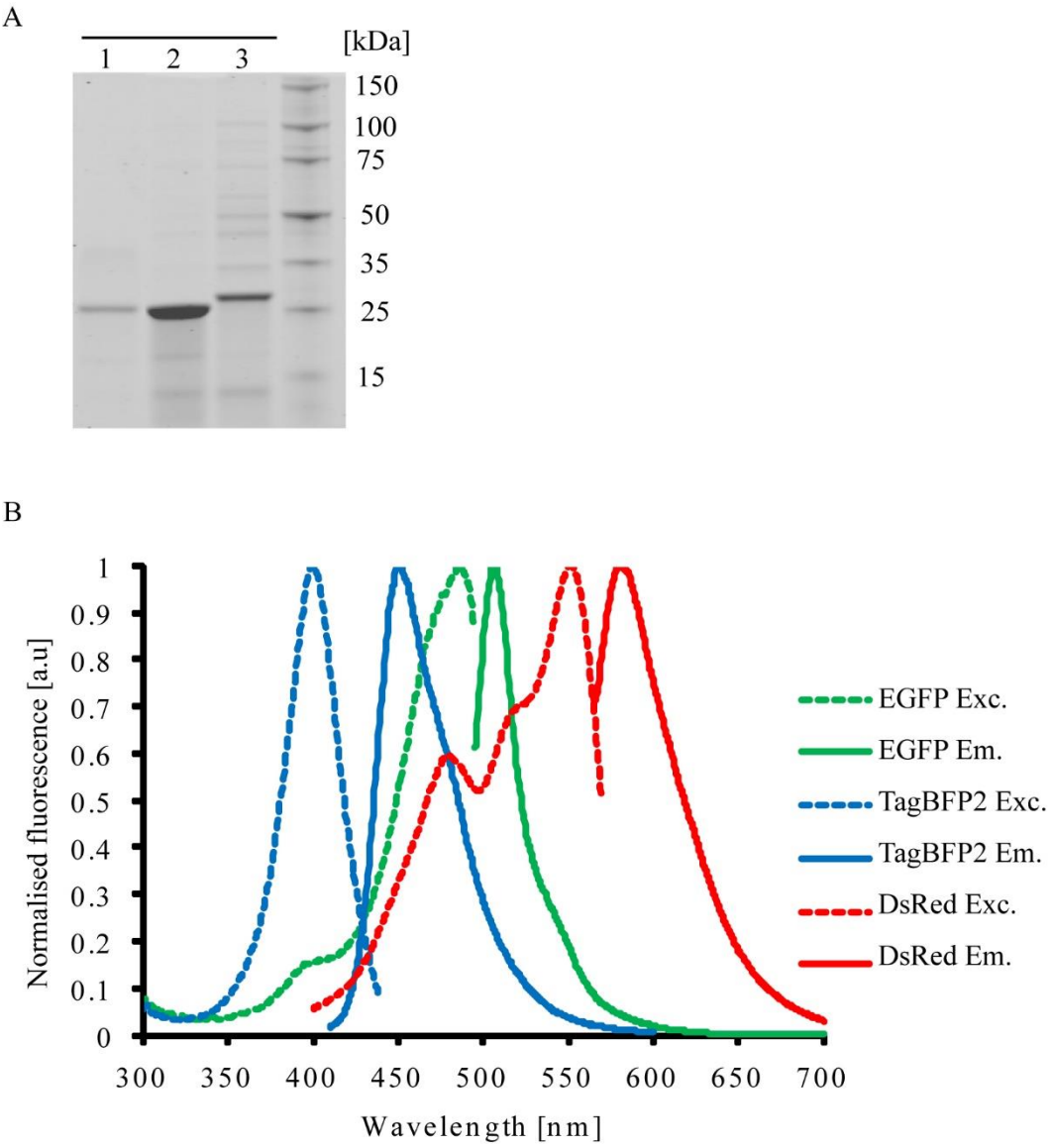

Figure 3.3. Fluorescent protein production. (A) Purification products of TagBFP2, EGFP, and DsRed-Express. Products ran on 4-10 % SDS -PAGE gel and analysed via coomassie staining. Lane 1 TagBFP2, Lane 2 EGFP, and Lane 3 DsRed-Express, ~25-27 kDa. (B) Fluorescence excitation and emission spectra of TagBFP2 excitation (Em.457 nm) and emission (Exc.402 nm), EGFP excitation (Em. 507 nm) and (emission Exc. 488 nm), and DsRed-Express excitation (Em.583 nm) and emission (Exc.556 nm). (Figure modified from [314])

3.3.2 Metallochelate coupling of fluorescent proteins to PtCP-NTA

With the production of FPs optimised, we set out to evaluate metallochelate coupling via their respective His_6-tags to the NTA group on the O_2-sensitive phosphorescent dye, PtCP-NTA. Metallochelate coupling of EGFP to PtCP-NTA was carried out in the presence of $ZnSO_4$, providing Zn^{2+} ions for chelation. We carried out optimisation experiments with various ratios of EGFP to PtCP-NTA and found that 1.5 to 2 times molar excess of PtCP-NTA was optimal (Fig 3.4). The results of metallochelate coupling showed an approximately >40 % yield of complexation of PtCP-NTA to EGFP (see Materials and Methods section 2.2.5), compared to the negative control as seen from the absorbance spectra (Fig 3.4 A). EGFP-PtCP-NTA complex displayed similar fluorescence to that of uncoupled EGFP, along with presence of phosphorescence emission band (650 nm) sensitive to O_2 (Fig 3.4 B).

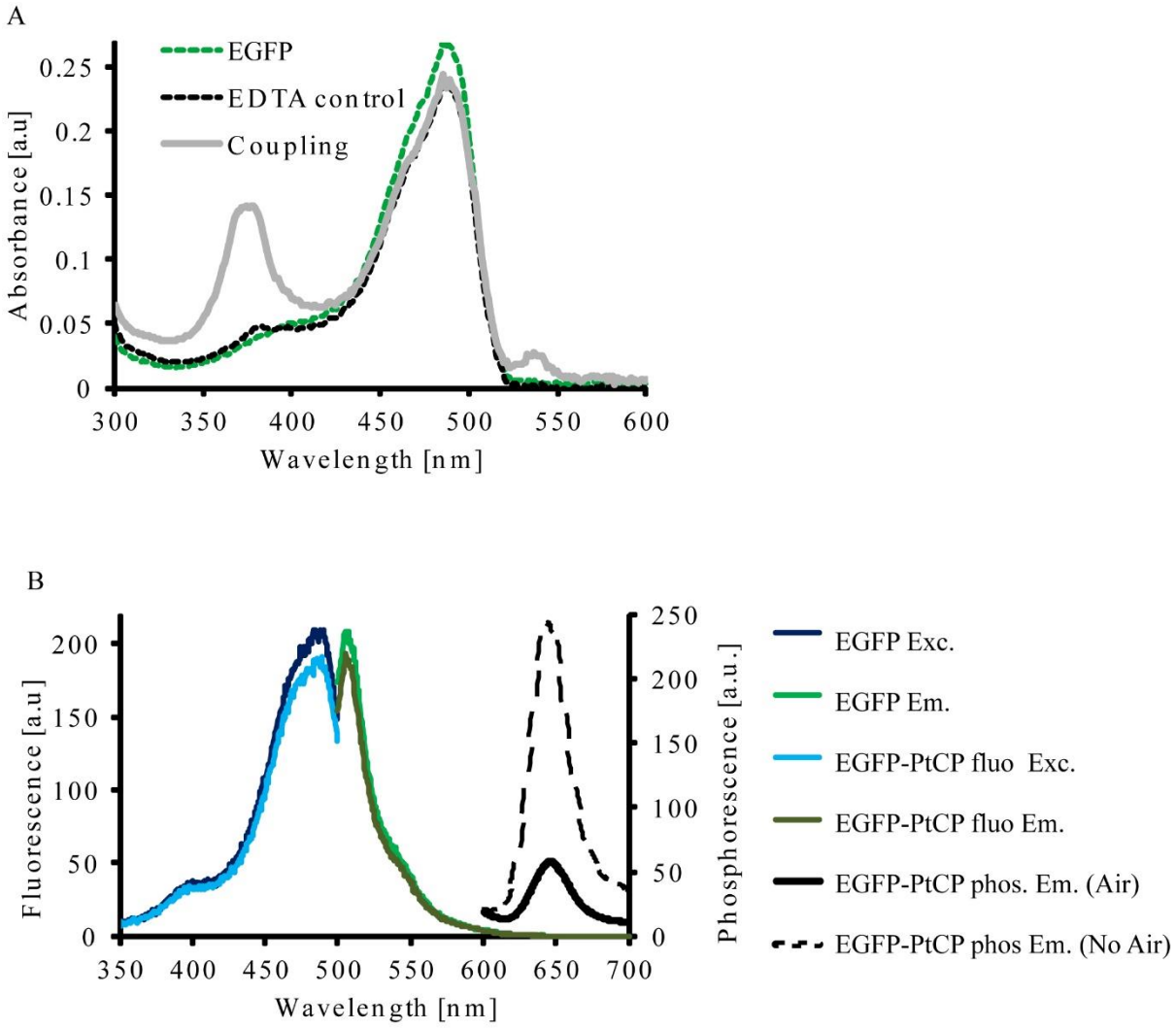

Figure 3.4. Metallochelate coupling of EGFP to PtCP-NTA. (A) Absorbance spectra of EGFP, coupled EGFP-PtCP, and negative EDTA control. Peak at 380 nm for PtCP-NTA confirms efficient coupling. (B) Luminescent properties of coupled EGFP and PtCP-NTA. Fluorescence excitation (Em. 507 nm) and emission (Exc. 488 nm) of EGFP and EGFP-PtCP. With phosphorescence emission (Exc. 380 nm) spectra of EGFP-PtCP, under oxygenated and deoxygenated conditions. (Figure modified from [314])

We then set out to evaluate metallochelate coupling of PtCP-NTA to other N-Terminally His_6-tagged FPs, TagBFP2 and DsRed Express (Fig 3.5 and 3.6). Metallochelate coupling was carried out using the conditions optimised previously with EGFP. TagBFP2-PtCP-NTA complex displayed similar fluorescence to that of uncoupled TagBFP2 (Fig 3.4 A). The presence of a phosphorescence emission band at 650nm showed that metallochelate coupling was successful (Fig 3.5 A). The complex was also sensitive to changes in O_2 (Fig 3.5 B).

A

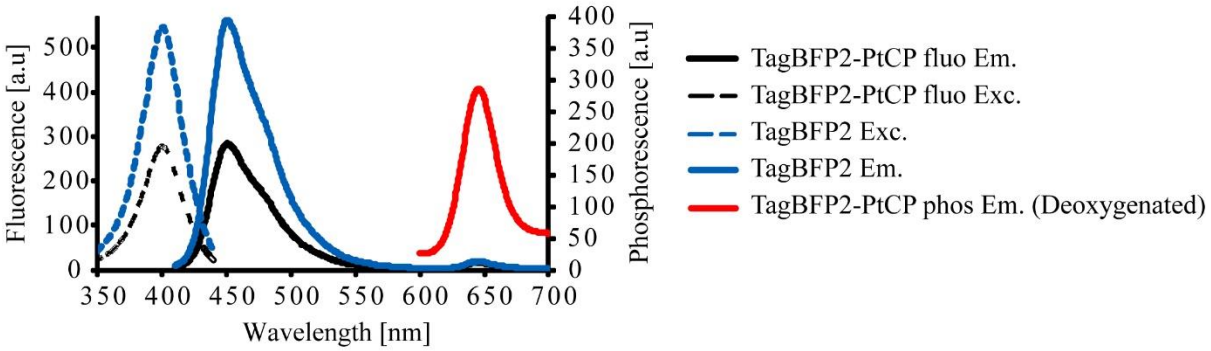

B

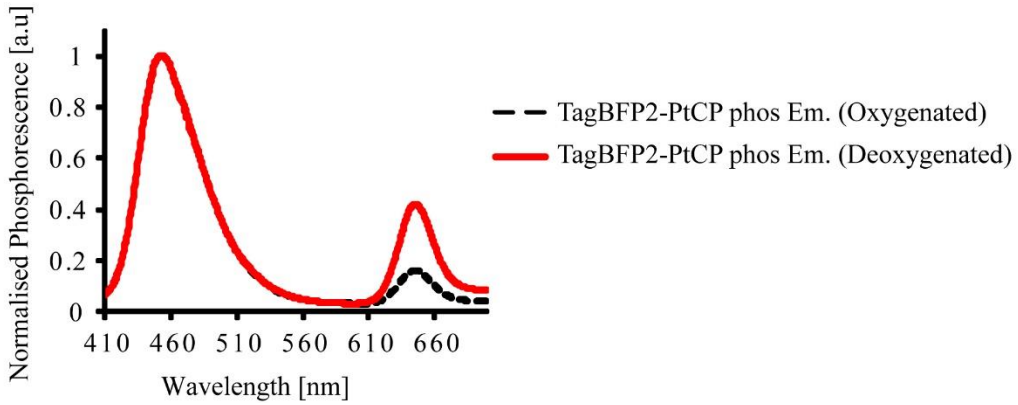

Figure 3.5. TagBFP2 and coupled TagBFP2-PtCP luminescence spectra. (A) Fluorescence excitation (Em.457nm) and emission (Exc.402nm) spectra of TagBFP2 and coupled TagBFP2-PtCP. With deoxygenated phosphorescence spectra of coupled TagBFP2-PtCP. (B) Phosphorescence emission (Ex.380nm) of coupled TagBFP2-PtCP with response to deoxygenation. (Figure modified from [314])

DsRed Express-PtCP-NTA complex displayed similar fluorescence to that of uncoupled DsRed Express. The presence of a phosphorescence emission band at 650nm showed that metallochelate coupling was successful (Fig 3.6 A). The complex was also sensitive to changes in O_2 (Fig 3.6 B). Overall, metallochelate coupling with FP displayed that metallochelate coupling is a viable strategy for large proteins.

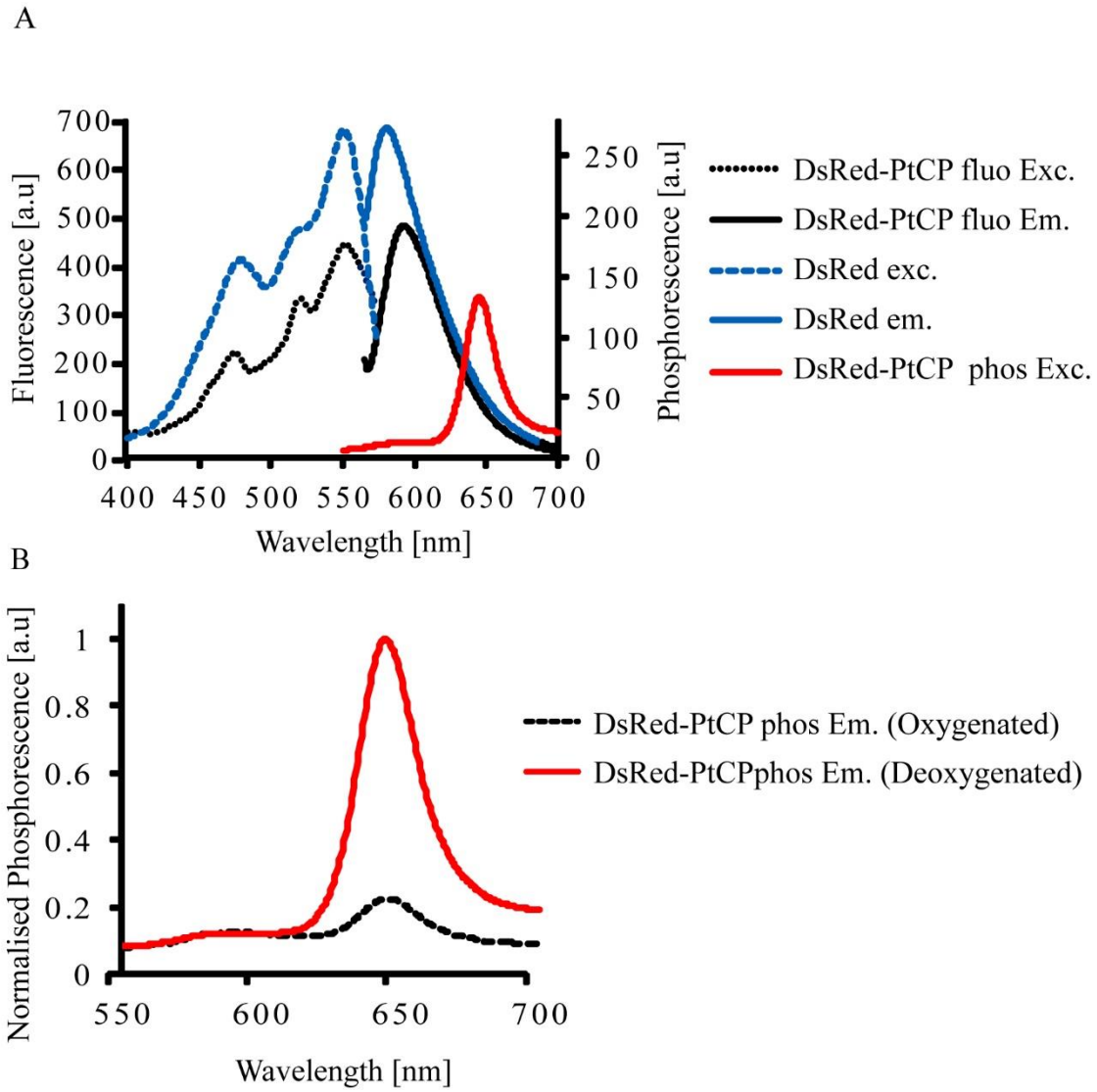

Figure 3.6. DsRed and coupled DsRed-PtCP luminescence spectra. (A) Fluorescence excitation (Em.583nm) and emission (Exc.556nm) spectra of DsRed and coupled DsRed-PtCP. With deoxygenated phosphorescence spectra of coupled DsRed-PtCP. (B) Phosphorescence emission (Ex.380nm) of Coupled DsRed-PtCP with response to deoxygenation. (Figure modified from [314])

3.3.3 Optimisation of ELPCP production and metallochelate coupling to PtCP-NTA

We first evaluated metallochelate coupling with N-terminal His_6-tagged ELPCP (His_6-ELPCP) and C-terminal His_6-tagged ELPCP (ELPCP -His_6) (Fig 3.7 A) to PtCP-NTA, using the conditions used for coupling to FPs. We produced and purified both ELPCP protein constructs as described in materials and methods section 2.2.4.2 and as shown in the schematic below (Fig 3.7 A), obtaining proteins and assembled VLPs of the correct size for both as shown on SDS -PAGE gel (Fig 3.7 B) and DLS measurement (see Materials and Methods section 2.2.11) (Fig 3.7 C-D). Coupling to dimer forms of both His_6-ELPCP and ELPCP-His_6 was successful, however, when we carried out assembly in

'Assembly dialysis buffer' pH5 we did not obtain VLPs of the correct size in the case of His_6-ELPCP. We theorised that the N terminal His_6-tag of His_6-ELPCP was facing the internal cavity of the assembled VLPs. Therefore, when coupled to PtCP-NTA, it sterically hindered assembly. C-terminal His_6-tagged ELPCP in its dimer form achieved 65% coupling efficiency (see Materials and Methods section 2.2.5) compared to the EDTA control (Fig 3.7 E). After assembly we obtained VLPs of the correct size at ~28nm.

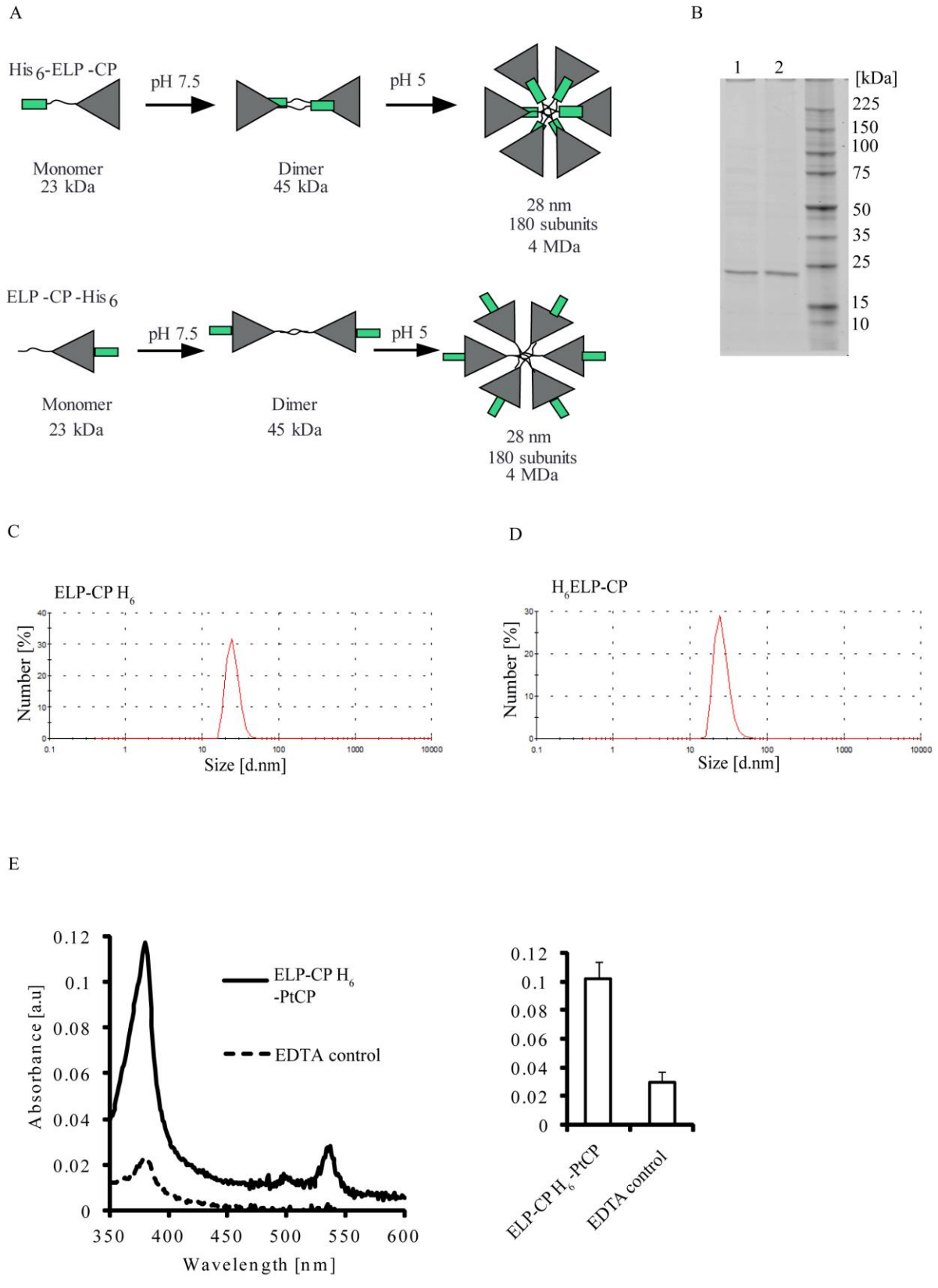

Figure 3.7. ELP-CP production and coupling to PtCP-NTA. (A) Schematic representation of ELPCP-H_6. And H_6.-ELPCP constructs and pH assembly process. (B) Purification products of ELPCP-H_6. And H_6.-ELPCP. Products ran on 4-10% SDS -PAGE gel lanes 1 and 2 respectively and analysed via coomassie staining. (C and

D) Nanoparticle sizes of (B) ELPCP-H_6 and (C) H_6.-ELPCP. (E) Absorbance spectra of ELPCP-H_6-PtCP/Zn^{2+} complex in comparison with EDTA negative control. (Figure modified from [314])

We then compared ELPCP-H_6-PtCP to the commercial O_2 probe MitoXpress (Luxcel biosciences) in terms of their phosphorescence and O_2 sensitivity. The VLPs showed ~7 times higher phosphorescence intensity under deoxygenated conditions than MitoXpress (Fig 3.8 A). This is possibly due to the higher dye content of ~117 molecules of PtCP per capsid at 65% coupling efficiency, whereas MitoXpress possess a yield of coupling in the ratio of 1:3 to 1:5 of bovine serum albumin protein to dye. When deoxygenated VLPs demonstrated a 5.3-fold increase in phosphorescence intensity compared to 2.45-fold increase for MitoXpress (Fig 3.8 B). In terms of phosphorescence lifetime VLPs showed ~37 times higher signals when deoxygenated than MitoXpress, however its lifetime range of 27 – 67 µs was similar to that of MitoXpress (Fig 3.8 C). This is possibly due to self-quenching of PtCP or quenching by the protein backbone.

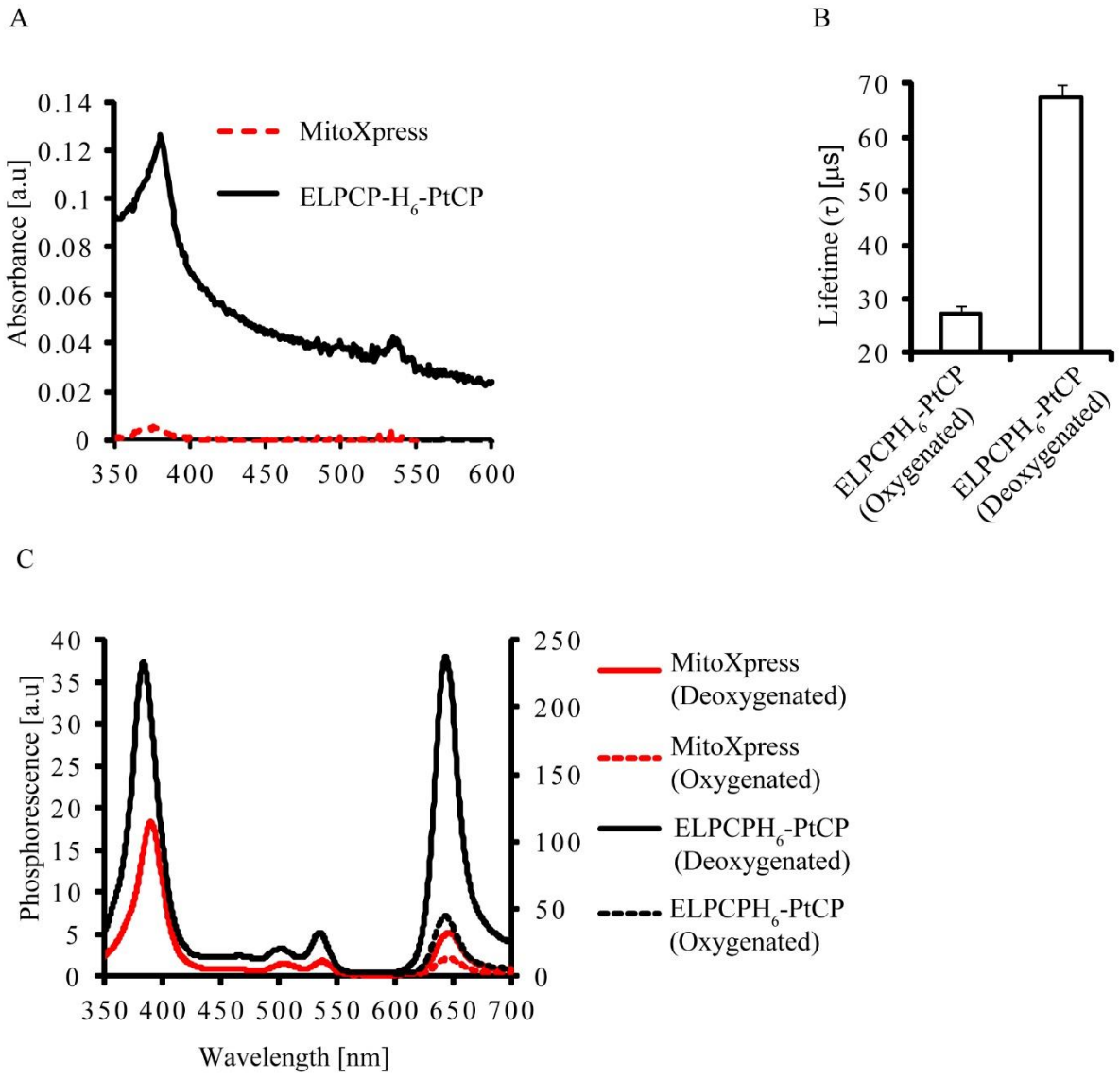

Figure 3.8. Comparison of ELPCPH$_6$-PtCP and MitoXpress phosphorescence and oxygen sensitive properties. (A) Absorbance of ELPCPH$_6$-PtCP and MitoXpress, both at 15 nM concentration. (B) Phosphorescence lifetime response to oxygenation of ELPCPH$_6$-PtCP. (C) Phosphorescence and excitation (Em.650nm) and emission (Exc.380nm) spectra of ELPCPH$_6$-PtCP and MitoXpress both at 7.5 nM concentration, with response to oxygenation. (Figure modified from [314])

3.4 Discussion.

The aim of this research was to produce new O_2-sensitive probes via metallochelate coupling to monomeric proteins and protein subunits of self-assembling protein complexes. We hypothesised that metallochelate coupling was a viable strategy due to both the high binding affinity of histidine tags and NTA-Ni^{2+} with a dissociation constant between approximately 7 x 10^{-8} and 7 x 10^{-7} M [444] and also the compatibility of coupling the NTA group (on PtCP-NTA) to His_6-tagged protein subunits of monomeric FPs and multi protein VLPs. We tested this by first optimising conditions for coupling

PtCP-NTA to monomeric FP EGFP in the design of ratiometric O_2-sensitive probes. Here we observed a >40% yield of coupling of PtCP-NTA to EGFP compared to the EDTA negative control (Fig 3.4 A). The coupled EGFP showed no perturbing effects of coupling to its fluorescence when compared to uncoupled EGFP (Fig 3.4 B). Coupled EGFP also displayed phosphorescence emission peak at 650 nm, which was responsive to changes in O_2 (Fig 3.4 B). We then expanded our evaluation of metallochelate coupling to FPs TagBFP2 and DsRed-express. Similarly, to EGFP we observed successful coupling in terms of no perturbing effects of coupling on the fluorescence spectra and the presence of phosphorescence emission at 650nm, demonstrating responsiveness to changes in O_2 (Fig 3.5 and 3.6). The results here show that metallochelate coupling is a viable strategy for the coupling of His_6-tagged monomeric FPs to oxygen sensitive PtCP-NTA, producing O_2-sensitive complexes that have combined fluorescence of a wide array of monomeric FPs. Such complexes can be used for ratiometric-based measurements of O_2, where FP can be used as O_2-insensitive reference. The coupling yield here of ~40% along with the brightness of the probe can be improved by introducing more NTA groups to PtCP porphyrin dye, increasing the number of His_6 tags on the FPs, and possibly by optimising the chelating metal ion concentration further. The ability to potentially couple to any monomeric FP could allow for flexibility in experimental design. For example, coupling with far red or infrared FPs could expand the usage to high resolution imaging from confocal fluorescence imaging, due to increased light penetration depth.

We moved forward to a more complex protein system of self-assembling VLPs. We wanted to evaluate whether metallochelate coupling and the coupling of PtCP-NTA to protein subunits of the VLPs would perturb its self-assembly process. We carried out coupling of PtCP-NTA with N-terminally and C-terminally His_6-tagged ELPCP protein subunits (Fig 3.7 A-D). From the N-terminal His_6-tagged coupling, we did not obtain VLPs of the expected size. This suggested that the self-assembly process of ELPCP VLPs was hindered by the presence of the PtCP dye on the inside of the ELPCP internal cavity. This was confirmed when we obtained ELPCP-H_6-PtCP VLPs of the correct size ~28nm with the C-terminal His_6-tagged subunits, in which the PtCP dye molecules are expressed on the outside of the ELPCP VLPs. We achieved coupling efficiency of ~65%, compared to the EDTA control (Fig 3.7 E). We then compared the ELPCP-H_6-PtCP complex to commercial O_2-sensitive probe MitoXpress. The ELPCP-H_6-PtCP VLPs displayed ~25.8 times higher absorptivity (Fig 3.8 A) and ~7 times higher phosphorescence intensity than MitoXpress (Fig 3.8 C). This is due to the greater number of PtCP dye molecules attached to the VLPs than MitoXpress, with ~117 per VLP. When deoxygenated, the VLPs displayed a 5.3-fold increase in phosphorescence intensity compared to the 2.45-fold increase in MitoXpress (Fig 3.8 C). When comparing phosphorescence lifetimes, the VLPs showed ~37 times higher signals when deoxygenated. However, the lifetime range of 27-67 µs was similar to MitoXpress (Fig 3.8 B). This similar range in lifetime could possibly be due to self-quenching of PtCP or quenching by the protein backbone of the VLP subunits. The results here show that metallochelate coupling is a

viable strategy for the coupling of His- tagged protein subunits of VLPs to O_2-sensitive PtCP-NTA, and the VLP subsequent self-assembly.

The most significant result here is the first example of a phosphorescent VLP structure, which allows for multiple coupling of Pt-porphyrins, conferring higher brightness, high lifetime signals and increased sensitivity in response to O_2 than commercial probe MitoXpress. The main advantage lies with the ability to attach peptide targeting sequences to the VLPs for targeted delivery of the Pt-porphyrins to cells and tissues. Similarly, to FP, the coupling efficiency of ~65% which can potentially be improved upon by increasing NTA groups on the Pt-porphyrins and the number of His_6 tags on the protein subunits. The phosphorescent brightness can be improved using brighter and more photostable Pt-porphyrin dyes like PtTFPP and Pt-benzoporphyrin derivatives. However, their hydrophobicity and nonspecific binding to proteins would need to be decreased for this to be viable. In its current form the ELPCP-H_6-PtCP VLPs can be applied in time-resolved fluorescence microplate reader measurements. If increased brightness and cell specific targeting can be achieved, then fluorescence microscope imaging can be applied for cell studies. However, with the use of VLPs and other self-assembling protein nanoparticles, complex issues are raised with regards to the dynamic interactions of nanoparticle materials and biological systems. These interactions lead to the formation of protein coronas, particle wrapping, intracellular uptake and subcellular localisations, and effects on cellular processes. The understanding of these nano-bio interfaces and their effects are key to designing nanoparticle constructs with properties that can improve intracellular and subcellular staining, while addressing concerns with immunogenicity and toxicity. However, investigating these interfaces isn't straight forward, and progress to date has been slow due to the dynamic states of the interfaces, thereby hindering progress of nanoparticle material development and ultimately their applications.

3.5 Conclusion

Overall, we have demonstrated that metallochelate coupling is a viable strategy for conjugation of NTA expressing Pt-porphyrins to His_6-tagged monomeric proteins and self-assembling VLPs. Coupling to VLPs allows for the first instance of a phosphorescence VLP structure. The flexibility to potentially couple any suitable monomeric FP or VLP subunit for assembly to an NTA expressing Pt-porphyrin or dye molecule makes metallochelate coupling a very attractive methodology for conjugation.

Chapter 4: Design and development of ferritin-based nanoparticles for pH and O_2 imaging

4.1 Introduction

Ferritin is a major iron storage protein found in most living organisms, including mammals [364], bacteria [365], and plants [366]. Mammalian ferritin is composed of 24 subunits of either 21 kDa heavy (FTNH) or 19 kDa light (FTNL) chains [367] (Fig 4.1 A & B). The fully assembled ferritin folds into a 24-mer spherical cage-like structure, 450 kDa in size, with an internal cavity of 8 nm and an external size of 12 nm [368] (Figure 4.1 B). The primary role of ferritin is iron storage, and the transportation to and from cells via receptor mediated endocytosis. Ferritin's intrinsic ability to enter cellular cytosol via ferritin receptors such as TfR-1 and TfR-2 in both murine and human cells [378] along with T cell immunoglobulin and mucin domain containing 2 (TIM-2) [369, 370] and scavenger receptor class A, member 5 (Scara5) [379] receptors in murine cells, makes it advantageous for biomedical applications in human cell and tissues models as well as mouse models. Ferritin can be functionalised genetically and chemically at its exterior to express a wide array of proteins such as targeting peptides, fluorescent and dye molecules [381], and antibodies [382, 383]. Ferritin's interior cavity allows the encapsulation of drugs and imaging agents [384, 385]. There are several ways of functionalising the ferritin structure, either externally or internally.

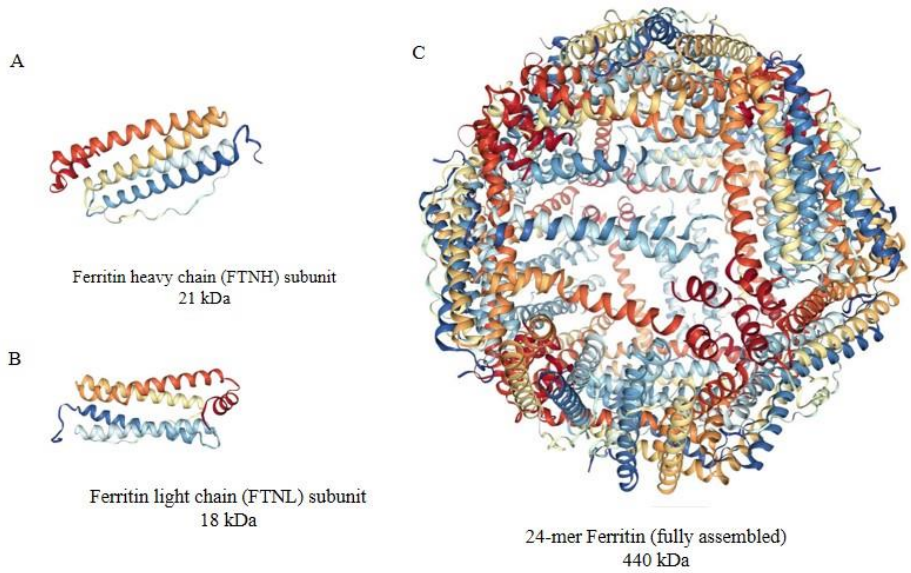

Figure 4.1. Resolved protein structures of (A) human ferritin heavy chain subunit 21 kDa, (B) human ferritin light chain subunit 18 kDa, (C) fully assembled 24-mer human ferritin 440 kDa (10.2210/pdb1FHA/pdb [445]). Images from [446].

4.1.1. Ferritin chemical modification

Ferritin nanoparticles can be chemically modified via reactive amino acid side-chains such as lysine, cysteine, aspartate, and glutamate present on the exterior of the structure [317]. Lysine amino acids are modified via N-hydroxysuccinimide esters' (NHS-esters) reaction with the N-terminal primary amine group ($-NH_2$). Cysteine amino acids are conjugated at their thiol groups via Michael acceptors, such as maleimides, whereas carboxylic amino acids aspartate, and glutamate are modified by activating carboxylic acid groups with 1-Ethyl-3-(3-dimethylaminopropyl)carbodiimide (EDC), which can then react with NHS to form an NHS-ester group. This NHS-ester group is then conjugated to a ligand, expressing a primary amine like that of lysine conjugations. Several fluorescent molecules have been successfully attached to the ferritin nanoparticle surface, such as Cy5.5 and Alexa Fluor 488 [389], via NHS-ester chemistry and Fluorescein isocyanate (FITC) [386-388] using isothiocyanate chemistry. Ferritin nanoparticles have also been PEGylated through maleimide [392] or EDC [393] chemistry, to alter its pharmacokinetics and biodistribution. Here, we utilised the coupling of fluorophores: Alexa Fluor 488 to lysine amino acids via amine group NHS-ester bioconjugation, and isothiocyanate coupling with fluorescein isothiocyanate (FITC), to localise our nanoparticle constructs in cell models.

4.1.2 Ferritin genetic engineering

Ferritin subunits can also be genetically engineered to express targeting peptides, antigens, and FPs. Both the C and N- terminal of the FTNH subunit sequence can be engineered to express recombinant protein sequences of interest. When engineering at the N-terminus, the protein is expressed externally; for the C-terminal, expression is internal. However, there are conflicting reports in the literature that demonstrate genetic linkage of recombinant proteins to the C-terminus result in the FTNH, expressing the engineered C-terminus externally when ferritin is fully assembled [383, 394]. This research is conflicting to our own experiences with engineering ferritin at the C-terminus, in that we found that the self-assembly process of ferritin is perturbed when we functionalised ferritin with FPs at the C-terminus. It is possible that the size of the linker used here could allow enough spatial separation for the engineered protein to be expressed outside and for correct ferritin assembly. FTNH has been genetically engineered at the N-terminus to express the cell receptor targeting peptide, RGD-4C for the targeting of αvβ3 integrin [447], which is implicated in angiogenic tumour vasculature as biomarkers for inflammation and angiogenesis. The fully assembled ferritin showed no inhibiting affects to its structure, with a higher affinity for the αvβ3 integrin expressing macrophage cells. The RGD-4C engineered ferritin was then loaded with Cu^{2+}-complexed Dox via encapsulation for targeted drug delivery to the glioblastoma tumor model U87MG [395]. This displayed longer circulation half-life, reduced cardiotoxicity, and higher tumor uptake. However, there is debate on whether it is the peptides,

the passive transport (e.g. endocytosis), or the intrinsic targeting property of the nanoparticle that is directing the delivery.

Here, we aim to functionalise ferritin nanoparticles by genetic engineering to express a range of FPs for localisation, and to produce biosensor nanoparticle constructs, e.g. quantitative (FLIM) imaging of pH using pH-sensitive FPs. We are also aiming for the expression of targeting peptides to optimise biodistribution and specific cell targeting for intracellular staining. Intracellular pH gradients play important roles in cellular processes such as proliferation, senescence, and apoptosis, and is tightly regulated within mammalian cells and organelles. The organelles of a cell require a different range of pH to carry out their physiological functions [448]. Pathologic conditions can significantly alter intracellular and extracellular pH through effects on ion homeostasis. pH is an important biomarker for disease states, such as cancer and neurological disorders [449, 450], and therefore requires the development of novel biosensors for detection. FPs are sensitive to changes in pH due to protonation at their chromophore, altering its conformation and its photophysical properties. A range of FPs such as pHRed and ECFP can measure pH changes due to responses in their fluorescence lifetimes [212, 213]. Here we carried out genetic engineering to produce FTNH that expresses ECFP, developing a pH-sensitive nanoparticle probe.

Through the attachment of the cell penetrating peptide Bactenecin 7 [446] we aim to improve cellular uptake and intracellular staining. BN7 is derived from antimicrobial protein against gram negative bacteria, which has been used to efficiently load Pt(II) coproporphyrin I (PEPP0) into various mammalian cell types including PC12, HCT116, SH-SY5Y and HeLa. We also genetically attached a cell targeting peptide to FTNH, α-Enolase–binding peptide, for the specific uptake into the colon cancer cell line HCT116 [451].

4.1.3 Ferritin encapsulation

The widely known approach of functionalising ferritin for loading cargo molecules is via encapsulation. The structure and self-assembly process of ferritin has been found to be regulated by changes in pH. At low pH, the ferritin structure is disassembled into its 24 subunit parts and reassembled as pH is increased back to neutral. This allows for the encapsulation of various cargos within the fully assembled ferritin's internal 8 nm-sized cavity.

We hypothesised that the pH-dependent assembly process of ferritin nanoparticles from its subunits could be utilised to encapsulate the Pt-porphyrin-based O_2 probe, Pt-Glc [196], creating O_2-sensitive nanoparticles for intracellular imaging. This is based on research in which the Pt-based drug compound, Cisplatin, was successfully encapsulated within ferritin nanoparticles [452, 453]. X-ray crystallography found that the Pt centre of Cisplatin was coordinated to the interior ferritin core, bound to five amino

acid residues on the FTNH subunits, His^{136} and Lys^{68}, His^{105}, Cys^{90}, and Cys^{102} [397]. Therefore, evidence shows that Pt-based compounds are complexed within the ferritin structure when encapsulated.

4.2 Aims

Here, we set out to design intracellular nanoparticle probes for live cell imaging based on ferritin self-assembling protein nanocages, for the measurement of intracellular pH and O_2. We aimed to achieve this by employing various strategies and techniques: (i) by genetic engineering for the expression of FPs for localisation and pH sensor applications and targeting peptides for cell-specific targeting (Fig 4.1 A). (ii) Through chemical modification for the attachment of fluorescent molecules for localisation (Fig 4.1 B). (iii) With the encapsulation of the O_2-sensitive phosphorescent probe, Pt-Glc, into the internal cavity of the assembled ferritin structure (Fig 4.1 C).

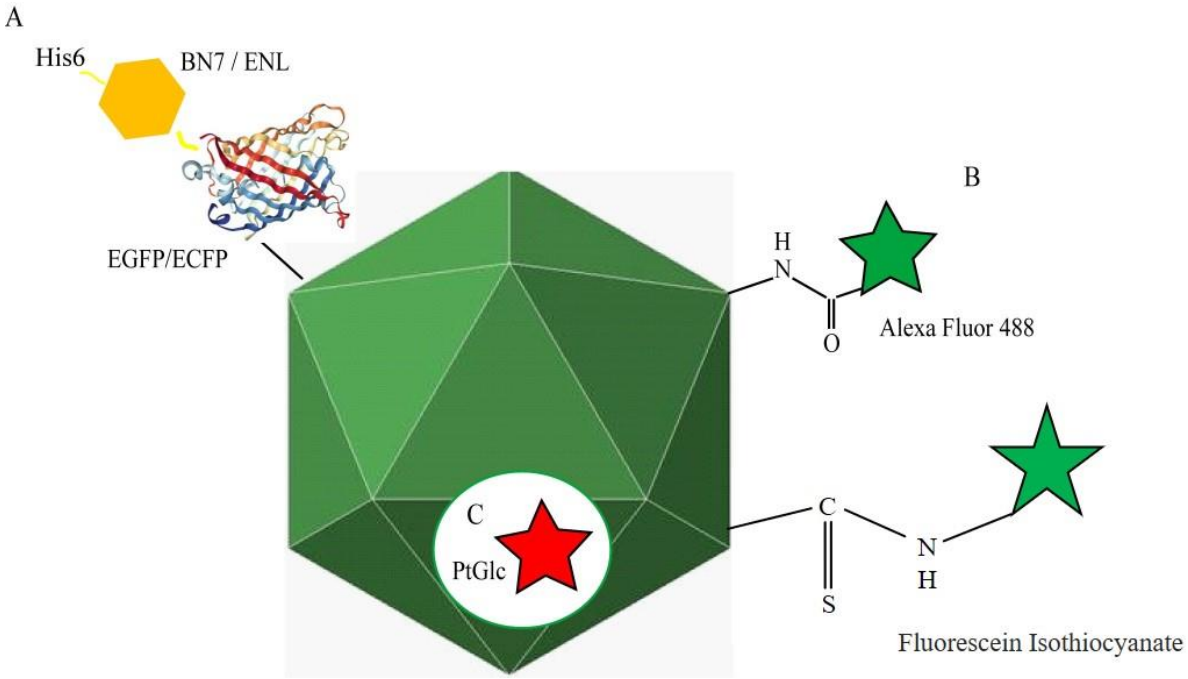

Figure 4.2 Schematic representation strategies for the functionalisation of ferritin. (A) Genetic engineering for expression of FP and cell penetrating peptides, for example EGFP and ECFP along with BN7 and ENL. (B) Chemical modification for expression of fluorophores via amino acid bioconjugations, for example NHS-ester amine coupling to Alexa Fluor 488 and isothiocyanate coupling with FITC. (C) Encapsulation via pH dependent disassembly and reassembly, for example O_2 sensitive phosphorescent dye Pt-Glc.

4.3 Results

4.3.1 Development of genetically engineered ferritin nanoparticles

Based on research by Kim et al. 2011, [454] in which FTNH subunits were genetically engineered at the C-terminus to express EGFP, we carried out proof-of-concept experiments to examine the types of FPs that could be successfully expressed on the FTNH subunit. However, we were unsuccessful in obtaining correctly sized nanoparticles of fully assembled ferritin expressing EGFP.

We hypothesised that the expression of EGFP on the C-terminal of the FTNH subunit would expose EGFP to the interior of the ferritin structure, therefore impeding self-assembly. Thus, we produced two constructs of FTNH genetically expressing EGFP at its N-terminus (Fig 4.3 A). Construct 1 and 2 both consisted of His_6 for protein purification, BN7 cell penetrating peptide (amino acid sequence: val- val- ala- ala- arg- val- val- leu- met- val- arg- arg) for increased cell penetration, with EGFP attached to ferritin by a short linker (amino acid sequence: pro- gly- gly- gly- gly- ser -gly- gly- gly- thr- gly- gly- gly- ser- gly- gly) to facilitate an increase in protein folding of both proteins. In the case of Construct 1, a second oligohistidine sequence, His_7, was inserted between EGFP and the BN7 to allow for protein folding of EGFP, as well as providing a potential second protein purification tag. We cloned both constructs into pQE-30 His_6-tagged expression vector and transfected them into *E.coli* SG13009 cells (Qiagen). Following production at 37°C until OD600= ~0.4, we induced with 0.125 mM IPTG for 16 hours. We then subsequently purified both recombinant protein constructs under native conditions using His_6-tagged Ni^{2+}-NTA affinity chromatography (see Materials and Methods 2.2.4.3). We obtained protein yields of ~12 mg/L with a folding rate of ~30-40% for EGFP in both constructs (assessed by UV-Vis spectroscopy). We then measured the nanoparticle size via dynamic light scattering (DLS) (see materials and methods section 2.2.11) (Fig 4.3 A & B) and observed nanoparticles of the correct size at 23 nm. The attachment of EGFP to the N-terminal end of FTNH allowed for the assembly of ferritin nanoparticles, with EGFP expressed to the exterior of the nanoparticle constructs, therefore demonstrating that the attachment of FP EGFP to FTNH via genetic engineering is a viable strategy, with potential for applications to other FPs. Next, we wanted to examine whether attachment to FTNH perturbs the photophysical properties of EGFP. We compared EGFP fluorescence spectra for Constructs 1, 2 and the untagged EGFP and found that attachment to FTNH does not affect the fluorescence spectra of EGFP (Fig 4.3 C). We wanted to then examine fluorescent molecules like Alexa Fluor 488 or FITC coupled to horse spleen derived FTNH (hoFTN), and how they would compare to genetically expressed EGFP-FTNH constructs in terms of their photophysical properties and cell staining. We carried out amine deprotonation of lysine groups on hoFTN with NHS-ester of Alexa Fluor 488 (see materials and methods section 2.2.5), achieving a ratio of 24:1 of Alexa Fluor 488 to hoFTN when assembled. Similarly to Constructs 1 and 2, we measured nanoparticle size via DLS and obtained

nanoparticles of ~23 nm (Fig 4.3 D). We then assessed the photophysical properties of the Alexa Fluor 488 coupled to hoFTN compared to uncoupled and observed no perturbing effects of coupling (Fig 4.3 E). We find in all cases that whilst the fluorescent spectra of the fluorophore or fluorescent proteins are unperturbed by coupling, there is a loss of fluorescent brightness when they are coupled to the ferritin structure. This could be due to suboptimal protein folding in the case of EGFP or suboptimal attachment of the fluorophores to the exterior of the ferritin structure in the case of Alexa Fluor 488, and possible quenching of fluorescence emission by the ferritin protein structure.

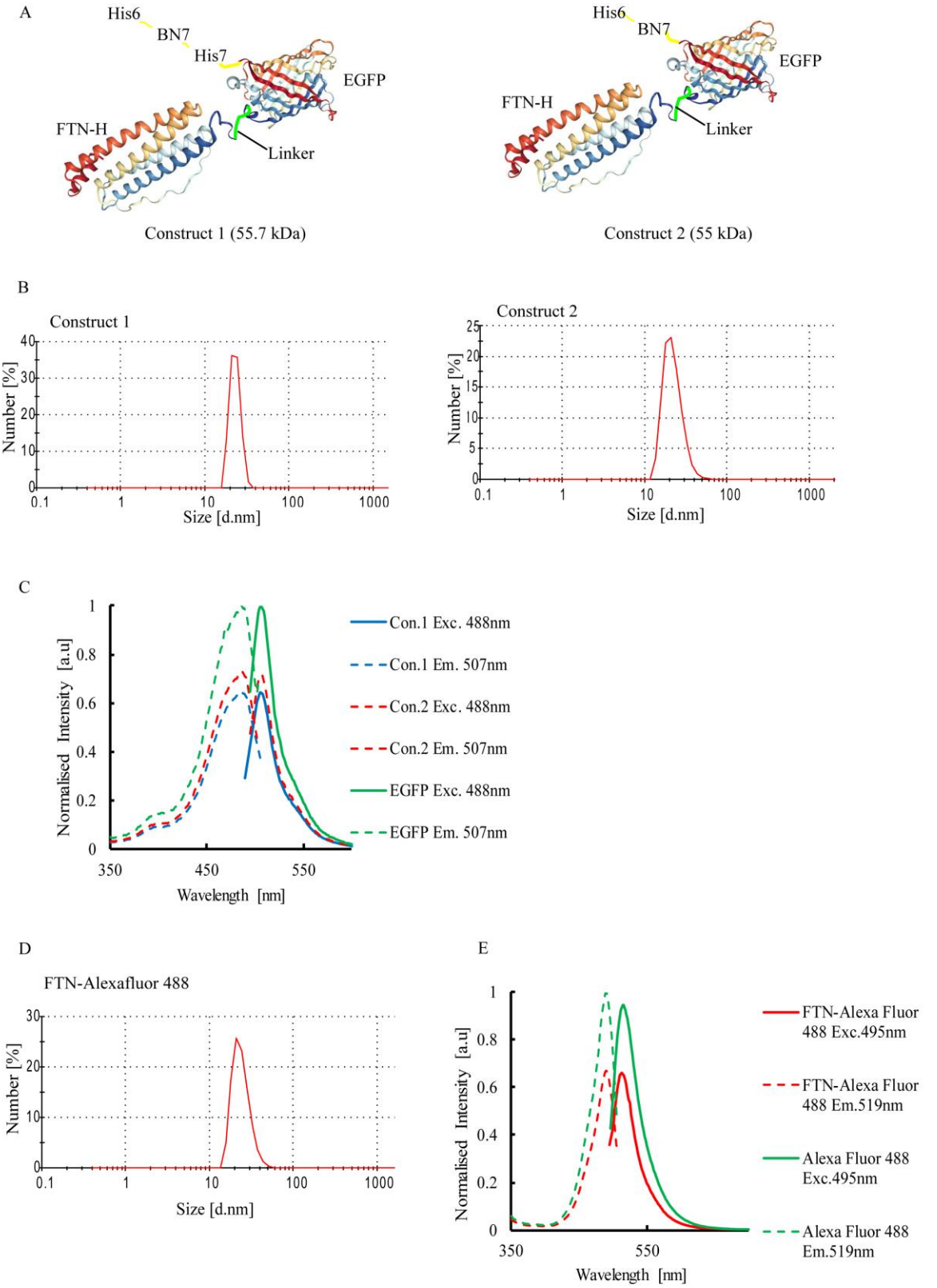

Figure 4.3. Design and evaluation of FTNH-EGFP and hoFTN-Alexa Fluor 488 constructs. (A) Structures of FTNH-EGFP constructs 1 and 2. Construct 1 consisted of FTNH attached to EGFP via short linker, with BN7 cell penetrating peptide and His_6 purification tag. Construct 2 consisted of FTNH attached to EGFP via short linker, with His7 purification tag, BN7 cell penetrating peptide and His_6 purification tag. (B) Nanoparticle sizes of constructs 1 and 2 at ~23 nm. (C) Fluorescence excitation (Em. 507 nm) and emission (Exc. 488 nm) spectra of

EGFP attached to Construct 1 and 2 with uncoupled EGFP, normalised to uncoupled EGFP. (D) Nanoparticle size of hoFTN-Alexa Fluor 488 at ~23nm.) (E)Fluorescence excitation (Em. 507nm) and emission (Exc. 488nm) spectra of hoFTN-Alexa Fluor 488 with uncoupled Alexa Fluor 488, normalised to uncoupled Alexa Fluor 488.

4.3.1.1 Evaluation of genetic engineered and chemically modified ferritin constructs in cells

We then set out to evaluate Construct 1 and 2, along with hoFTN-Alexa Fluor 488, with the cell model of mouse embryonic fibroblast (MEF) cells visualised with the Tetramethylrhodamine Methyl Ester, Perchlorate (TMRM) mitochondrial stain. We observed no visible toxicity to the cells for all the constructs. When subsequently analysed and compared, fluorescence intensity of all three constructs showed that Construct 1 provided significantly higher brightness and cell staining than construct 2 and hoFTN-Alexa Fluor 488 (Fig 4.4 C). This result is possibly due to the extra His_7 tag acting as a linker, increasing EGFP folding and brightness. Then in comparing EGFP-FTNH genetic fusion constructs 1 & 2 to chemically modified hoFTN-Alexa Fluor 488, it is possible to conclude that EGFP genetic coupling provides a brighter more efficient nanoparticle construct.

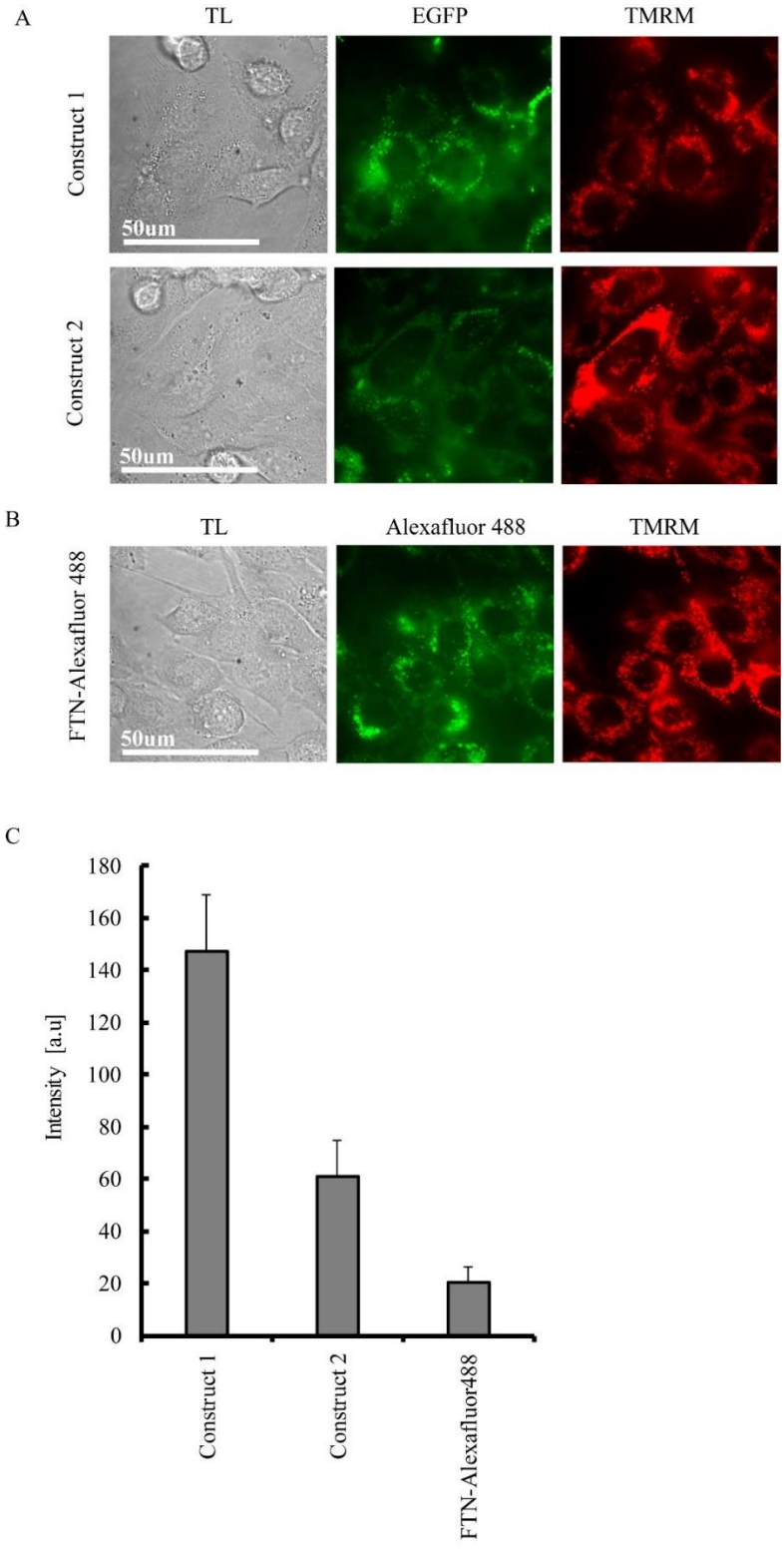

Figure 4.4. Evaluation of FTNH-EGFP and hoFTN-Alexa Fluor 488 constructs in cell-based model. Transmission light (TL), EGFP or Alexa Fluor 488 (470 nm exc., 510-650 nm em.) and TMRM (590 nm exc., 600-650 nm em.) microscopy images. Fluorescence microscope images of MEF cells incubated with (A) FTNH-EGFP constructs 1 and 2 (0.2 µM concentration of ferritin, 16 hours) and counterstained with TMRM (0.2 nM, 30 minutes). (B) hoFTN-Alexa Fluor 488 (0.2 µM concentration of hoFTN, 16 hours) and counterstained with

TMRM (0.2 nM, 30 minutes). (C) Comparison of FTNH-EGFP constructs and hoFTN-Alexa Fluor 488 fluorescence intensities.

Following on from our successful proof of concept EGFP-FTNH genetic Construct 1, we set out to develop ferritin nanoparticle probes capable of measuring intracellular pH through FLIM. We carried out genetic engineering, removing EGFP from construct 1 and replacing with the pH-sensitive FP ECFP (Fig 4.5 A), and inserting a secondary cell penetrating peptide α-Enolase (ENL) (amino acid sequence: val- val- ala- ala- arg- val- val -leu -met -val -arg -arg) for colon cancer cell targeted delivery. This construct is referred to as ECFP-FTNH. As with the previous constructs, we cloned ECFP-FTNH into pGe30 His_6-tagged expression vector and transfected them into the SG13009 strain *E.coli* cells (Qiagen) (see materials and methods section 2.2.3.4) . Following production at 37°C until OD600= ~0.4, we induced with 0.125mM IPTG for 16 hours room temperature. We then subsequently purified under native conditions using His_6-tagged Ni^{2+}-NTA affinity chromatography (see materials and methods 2.2.4.3) and evaluated the purity of the proteins via SDS-PAGE (Fig 4.5 B) with yields of 6.8mg/L culture, and a folding rate of 64% (assessed by UV-Vis spectroscopy). We found from the SDS-PAGE that the protein solution purified contained presence of degradation products and aggregated proteins. We attempted to alter purification conditions, however the conditions used her were found to be the most optimal for purification and protein yield. We wanted to then examine any obstructing effects on ECFP photophysical properties of coupling to FTNH. We observed good sensitivity to changes of pH in fluorescence intensity, with a 1.6-fold increase from pH 5 to pH 8 (Fig 4.5 D).

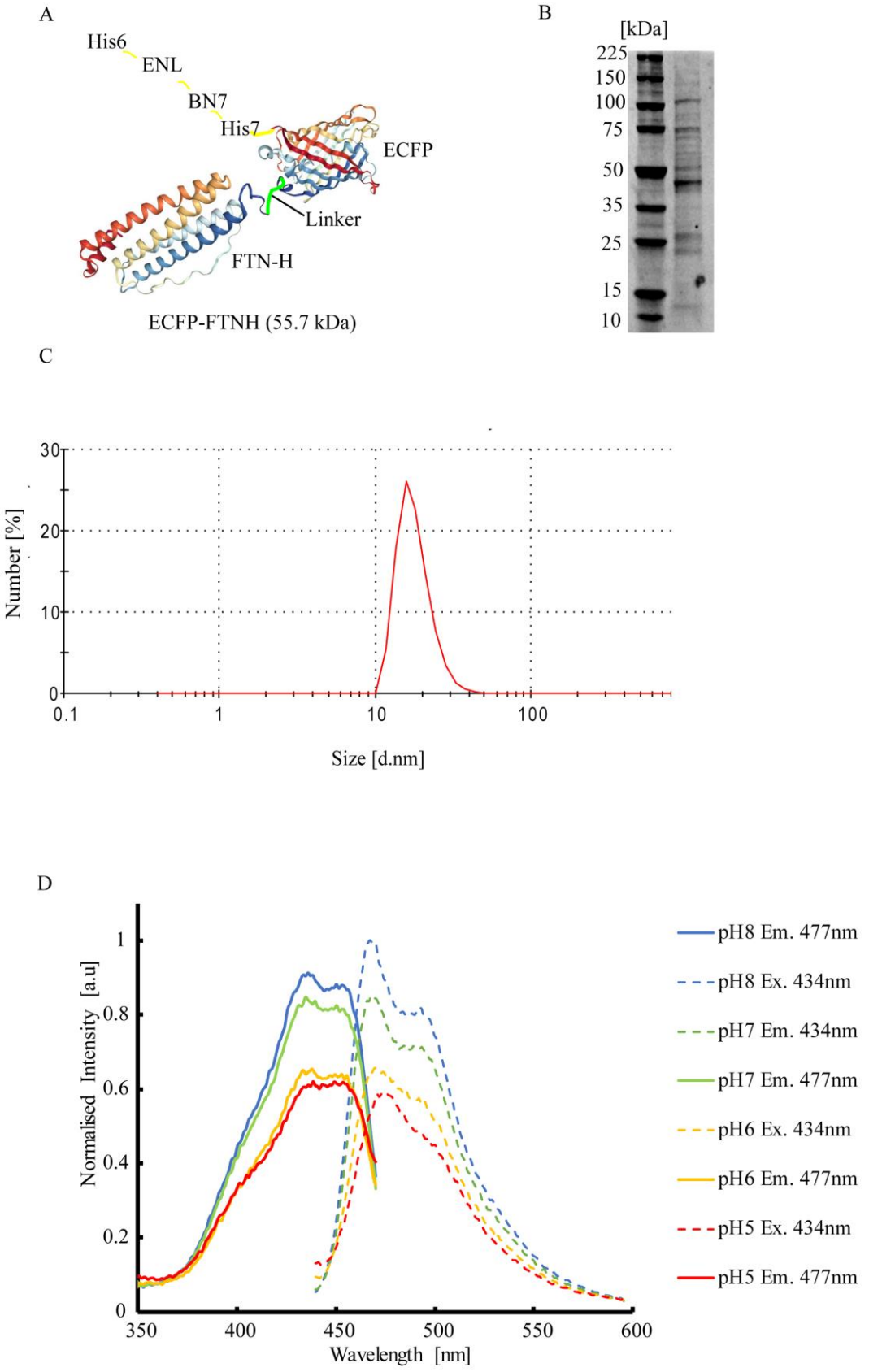

Figure 4.5. Design and evaluation of FTNH-ECFP construct. (A) Structure of FTNH-ECFP construct consisting of FTNH attached to ECFP via short linker, with His7 purification tag, cell penetrating peptides BN7 and ENL, and His_6 purification tag. (B) Purification products of FTNH-ECFP. 4-10% SDS -PAGE and analysed via

Coomassie staining with FTNH-ECFP ~45kDa.(C) Nanoparticle size of FTNH-ECFP constructs at ~23 nm.(D) Fluorescence excitation (em. 477nm) and emission (exc. 434 nm) spectra of FTNH-ECFP with fluorescence intensity responses to changes in pH.

We then assessed the fluorescence lifetime response to changes in pH of ECFP-FTNH compared to uncoupled ECFP. We observed that ECFP-FTNH displayed a fluorescence lifetime response of 0.45 ns; 1.37 ns at pH4.5 to 1.82 ns at pH8 in solution (Fig 4.4 A &C), compared to uncoupled ECFP, which demonstrated a lifetime change of 0.72 ns: 1.35 ns at pH4.5 to 2.07 ns at pH8 (Fig 4.6 B & C).

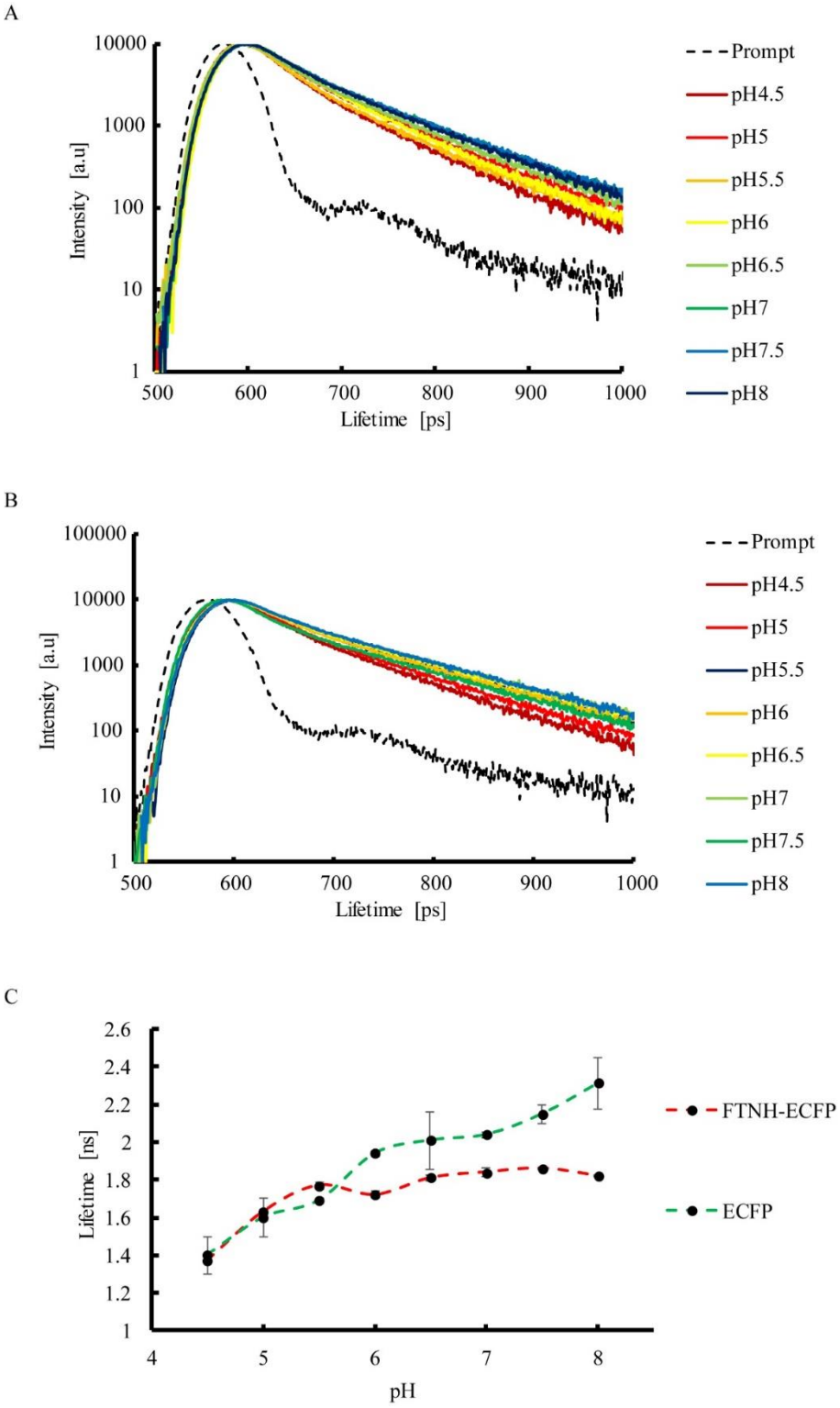

Figure 4.6. Fluorescence lifetime decays for FTNH-ECFP construct and uncoupled ECFP measured in solutions buffered at different pH values. (A) FTNH-ECFP lifetime decays in buffered pH solutions 1.37ns (pH4.5) to 1.82ns (pH8). (B) Uncoupled ECFP lifetime decays in buffered pH solutions 1.35ns (pH4.5) to 2.07ns at pH8**.** Prompt (background) fluorescence signals are also shown. (C) Changes in lifetime with pH of FTNH-ECFP response of 0.45ns and uncoupled ECFP response of 0.72ns.

4.3.2 Design of O_2 sensitive ferritin nanoparticles by encapsulation of Pt-Glc

We set out to evaluate whether encapsulation was a viable strategy in developing O_2-sensitive ferritin nanoparticles. Ferritin can be disassembled and reassembled by altering the pH of its solution, meaning that assembled ferritin disassembles into its subunits at low pH (~pH 2) and reassembles into its protein cage structure at high pH (~pH 9). Here, we utilised this intrinsic property to encapsulate the O_2-sensitive phosphorescence probe Pt-Glc within hoFTN. Pt-Glc is one of the most widely applied O_2-sensitive probes in 3D cell and tissue models, displaying hydrophilicity, minimal aggregation and self-quenching, with in-depth staining of many cell types and cellular aggregates [196], along with tissue models such as mouse intestinal organoids [73]. These advantageous characteristics and applications, along with studies showing the Pt-based drug , Cis-platin, are coordinated to FTNH when encapsulated, making Pt-Glc an ideal probe for our experiments [452, 453].

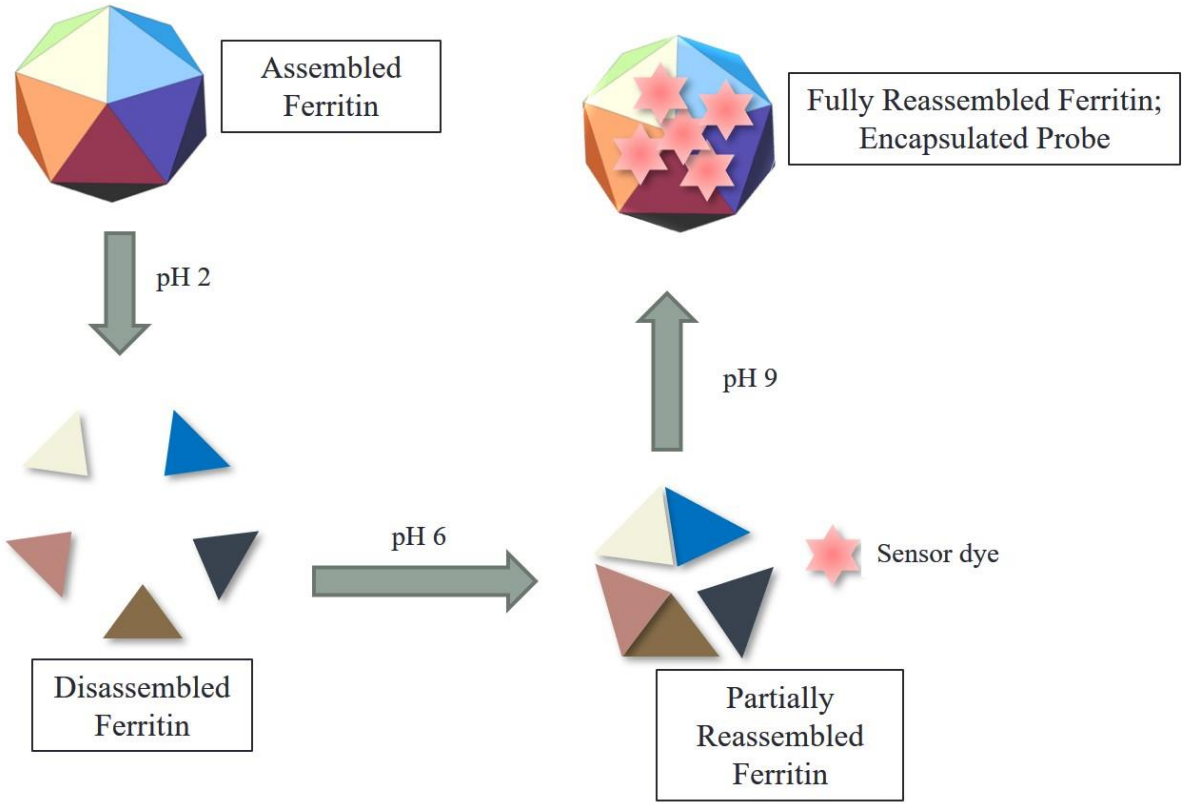

Figure 4.7. Disassembly and reassembly of ferritin via alteration of pH. After dialysis at pH 6 we added Pt-Glc to the solution of partially reassembled ferritin, and increased pH to 9 via dialysis with 0.2M Tris pH 9 buffer; this fully reassembles ferritin and encapsulates the sensor dye within its cavity.

We first wanted to determine the optimal concentration of Pt-Glc that could be encapsulated within the structure of hoFTN, without interfering with its self-assembly process. We initially selected ratios of 1:8, 1:16, and 1:32 , to represent the ratios between hoFTN and Pt-Glc. We carried out the disassembly and reassembly process (Fig 4.4), and measured nanoparticle sizes via DLS to determine the effects of encapsulation on ferritin. We observed hoFTN nanoparticles of correct sizes in all three conditions (Fig 4.5 B, D, & F). We then evaluated the phosphorescence brightness of hoFTN encapsulated Pt-Glc compared to free Pt-Glc of the same concentration (Fig 4.5 A, C, & E). We found that hoFTN encapsulated Pt-Glc was brighter than the free Pt-Glc in all three conditions, with 1:32 being the most optimal ratio, possessing a 5-fold increase over 1:8, a 1.6-fold increase over 1:16, and a 10-fold increase over free Pt-Glc of the same concentration (3.2 nmoles).

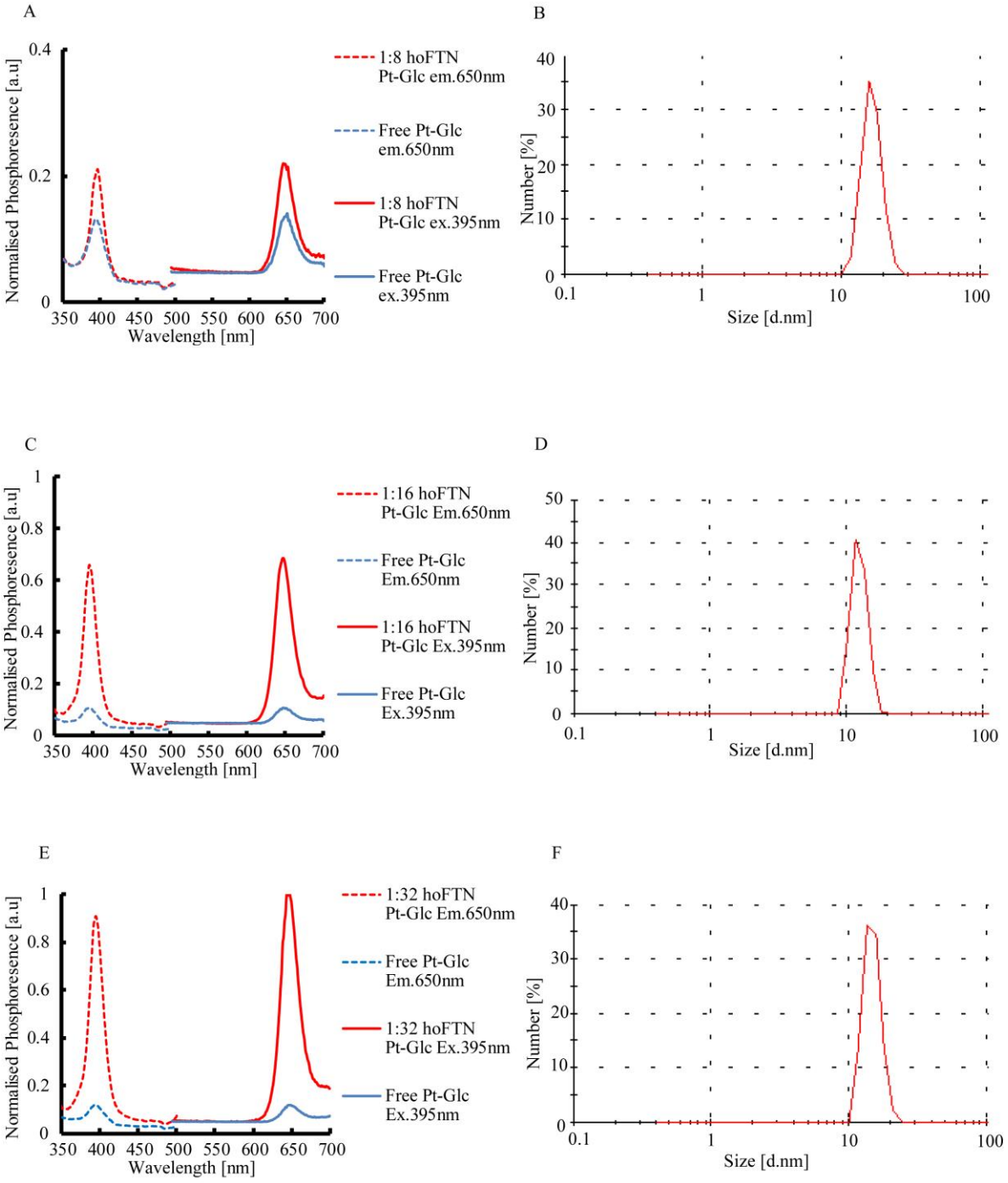

Figure 4.8. Evaluation of hoFTN encapsulated Pt-Glc. Phosphorescence emission (ex.395 nm) and excitation (em.650 nm) spectra of hoFTN encapsulated Pt-Glc and unencapsulated Pt-Glc. Ratios of hoFTN to Pt-Glc (A) 1:8. (C) 1:16. (E) 1:32. Measurement of nanoparticle sizes (B) 1:8. (D) 1:16. (F) 1:32. Spectra normalised to 1:32 hoFTN Pt-Glc phosphorescence spectra.

To localise the hoFTN encapsulated Pt-Glc construct in cell and tissue culture, we needed to attach fluorophore to the outside of the hoFTN structure. The use of EGFP-FTNH or ECFP-FTNH for encapsulation here is not possible as we observed that upon disassembly and reassembly, we could not

obtain nanoparticles of the correct sizes, we believe this is due to a steric hinderance of the reassembly process by the large size of the FP. Having already carried out bioconjugation of Alexa Fluor 488 to hoFTN, we selected a second fluorescent molecule and strategy of isothiocyanate coupling with fluorescein to compare the suitability of both. In the case of FITC, we used higher ratios, as its brightness is reportedly less than that of Alexa Fluor 488. Here, we found that 1:120 gave the optimal fluorescence brightness (Fig 4.9 A), with no aggregation of hoFTN nanoparticles (Fig 4.9 B). From the fluorescence spectra of both FITC and Alexa Fluor 488, we observed no perturbing effects on photophysical properties after coupling to hoFTN. We moved forward with FITC fluorescent molecules due to an easier coupling protocol and cost efficiency.

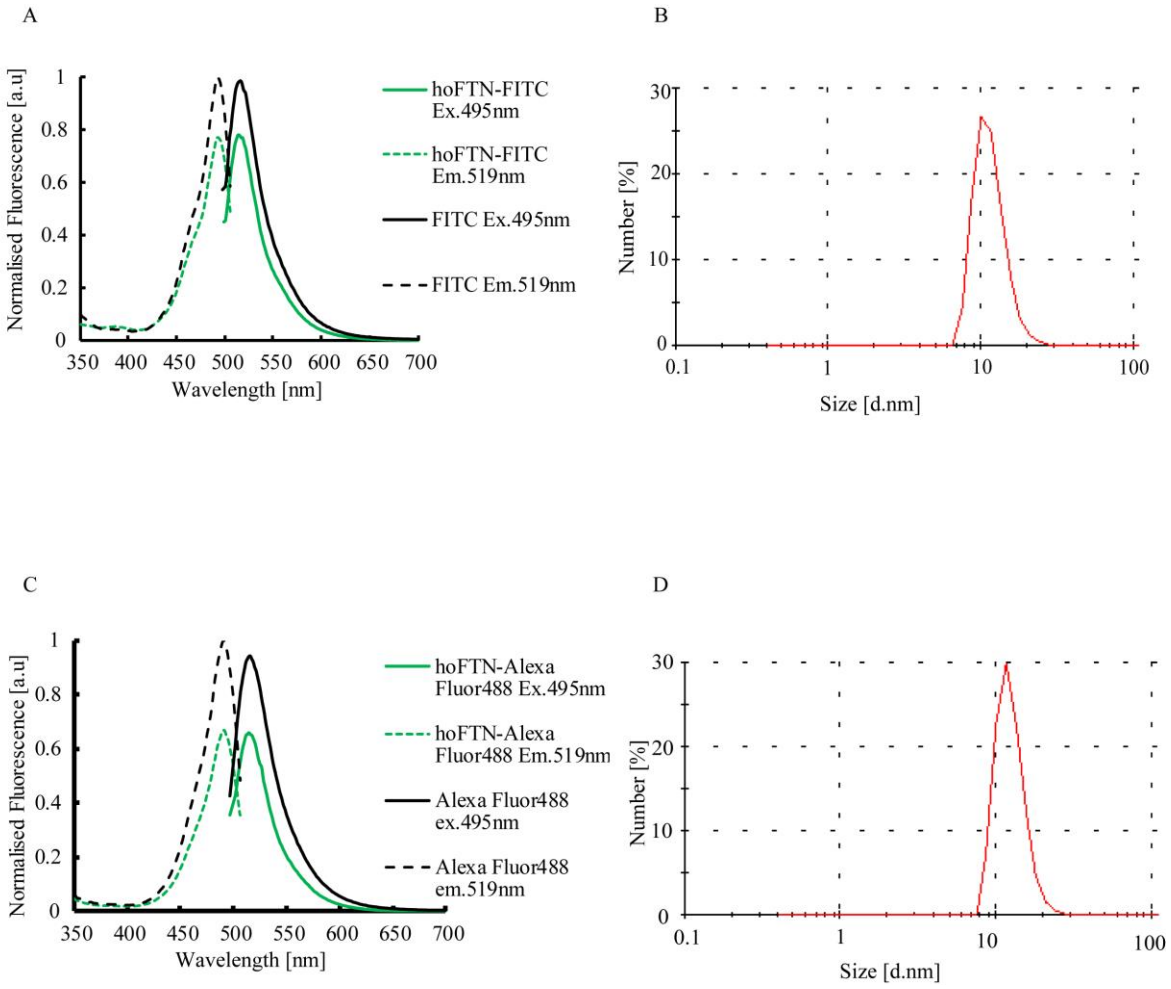

Figure 4.9. Labelling ferritin with FITC and Alexa Fluor488. Fluorescence emission (ex.495 nm) and excitation (em.519 nm) spectra of coupled FITC-hoFTN and Alexa Fluor488- hoFTN, with uncoupled FITC and Alexa Fluor488. (A) Coupled FITC- hoFTN compared to uncoupled FTIC. (C). Coupled Alexa Fluor488- hoFTN compared to uncoupled Alexa Fluor488. Nanoparticle size graphs by DLS of (B) hoFTN-FITC and (D) hoFTN-Alexa Fluor 488.

We carried out encapsulation with optimised 1:32 ratio conditions of hoFTN to Pt-Glc, then, after encapsulation was completed, we carried out bioconjugation to FITC fluorophore with 1:120 ratio conditions previously optimised. We obtained nanoparticles of the expected size (Fig 4.10 C), as well as an increased phosphorescence brightness of hoFTN encapsulated Pt-Glc, compared to the free Pt-Glc, with a 10-fold increase in brightness (Fig 4.10 A). We then evaluated its response to oxygenation and observed a 2.5-fold increase in phosphorescence intensity when we deoxygenated the solution (Fig 4.10. B), demonstrating that the hoFTN Pt-Glc nanoparticles are responsive to changes in O_2.

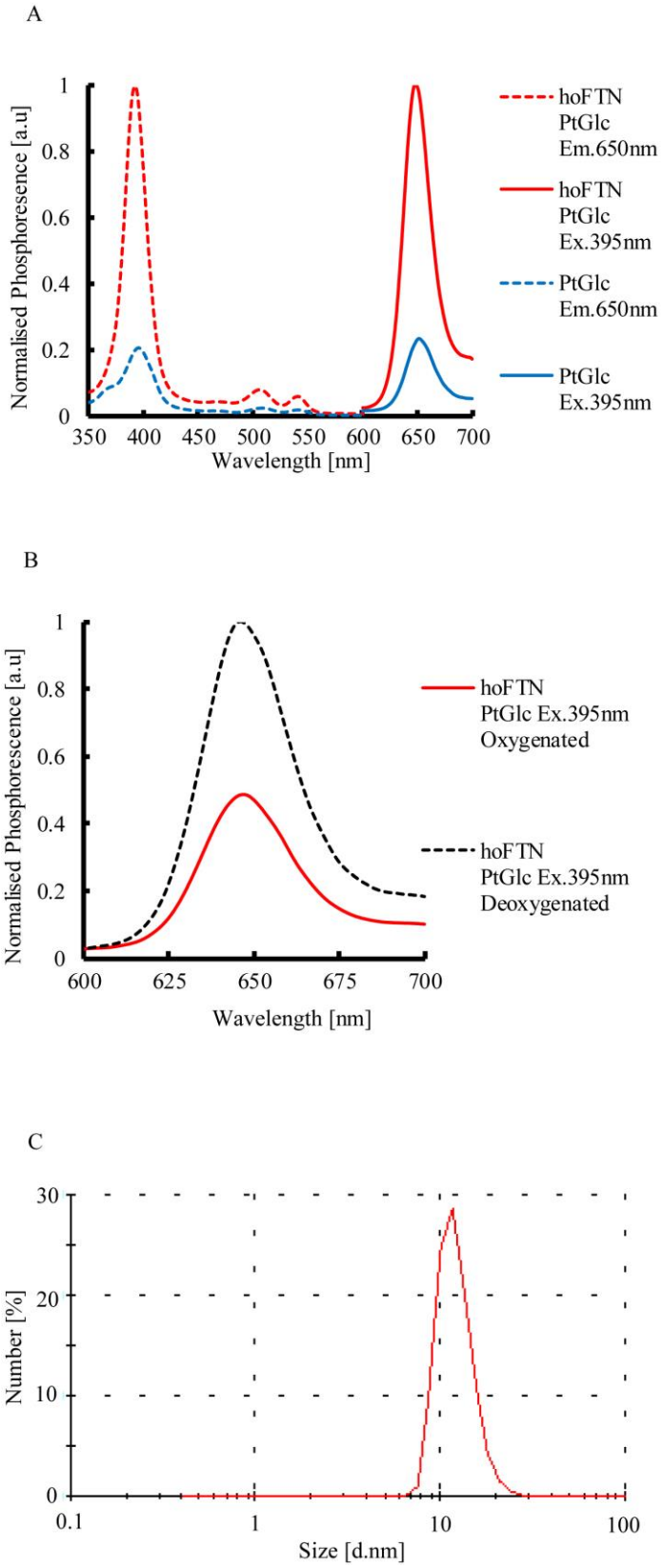

Figure 4.10. hoFTN Pt-Glc construct characterisation. (A) Phosphorescence emission (ex.395 nm) and excitation (em.650 nm) spectra of hoFTN Pt-Glc and unencapsulated Pt-Glc. (B) Phosphorescence emission (Ex.380 nm) of hoFTN Pt-Glc with response to deoxygenation. (C) Measured nanoparticle size via DLS; obtained nanoparticles of 12.25 nm.

4.3.2.1 Evaluation of O_2 sensitive hoFTN Pt-Glc nanoparticle construct in cells

We set out to evaluate hoFTN Pt-Glc nanoparticle construct in comparison with free Pt-Glc in MEF cells, visualised with TMRM cell mitochondrial stain. We observed no visible cellular toxicity, with comparable intracellular staining of hoFTN Pt-Glc nanoparticles to free Pt-Glc (Fig 4.11 A & B). From lack of whole cell staining and presence of granular like staining pattern inside the cells it is possible to conclude that both the hoFTN Pt-Glc nanoparticles and the free Pt-Glc dye molecules was found to be confined to endosomes. This potentially restricts our constructs and subsequent imaging to the endosomal pathway of the cell and limits long term applications due to degradation. We carried out analysis of fluorescence brightness and phosphorescence lifetimes of both hoFTN Pt-Glc nanoparticles and free Pt-Glc (Fig 4.11 C & D). We observed similar fluorescence intensity over 20 hours, with Pt-Glc possessing longer lifetime of ~20 µs compared to the hoFTN Pt-Glc lifetime of ~15 µs. Free Pt-Glc was also observed to load into cells at a faster rate (Fig 4.11 C).

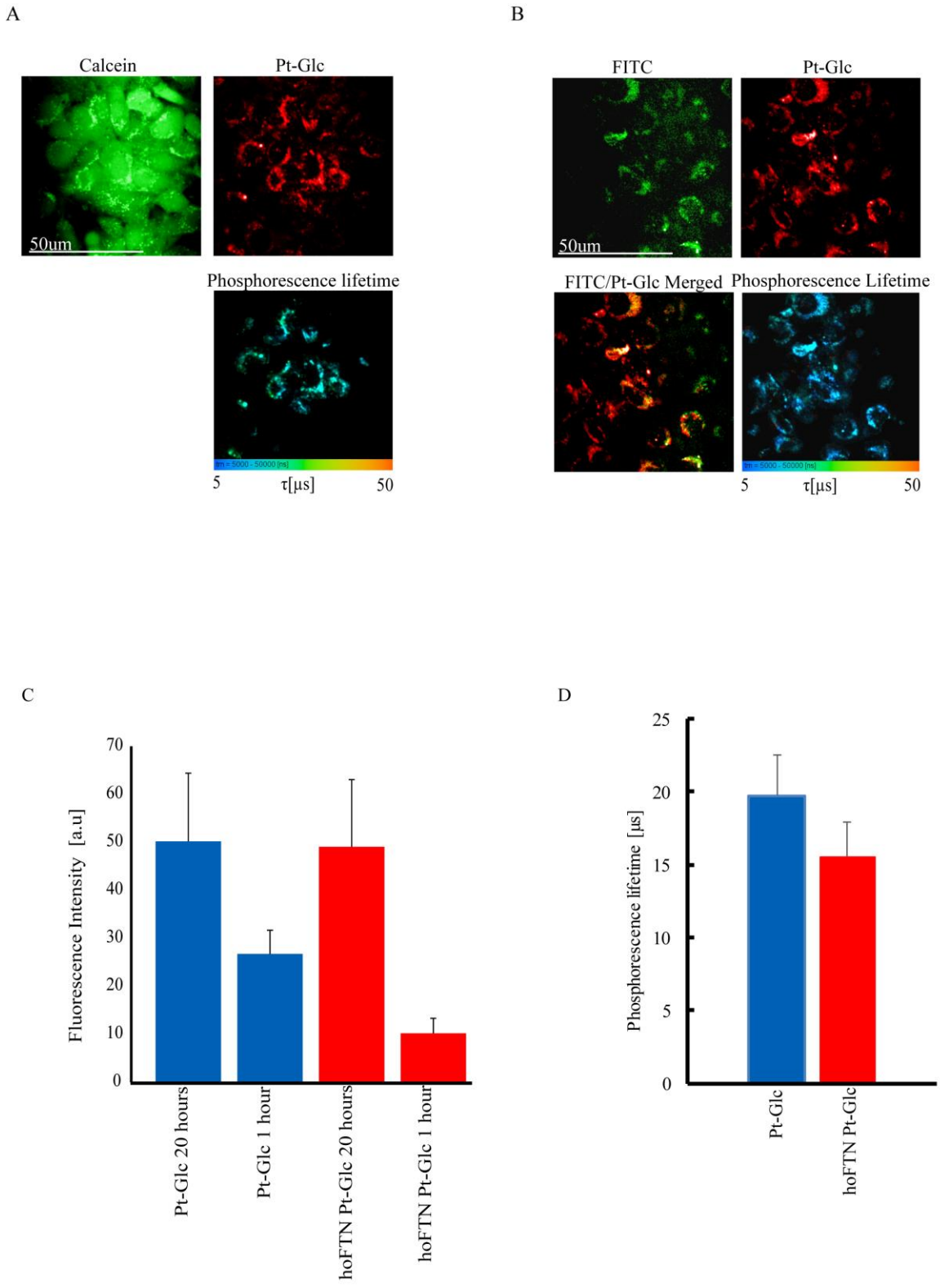

Figure 4.11. Evaluation of FITC-hoFTN Pt-Glc construct in MEF cell model. Confocal microscopy images of MEF cells stained with: (A) Pt-Glc (2.5 µM, 2 hours) and calcein (1 µM, 30 minutes ex. 470 nm). (B) hoFTN

Pt-Glc (2.5 µM, 20 hours; ex. 405 nm) Pt-Glc (2.5 µM, 20 hours; ex. 405 nm). (C) Fluorescence intensity comparison of free Pt-Glc and hoFTN Pt-Glc at 2 and 20 hours. (D) Phosphorescence lifetime comparison of free Pt-Glc and hoFTN Pt-Glc.

4.4 Discussion

We set out to develop nanoparticle biosensors for live cell imaging based on ferritin self-assembling protein nanocages, for the measurement of intracellular pH and O_2. To achieve such nanoparticle probes, we utilised three strategies consisting of: (i) genetic engineering, (ii) chemical modification, and (iii) encapsulation. We initially wanted to evaluate whether genetic engineering of FTNH with cell penetrating peptides and FPs was a viable strategy. We designed two constructs, both expressing EGFP and BN7 cell penetrating peptide.

We observed no impeding effects on ferritin self-assembly or on the spectral properties of EGFP. However, EGFP-FTNH suffered a decrease in fluorescence brightness compared to uncoupled EGFP (Fig 4.3 A-C). This is most likely due to a suboptimal protein folding of EGFP attached to FTHH, which may be improved through the introduction of a longer linker sequence between FTNH and EGFP. It could also potentially be due to the presence of solution FRET, quenching the fluorescence of the donor, EGFP, as a result of the close proximity and spectral overlap of the EGFP molecules on the ferritin nanoparticles. This could potentially be investigated by decreasing the number of FTNH subunits expressing EGFP that subsequently form the fully assembled ferritin structure, thereby decreasing the proximity of EGFP molecules. We then compared chemical modifications of hoFTN with fluorophore Alexa Fluor 488 to genetic expression of EGFP-FTNH in terms of fluorescent brightness and cell staining. Like EGFP-FTNH, we observed no inhibiting affects to ferritin self-assembly or to the spectral properties of Alexa Fluor 488, with coupled Alexa Fluor 488 possessing lower fluorescence brightness than uncoupled Alexa Fluor 488. This is possibly due to suboptimal bioconjugation, or solution FRET, quenching the fluorescence of the donor, Alexa Fluor 488, due to the close proximity of fluorophores and potential spectral overlap (Fig 4.3 D & E). We characterised both EGFP-FTNH constructs and hoFTN-Alexa Fluor 488 in MEF cells, selecting this cell line for initial examinations due to the abundance of fibroblasts mammalian tissues and as their large spindle structure is ideal for the visualisation of intracellular staining. In both EGFP-FTNH constructs and hoFTN-Alexa Fluor 488, we observed similar staining confined to endosomes (Fig 4.3 A & B). Due to the lack of the BN7 cell penetrating peptide on the hoFTN-Alexa Fluor construct, it is possible to conclude that BN7 is not involved in cellular uptake for the EGFP-FTNH constructs, and that the mechanism of the uptake of ferritin nanoparticles is through endocytosis. In comparing fluorescence intensity from MEF cell staining (Fig 4.4 C), we observe that Construct 1 is the brighter of the two genetically engineered EGFP-FTNH constructs, possibly due to an extra His_7 tag acting as a linker, allowing for better protein folding.

The two EGFP-FTN constructs are brighter than hoFTN-Alexa Fluor 488, concluding that genetic attachment of EGFP to FTNH allows for the controlled expression of 1 molecule of EGFP per FTNH subunit, resulting in the expression of 24 molecules of EGFP per fully assembled ferritin nanoparticle. With this in mind, it is clear that, in the case of chemical modification by bioconjugation of Alexa Fluor 488 to amine groups of lysine amino acids, the strategy will not result in the same optimal controlled attachment of the fluorophore to the assembled hoFTN nanoparticles.

The proof of concept studies for EGFP-FTNH constructs showed that genetic engineering is a viable strategy in functionalising ferritin nanoparticles. From these results, we hypothesised that other FPs that are responsive in FLIM to changes in pH could be attached in place of EGFP. In EGFP-FTNH construct 1, we replaced EGFP with the pH-sensitive ECFP and inserted the cell targeting peptide α-Enolase, which has been shown to enhance cellular uptake into colorectal cancer cells [451] (Fig 4.5 A). We obtained nanoparticles of the correct size, with no perturbing effects of genetic attachment on either FTNH assembly or ECFP spectral properties (Figure 4.4 C & D). We observed changes in fluorescence intensity in response to changes in pH, with a 1.6-fold increase from pH 5 to pH 8 (Figure 4.5 C & D). ECFP-FTNH was also shown to be responsive in fluorescence lifetime to changes in pH, with a 0.45ns response (1.37ns at pH 4.5 to 1.82ns at pH 8), compared to that of 0.72ns of the uncoupled ECFP (1.35ns at pH 4.5 to 2.07ns at pH 8) (Fig 4.6). This decreased fluorescence lifetime response could be a result of a suboptimal protein folding, or due to solution FRET quenching the ECFP donor's excited state lifetime by other ECFP molecules in close proximity on the ferritin nanoparticles.

We then moved forward to evaluate the ECFP-FTNH construct in cell-based models of HCT116 and MEF. Unfortunately, to visualise the construct in cells via confocal microscopy with FLIM, a higher concentration was needed. This was observed to be very toxic to cells, resulting in high incidences of cell death. Our attempts to increase brightness of ECFP-FTNH to date have not yielded any significant improvements.

We evaluated the strategy of pH dependent disassembly and reassembly encapsulation to develop O_2-sensitive, ferritin-based nanoparticles, encapsulating the O_2-sensitive phosphorescent probe Pt-Glc. We carried out proof of concept experiments, determining a 1:32 ratio of the hoFTN molecule to Pt-Glc molecules to be optimal in terms of phosphorescence brightness and minimal interference with the reassembly process of hoFTN (Fig 4.7). We then successfully attached FITC via isothiocyanate coupling at 1:120 ratio, to localise the hoFTN-Pt-Glc construct in cell-based models (Fig 4.9 A & B). We observed a higher phosphorescence intensity signal in hoFTN-Pt-Glc constructs than free Pt-Glc. This is possibly due to the concentrated number of Pt-Glc molecules in close proximity within the ferritin structure, rather than being diffused throughout the media (Fig 4.10 A). Another possible reason could be potentially due to the presence of imidazole from protein purification, which has been shown to increase phosphorescence of gadolinium-porphyrin based dye gadolinium-coordinated

hematoporphyrin monomethyl ether, by partially inhibiting energy transfer from the lowest triplet state of the compound to the oxygen molecules [455]. hoFTN-Pt-Glc was observed to be responsive to changes in oxygenation, with increased phosphorescence when deoxygenated (Fig 4.10 B), showing that the construct was sensitive to oxygenation in phosphorescence intensity.

In characterisation of hoFTN-Pt-Glc nanoparticles in MEF cells via confocal PLIM, we observed a comparable intracellular staining of the nanoparticles and free Pt-Glc confined to endosomes (Fig 4.10 A-B) with a granular appearance that has been commonly observed for fluorescently labelled nanoparticles trapped in endosomes of the cell [456]. From merged FITC and Pt-Glc signals, we observed co-localisation hoFTN with Pt-Glc (Fig 4.11 B); therefore, combined with relative staining efficiency of 2 to 20 hours (Fig 4.11 B) it is possible to conclude that Pt-Glc remains encapsulated within the ferritin structure after entering the cell. From analysis of fluorescence brightness and phosphorescence lifetimes of hoFTN-Pt-Glc and free Pt-Glc (Fig 4.11 C & D), we observed a higher intensity of free Pt-Glc after 2 hours than hoFTN-Pt-Glc, suggesting faster loading of Pt-Glc, which has previously shown cellular staining in a range of cell types [196]. Free Pt-Glc also displayed a longer phosphorescence lifetime of ~20 μs, compared to a hoFTN-Pt-Glc lifetime of ~15 μs. This decrease could be due to the quenching of phosphorescence lifetime as a result of high concentration of and proximity to the Pt-Glc molecules, or from the protein-based backbone of the construct. It is therefore possible to conclude that encapsulation here does not improve intracellular staining, nor does it achieve whole cell staining or show increases in phosphorescence lifetime, which is similarly seen in the genetically engineered construct of EGFP -FTNH and hoFTN-Alexa Fluor 488. Endosomal escape could potentially be plausible here through the use of peptides to destabilise the endosomes, e.g. endosomolytic dfTAT, a disulphide bond dimer of TAT peptide attached to fluorophore tetramethylrhodamine (TRITC), which induces endosomal leakage [457]. Endosomal escape could also be achieved through the use of noncovalent cell penetrating cargo linkers, e.g. TAT-fused calmodulin (TAT-CaM) attached to the cargo by a calmodulin binding site which releases the cargo from the early endosome due to its low Ca^{2+} environment [458].

4.5 Conclusion

The strategies for ferritin nanoparticle design described and evaluated here allow for an interchangeable approach for live cell imaging, where a wide range of FPs, fluorophores and sensor probes for biosensing applications and targeting peptides for specific cell targeting can be attached to suit the applications of specific experiments. In the case of encapsulation, we found that the strategy was hard to reproduce correctly each time in terms of obtaining nanoparticles of the correct size. Special care must be taken during the selection regarding the size and charge of sensor dyes, fluorophores and

targeting peptides, which may interfere with the reassembly process. The toxicity of the genetically engineered ferritin constructs was also a key issue, where the constructs were not bright enough for the confocal FLIM imaging in cells, and therefore higher concentrations were needed. An overall issue with ferritin nanoparticle constructs made by encapsulation or genetic engineering was poor intracellular staining confined to the endosomes of cells. This could potentially be overcome through strategies of the destabilisation of endosomes through reagents, cleavable linkers and non-covalent attachments to free the nanoparticle from the cell penetrating peptide evading the early endosome.

Chapter 5: Development of hybrid cellulose scaffold for FLIM for tissue engineering applications

5.1 Introduction

5.2.1 Cellulose scaffold materials and applications

Cellulose is the most abundant organic polymer on the planet, with many applications in tissue engineering, biosensing and biomaterials research [77]. In tissue engineering applications, cellulose displays the features of an ideal scaffold for cell and tissue growth. This is due to cellulose possessing structural similarities with ECM, mimicking its mechanical properties. Cellulose is also biocompatible due to its biological nature. It is also cost effective to produce. Cellulose is utilised as a 3D scaffold material in the form of extracts or processed cellulose materials with nano-size dimensions, known as nanocellulose. Such materials are subdivided into three groups: CNCs, NFC and BC. Nanocellulose as a scaffold material [76, 78, 79] has found applications in cartilage tissue regeneration [80], bone tissue [81], differentiating endothelial cells [82] and more. Nanocellulose scaffolds can be modified to improve cell adhesion, biocompatibility and provide a flexible scaffold architecture: i. chemically with polyethyleneglycole, thiols and other oligo- and polymers [79], ii. by using proteins with cellulose-binding domains [76, 459] and iii. biosynthetically [93]. Recently, the concept of using decellularised plant materials, such as leaves and stems, was proposed as an alternative scaffold for animal tissue engineering [460, 461]. Such decellularised plant materials show tuneable physical characteristics in regard to their porosity and tensile strength, with the presence of a vascular network, and are highly compatible with further modification with extracellular matrix components and other molecules [461], making decellularised plant materials a promising and versatile scaffold material for animal tissue engineering.

Nanocellulose can be modified for biosensing applications, for example, with nanocrystals [94] and gold nanoparticles immobilised via antibodies [95]. One such way of labelling the nanocellulose scaffold is through the use of protein binding domains. Carbohydrate binding modules (CBMs) are protein domains found in carbohydrolase enzymes, where their major function is to bind the enzyme to the carbohydrate substrate for hydrolysis. CBMs were previously known as CBDs due to initial discovery of cellulose binding properties, however the nomenclature has been updated from CBDs to CBMs due to the discovery of domains present in enzymes that do not hydrolyse cellulose. CBMs are grouped into families based on amino acid similarity, with 83 defined to date from the Carbohydrate-Active enZymes Database (CAZy) [462], and have been utilised for attachment of proteins to cellulose scaffolds for labelling and immobilisation, as well as protein purification. Approximately 200 protein domains binding the cellulose exist, varying in structure, size (4-20 kDa) and specificity towards cellulose [463]. The binding of cellulose can be reversed by the presence of denaturants or competitive

elution with cellobiose. In particular, *Cellulomonas fimi* CenA protein fragment [464] (termed as CBD) was successfully used as an affinity tag in bacterial, yeast and mammalian expression systems, maintaining solubility and folding of fused proteins. However, CBMs for specific and affinity modification of cellulose-based scaffolds are rarely used in tissue engineering [76].

5.1.2 Fluorescent protein-based biosensors for pH and calcium imaging

Functional analysis of biomarkers and monitoring of 3D engineered model development is of increasing importance in regards to the successful utilisation of the full potential and variety of scaffold materials [465-467]. For example, stem cell niche growth in a 3D culture depends heavily on both external and internal signals from physical, chemical and biological factors such as pH, Ca^{2+}, material stiffness, extracellular matrix and others [468]. Therefore, the non-invasive and quantitative measurements of such factors would allow for the development of a physiologically relevant stem cell niche. Extracellular acidification is indicative of the glycolytic flux, and thus can be directly used to analyse the cell energy budget in terms of oxidative phosphorylation, glycolysis and other cell energy production pathways [469]. Consequently, extracellular acidification is an imperative biomarker for cancer and normal non-transformed tissues and its control is of significant importance [470]. Extracellular acidification has been observed to play a key role in bone tissue engineering [471], drug and growth factor delivery [472] and modelling of extracellular matrix [473]. Acidification can be quantitatively measured using FPs. Changes in pH affect protonation of the FP's chromophore at the phenolic hydroxyl site, altering its spectral properties, such as fluorescence intensity and lifetime. The chromophore's pKa value can be altered by mutagenesis to generate FPs with different sensitivities to a range of pH values [474]. ECFP is a pH sensitive FP with a pKa of 4.7, that undergoes changes in its fluorescence lifetime of 0.8ns from pH 5 (~1.4 ns) to pH 7 (~2.2 ns) at 37°C. The most popular FP-based pH sensors are ECFP, pHRed and superfolder YFP (sfYFP). ECFP has been successfully applied as a pH sensor via fluorescence lifetime imaging microscopy (FLIM) in PC12 cells [212]. pHRed is a ratiometric single red protein pH sensor derived from the FP mKeima. pHRed exhibits changes in fluorescence lifetime of ~0.4ns over a range of pH 5 to pH 8, and has been successfully applied to the imaging of pH changes in cytosol and mitochondria [213]. YFP is environmentally sensitive to changes in pH and Cl^-. This sensitivity to pH has been used in the development of YFP-based pH sensors. sfYFP is a ratiometric pH sensor suitable for the range of pH within pH 6 to pH 8.4, and has been successfully attached to synthetic organic polymers and other matrices [92]. While EYFP has also displayed applications in cytosolic, golgi, and mitochondrial matrix pH analysis, EYFP and sfYFP applications in FLIM have yet to be examined.

Extracellular Ca^{2+} regulation is of key importance in most cells and tissues in the body due to its important roles in cell signalling and extracellular matrix remodelling, which can be observed in the stimulation of goblet cell differentiation in the gastrointestinal tract [475], and affects cell bioenergetics in neurosecretory cells [476]. Extracellular Ca^{2+} signalling is also implicated in tumour progression, with consequences in proliferation, invasion and sensitivity to cell death, with specific Ca^{2+} signalling pathways identified in the establishment and preservation of multidrug resistance and the tumour microenvironment [477]. GECIs are a widely used tool for Ca^{2+} imaging, in which upon binding of Ca^{2+} they undergo a conformational change resulting in an alteration in fluorescence intensity. The GCaMP series is the most popular of the GECIs. It is comprised of a Ca^{2+} binding protein calmodulin (CAM) attached to a binding motif M13 and a circularly permuted green fluorescent protein (cpEGFP). The binding of Ca^{2+} induces a conformational change that alters the chromophore's protonation state, increasing fluorescence intensity. GCaMP2 was developed with improved stability at a mammalian body temperature of 37°C, facilitating the first measurements *in vivo* with high signal-to-noise ratio [478]. The resolving of GCaMP2 crystal structure has served as the basis for the structural developments in improving the GCaMP series [479] from the breakthrough GCaMP3, which is useful for imaging neuronal activity to current GCaMP6 [480, 481]. Current advancements have been in the development of red fluorescent-based variants of RCaMP, such as mRuby derived RCaMP [482]. Red fluorescent variants would be preferable to green due to lower phytotoxicity and higher tissue penetration. Other Ca^{2+} indictors utilise two FP FRET, such as the TN series (e.g. TN-XL, -XXL and Twtich) [483-485], which uses troponin C instead of CAM to induce conformational change and bring the FP FRET pair closer in proximity. This allows for FRET to occur, increasing fluorescence intensity and fluorescence lifetime changes in the donor fluorophore for FLIM-FRET measurements.

Sensor probes such as small molecule dyes, nanoparticles, and FPs allow for the real time monitoring and quantitative measurement of extracellular pH and Ca^{2+}, which as of yet have not been applied in tissue-engineered constructs. Here, quantitative measurements are carried out by either ratiometric intensity-based detection or FLIM [486]. As lifetime is an intrinsic property of a fluorophore, FLIM based measurements are more reliable than intensity-based measurements. Therefore, results are largely independent from fluorophore concentration and imaging is not affected by issues of light scattering, photobleaching, or variations in excitation light [163]. FLIM-based pH sensing can be carried out using a number of proteins, such as enhanced cyan FP (ECFP) [212] and FP pHRed [487], some small molecule dyes [215, 488] and pH-sensitive nanoparticles [214]. The number of Ca^{2+}-sensing probes is also comprehensive, ranging from dyes to advanced FPs, with some of them suitable for FLIM [216, 489-491].

5.2 Aims

Here we set out to design extracellular pH and Ca^{2+} sensitive protein-based biosensor probes for the attachment via CBM , CBD_{cenA} from *Cellulomonas fimi* to cellulose scaffolds for FLIM measurements in 3D tissue models and organoids.

5.3 Results

5.3.1 Design of cellulose binding domain biosensors CBD-ECFP and CBD-GCaMP2

Initially we designed two FLIM protein-based biosensor probes containing CBD_{cenA} from *C.fimi* (CBD), genetically attached to either ECFP for pH measurements or to gCAMP2 for Ca^{2+} measurements [492, 493] via a short linker to facilitate the improvement of the folding rate of produced proteins. We cloned both constructs into pQE-30 His_6-tagged expression vectors and transfected them into the SG13009 strain of *E.coli* cells (see materials and methods section 2.2.4.4).Following production at 37°C until OD600= ~0.4, we induced with 0.125 mM IPTG for 16 hours (see Materials and Methods 2.2.4.4). We then subsequently purified both recombinant protein constructs under native conditions using His_6-tagged Ni^{2+}-NTA affinity chromatography. We then evaluated the purity of the proteins via SDS-PAGE (Fig 5.1B & D), with yields of ~6 mg/L culture, and a folding rate of 55 to 70% (assessed by UV-Vis). We then evaluated the biosensing properties of the two constructs in solution. We observed good sensitivity through changes in fluorescent intensity to the respective analytes (pH, Ca^{2+}) comparable to the untagged proteins, with a 2-fold increase in CBD-ECFP and 1.25-fold increase in CBD-gCAMP2 (Fig 5.1 C & E).

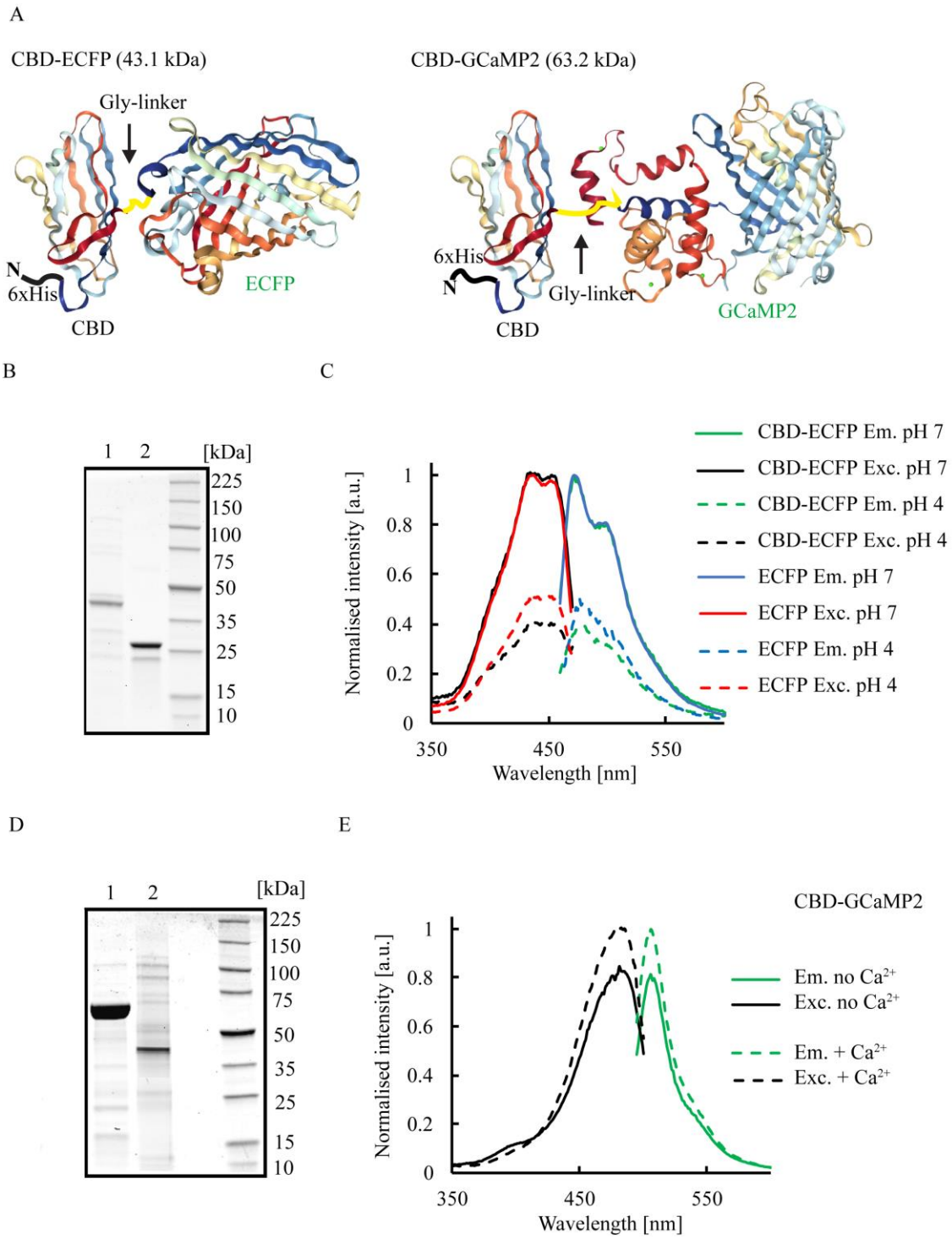

Figure 5.1. Design and evaluation of CBD-tagged biosensors. (A) Structures of protein biosensor constructs. CBD C-terminally attached to the N terminal of ECFP or GCaMP2 via Gly-linker. (B) Purification products of CBD-ECFP, and ECFP. Products ran on 4-10% SDS -PAGE and analysed via coomassie staining. Lane 1 CBD-ECFP ~40 kDa and Lane 2 ECFP~27 kDa. (C) Fluorescence excitation (Em. 477 nm) and emission (Exc. 434 nm) spectra of CBD-ECFP and ECFP with fluorescence intensity responses to changes in pH. (D) Purification products of CBD-GCAMP2 and GCaMP2. Products ran on 4-10% SDS -PAGE and analysed via coomassie staining. Lane

1 CBD-GCaMP2 ~60 kDa, Lane 2 gCAMP2 ~47 kDa. (E) Fluorescence excitation (Em. 507 nm) and emission (Exc. 488 nm) spectra of CBD-GCaMP2 and GCaMP2 with fluorescence intensity responses to changes in Ca^{2+}. (Figure reproduced from [494])

CBD-ECFP also displayed a response in lifetime of 0.3 ns; 1.9 ns at pH 4.5 to 2.2 ns at pH 8 in solution (Fig 5.2 B). Compared to untagged ECFP response in lifetime of 0.29 ns: 1.89 ns at pH 4.5 to 2.18 ns at pH 8 (Fig 5.2 A). Therefore, the genetic attachment of CBD to the respective FPs did not affect their photophysical properties.

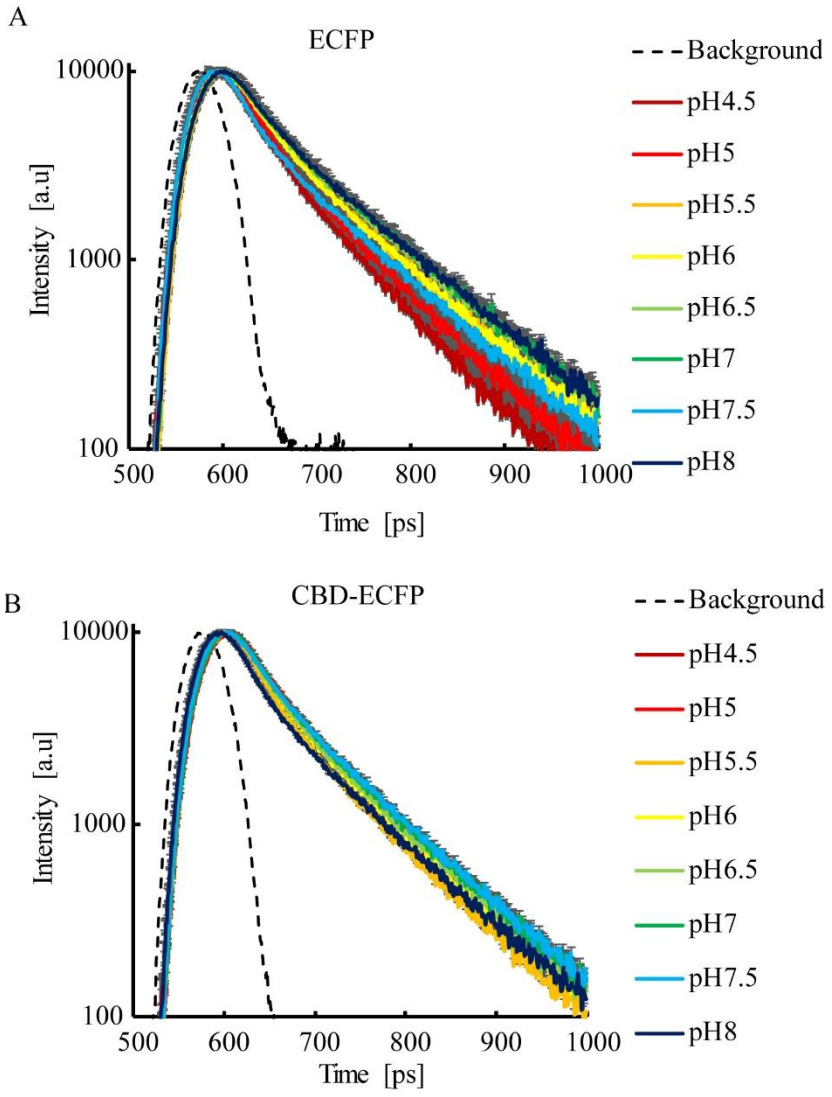

Figure 5.2. Fluorescence lifetime decays for ECFP and CBD-ECFP proteins measured in solution at different pH. (A) ECFP lifetime decays in buffered pH solutions 1.35 ns (pH 4.5) to 2ns (pH 8). (B) CBD-ECFP lifetime decays in buffered pH solutions 1.89 ns (pH 4.5) to 2.18 ns (pH 8). Standard deviations are shown in grey. Prompt (background) fluorescence signals are also shown. (Figure reproduced from [494])

5.3.2 Staining of cellulose materials and sensing properties

We selected three different types of cellulose scaffold materials for labelling with our CBD-based biosensors due to their respective characteristics: NFC material is commercially available as GrowDex matrix – a hydrogel with tunable viscosity. BC is produced by *Gluconacetobacter xylinus*, forming scaffold material with a high mechanical strength and large surface area. Finally, decellularised plant materials provide a pre-vascularised scaffold with high tensile strength and tunability.

First, we set out to evaluate the labelling of GrowDex with our biosensor CBD-ECFP. We observed efficient staining, distinct from background signals with concentrations over 2 µM per 0.5% volume of GrowDex, incubated for 15 minutes at room temperature (Fig 5.3 A). The staining of GrowDex was concentration dependent and the CBD-ECFP signal reached saturation at ~10 µM concentration (Fig 5.4 A). CBD-ECFP staining was also observed to be stable, decreasing after 10 days of storage at 4 ^{0}C in solution (Fig 5.4 B). Untagged ECFP also displayed an insignificant degree of staining with GrowDex, as seen from background signals (Fig 5.4 E). Furthermore, optical sectioning using confocal microscopy confirmed efficient 3D, in-depth staining of GrowDex with CBD-ECFP (Fig 5.3 B). We carried out the same procedures with CBD-GCaMP2, where we observed similar data possessing comparable kinetics of staining, along with staining efficiency and storage stability (Fig 5.4 C, D & F).

The BC samples were produced by our colleagues from the Institute for Regenerative Medicine, (I.M. Sechenov First Moscow State University, Moscow, Russian Federation), using conventional methods [495]. The BC samples were cut into small pieces (~2x5 mm) for easier applications in the experiments. The BC showed similar staining efficacy and stability with CBD-ECFP as it did with the GrowDex matrix (Fig 5.4 A & B). However, 3D reconstruction of labelled BC showed its highest brightness at both the periphery and surface regions of ~ 20-30 µm depth (Fig 5.3 B). BC therefore suffered from poor staining distribution as observed from previous fluorescence microscope images and 3D reconstructions. This loss of brightness could be explained by the possible limited light penetration, due to BC being more solid and less transparent in nature than our example of GrowDex, especially when used with the blue-green emitting ECFP protein.

In conclusion, we observed efficient staining of our selected cellulose scaffold materials – GrowDex and BC with CBD-ECFP and CBD-GCaMP2. In the case of GrowDex, we achieved better staining efficacy and specificity than seen in BC. This is possibly due to the nanofiblar patch-like structure of GrowDex, whereas, in the case of BC, light penetration was a significant issue due to the less-than-transparent nature of the material, thereby limiting the use of BC.

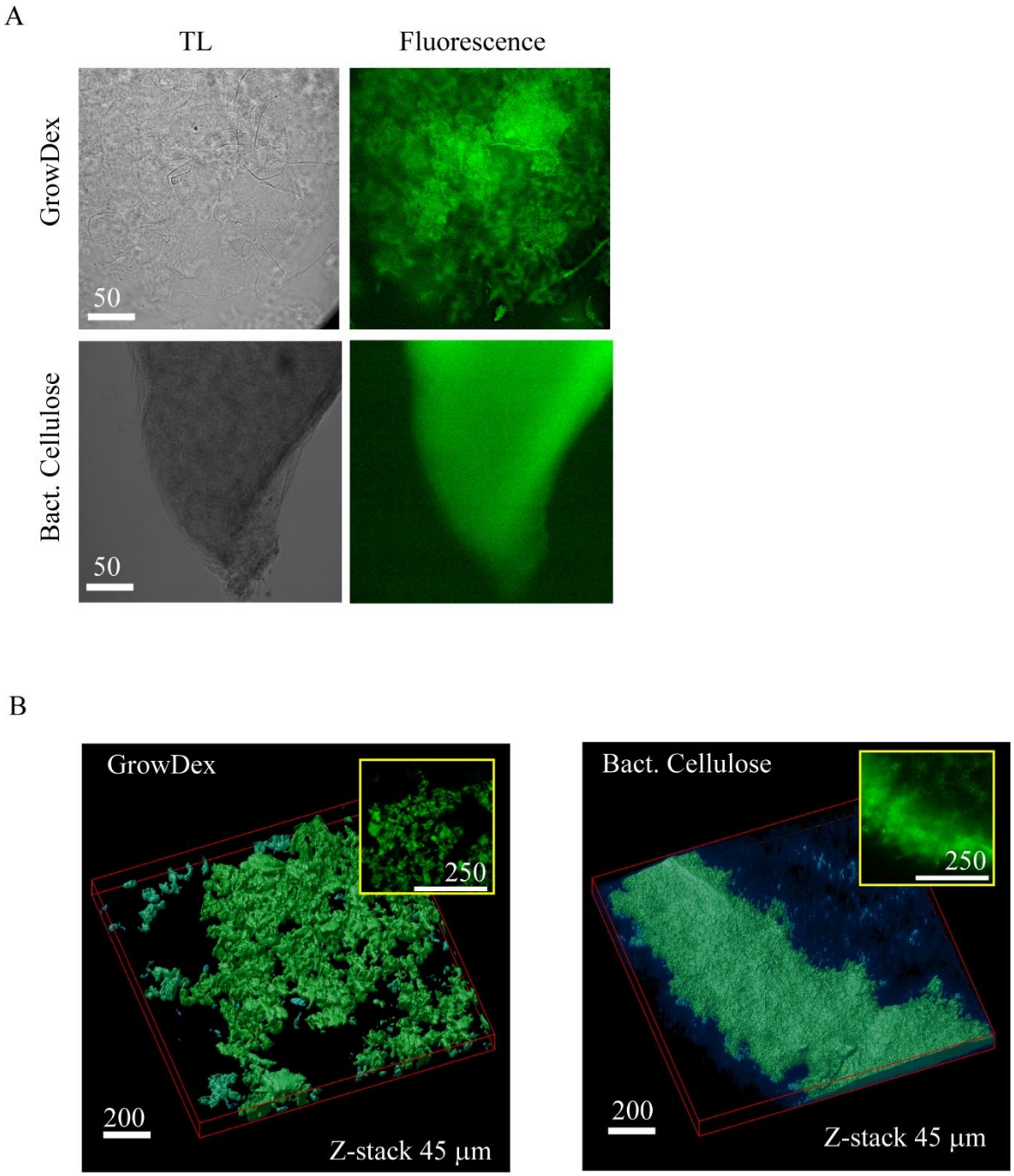

Figure 5.3. Staining of Growdex and BC scaffolds with CBD-ECFP. (A) transmission light (TL) and fluorescence (470 nm exc., 510-650 nm em.) microscopy images of GrowDex and BC stained with CBD-ECFP (5 µM, 15 min). (B) 3D reconstructions (45 µm Z stack) of CBD-ECFP-labelled GrowDex and BC scaffolds (447 nm exc., 512-536 nm em.) (3D reconstructions carried out with supervisor Dr. Ruslan Dmitriev). Fluorescence images of GrowDex and BC were processed using deconvolution in SVI Huygens software. The Scale bar is in µm. (Figure reproduced from [494])

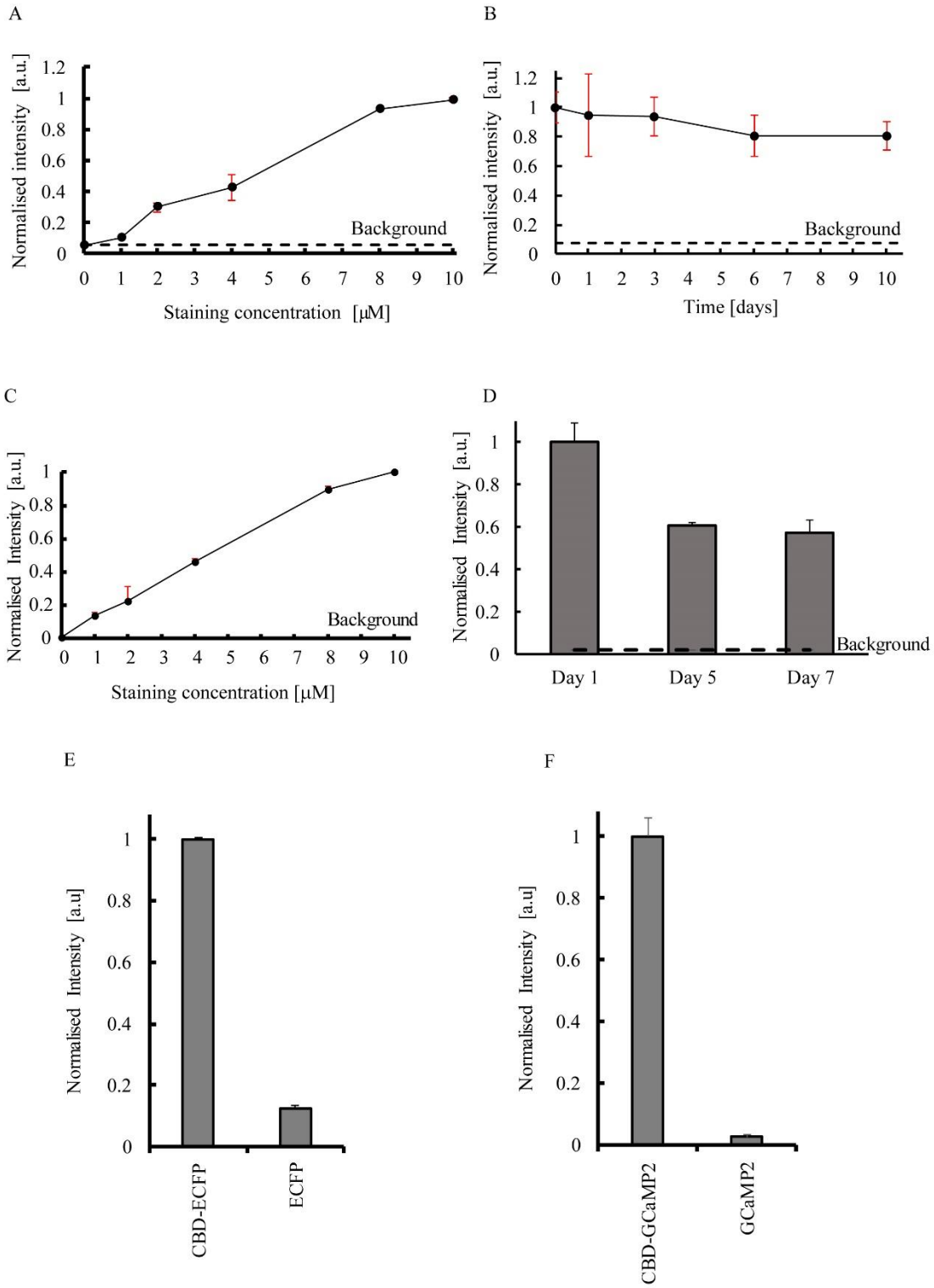

Figure 5.4. Concentration dependent staining and stability of CBD-ECFP and CBD-GCaMP2 with GrowDex scaffold. (A) Concentration-dependent staining of GrowDex with 1 to 10 µM CBD-ECFP (incubation time 15 min, in PBS) The data were normalised to the maximal background-corrected fluorescence signals. (B) Stability of CBD-ECFP labelled GrowDex scaffold, fluorescence measured by microscopy of the sample (labelled with 10 µM, 15 min) over 10 days. (C) Concentration-dependent staining of GrowDex with 1 to 10 µM CBD-GCaMP2 (incubation time 15 min, in PBS). (D) Stability of CBD-GCaMP2-labelled GrowDex scaffold fluorescence

measured by microscopy of the sample (labelled with 10 µM, 15 min) over 7 days. (E) Comparison of staining of GrowDex with CBD-ECFP and ECFP. (F) Comparison of staining of GrowDex with CBD-GCaMP2 and GCaMP2. Both Growdex and BC matrices were incubated with 10 µM of respective proteins for 15 min in PBS, washed and measured on fluorescence microscope (470 nm exc., 510-560 nm em.). The data here was normalised to the initial background-corrected fluorescence. (Figure reproduced from [494])

5.3.3 FLIM calibrations of GrowDex with CBD-ECFP and CBD-GCaMP2 in solution

Due to suboptimal brightness and staining distribution in BC samples, we moved forward with GrowDex for evaluation of FLIM response with CBD-ECFP and CBD-GCaMP2. We carried out FLIM experiments in buffered solutions with different pH values for CBD-ECFP (pH 5.5 – 8) and different concentrations of Ca^{2+} (0 to 5 mM $CaCl_2$) (See Materials and Methods section 2.2.7.2). The CBD-ECFP fluorescence decay curves were fitted using a double-exponential function and showed pH-sensitive changes observed from the distribution histograms and FLIM images, with 1.9 ns at pH 6 and 2.3 ns at pH 8, for a change of 0.4 ns (Fig 5.5 B & C). Calibration of pH across a physiological range of pH 5.5 to pH 8 showed a change in lifetime of 0.7 ns, and the calibration demonstrates the highest sensitivity of the CBD-ECFP in range of pH 5.5 to 7 (Fig 5.5 D). CBD-ECFP demonstrated pKa values close to the literature data for ECFP (pka ~ 4.7). However, despite being acidic, the pKa values are still useful for cellular pH measurements due to the acidic nature of the intracellular organelles and extracellular acidification. Therefore, CBD-ECFP can be potentially used for quantitative FLIM-based pH sensing.

We carried out similar experiments with CBD-GCaMP2 and GrowDex. Here we evaluated CBD-GCaMP2 protein's potential use as a FLIM biosensor for changes in Ca^{2+}. GCaMP series constructs have mostly been successful in *in vivo* intensity-based measurements, however, research analysing the photophysical properties for GCaMP2, GCaMP3, and GCaMP5 detected fluorescence lifetime responses in buffers of $CaCl_2$ under two photon excitation [496]. We therefore hypothesised that GCaMP2 could be applicable in FLIM with responses in lifetime caused by changes in the concentration of Ca^{2+}. We incubated CBD-GCaMP2 in solutions of $CaCl_2$.ranging in concentration from 0 – 5mM Ca^{2+}. Unfortunately, we did not observe any response in fluorescence lifetime, this could be due suboptimal protein folding or the high affinity nature of GCaMP2 for Ca^{2+}ions makes it more suitable for lower, intracellular Ca^{2+} concentration ranges of approximately 100 nM [497], whereas we require a lower affinity Ca^{2+} sensor for higher concentrations present in extracellularly.

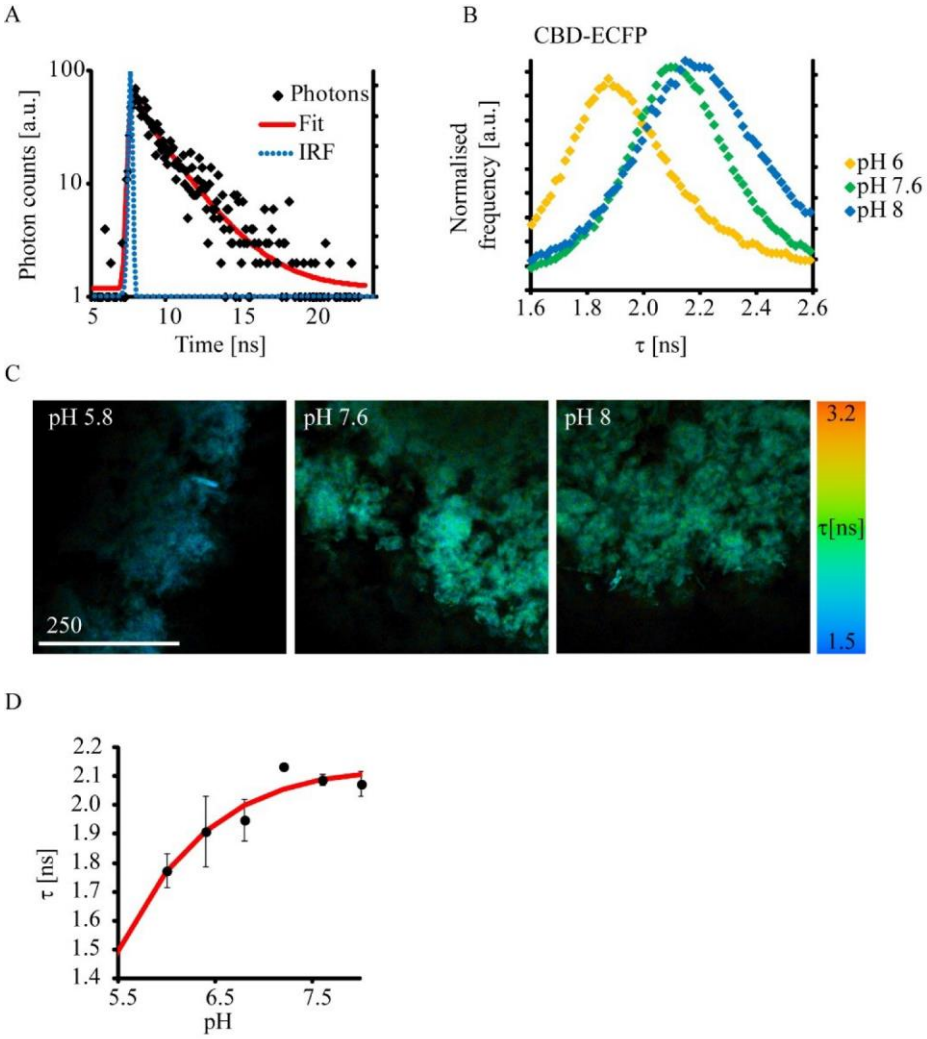

Figure 5.5. Evaluation of CBD-ECFP labelled GrowDex biosensing scaffold in FLIM. (A) Fluorescence decay of CBD-ECFP labelled GrowDex matrix (exc. 447 nm, em. 512-536 nm). (B) Fluorescence lifetime distributions (normalised by area) for CBD-ECFP GrowDex matrix exposed to different pH 5.5 to 8 at 37 ºC. (C) Fluorescence lifetime images for CBD-ECFP labelled GrowDex matrix at different pH from pH 5.5 to 8. Scale bar is in µm. (FLIM measurements carried out with supervisor Dr. Ruslan Dmitriev). (Figure reproduced from [494])

In conclusion, both CBD protein biosensors displayed strong ability to label cellulose scaffolds and demonstrated attractiveness in applications as biosensing reagents. However, only the CBD-ECFP displayed reasonable evidence for its pH-sensing properties, with applications in analysis of extracellular acidification environment in cells and tissues, as well as demonstrating the potential for the cloning of a range of other prospective biosensors with the CBD tag.

5.3.4 Design of cellulose binding domain biosensor CBD-EYFP

Following on from the design and application of CBD-ECFP and CBD-GCaMP2, we designed a second generation of a pH-sensitive FLIM protein-based biosensor, containing EYFP connected to CBD via a short, Gly-rich linker. Like the previous CBD-based recombinant proteins, we cloned the CBD-EYFP construct into a pQE-30 His_6-tagged expression vector and transfected it into an SG13009 strain of *E.coli* cells. Using the previously optimised bacterial production conditions of 37°C until OD600= ~0.4, we induced with 0.125mM IPTG for 16 hours and purified under native conditions using His_6-tagged Ni^{2+}-NTA affinity chromatography. The purity of the CBD-EYFP recombinant protein was evaluated via SDS-PAGE gel electrophoresis (Fig 5.9 B), with a yield of ~ 2.55 mg/L culture and a folding rate of 44% (assessed by UV-Vis). We then evaluated pH sensing properties of CBD-EYFP in solution, with a 5-fold increase from pH4 to pH7 (Fig 5.9 C). Therefore, the genetic attachment of CBD to EYFP did not affect it's photophysical properties. We then assessed CBD-EYFP staining of the GrowDex matrix, observing an efficient staining distinct from background signals with concentrations over 2 µM per 0.5% volume of GrowDex, incubated for 15 minutes at room temperature (Fig 5.9 D). Similarly, for CBD-ECFP and CBD-GCaMP2, the staining of GrowDex in the case of CBD-EYFP was concentration dependent, with the signal reaching saturation at ~10µM concentration (Fig 5.9 E).

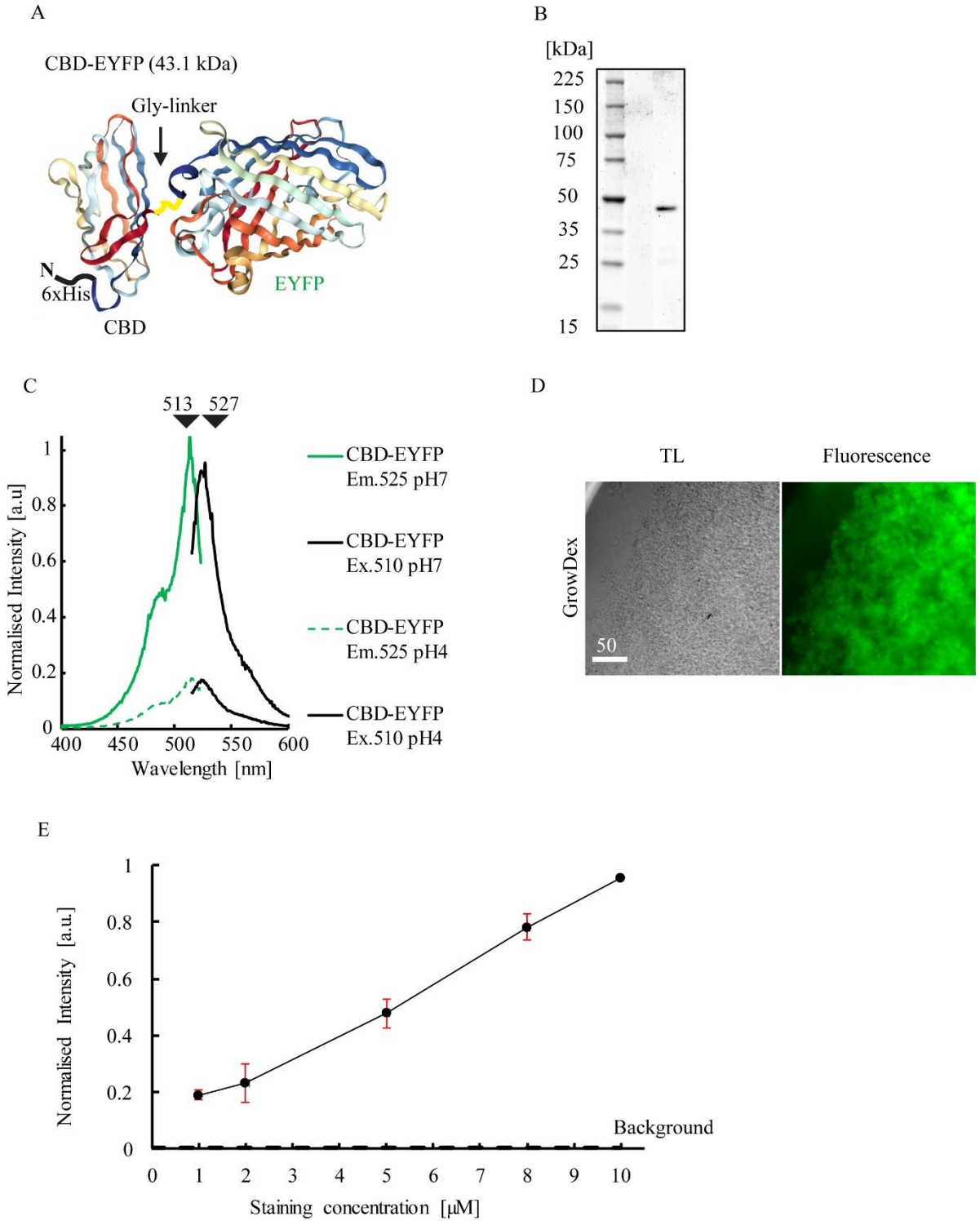

Figure 5.6. Design and evaluation of CBD-EYFP. (A) Structures of protein biosensor construct. CBD-YCFP with CBD C terminally attached to the N terminal of EYFP via Gly-linker. (B) Purification products of CBD-EYFP. Ran on 4-10% SDS-PAGE and analysed via Coomassie staining with Lane 1 CBD-EYFP ~43 kDa (C Fluorescence excitation (Em. 525 nm) and emission (Exc. 10 nm) spectra of CBD-EYFP with fluorescence intensity responses to changes in pH. (D) Transmission light (TL) and fluorescence (470 nm exc., 510-650 nm em.) microscopy images of GrowDex labelled with CBD-EYFP (5 µM, 15 min). The Scale bar is in µm. (E)

Concentration-dependent staining of GrowDex with 1 to 10 µM CBD-EYFP (incubation time 15 min, in PBS) The data were normalised to the maximal background-corrected fluorescence signals.

5.3.5 FLIM calibrations of GrowDex with CBD-EYFP in solution.

We wanted to evaluate CBD-EYFP labelled GrowDex fluorescence lifetime response to changes in pH via FLIM. We carried out FLIM experiments in buffered solutions with different pH values (pH 5.5 – 8). The CBD-EYFP fluorescence decay curves were fitted using double-exponential function and showed pH-sensitive changes observed from the distribution histograms and FLIM images, with 2.55 ns at pH 5.5 and 2.9 ns at pH 6.8, for a change of 0.3 ns (Fig 5.10 B & C). Calibration of pH across a physiological range of pH 5.5 to pH 8 showed a change in lifetime of 0.2 ns, and that the highest sensitivity of CBD-EYFP is within the range of pH 5.5 to 7 (Fig 5.10 D). However, for CBD-EYFP, the change in lifetime is shorter than that of CBD-ECFP and shows limited sensitivity above pH 7. This is possibly due to the high pKa value of EYFP at ~6.9. Overall, from the comparison of CBD-EYFP to CBD-ECFP, the later appears to be the most useful in terms of quantitative FLIM-based pH sensing, due to its longer lifetime and sensitivity to lower acidic pH values. However, for intensity-based measurements, CBD-EYFP possess a 5- fold increase in change of pH from 4 to 7, whereas CBD-ECFP displayed a 2-fold increase across the same range.

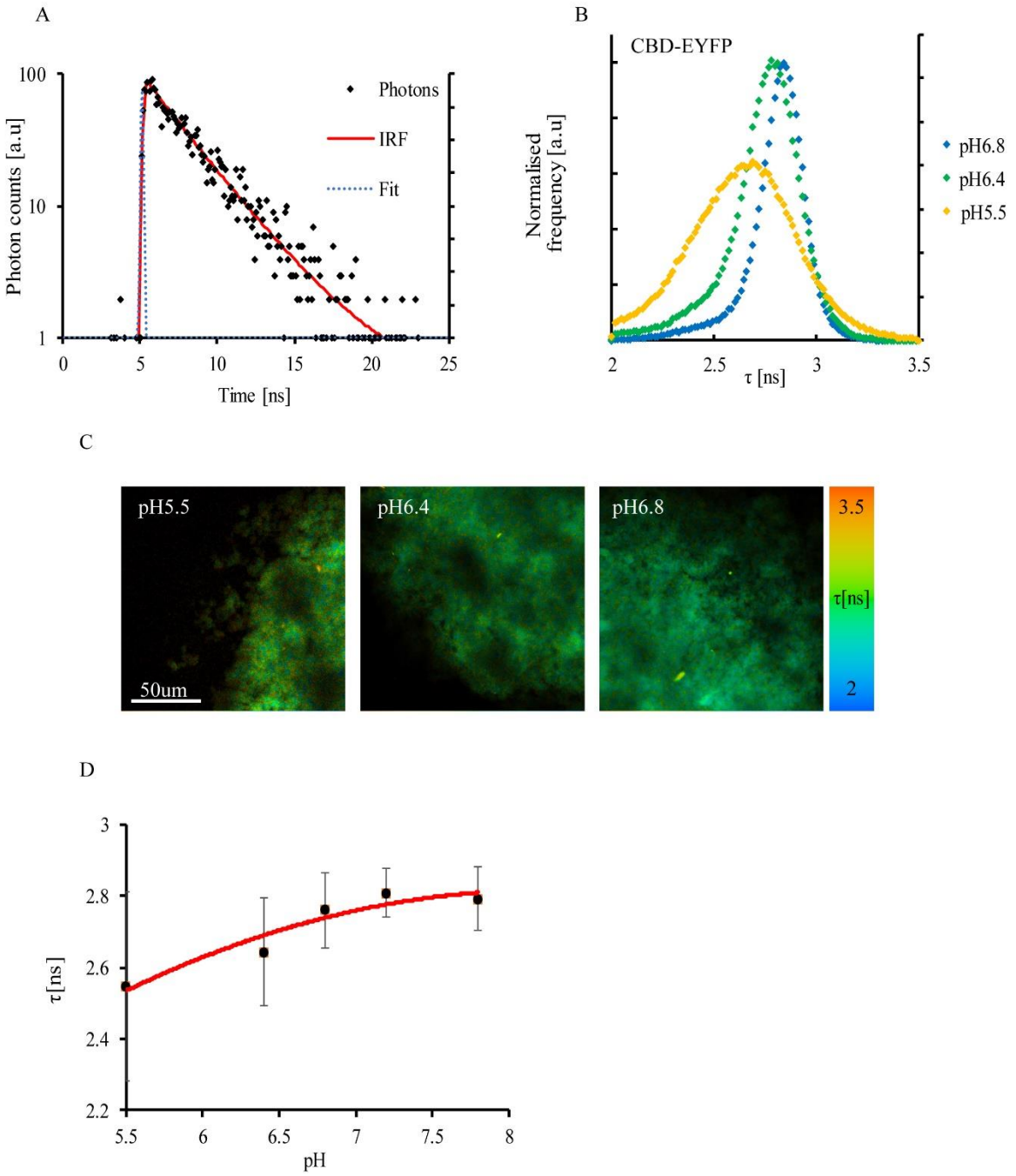

Figure 5.7. Evaluation of CBD-EYFP labelled GrowDex biosensing scaffold in FLIM. (A) Fluorescence decay of CBD-ECFP labelled GrowDex matrix (exc. 447 nm; em. 512-536 nm). (B) Fluorescence lifetime distributions (normalised by area) for CBD-EYFP GrowDex matrix exposed to different pH 5.5 to 8 at 37 ºC. (C) Fluorescence lifetime images for CBD-EYFP labelled GrowDex matrix at different pH. Scale bar is in µm. (D) pH FLIM calibration of CBD-EYFP labelled GrowDex from pH 5.5 to 8.

5.3.6 Decellularised plant materials as cell culture scaffolds

Decllualrised plant materials have been recently proposed as an alternative, viable scaffold material for cell culture, possessing good porosity and a pre-existing vascular system. We tested 3 plant-based materials produced from celery stems, carrot, and potato tubers. We selected celery stems and carrot tubers here due to the dicot arranged central vasculature system consisting of large vessels present with high potential for cell and tissue culture. Potato was selected for its contrasting low porosity and structural stiffness for applications with cell cultures that grow and differentiate differently with varying matrix stiffness.

We cut the celery stem, carrot, and potato tubers into small ~1 mm thick section, and subsequently carried out the decellularisation process (see Materials and Methods section 2.2.7.1). After decellularisation, the celery and carrot sections became optically transparent, while the potato sections remained optically opaque (Fig 5.11 A). We then wanted to evaluate CBD-EYFP staining with the decellularised plant materials and determine whether there was any autofluorescence present. We incubated all three decellularised sections in 5 µM CBD-EYFP for 15 minutes in PBS (pH 7.4) (Fig 5.11 B). We observed efficient staining of all three decellularised plant materials, with all three displaying no background fluorescence. However, only the decellularised celery provided the most optically transparent decellularised plant material, with the carrot and potato tubulars being thick and significantly less transparent. Further complications arose from use of the potato tubers, in that their heavy starch content made them very prone to breaking apart. Therefore, we proceeded with experiments using decellularised materials from celery due to its optical transparency and presence of large vessels with honeycomb-like structures for cell culture, which was beneficial for uniform size distribution of cell aggregates. CBD-EYFP remained stably attached to celery for over 7 days (Fig 5.11 C), allowing for long term biosensing applications.

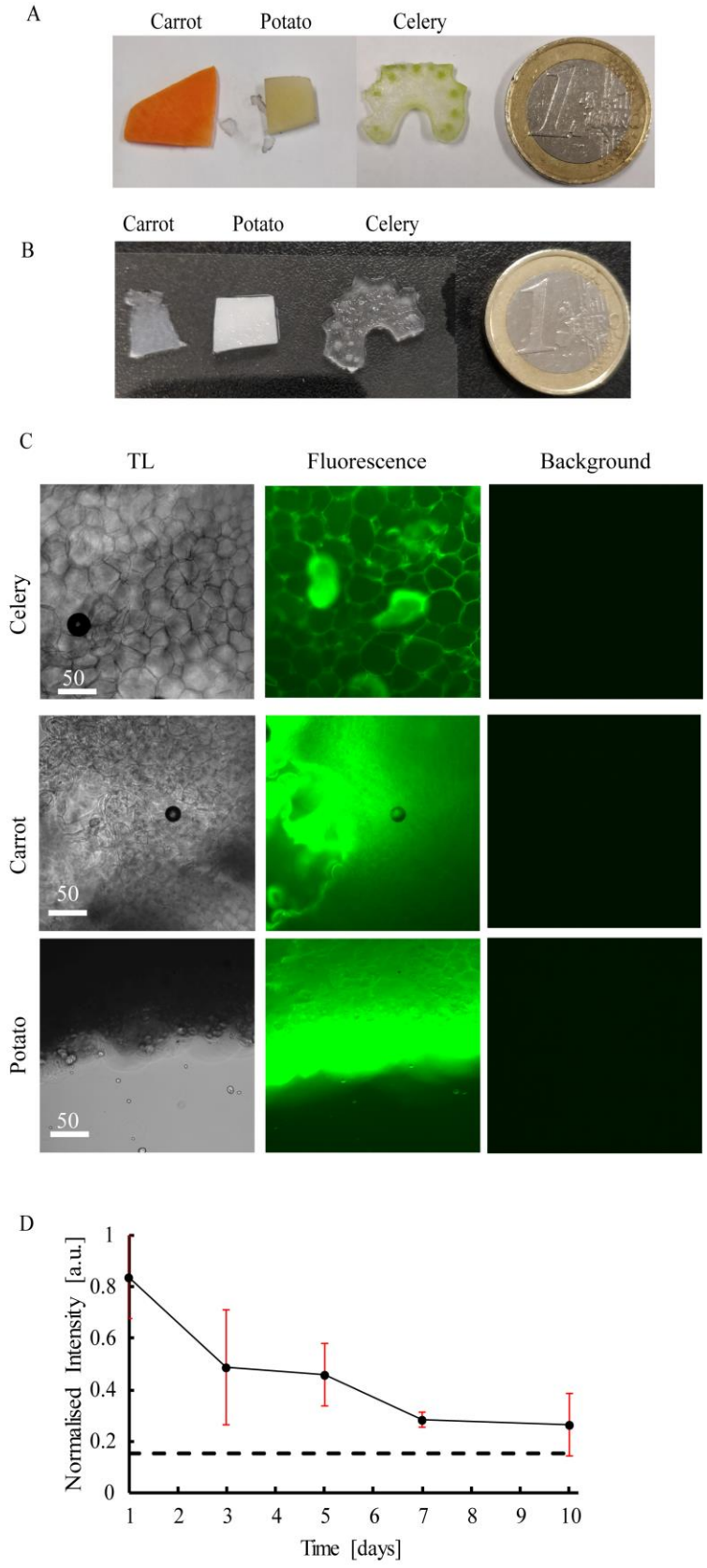

Figure 5.8. Production and staining of decellularised plant materials for cell culture. (A) Photographs of celery stem, carrot and potato tuber sections before and (B) after decellularisation. A one-euro coin is shown for scale. (C) Transmission light and widefield fluorescence (470 nm exc., 510-560 nm em.) microscopy images for

stem, carrot and potato tuber sections after decellularisation and following labelling with CBD-EYFP. The same acquisition settings were used for fluorescence images. Scale bar is in µm. (D) Storage stability of labelled decellularised celery (5 µM, 15 minutes) over 10 days.

We then set out to evaluate the viability of decellularised celery scaffolds for applications in cell and tissue cell culture. We initially wanted to examine decellularised celery's ability to support cell growth using HCT116 cells. Disappointingly, observed cell growth was suboptimal, with many cells not attaching to the scaffold. However, work carried out by Dr. R. Dmitriev and Dr. I. Okkelman demonstrated the growth of small intestinal organoids within the decellularised celery scaffold material coated in Matrigel to support growth of the organoids and labelled with CBD-ECFP to measure responses in pH. Multiplexed FLIM-PLIM microscopy was subsequently carried out with the CBD-ECFP labelled decellularised celery scaffold for extracellular pH measurements in FLIM, and the organoid culture was labelled with the phosphorescent O_2-sensitive probe Pt-Glc for O_2 measurements in PLIM. This allowed for the study of live organoid oxygenation and extracellular acidification, analysing the dynamics of both pH and O_2 at rest and upon stimulations with mock (DMSO) and FCCP. The organoid culture was found to be deoxygenated at rest, with low extracellular pH. After stimulation with FCCP, a drop in pH was detected, with no decreases in oxygenation (possibly due to the already hypoxic state of the organoid), confirming the growth of viable and metabolically active organoids in the decellularised celery scaffold material.

Table 5.1. Comparison of CBD based biosensors. Comparing stability, lifetime in solution and applications of pH Sensitive CBD-ECFP and CBD-EYFP and Ca^{2+} CBD-GCaMP2**.**

Name	Sensitive to	Stability	Initial lifetime (τ_i) (ns)	Final lifetime (τ_f) (ns)	Change in lifetime ($\Delta\tau$) (ns)	Comments
CBD-ECFP	pH	Over 10 days on GrowDex and decellularised materials.	1.5 ns at pH 5.5	2.2 ns at pH 8	0.7 ns	Longer lifetime changes over physiological range of pH compared to EYFP. Applied in detection of extracellular pH changes in FLIM with HCT116 cells and organoid model (with joint O_2 PLIM)
CBD-EYFP	pH	Over 10 days on GrowDex and decellularised materials.	2.55 ns at pH 5.5	2.75 ns at pH 8	0.2ns	Shorter lifetime changes over physiological range of pH compared to ECFP.
CBD-GCaMP2	Ca^{2+}	7 days on GrowDex.	N/A	N/A	N/A	No response to changes of Ca^{2+} in FLIM.

5.3.7 Extracellular acidification in 3D culture of cancer cells

We set out to evaluate the CBD-ECFP labelled GrowDex scaffold to support cell growth and detect changes in extracellular acidification via FLIM in work executed in cooperation with supervisor Dr. Ruslan Dmitriev. We first wanted to see if the presence of CBD-ECFP on the GrowDex scaffold could alter cell growth. Therefore, we tested CBD-ECFP labelled and unlabelled GrowDex scaffolds with a culture of human colon cancer HCT116 cells visualised with Hoechst 33342 nucleic acid cell marker. We observed comparable cell growth between the labelled and unlabelled Growdex matrix (Fig 5.6), which continued for more than 3-7 days with cells forming multi-cellular aggregates. BC was also tested, however, disappointingly, the HCT116 wild-type (WT) cells grown in the scaffold were of a lesser efficiency, possibly due to lower porosity of the thicker BC.

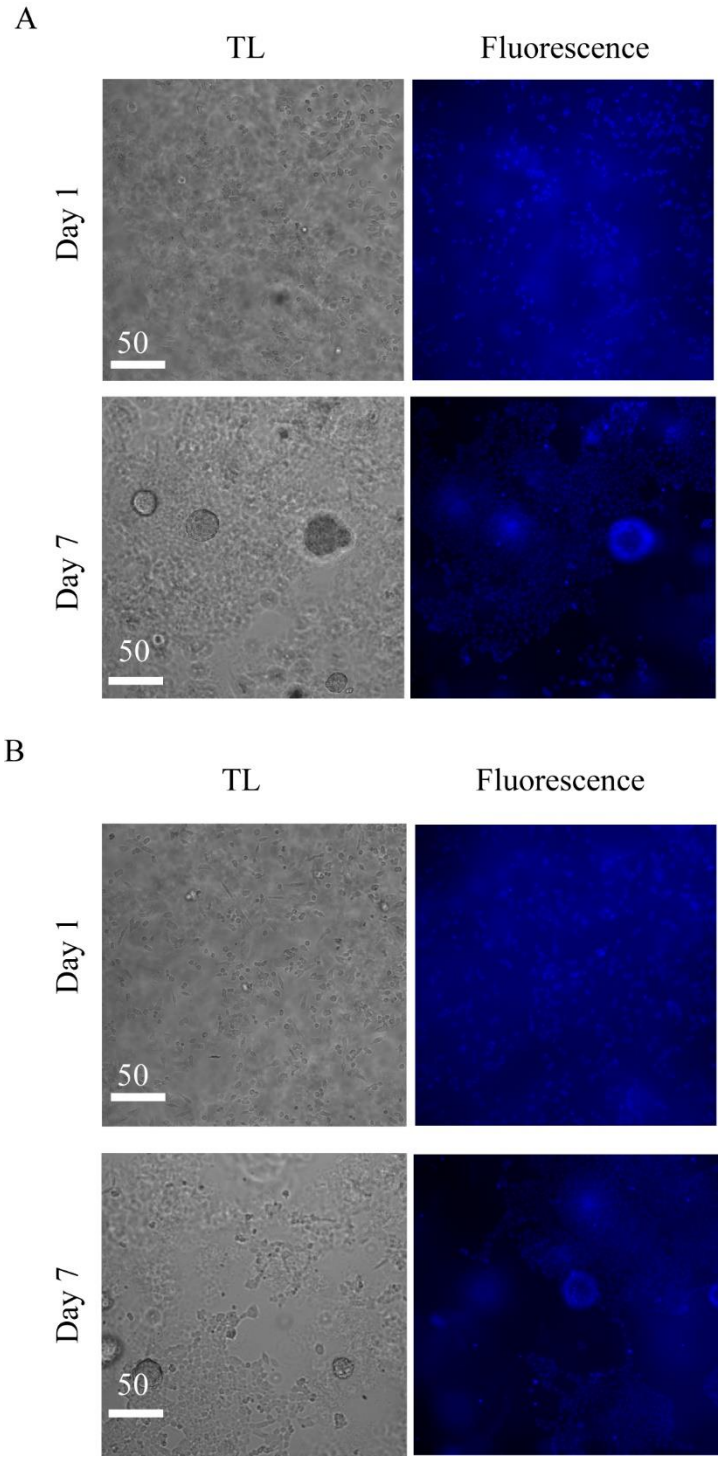

Figure 5.9. Cell growth in unlabelled and CBD-ECFP-labelled Growdex. HCT116 cells were seeded and grown for 0-7 days in either (A) labelled (5 µM CBD-ECFP, 15 min) or (B) unlabelled Growdex matrices. Quantified by using fluorescence microscopy with Hoechst 33342 staining (1 µM, 30 min, 390 nm exc.). Note that in Growdex cells tend to form multicellular aggregates over time. Scale bar is in µm (Experiment carried out with supervisor Dr. Ruslan Dmitriev). (Figure reproduced from [494])

We then evaluated CBD-ECFP extracellular pH sensitivity with HCT116 cells, using both WT and the oxidative phosphorylation deficient knock-out cell line $SCO_2^{-/-}$, with $SCO_2^{-/-}$ being of particular interest as it acidifies its environment more strongly than the WT cell line [498]. A problem we first encountered was the issue of a shaking and vibration of the scaffold when viewed under the confocal microscope, due to its upright architecture and dipped objective lens. To resolve this issue, we imbedded the scaffold with HCT116 cells (WT and $SCO_2^{-/-}$) within the collagen-rich Matrigel matrix. We selected Matrigel to support and hold the cellulose matrices in place for the confocal experiments, and in addition, Matrigel is also known to support both the survival and growth of cancer cell aggregates. We observed comparable growth over 3 days, with cells forming small 3D cellular aggregates (Fig 5.10 A) which were visualised with the mitochondrial marker, TMRM. These results again demonstrate that the CBD protein-based biosensor has no effect on cell growth, and that the cellulose scaffold supports the growth of a 3D cell culture. Moreover, we also observed no evidence of non-specific staining of Matrigel with CBD-ECFP.

We then carried out FLIM with both HCT116 WT and $SCO_2^{-/-}$ cells in CBD-ECFP labelled GrowDex, embedded in Matrigel. When comparing average fluorescence lifetimes with WT and $SCO_2^{-/-}$ HCT116 cell cultures, we observed similar pH values of pH 7.6 to 8, thereby demonstrating an absence of the acidification of the cell culture medium (Fig 5.10 B). However, when we treated $SCO_2^{-/-}$ HCT116 cells with the mitochondrial uncoupler, FCCP, we observed a minor decrease in extracellular pH corresponding to acidification of the cell culture media. This decrease was detected by fluorescence lifetime histogram (Fig 5.11 D), and not observed with the mock DMSO treatment (Fig 5.10 C). Due to a pKa of ~ 4.7, ECFP at this pH range displays high variability and low sensitivity. However, despite this issue, we were able to identify decreases in fluorescence lifetimes and pH for the FCCP-treated samples.

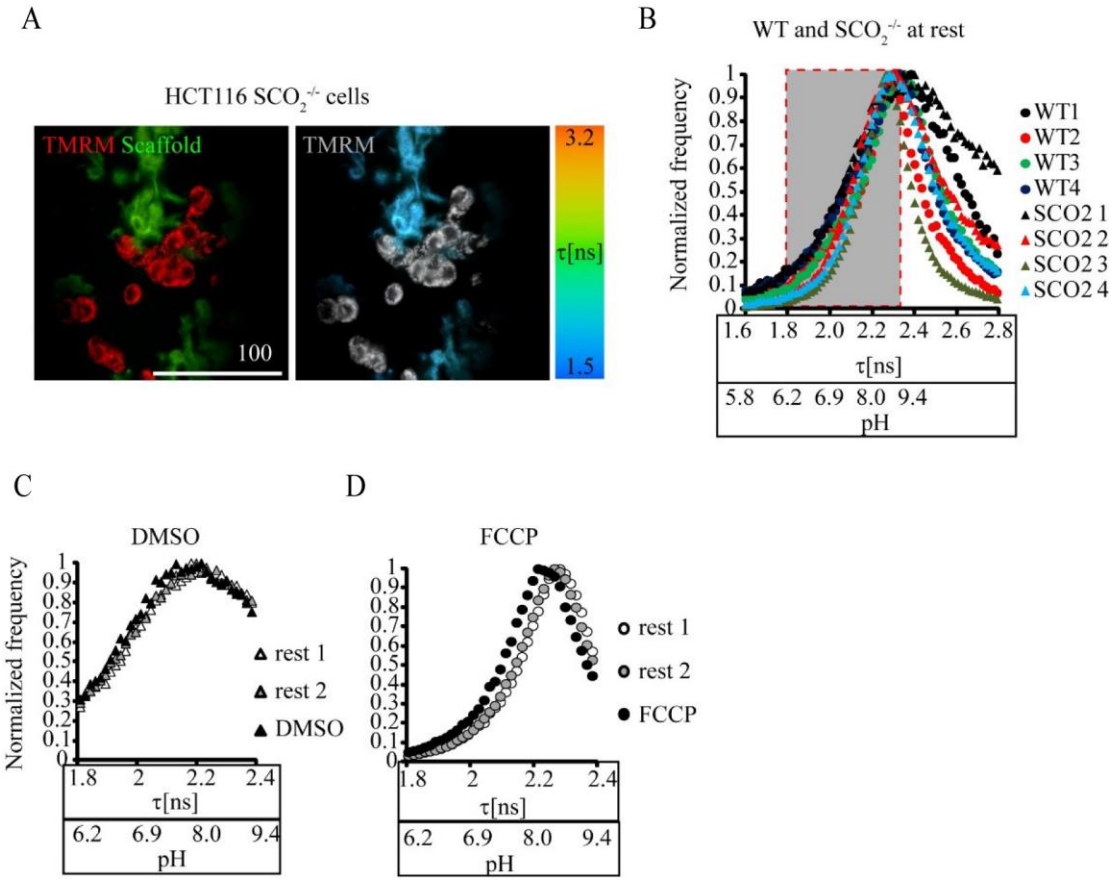

Figure 5.10. FLIM of extracellular pH using CBD-ECFP labelled GrowDex scaffolds with HCT116 cells. (A) Optical section of HCT116 $SCO_2^{-/-}$ cells stained with TMRM (in red) growing within CBD-ECFP scaffold (in green) and shown co-localisation in intensity images and FLIM images. (B) Fluorescence lifetime distribution histograms for resting wild type and $SCO_2^{-/-}$ HCT116 cells (normalised by height). Measured fluorescence lifetime distribution histograms for $SCO_2^{-/-}$ cells treated with (C) DMSO and (D) FCCP. Scale bar is in µm. (FLIM measurement carried out with supervisor Dr. Ruslan Dmitriev). (Figure modified from [494])

We then carried out 3D reconstruction of HCT116 cells labelled with TMRM grown in CBD-ECFP labelled GrowDex, which was embedded in Matrigel via confocal microscopy with 76 µm thick Z stacks (Fig 5.10). From this 3D reconstruction we observed that the HCT116 cells grew within the GrowDex scaffold, forming 3D cellular aggregates and did not simply attach to the exterior of the scaffold.

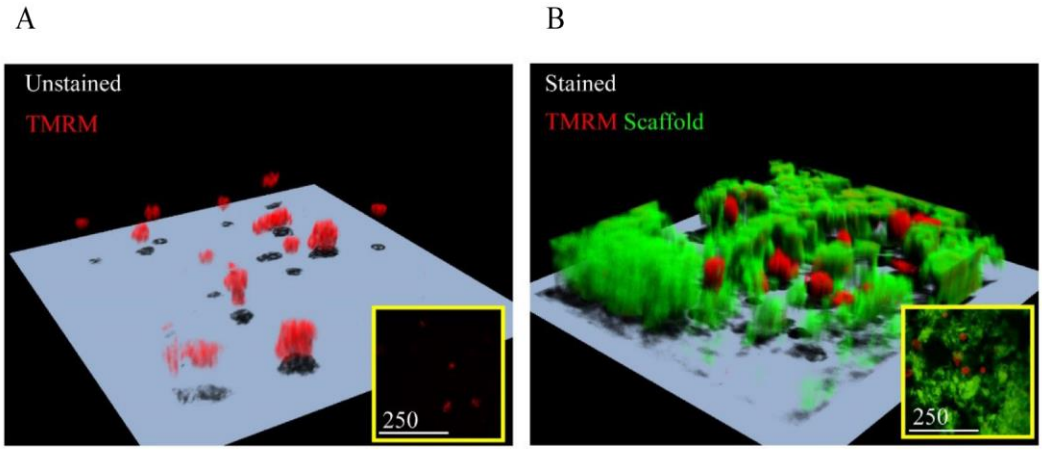

Figure 5.11. 3D reconstruction of cells grown within GrowDex. 3D reconstructions (76 µm thick Z stacks) of Growdex scaffolds embedded in Matrigel, with HCT116 cells stained with TMRM (in red) without CBD-ECFP (A) and with CBDECFP (in green) (B). (3D reconstructions carried out with supervisor Dr. Ruslan Dmitriev). (Figure modified from [494])

Overall, we demonstrated that CBD-ECFP labelled GrowDex scaffolds are compatible with cancer cell growth and subsequent analysis with FLIM methodology, and allow growth of cultured cells throughout the scaffold. However, we were not able to produce high cell densities in BC scaffolds, but GrowDex matrix did allow for the efficient formation of small cell aggregates with no visible negative effects on the cell growth.

5.4 Discussion

The aim of this research was the development of hybrid biosensing cellulose scaffold materials capable of measuring extracellular pH and Ca^{2+} in 3D cell culture. We hypothesised and subsequently proved that through genetic engineering used to fuse CBD to FLIM-responsive FPs with pH or Ca^{2+} sensitivity, this would allow for the attachment of the protein-based biosensor probes to the cellulose scaffold materials. Here, we designed three such recombinant proteins with CBD attached to ECFP or EYFP for extracellular pH measurements and GCaMP2 for Ca^{2+} measurements, evaluating their attachment to cellulose scaffold-based materials: GrowDex, BC and decellularised plant materials. Then, subsequently, these CBD-biosensors were used in the measuring of extracellular pH and Ca^{2+} in 3D cell cultures in FLIM.

First, we wanted to examine whether attachment of CBD to FPs affects their photophysical properties (Fig 5.1 and Fig 5.9). In all cases, we obtained recombinant proteins of the correct sizes with a 44-70% protein folding rate. In the case of CBD-ECFP, we observed a 2-fold increase in intensity response to changes in pH from 4 to 7 (Fig 5.1 C). Furthermore CBD-ECFP displayed responses in lifetime of 0.29

ns in solution: 1.89 ns at pH 4.5 to 2.18 ns at pH 8 (Fig 5.2). For CBD-GCaMP2, we observed a 1.25-fold increase in intensity response to changes in Ca^{2+}(Fig 5.1 E). Finally, in the case of CBD-EYFP, we observed a 5-fold increase in intensity response to changes in pH from 4 to 7 (Fig 5.9 C). Therefore, it is possible to conclude that the genetic attachment of CBD to the respective FPs did not affect their photophysical properties. When evaluating the staining of cellulose scaffold materials and the sensing properties of the protein-based biosensing probes, we found that the CBD tag facilitated stable attachment for over 7 to 10 days in GrowDex (Fig 5.3 B & D) and the decellularised celery scaffolds (Fig 5.11 C). This long-term labelling stability would allow for the growth of cell and tissue cultures within the scaffold for a period of at least 7 days, allowing for the continued measurement of cellular growth and differentiation during this time, for example, in the case of monitoring stem cell growth and differentiation, and in organoid tissue development. Also evaluated was an optimal concentration for clear visualisation of fluorescence, with the saturation of ECFP (Fig 5.3 A), EYFP (Fig 5.9 E) and GCaMP2 (Fig 5.3 C) signal at concentrations of 10 µM, with 5 µM concentration optimal for imaging experiments with fluorescence and confocal microscopy.

CBD-EYFP was developed to examine if the fluorescence lifetime response to pH changes with ECFP could be improved upon. However, in comparing CBD-ECFP and CBD-EYFP in their performance of pH FLIM with GrowDex, we see that CBD-ECFP possess a significantly broader response to changes in pH from pH 5.5 to pH 8 with a change in fluorescence lifetime of 0.7 ns (Fig 5.5), whereas with CBD-EYFP there is a change of only 0.2 ns in the same pH range (Fig 5.10) (Table 5.1). With CBD-GCaMP2, although we observed a response to Ca^{2+} in intensity, it did not display sensing properties in FLIM. Encouragement, however, should be taken from the evidence that CBD can be easily fused to a vast array of ever-expanding numbers of FPs suitable for FLIM applications. The performance of pH sensing through FLIM can be improved upon with the use of other pH sensitive FPs, such as pHRed, which displayed a 0.4 ns lifetime response in solution, and a 0.3 ns response in the mouse neuroblastoma cell line, Neuro2a, within a pH range of 5 to 8 [213]. pHRed is also two-photon excitable, and emits red fluorescence, allowing for reduced phototoxicity and further in-depth imaging. In the case for Ca^{2+} FLIM measurements, indicators that utilise a Ca^{2+} binding protein between a FP FRET pair have found applications in FLIM-FRET imaging, wherein the fluorescence lifetime measurements are made from the decrease in the lifetime of the donor fluorophore during FRET. A FLIM probe based on calmodulin-dependent protein kinase II (CaMKII) and a FRET pair of mRFP and GFP displayed a fluorescence lifetime response to changes in Ca^{2+} concentrations in HEK293T cells upon stimulation with Ca^{2+} ionophore, 4-Br-A23182, with changes in lifetime of ~1.01 ns over 10 minutes [499]. The mTFP-TnC-Cit FLIM-FRET Ca^{2+} sensor was developed with a FRET pair of monomeric teal FP (mTFP1) as a FRET donor, with Citrine FP as a FRET acceptor, with both FPs attached by a Troponin-C fragment for Ca^{2+} binding. mTFP-TnC-Cit displayed changes in lifetime of ~0.33ns in solution from 0 µM to 40 µM Ca^{2+}, and ~0.15 ns after stimulation with Ca^{2+} ionophore, ionomycin, in HEK293T cells [500].

We selected three cellulose scaffolds, all with their own strengths and potential drawbacks, depending on their cell culture applications: GrowDex due to its' tuneable viscosity, BC for its' large surface area and high mechanical strength, and decellularised plant materials, as they provide a pre-vascularised scaffold with high tensile strength and tunability. With all three scaffold materials, we set out to evaluate their respective compatibility in labelling with protein-based biosensors and cell culture applications. In the case of BC, we observed poor staining distribution of the CBD-tagged, protein-based biosensors (Fig 5.3). This is possibly due to limited light penetration as a result of BC being thick and opaque in nature, and limitations in imaging high depths, with a blue-green emission from ECFP and GCaMP2. In contrast, both GrowDex (Fig 5.3) and decellularised celery (Fig 5.11) provided cellulose scaffold materials that were optically clear and achieved both specific and high staining efficiency. This is due to a nanofibrillar patch-like structure in the case of GrowDex, and high porosity of the decellularised celery. CBD-ECFP labelled GrowDex provided a hybrid scaffold material compatible with cancer cell growth (WT and $SCO_2^{-/-}$ HCT116 cell cultures) and the formation of small cellular aggregates within the scaffold (Fig 5.7 A-C). The formation of such aggregates is highly advantageous for extracellular measurement of pH due to stronger extracellular acidification. The GrowDex hydrogel scaffold has potential to be highly flexible in compatibility with a wide range of cell lines due to the ability to alter the hydrogel's concentration. GrowDex has been shown to support the development of the stem cell niche with the formation of spheroid cultures of human pluripotent stem cells (hPSCs), grown at 0.5%, supporting hPSCs pluripotency over 26 days, along with hydrogel's enzymatic removal facilitating cellular differentiation [84]. HepaRG liver progenitor cells also form multicellular spheroids within 1% GrowDex, displaying structural hallmarks of liver tissue [501]. NRAS mutated cutaneous melanoma (MUG-Mel2) formed spheroids in GrowDex at 0.4%, with maintenance of natural cell behavior [502]. Cultures of multipotent human adipose tissue-derived and bone marrow-derived mesenchymal stem cells (adMSCs and bmMSCs) were grown in 0.2 and 0.5% GrowDex, which supported cellular differentiation into osteogenic cells within the scaffold [503]. Cellulose scaffolds compared to synthetic scaffolds degrade at a much slower rate with mammalian cell and tissue models. This is due to the presence of cellulose 1,4-glycosidic bond which is only cleaved by cellulolytic enzymes, found in microbial or fungal cells. Whilst advantageous for cell and tissue culture in long term cultures, its usage as a tissue engineering scaffold for tissue regeneration is limited. Here, the cellulose scaffold's structure and crystallinity would need to be altered, for example, by oxidization, making it susceptible to hydrolysis [504]. BC has found such applications as a scaffold in the tissue replacement of cartilage and engineered blood vessels [505, 506]. Cellulose scaffolds have therefore been applied as a scaffold material for a wide array of cell lines, including stem and cancer cell types supporting a 3D organization, as well as in tissue engineering for regenerated tissues for transplantation. This makes cellulose scaffolds ideal matrices in 3D cell and tissue culture, and regenerative medicine.

We subsequently evaluated extracellular acidification of HCT116 cells with the CBD-ECFP labelled GrowDex scaffold via FLIM. After treating $SCO_2^{-/-}$ HCT116 cells with the mitochondrial uncoupler, FCCP, we observed a minor decrease in extracellular pH corresponding to the acidification of the cell culture media (Fig 5.7 D-G). Here, the CBD-ECFP labelled GrowDex scaffold was able to identify statistically significant decreases in fluorescence lifetimes and pH for FCCP-treated samples via FLIM. CBD-ECFP labelled decellularised celery provided a hybrid scaffold material with the compatibility in 3D cell culture of small intestinal organoids. Experiments carried out by Dr. R. Dmitriev and Dr. I. Okkelman, published in [494], showed that CBD-ECFP labelled decellularised celery provided scaffold material for the growth of viable and metabolically active organoid cultures, with applications in the combined monitoring of extracellular pH and cellular O_2 in FLIM and PLIM respectively. Therefore, CBD-ECFP labelled GrowDex and decellularised celery provided hybrid scaffold materials for potential dual extracellular pH and intracellular O_2 monitoring in the real time assessment of mitochondrial function, glycolysis, redox status, and the overall balance of energy production mechanisms. All of these cellular functions exist in dynamic states during cell proliferation and differentiation, or upon drug treatment in both stem and cancer cell cultures.

5.5 Conclusion

Through this research we have developed protein-based biosensor probes that, through genetic engineering, can be altered to fuse CBD to a wide array of FPs suitable for FLIM applications in measuring extracellular pH and a range of metabolic gradients, as well as the potential application of modular peptides for cell differentiation [507]. The cellulose scaffolds GrowDex and decellularised plant materials (i.e. celery), along with the labelling strategy developed here provide the potential for combined multiplexed FLIM-PLIM imaging of 3D models, such as cellular aggregates and organoid cultures. The use of such hybrid biosensing scaffold materials will allow for the real time monitoring of dynamic cellular processes and mechanisms that take place during cellular proliferation, differentiation and drug treatments. The real time assessment abilities will allow for improvement in the production of a physiologically relevant cell and tissue model for tissue engineering applications.

6. Overall conclusion

The development of non-invasive biosensor constructs that allow for quantitative imaging of metabolic intracellular and extracellular gradients of cells and tissues, grown in tissue engineered models, is key to producing physiologically relevant models, truly representative of normal and diseased states. This thesis has demonstrated the development of protein-based biosensors for hybrid scaffold design, measuring the extracellular pH of small cellular aggregates via FLIM, along with the evaluation of design strategies for self-assembling protein nanoparticle-based biosensors for measurements of intracellular O_2 via PLIM and ratiometric-based measurements, as well as intracellular pH for FLIM applications.

Hybrid scaffold materials developed here are composed of genetically engineered protein-based biosensor probes, sensitive to pH (CBD-ECFP and CBD-EYFP) and Ca^{2+} (CBD-GCaMP2) in intensity and FLIM and attached via CBD to cellulose scaffolds including nanofibrillar GrowDex, BC and decellularised plant materials. Out of the three cellulose scaffold materials, GrowDex and decellularised celery were optically clear and achieved both specific and high staining efficiency with all three biosensor constructs. In the case of CBD-ECFP and CBD-EYFP labelled GrowDex, the hybrid scaffold demonstrated pH sensitivity in fluorescence lifetime. This allowed for applications in FLIM-based measurements of extracellular pH, with CBD-ECFP demonstrating a broader response in FLIM, displaying lifetime changes of 0.7 ns over a pH range of 5.5 to 8, compared to the 0.2 ns change over the same range for CBD-EYFP. However, in the case of CBD-GCaMP2, despite displaying responses to Ca^{2+} in intensity, it showed no such response in FLIM. From these results, it is evident that the protein-based biosensor construct design can potentially facilitate the successful attachment of CBD to a vast array of FLIM responsive FPs, such as ECFP and pHRed for pH measurements, and CaMKII based FRET pair of mRFP and GFP, and mTFP-TnC-Cit for Ca^{2+} measurements, which possess better characteristics for biosensing applications. The most promising result came from the success of the CBD-ECFP labelled GrowDex hybrid scaffold which supported the growth of 3D cultured human colon cancer cells HCT116, with the ability to measure real time changes in extracellular pH. Using the CBD-ECFP labelled GrowDex hybrid scaffold, we were able to detect decreases in pH after stimulation with the mitochondrial uncoupler FCCP. The development of new protein-based biosensor constructs with genetic attachments of CBD to pH FLIM sensitive FPs and FRET-FLIM sensitive Ca^{2+} indicators are underway, with the aim of improving FLIM responses. The expanded research into the described hybrid cellulose scaffold materials will allow for the real time monitoring of dynamic cellular processes that govern cellular proliferation, differentiation and response to drug treatments, thereby improving the physiological relevance of cell and tissue models of normal and diseased states.

Current intracellular imaging is reliant on synthetically based nanoparticles, which suffer from issues with suboptimal intracellular staining, along with high toxicity and immunogenicity. Here, we evaluated several design strategies for the development of self-assembling protein nanoparticle constructs based on the ELP-CP and protein nanocage ferritin. Such constructs hold promise due to their biological nature and low immunogenicity, making them more biocompatible and biodegradable, and thereby reducing toxicity and immunogenic responses. They are also amenable to multiple strategies of functionalisation such as genetic engineering, chemical modification, and encapsulation.

Metallochelate coupling is an existing immobilisation, purification, and labelling technique where histidine-tagged recombinant proteins are bound to NTA or IDA groups. These groups form a complex with transition metal ions (i.e. Zn^{2+}, Ni^{2}+, Co^{2+}, or Cu^{2+}) which then co-ordinate histidine amino acids expressed on the recombinant protein. We evaluated metallochelate coupling as a viable strategy for the design of intracellular O_2 probes. Here, we produced ratiometric-based O_2-sensitive phosphorescent probes from EGFP, TagBFP2 and DsRed-express coupled to PtCP-NTA. The resulting coupled FPs demonstrate no perturbing effects of coupling to their fluorescence properties and display O_2-sensitive phosphorescence responses. This produces O_2-sensitive complexes that have combined fluorescence, which can be applied in ratiometric-based measurements of both extracellular and intracellular O_2, where FP is used as O_2-insensitive reference. The potential exists to attach a wide array of monomeric FPs allows for flexibility in experimental design, with coupling to far red FPs facilitating high resolution imaging due to increased imaging depth. The biggest result here was the first known example of the development of an O_2-sensitive ELP-CP-PtCP-NTA. Here, we carried out the metallochelate coupling of PtCP-NTA with C-terminally His_6-tagged ELPCP protein subunit. We achieved coupling efficiency of ~65% and the VLP displayed ~25.8 times higher absorptivity and ~7 times higher phosphorescence intensity with comparable phosphorescence lifetime range to that of the commercial O_2-sensitive probe MitoXpress. Metallochelate coupling can potentially allow for the attachment of targeting peptides for the cell specific delivery of the VLPs. The coupling efficiency can potentially be improved with the introduction of more NTA groups on the Pt-porphyrins and increasing the number of His_6 tags on the protein subunits. ELPCP-H_6-PtCP VLPs can be applied in time-resolved fluorescence microplate reader measurements. If increased brightness and cell specific targeting can be achieved, then fluorescence microscope imaging can be applied for cell studies.

In addition to metallochelate coupling in self-assembling protein nanoparticle biosensor design, we evaluated genetic engineering, chemical modification and encapsulation as viable strategies for the development of pH and O_2-sensitive ferritin nanoparticles. With genetic engineering, we designed two recombinant ferritin nanoparticle constructs: EGFP-FTNH expressing the cell penetrating peptide BN7, and the pH sensitive ECFP-FTN expressing BN7 and the cell targeting peptide ENL. In both genetically engineered constructs, we observed no perturbing effects to ferritin self-assembly or to the spectral properties of EGFP and ECFP. With ECFP-FTN displaying responses in intensity and lifetime, with

changes of 0.45 ns over a pH range of 4.5 to 8. However, in the case of EGFP-FTNH intracellular staining of MEF cells, it was observed to be suboptimal and confined to endosomes, and ECFP-FTNH proved to be toxic to HCT116 cells. We then finally evaluated the strategy of pH dependent disassembly and reassembly encapsulation to develop O_2-sensitive ferritin-based nanoparticles, encapsulating the O_2-sensitive phosphorescent probe Pt-Glc (hoFTN Pt-Glc). We observed a higher phosphorescence intensity signal in hoFTN-Pt-Glc constructs than free Pt-Glc. This is possibly due to the high number of Pt-Glc molecules in close proximity within the ferritin structure, rather than being diffused throughout the media or sample. Another potential explanation for this increase in phosphorescence intensity could be due to the presence of imidazole used for protein purification, which has been shown to increase phosphorescence of gadolinium-porphyrin based dye {Zang, 2016 #511}. hoFTN-Pt-Glc was also observed to be responsive to changes in oxygenation, with increased phosphorescence intensity when deoxygenated. However, in characterising the construct in MEF cells, we observed suboptimal intracellular staining, with the construct being trapped within the endosomes. The uptake of hoFTN Pt-Glc into MEF cells was observed to be slower than free Pt-Glc and possessed shorter phosphorescence lifetimes. These results showed that the encapsulation of Pt-Glc into ferritin in its current form did not improve intracellular staining, phosphorescence intensity or lifetime in cells. Improvements could be possible with the attachment of a wider range cell penetrating and targeting peptides that can escape the early endosome pathway. Despite the results in cell models, the strategies of genetic engineering and encapsulation displayed an interchangeable approach to the design of ferritin constructs for potential tailoring to experimental requirements in live cell imaging applications.

The application of nanoparticles such as self-assembling protein nanoparticles in cell and tissue models is a complex area, in which issues are raised regarding the set of dynamic interactions of nanoparticle materials and biological systems being probed. These interactions lead to the formation of protein coronas. As well as this, intracellular uptake and subcellular localisations can cause effects on cellular processes. To develop nanoparticle constructs with optimal intracellular staining and sub cellular localisations, these nano-bio interfaces and their effects need to be studied. However, such studies are not straight forward, hindering the progress of nanoparticle development. The strategies evaluated here could potentially aid in the development of protein-based nanoparticles that could probe these interfaces due to the interchangeable nature of the attachments being expressed, such as targeting peptides for specific cell and subcellular staining, and fluorophores allowing for localisation.

The most promising results came from the development of hybrid scaffold materials for FLIM in 3D tissue engineering, providing the potential for multiplexed PLIM-FLIM imaging of 3D models such as cellular aggregates and intestinal organoids. Hybrid scaffold materials of this nature would allow for a less invasive approach in real time monitoring of cell and tissue models, compared to intracellular nanoparticles, whose interactions with subcellular organelles and cellular processes are largely unknown along with the complexity of nano-bio interfaces are as of yet poorly understood.

The results presented in this thesis demonstrate the development and evaluation of multiple strategies in the production of hybrid scaffold materials and self-assembling protein nanoparticles, with an interchangeable approach to construct design. The flexibility in biosensor design could potentially allow for the quantitative imaging of multiple metabolites via FLIM and PLIM, aiding in the development of physiologically relevant tissue engineered models.

Thesis outcomes

Peer reviewed papers:

- "Cellulose-Based Scaffolds for Fluorescence Lifetime Imaging-Assisted Tissue Engineering", (Acta Biomateriala, 2018) Authors: Neil O'Donnell, Irina A. Okkelman, Shannen A. Ruane, Peter Timashev, Tatyana I. Gromovykh, and Ruslan I. Dmitriev.
- "Metallochelate Coupling of Phosphorescent Pt-Porphyrins to Peptides, Proteins, and Self-Assembling Protein Nanoparticles" (ACS Bioconjugate Chemistry, 2016). Authors: Ruslan I. Dmitriev, Neil O'Donnell, and Dmitri B. Papkovsky.

Book chapter:

- "Three-Dimensional Tissue Models and Available Probes for Multi-Parametric Live Cell Microscopy Of 3D Tissue Models: A Brief Overview" (Springer Link, 2017; Review). Authors: Neil O'Donnell, and Ruslan I. Dmitriev.

Published conference abstracts:

- "Hybrid biosensing cellulose-based scaffolds for imaging-assisted tissue engineering" (FASEB, 2018) Authors: Neil O'Donnell, Irina A. Okkelman, Shannen A. Ruane, Peter Timashev, Tatyana I. Gromovykh, and Ruslan I. Dmitriev

Conference presentations:

- **Poster presentation:** "Ferritin nanoparticles improve intracellular delivery of phosphorescent oxygen-sensitive probe" EUROPT(R)ODE XIII. Graz, Austria. March 20 - 23, 2016

Bibliography

[1] H.K. Kleinman, D. Philp, M.P. Hoffman, Role of the extracellular matrix in morphogenesis, Curr Opin Biotechnol 14(5) (2003) 526-32.
[2] S. Neelam, P.R. Hayes, Q. Zhang, R.B. Dickinson, T.P. Lele, Vertical uniformity of cells and nuclei in epithelial monolayers, Scientific Reports 6 (2016) 19689.
[3] K. Tanner, M.M. Gottesman, Beyond 3D culture models of cancer, Science translational medicine 7(283) (2015) 283ps9-283ps9.
[4] X. Xu, M.C. Farach-Carson, X. Jia, Three-Dimensional In Vitro Tumor Models for Cancer Research and Drug Evaluation, Biotechnology advances 32(7) (2014) 1256-1268.
[5] E. Fennema, N. Rivron, J. Rouwkema, C. van Blitterswijk, J. de Boer, Spheroid culture as a tool for creating 3D complex tissues, Trends Biotechnol 31(2) (2013) 108-15.
[6] A. Fatehullah, S.H. Tan, N. Barker, Organoids as an in vitro model of human development and disease, Nat Cell Biol 18(3) (2016) 246-54.
[7] K.M. Yamada, E. Cukierman, Modeling Tissue Morphogenesis and Cancer in 3D, Cell 130(4) (2007) 601-610.
[8] E. Lozano, M. Segarra, A. García-Martínez, J. Hernández-Rodríguez, M.C. Cid, Imatinib mesylate inhibits in vitro and ex vivo biological responses related to vascular occlusion in giant cell arteritis, Annals of the Rheumatic Diseases 67(11) (2008) 1581-1588.
[9] A. Arslan-Yildiz, R. El Assal, P. Chen, S. Guven, F. Inci, U. Demirci, Towards artificial tissue models: past, present, and future of 3D bioprinting, Biofabrication 8(1) (2016) 1758-5090.
[10] E. Marangoni, A. Vincent-Salomon, N. Auger, A. Degeorges, F. Assayag, P. de Cremoux, L. de Plater, C. Guyader, G. De Pinieux, J.-G. Judde, M. Rebucci, C. Tran-Perennou, X. Sastre-Garau, B. Sigal-Zafrani, O. Delattre, V. Diéras, M.-F. Poupon, A New Model of Patient Tumor-Derived Breast Cancer Xenografts for Preclinical Assays, Clinical Cancer Research 13(13) (2007) 3989-3998.
[11] E.C. Costa, V.M. Gaspar, P. Coutinho, I.J. Correia, Optimization of liquid overlay technique to formulate heterogenic 3D co-cultures models, Biotechnol Bioeng 111(8) (2014) 1672-85.
[12] R. Foty, A Simple Hanging Drop Cell Culture Protocol for Generation of 3D Spheroids, Journal of Visualized Experiments : JoVE (51) (2011) 2720.
[13] Y. Markovitz-Bishitz, Y. Tauber, E. Afrimzon, N. Zurgil, M. Sobolev, Y. Shafran, A. Deutsch, S. Howitz, M. Deutsch, A polymer microstructure array for the formation, culturing, and high throughput drug screening of breast cancer spheroids, Biomaterials 31(32) (2010) 8436-44.
[14] N.S. Bhise, V. Manoharan, S. Massa, A. Tamayol, M. Ghaderi, M. Miscuglio, Q. Lang, Y. Shrike Zhang, S.R. Shin, G. Calzone, N. Annabi, T.D. Shupe, C.E. Bishop, A. Atala, M.R. Dokmeci, A. Khademhosseini, A liver-on-a-chip platform with bioprinted hepatic spheroids, Biofabrication 8(1) (2016) 1758-5090.
[15] P.A. Kenny, G.Y. Lee, C.A. Myers, R.M. Neve, J.R. Semeiks, P.T. Spellman, K. Lorenz, E.H. Lee, M.H. Barcellos-Hoff, O.W. Petersen, J.W. Gray, M.J. Bissell, The morphologies of breast cancer cell lines in three-dimensional assays correlate with their profiles of gene expression, Molecular oncology 1(1) (2007) 84-96.
[16] A.C. Luca, S. Mersch, R. Deenen, S. Schmidt, I. Messner, K.-L. Schäfer, S.E. Baldus, W. Huckenbeck, R.P. Piekorz, W.T. Knoefel, A. Krieg, N.H. Stoecklein, Impact of the 3D Microenvironment on Phenotype, Gene Expression, and EGFR Inhibition of Colorectal Cancer Cell Lines, PLoS One 8(3) (2013) e59689.
[17] V. Härmä, J. Virtanen, R. Mäkelä, A. Happonen, J.-P. Mpindi, M. Knuuttila, P. Kohonen, J. Lötjönen, O. Kallioniemi, M. Nees, A Comprehensive Panel of Three-Dimensional Models for Studies of Prostate Cancer Growth, Invasion and Drug Responses, PLoS One 5(5) (2010) e10431.
[18] J. Laurent, C. Frongia, M. Cazales, O. Mondesert, B. Ducommun, V. Lobjois, Multicellular tumor spheroid models to explore cell cycle checkpoints in 3D, BMC Cancer 13(1) (2013) 73.
[19] F. Hirschhaeuser, H. Menne, C. Dittfeld, J. West, W. Mueller-Klieser, L.A. Kunz-Schughart, Multicellular tumor spheroids: an underestimated tool is catching up again, J Biotechnol 148(1) (2010) 3-15.
[20] J. Liao, F. Qian, N. Tchabo, P. Mhawech-Fauceglia, A. Beck, Z. Qian, X. Wang, W.J. Huss, S.B. Lele, C.D. Morrison, K. Odunsi, Ovarian Cancer Spheroid Cells with Stem Cell-Like Properties

Contribute to Tumor Generation, Metastasis and Chemotherapy Resistance through Hypoxia-Resistant Metabolism, PLoS One 9(1) (2014) e84941.
[21] P. Longati, X. Jia, J. Eimer, A. Wagman, M.-R. Witt, S. Rehnmark, C. Verbeke, R. Toftgård, M. Löhr, R.L. Heuchel, 3D pancreatic carcinoma spheroids induce a matrix-rich, chemoresistant phenotype offering a better model for drug testing, BMC Cancer 13(1) (2013) 95.
[22] D. Herrmann, J.R.W. Conway, C. Vennin, A. Magenau, W.E. Hughes, J.P. Morton, P. Timpson, Three-dimensional cancer models mimic cell–matrix interactions in the tumour microenvironment, Carcinogenesis 35(8) (2014) 1671-1679.
[23] H. Dolznig, C. Rupp, C. Puri, C. Haslinger, N. Schweifer, E. Wieser, D. Kerjaschki, P. Garin-Chesa, Modeling colon adenocarcinomas in vitro a 3D co-culture system induces cancer-relevant pathways upon tumor cell and stromal fibroblast interaction, Am J Pathol 179 (2011).
[24] L. Bingle, C.E. Lewis, K.P. Corke, M.W.R. Reed, N.J. Brown, Macrophages promote angiogenesis in human breast tumour spheroids in vivo, British Journal of Cancer 94(1) (2006) 101-107.
[25] T.J. Bartosh, J.H. Ylostalo, A. Mohammadipoor, N. Bazhanov, K. Coble, K. Claypool, R.H. Lee, H. Choi, D.J. Prockop, Aggregation of human mesenchymal stromal cells (MSCs) into 3D spheroids enhances their antiinflammatory properties, Proc Natl Acad Sci U S A 107(31) (2010) 13724-9.
[26] I.A. Potapova, P.R. Brink, I.S. Cohen, S.V. Doronin, Culturing of human mesenchymal stem cells as three-dimensional aggregates induces functional expression of CXCR4 that regulates adhesion to endothelial cells, J Biol Chem 283(19) (2008) 13100-7.
[27] S.H. Bhang, S. Lee, J.Y. Shin, T.J. Lee, B.S. Kim, Transplantation of cord blood mesenchymal stem cells as spheroids enhances vascularization, Tissue Eng Part A 18(19-20) (2012) 2138-47.
[28] S.A. Ruiz, C.S. Chen, Emergence of patterned stem cell differentiation within multicellular structures, Stem Cells 26(11) (2008) 2921-7.
[29] D. Ma, L. Ren, Y. Liu, F. Chen, J. Zhang, Z. Xue, T. Mao, Engineering scaffold-free bone tissue using bone marrow stromal cell sheets, J Orthop Res 28(5) (2010) 697-702.
[30] A.A. Abdeen, J.B. Weiss, J. Lee, K.A. Kilian, Matrix composition and mechanics direct proangiogenic signaling from mesenchymal stem cells, Tissue Eng Part A 20(19-20) (2014) 2737-45.
[31] Y. Li, G. Guo, L. Li, F. Chen, J. Bao, Y.J. Shi, H. Bu, Three-dimensional spheroid culture of human umbilical cord mesenchymal stem cells promotes cell yield and stemness maintenance, Cell Tissue Res 360(2) (2015) 297-307.
[32] Y. Xu, T. Shi, A. Xu, L. Zhang, 3D spheroid culture enhances survival and therapeutic capacities of MSCs injected into ischemic kidney, J Cell Mol Med 20(7) (2016) 1203-13.
[33] P.J. Amos, S.K. Kapur, P.C. Stapor, H. Shang, S. Bekiranov, M. Khurgel, G.T. Rodeheaver, S.M. Peirce, A.J. Katz, Human adipose-derived stromal cells accelerate diabetic wound healing: impact of cell formulation and delivery, Tissue Eng Part A 16(5) (2010) 1595-606.
[34] F. Pampaloni, N. Ansari, E.H.K. Stelzer, High-resolution deep imaging of live cellular spheroids with light-sheet-based fluorescence microscopy, Cell and Tissue Research 352(1) (2013) 161-177.
[35] R.I. Dmitriev, S.M. Borisov, H. Düssmann, S. Sun, B.J. Müller, J. Prehn, V.P. Baklaushev, I. Klimant, D.B. Papkovsky, Versatile Conjugated Polymer Nanoparticles for High-Resolution O2 Imaging in Cells and 3D Tissue Models, ACS Nano 9(5) (2015) 5275-5288.
[36] J. Jenkins, S.M. Borisov, D.B. Papkovsky, R.I. Dmitriev, Sulforhodamine nanothermometer for multiparametric fluorescence lifetime imaging microscopy, Analytical chemistry 88(21) (2016) 10566-10572.
[37] K. König, A. Uchugonova, E. Gorjup, Multiphoton fluorescence lifetime imaging of 3D-stem cell spheroids during differentiation, Microscopy research and technique 74(1) (2011) 9-17.
[38] M.A. Lancaster, J.A. Knoblich, Organogenesis in a dish: Modeling development and disease using organoid technologies, Science 345(6194) (2014).
[39] M. Fujii, M. Matano, K. Nanki, T. Sato, Efficient genetic engineering of human intestinal organoids using electroporation, Nat Protoc 10(10) (2015) 1474-85.
[40] M. Takasato, P.X. Er, H.S. Chiu, B. Maier, G.J. Baillie, C. Ferguson, R.G. Parton, E.J. Wolvetang, M.S. Roost, S.M. Chuva de Sousa Lopes, M.H. Little, Kidney organoids from human iPS cells contain multiple lineages and model human nephrogenesis, Nature 526(7574) (2015) 564-568.
[41] M.A. Lancaster, M. Renner, C.-A. Martin, D. Wenzel, L.S. Bicknell, M.E. Hurles, T. Homfray, J.M. Penninger, A.P. Jackson, J.A. Knoblich, Cerebral organoids model human brain development and microcephaly, Nature 501(7467) (2013) 373-379.

[42] M. Völkner, M. Zschätzsch, M. Rostovskaya, Rupert W. Overall, V. Busskamp, K. Anastassiadis, Mike O. Karl, Retinal Organoids from Pluripotent Stem Cells Efficiently Recapitulate Retinogenesis, Stem Cell Reports 6(4) (2016) 525-538.
[43] K.W. McCracken, E.M. Cata, C.M. Crawford, K.L. Sinagoga, M. Schumacher, B.E. Rockich, Y.H. Tsai, C.N. Mayhew, J.R. Spence, Y. Zavros, J.M. Wells, Modelling human development and disease in pluripotent stem-cell-derived gastric organoids, Nature 516(7531) (2014) 400-4.
[44] B.R. Dye, D.R. Hill, M.A.H. Ferguson, Y.-H. Tsai, M.S. Nagy, R. Dyal, J.M. Wells, C.N. Mayhew, R. Nattiv, O.D. Klein, E.S. White, G.H. Deutsch, J.R. Spence, In vitro generation of human pluripotent stem cell derived lung organoids, eLife 4 (2015) e05098.
[45] K.R. Koehler, J. Nie, E. Longworth-Mills, X.-P. Liu, J. Lee, J.R. Holt, E. Hashino, Generation of inner ear organoids containing functional hair cells from human pluripotent stem cells, Nature biotechnology 35 (2017) 583.
[46] J. Lee, R. Böscke, P.-C. Tang, B.H. Hartman, S. Heller, K.R. Koehler, Hair Follicle Development in Mouse Pluripotent Stem Cell-Derived Skin Organoids, Cell Reports 22(1) (2018) 242-254.
[47] P. Guye, M.R. Ebrahimkhani, N. Kipniss, J.J. Velazquez, E. Schoenfeld, S. Kiani, L.G. Griffith, R. Weiss, Genetically engineering self-organization of human pluripotent stem cells into a liver bud-like tissue using Gata6, Nature Communications 7 (2016) 10243.
[48] E.L. Moreno, S. Hachi, K. Hemmer, S.J. Trietsch, A.S. Baumuratov, T. Hankemeier, P. Vulto, J.C. Schwamborn, R.M.T. Fleming, Differentiation of neuroepithelial stem cells into functional dopaminergic neurons in 3D microfluidic cell culture, Lab on a Chip 15(11) (2015) 2419-2428.
[49] A. Khademhosseini, G. Eng, J. Yeh, P.A. Kucharczyk, R. Langer, G. Vunjak-Novakovic, M. Radisic, Microfluidic patterning for fabrication of contractile cardiac organoids, Biomedical Microdevices 9(2) (2007) 149-157.
[50] M.J. Workman, M.M. Mahe, S. Trisno, H.M. Poling, C.L. Watson, N. Sundaram, C.-F. Chang, J. Schiesser, P. Aubert, E.G. Stanley, A.G. Elefanty, Y. Miyaoka, M.A. Mandegar, B.R. Conklin, M. Neunlist, S.A. Brugmann, M.A. Helmrath, J.M. Wells, Engineered human pluripotent-stem-cell-derived intestinal tissues with a functional enteric nervous system, Nat Med 23(1) (2017) 49-59.
[51] L. Huang, A. Holtzinger, I. Jagan, M. BeGora, I. Lohse, N. Ngai, C. Nostro, R. Wang, L.B. Muthuswamy, H.C. Crawford, C. Arrowsmith, S.E. Kalloger, D.J. Renouf, A.A. Connor, S. Cleary, D.F. Schaeffer, M. Roehrl, M.S. Tsao, S. Gallinger, G. Keller, S.K. Muthuswamy, Ductal pancreatic cancer modeling and drug screening using human pluripotent stem cell- and patient-derived tumor organoids, Nat Med 21(11) (2015) 1364-71.
[52] J. Drost, R.H. van Jaarsveld, B. Ponsioen, C. Zimberlin, R. van Boxtel, A. Buijs, N. Sachs, R.M. Overmeer, G.J. Offerhaus, H. Begthel, J. Korving, M. van de Wetering, G. Schwank, M. Logtenberg, E. Cuppen, H.J. Snippert, J.P. Medema, G.J.P.L. Kops, H. Clevers, Sequential cancer mutations in cultured human intestinal stem cells, Nature 521(7550) (2015) 43-47.
[53] I.A. Okkelman, R.I. Dmitriev, T. Foley, D.B. Papkovsky, Use of Fluorescence Lifetime Imaging Microscopy (FLIM) as a Timer of Cell Cycle S Phase, PLoS One 11(12) (2016) e0167385.
[54] A.J. Walsh, R.S. Cook, M.E. Sanders, L. Aurisicchio, G. Ciliberto, C.L. Arteaga, M.C. Skala, Quantitative optical imaging of primary tumor organoid metabolism predicts drug response in breast cancer, Cancer research 74(18) (2014) 5184-5194.
[55] M.W. Tibbitt, K.S. Anseth, Hydrogels as extracellular matrix mimics for 3D cell culture, Biotechnol Bioeng 103(4) (2009) 655-63.
[56] S.K.H. Gulrez, S. Al-Assaf, Hydrogels: Methods of Preparation, Characterisation and Applications, 2011.
[57] B. Meadhbh Á, R. Audrey, G. Anne-laure, D.A. Cyril, N. Steven, T. Valerie, L. Pierre, 3D cell culture and osteogenic differentiation of human bone marrow stromal cells plated onto jet-sprayed or electrospun micro-fiber scaffolds, Biomedical Materials 10(4) (2015) 045019.
[58] P. Danilevicius, L. Georgiadi, C.J. Pateman, F. Claeyssens, M. Chatzinikolaidou, M. Farsari, The effect of porosity on cell ingrowth into accurately defined, laser-made, polylactide-based 3D scaffolds, Applied Surface Science 336 (2015) 2-10.
[59] J. Jenkins, R.I. Dmitriev, K. Morten, K.W. McDermott, D.B. Papkovsky, Oxygen-sensing scaffolds for 3-dimensional cell and tissue culture, Acta Biomaterialia 16 (2015) 126-135.
[60] E.S. Place, J.H. George, C.K. Williams, M.M. Stevens, Synthetic polymer scaffolds for tissue engineering, Chemical Society Reviews 38(4) (2009) 1139-1151.

[61] M.D. Shoulders, R.T. Raines, COLLAGEN STRUCTURE AND STABILITY, Annual review of biochemistry 78 (2009) 929-958.
[62] V.V. Artym, K. Matsumoto, Imaging Cells in Three-Dimensional Collagen Matrix, Current protocols in cell biology / editorial board, Juan S. Bonifacino ... [et al.] CHAPTER (2010) Unit-10.1820.
[63] D.L. Holliday, K.T. Brouilette, A. Markert, L.A. Gordon, J.L. Jones, Novel multicellular organotypic models of normal and malignant breast: tools for dissecting the role of the microenvironment in breast cancer progression, Breast Cancer Res 11(1) (2009) 19.
[64] P.P. Provenzano, D.R. Inman, K.W. Eliceiri, J.G. Knittel, L. Yan, C.T. Rueden, J.G. White, P.J. Keely, Collagen density promotes mammary tumor initiation and progression, BMC medicine 6(1) (2008) 11.
[65] C.E. Barcus, P.J. Keely, K.W. Eliceiri, L.A. Schuler, Stiff collagen matrices increase tumorigenic prolactin signaling in breast cancer cells, Journal of Biological Chemistry 288(18) (2013) 12722-12732.
[66] C.E. Barcus, E.C. Holt, P.J. Keely, K.W. Eliceiri, L.A. Schuler, Dense Collagen-I Matrices Enhance Pro-Tumorigenic Estrogen-Prolactin Crosstalk in MCF-7 and T47D Breast Cancer Cells, PLoS One 10(1) (2015) e0116891.
[67] S. Joo, S.-H. Oh, S. Sittadjody, E.C. Opara, J.D. Jackson, S.J. Lee, J.J. Yoo, A. Atala, The effect of collagen hydrogel on 3D culture of ovarian follicles, Biomedical Materials 11(6) (2016) 065009.
[68] P.D. Yurchenco, Basement membranes: cell scaffoldings and signaling platforms, Cold Spring Harb Perspect Biol 3(2) (2011).
[69] H.K. Kleinman, G.R. Martin, Matrigel: basement membrane matrix with biological activity, Semin Cancer Biol 15(5) (2005) 378-86.
[70] G. Benton, H.K. Kleinman, J. George, I. Arnaoutova, Multiple uses of basement membrane-like matrix (BME/Matrigel) in vitro and in vivo with cancer cells, International Journal of Cancer 128(8) (2011) 1751-1757.
[71] K.J. Price, A. Tsykin, K.M. Giles, R.T. Sladic, M.R. Epis, R. Ganss, G.J. Goodall, P.J. Leedman, Matrigel Basement Membrane Matrix influences expression of microRNAs in cancer cell lines, Biochemical and Biophysical Research Communications 427(2) (2012) 343-348.
[72] M.E. Dolega, F. Abeille, N. Picollet-D'hahan, X. Gidrol, Controlled 3D culture in Matrigel microbeads to analyze clonal acinar development, Biomaterials 52 (2015) 347-357.
[73] I.A. Okkelman, T. Foley, D.B. Papkovsky, R.I. Dmitriev, Live cell imaging of mouse intestinal organoids reveals heterogeneity in their oxygenation, Biomaterials 146 (2017) 86-96.
[74] A. Nyga, U. Cheema, M. Loizidou, 3D tumour models: novel in vitro approaches to cancer studies, Journal of Cell Communication and Signaling 5(3) (2011) 239.
[75] T. Salo, M. Sutinen, E. Hoque Apu, E. Sundquist, N.K. Cervigne, C.E. de Oliveira, S.U. Akram, S. Ohlmeier, F. Suomi, L. Eklund, P. Juusela, P. Åström, C.C. Bitu, M. Santala, K. Savolainen, J. Korvala, A.F. Paes Leme, R.D. Coletta, A novel human leiomyoma tissue derived matrix for cell culture studies, BMC Cancer 15(1) (2015) 981.
[76] T. Abitbol, A. Rivkin, Y. Cao, Y. Nevo, E. Abraham, T. Ben-Shalom, S. Lapidot, O. Shoseyov, Nanocellulose, a tiny fiber with huge applications, Current opinion in biotechnology 39 (2016) 76-88.
[77] A.P.C. Almeida, J.P. Canejo, S.N. Fernandes, C. Echeverria, P.L. Almeida, M.H. Godinho, Cellulose-Based Biomimetics and Their Applications, Advanced Materials (2018) 1703655-n/a.
[78] D. Diekjürgen, D.W. Grainger, Polysaccharide matrices used in 3D in vitro cell culture systems, Biomaterials 141 (2017) 96-115.
[79] P.B. Malafaya, G.A. Silva, R.L. Reis, Natural–origin polymers as carriers and scaffolds for biomolecules and cell delivery in tissue engineering applications, Advanced drug delivery reviews 59(4) (2007) 207-233.
[80] A. Svensson, E. Nicklasson, T. Harrah, B. Panilaitis, D. Kaplan, M. Brittberg, P. Gatenholm, Bacterial cellulose as a potential scaffold for tissue engineering of cartilage, Biomaterials 26(4) (2005) 419-431.
[81] C. Demitri, M.G. Raucci, A. Giuri, V.M. De Benedictis, D. Giugliano, P. Calcagnile, A. Sannino, L. Ambrosio, Cellulose-based porous scaffold for bone tissue engineering applications: Assessment of hMSC proliferation and differentiation, Journal of Biomedical Materials Research Part A 104(3) (2016) 726-733.

[82] G. Feil, R. Horres, J. Schulte, A.F. Mack, S. Petzoldt, C. Arnold, C. Meng, L. Jost, J. Boxleitner, N. Kiessling-Wolf, Bacterial cellulose shifts transcriptome and proteome of cultured endothelial cells towards native differentiation, Molecular & Cellular Proteomics 16(9) (2017) 1563-1577.
[83] M. Pääkkö, M. Ankerfors, H. Kosonen, A. Nykänen, S. Ahola, M. Österberg, J. Ruokolainen, J. Laine, P.T. Larsson, O. Ikkala, T. Lindström, Enzymatic Hydrolysis Combined with Mechanical Shearing and High-Pressure Homogenization for Nanoscale Cellulose Fibrils and Strong Gels, Biomacromolecules 8(6) (2007) 1934-1941.
[84] Y.R. Lou, L. Kanninen, T. Kuisma, J. Niklander, L.A. Noon, D. Burks, A. Urtti, M. Yliperttula, The use of nanofibrillar cellulose hydrogel as a flexible three-dimensional model to culture human pluripotent stem cells, Stem Cells Dev 23(4) (2014) 380-92.
[85] M.M. Malinen, L.K. Kanninen, A. Corlu, H.M. Isoniemi, Y.-R. Lou, M.L. Yliperttula, A.O. Urtti, Differentiation of liver progenitor cell line to functional organotypic cultures in 3D nanofibrillar cellulose and hyaluronan-gelatin hydrogels, Biomaterials 35(19) (2014) 5110-5121.
[86] P. Ross, R. Mayer, M. Benziman, Cellulose biosynthesis and function in bacteria, Microbiol Rev 55(1) (1991) 35-58.
[87] J. Andersson, H. Stenhamre, H. Backdahl, P. Gatenholm, Behavior of human chondrocytes in engineered porous bacterial cellulose scaffolds, J Biomed Mater Res A 94(4) (2010) 1124-32.
[88] H. Ahrem, D. Pretzel, M. Endres, D. Conrad, J. Courseau, H. Müller, R. Jaeger, C. Kaps, D.O. Klemm, R.W. Kinne, Laser-structured bacterial nanocellulose hydrogels support ingrowth and differentiation of chondrocytes and show potential as cartilage implants, Acta Biomaterialia 10(3) (2014) 1341-1353.
[89] C. Weber, S. Reinhardt, K. Eghbalzadeh, M. Wacker, M. Guschlbauer, A. Maul, A. Sterner-Kock, T. Wahlers, J. Wippermann, M. Scherner, Patency and in vivo compatibility of bacterial nanocellulose grafts as small-diameter vascular substitute, Journal of vascular surgery (2017).
[90] J.R. Gershlak, S. Hernandez, G. Fontana, L.R. Perreault, K.J. Hansen, S.A. Larson, B.Y.K. Binder, D.M. Dolivo, T. Yang, T. Dominko, M.W. Rolle, P.J. Weathers, F. Medina-Bolivar, C.L. Cramer, W.L. Murphy, G.R. Gaudette, Crossing kingdoms: Using decellularized plants as perfusable tissue engineering scaffolds, Biomaterials 125 (2017) 13-22.
[91] P.B. Malafaya, G.A. Silva, R.L. Reis, Natural-origin polymers as carriers and scaffolds for biomolecules and cell delivery in tissue engineering applications, Adv Drug Deliv Rev 59(4-5) (2007) 207-33.
[92] T. Consolati, J.M. Bolivar, Z. Petrasek, J. Berenguer, A. Hidalgo, J.M. Guisan, B. Nidetzky, Biobased, Internally pH-Sensitive Materials: Immobilized Yellow Fluorescent Protein as an Optical Sensor for Spatiotemporal Mapping of pH Inside Porous Matrices, ACS Appl Mater Interfaces 10(8) (2018) 6858-6868.
[93] W. Thongsomboon, D.O. Serra, A. Possling, C. Hadjineophytou, R. Hengge, L. Cegelski, Phosphoethanolamine cellulose: A naturally produced chemically modified cellulose, Science 359(6373) (2018) 334-338.
[94] B. Schyrr, S. Pasche, G. Voirin, C. Weder, Y.C. Simon, E.J. Foster, Biosensors Based on Porous Cellulose Nanocrystal–Poly(vinyl Alcohol) Scaffolds, ACS Applied Materials & Interfaces 6(15) (2014) 12674-12683.
[95] A. Almeida, A.M.M. Rosa, A.M. Azevedo, D.M.F. Prazeres, A biomolecular recognition approach for the functionalization of cellulose with gold nanoparticles, Journal of Molecular Recognition 30(9) (2017) e2634-n/a.
[96] J.E. Hyeon, S.K. Shin, S.O. Han, Design of nanoscale enzyme complexes based on various scaffolding materials for biomass conversion and immobilization, Biotechnology Journal 11(11) (2016) 1386-1396.
[97] X. Meng, K.J. Edgar, "Click" reactions in polysaccharide modification, Progress in Polymer Science 53 (2016) 52-85.
[98] J.R.G. Navarro, G. Conzatti, Y. Yu, A.B. Fall, R. Mathew, M. Edén, L. Bergström, Multicolor Fluorescent Labeling of Cellulose Nanofibrils by Click Chemistry, Biomacromolecules 16(4) (2015) 1293-1300.
[99] J.R.G. Navarro, S. Wennmalm, J. Godfrey, M. Breitholtz, U. Edlund, Luminescent Nanocellulose Platform: From Controlled Graft Block Copolymerization to Biomarker Sensing, Biomacromolecules 17(3) (2016) 1101-1109.

[100] C.P. Radano, G.L. Baker, M.R. Smith, Stereoselective Polymerization of a Racemic Monomer with a Racemic Catalyst: Direct Preparation of the Polylactic Acid Stereocomplex from Racemic Lactide, Journal of the American Chemical Society 122(7) (2000) 1552-1553.
[101] H.T. Oyama, Y. Tanaka, A. Kadosaka, Rapid controlled hydrolytic degradation of poly(l-lactic acid) by blending with poly(aspartic acid-co-l-lactide), Polymer Degradation and Stability 94(9) (2009) 1419-1426.
[102] R. Tong, J. Cheng, Paclitaxel-Initiated, Controlled Polymerization of Lactide for the Formulation of Polymeric Nanoparticulate Delivery Vehicles, Angewandte Chemie 120(26) (2008) 4908-4912.
[103] R. Tong, J. Cheng, Ring-Opening Polymerization-Mediated Controlled Formulation of Polylactide− Drug Nanoparticles, Journal of the American Chemical Society 131(13) (2009) 4744-4754.
[104] J. Azzi, L. Tang, R. Moore, R. Tong, N. El Haddad, T. Akiyoshi, B. Mfarrej, S. Yang, M. Jurewicz, T. Ichimura, Polylactide-cyclosporin A nanoparticles for targeted immunosuppression, The FASEB Journal 24(10) (2010) 3927-3938.
[105] G. Vergnol, N. Ginsac, P. Rivory, S. Meille, J.M. Chenal, S. Balvay, J. Chevalier, D.J. Hartmann, In vitro and in vivo evaluation of a polylactic acid-bioactive glass composite for bone fixation devices, Journal of Biomedical Materials Research Part B: Applied Biomaterials 104(1) (2016) 180-191.
[106] S. Kaihara, S. Matsumura, A.G. Mikos, J.P. Fisher, Synthesis of poly(L-lactide) and polyglycolide by ring-opening polymerization, Nature Protocols 2 (2007) 2767.
[107] G. Bernardini, F. Chellini, B. Frediani, A. Spreafico, A. Santucci, Human platelet releasates combined with polyglycolic acid scaffold promote chondrocyte differentiation and phenotypic maintenance, Journal of biosciences 40(1) (2015) 61-69.
[108] E.D. Boland, G.E. Wnek, D.G. Simpson, K.J. Pawlowski, G.L. Bowlin, Tailoring tissue engineering scaffolds using electrostatic processing techniques: a study of poly (glycolic acid) electrospinning, Journal of Macromolecular Science, Part A 38(12) (2001) 1231-1243.
[109] L. Wang, N.H. Dormer, L.F. Bonewald, M.S. Detamore, Osteogenic differentiation of human umbilical cord mesenchymal stromal cells in polyglycolic acid scaffolds, Tissue Eng Part A 16(6) (2010) 1937-48.
[110] P. Gentile, V. Chiono, I. Carmagnola, P.V. Hatton, An overview of poly (lactic-co-glycolic) acid (PLGA)-based biomaterials for bone tissue engineering, International journal of molecular sciences 15(3) (2014) 3640-3659.
[111] H. Kobayashi, D. Terada, Y. Yokoyama, D.W. Moon, Y. Yasuda, H. Koyama, T. Takato, Vascular-inducing poly (glycolic acid)-collagen nanocomposite-fiber scaffold, Journal of biomedical nanotechnology 9(8) (2013) 1318-1326.
[112] A. Abbushi, M. Endres, M. Cabraja, S.N. Kroppenstedt, U.W. Thomale, M. Sittinger, A.A. Hegewald, L. Morawietz, A.-J. Lemke, V.-G. Bansemer, C. Kaps, C. Woiciechowsky, Regeneration of Intervertebral Disc Tissue by Resorbable Cell-Free Polyglycolic Acid-Based Implants in a Rabbit Model of Disc Degeneration, Spine 33(14) (2008) 1527-1532.
[113] M. Labet, W. Thielemans, Synthesis of polycaprolactone: a review, Chemical Society Reviews 38(12) (2009) 3484-3504.
[114] X. Wei, C. Gong, M. Gou, S. Fu, Q. Guo, S. Shi, F. Luo, G. Guo, L. Qiu, Z. Qian, Biodegradable poly(ε-caprolactone)–poly(ethylene glycol) copolymers as drug delivery system, International journal of pharmaceutics 381(1) (2009) 1-18.
[115] K. Lam, J. Schakenraad, H. Esselbrugge, J. Feijen, P. Nieuwenhuis, The effect of phagocytosis of poly (L-lactic acid) fragments on cellular morphology and viability, Journal of Biomedical Materials Research Part A 27(12) (1993) 1569-1577.
[116] H.-J. Sung, C. Meredith, C. Johnson, Z.S. Galis, The effect of scaffold degradation rate on three-dimensional cell growth and angiogenesis, Biomaterials 25(26) (2004) 5735-5742.
[117] Y. Ramot, M. Haim-Zada, A.J. Domb, A. Nyska, Biocompatibility and safety of PLA and its copolymers, Advanced Drug Delivery Reviews 107 (2016) 153-162.
[118] K. Fu, D.W. Pack, A.M. Klibanov, R. Langer, Visual Evidence of Acidic Environment Within Degrading Poly(lactic-co-glycolic acid) (PLGA) Microspheres, Pharmaceutical Research 17(1) (2000) 100-106.

[119] H. Nakahara, H. Misawa, A. Yoshida, T. Hayashi, M. Tanaka, T. Furumatsu, N. Tanaka, N. Kobayashi, T. Ozaki, Bone repair using a hybrid scaffold of self-assembling peptide PuraMatrix and polyetheretherketone cage in rats, Cell Transplant 19(6) (2010) 791-7.
[120] N. Kawazoe, C. Inoue, T. Tateishi, G. Chen, A cell leakproof PLGA-collagen hybrid scaffold for cartilage tissue engineering, Biotechnol Prog 26(3) (2010) 819-26.
[121] V. van Duinen, S.J. Trietsch, J. Joore, P. Vulto, T. Hankemeier, Microfluidic 3D cell culture: from tools to tissue models, Current Opinion in Biotechnology 35 (2015) 118-126.
[122] J.S. Jeon, S. Bersini, M. Gilardi, G. Dubini, J.L. Charest, M. Moretti, R.D. Kamm, Human 3D vascularized organotypic microfluidic assays to study breast cancer cell extravasation, Proc Natl Acad Sci U S A 112(1) (2015) 214-9.
[123] S.N. Bhatia, D.E. Ingber, Microfluidic organs-on-chips, Nat Biotech 32(8) (2014) 760-772.
[124] J.R. Anderson, D.T. Chiu, H. Wu, O. Schueller, G.M. Whitesides, Fabrication of microfluidic systems in poly (dimethylsiloxane), Electrophoresis 21(1) (2000) 27-40.
[125] A.Y. Hsiao, Y.-s. Torisawa, Y.-C. Tung, S. Sud, R.S. Taichman, K.J. Pienta, S. Takayama, Microfluidic system for formation of PC-3 prostate cancer co-culture spheroids, Biomaterials 30(16) (2009) 3020-3027.
[126] A. Piruska, I. Nikcevic, S.H. Lee, C. Ahn, W.R. Heineman, P.A. Limbach, C.J. Seliskar, The autofluorescence of plastic materials and chips measured under laser irradiation, Lab Chip 5(12) (2005) 1348-54.
[127] S.H. Au, M.D. Chamberlain, S. Mahesh, M.V. Sefton, A.R. Wheeler, Hepatic organoids for microfluidic drug screening, Lab on a Chip 14(17) (2014) 3290-3299.
[128] H.J. Kim, D.E. Ingber, Gut-on-a-Chip microenvironment induces human intestinal cells to undergo villus differentiation, Integr Biol 5(9) (2013) 1130-40.
[129] H.J. Kim, D. Huh, G. Hamilton, D.E. Ingber, Human gut-on-a-chip inhabited by microbial flora that experiences intestinal peristalsis-like motions and flow, Lab Chip 12(12) (2012) 2165-74.
[130] K.H. Benam, R. Villenave, C. Lucchesi, A. Varone, C. Hubeau, H.-H. Lee, S.E. Alves, M. Salmon, T.C. Ferrante, J.C. Weaver, A. Bahinski, G.A. Hamilton, D.E. Ingber, Small airway-on-a-chip enables analysis of human lung inflammation and drug responses in vitro, Nat Meth 13(2) (2016) 151-157.
[131] D. Huh, B.D. Matthews, A. Mammoto, M. Montoya-Zavala, H.Y. Hsin, D.E. Ingber, Reconstituting organ-level lung functions on a chip, Science 328(5986) (2010) 1662-8.
[132] A. Grosberg, P.W. Alford, M.L. McCain, K.K. Parker, Ensembles of engineered cardiac tissues for physiological and pharmacological study: heart on a chip, Lab Chip 11(24) (2011) 4165-73.
[133] A. Agarwal, J.A. Goss, A. Cho, M.L. McCain, K.K. Parker, Microfluidic heart on a chip for higher throughput pharmacological studies, Lab Chip 13(18) (2013) 3599-608.
[134] T.T. Nieskens, M.J. Wilmer, Kidney-on-a-chip technology for renal proximal tubule tissue reconstruction, Eur J Pharmacol 790 (2016) 46-56.
[135] M.J. Wilmer, C.P. Ng, H.L. Lanz, P. Vulto, L. Suter-Dick, R. Masereeuw, Kidney-on-a-Chip Technology for Drug-Induced Nephrotoxicity Screening, Trends in Biotechnology 34(2) (2016) 156-170.
[136] E.W.K. Young, M.W.L. Watson, S. Srigunapalan, A.R. Wheeler, C.A. Simmons, Technique for Real-Time Measurements of Endothelial Permeability in a Microfluidic Membrane Chip Using Laser-Induced Fluorescence Detection, Analytical Chemistry 82(3) (2010) 808-816.
[137] H. Ryu, S. Oh, H.J. Lee, J.Y. Lee, H.K. Lee, N.L. Jeon, Engineering a Blood Vessel Network Module for Body-on-a-Chip Applications, Journal of Laboratory Automation 20(3) (2015) 296-301.
[138] S. Kim, H. Lee, M. Chung, N.L. Jeon, Engineering of functional, perfusable 3D microvascular networks on a chip, Lab on a Chip 13(8) (2013) 1489-1500.
[139] M.W. van der Helm, A.D. van der Meer, J.C.T. Eijkel, A. van den Berg, L.I. Segerink, Microfluidic organ-on-chip technology for blood-brain barrier research, Tissue Barriers 4(1) (2016) e1142493.
[140] K.H. Benam, S. Dauth, B. Hassell, A. Herland, A. Jain, K.-J. Jang, K. Karalis, H.J. Kim, L. MacQueen, R. Mahmoodian, Engineered in vitro disease models, Annual Review of Pathology: Mechanisms of Disease 10 (2015) 195-262.
[141] E.W. Esch, A. Bahinski, D. Huh, Organs-on-chips at the frontiers of drug discovery, Nat Rev Drug Discov 14(4) (2015) 248-260.

[142] A.V. Kondrashina, D.B. Papkovsky, R.I. Dmitriev, Measurement of cell respiration and oxygenation in standard multichannel biochips using phosphorescent O2-sensitive probes, Analyst 138(17) (2013) 4915-4921.
[143] J.P. Wikswo, I. F. E. Block, D.E. Cliffel, C.R. Goodwin, C.C. Marasco, D.A. Markov, D.L. McLean, J.A. McLean, J.R. McKenzie, R.S. Reiserer, P.C. Samson, D.K. Schaffer, K.T. Seale, S.D. Sherrod, Engineering Challenges for Instrumenting and Controlling Integrated Organ-on-Chip Systems, IEEE Transactions on Biomedical Engineering 60(3) (2013) 682-690.
[144] S.V. Murphy, A. Atala, 3D bioprinting of tissues and organs, Nat Biotech 32(8) (2014) 773-785.
[145] A. Nadernezhad, N. Khani, G.A. Skvortsov, B. Toprakhisar, E. Bakirci, Y. Menceloglu, S. Unal, B. Koc, Multifunctional 3D printing of heterogeneous hydrogel structures, Sci Rep 6(33178) (2016).
[146] V.K. Lee, A.M. Lanzi, N. Haygan, S.-S. Yoo, P.A. Vincent, G. Dai, Generation of Multi-Scale Vascular Network System within 3D Hydrogel using 3D Bio-Printing Technology, Cellular and molecular bioengineering 7(3) (2014) 460-472.
[147] J.W. Jung, J.-S. Lee, D.-W. Cho, Computer-aided multiple-head 3D printing system for printing of heterogeneous organ/tissue constructs, Scientific Reports 6 (2016) 21685.
[148] Y. Zhao, R. Yao, L. Ouyang, H. Ding, T. Zhang, K. Zhang, S. Cheng, W. Sun, Three-dimensional printing of Hela cells for cervical tumor model in vitro, Biofabrication 6(3) (2014) 1758-5082.
[149] Y.J. Seol, H.W. Kang, S.J. Lee, A. Atala, J.J. Yoo, Bioprinting technology and its applications, Eur J Cardiothorac Surg 46(3) (2014) 342-8.
[150] X. Cui, T. Boland, D.D. D'Lima, M.K. Lotz, Thermal inkjet printing in tissue engineering and regenerative medicine, Recent Pat Drug Deliv Formul 6(2) (2012) 149-55.
[151] H. Gudapati, M. Dey, I. Ozbolat, A comprehensive review on droplet-based bioprinting: Past, present and future, Biomaterials 102 (2016) 20-42.
[152] F. Guillemot, A. Souquet, S. Catros, B. Guillotin, J. Lopez, M. Faucon, B. Pippenger, R. Bareille, M. Remy, S. Bellance, P. Chabassier, J.C. Fricain, J. Amedee, High-throughput laser printing of cells and biomaterials for tissue engineering, Acta Biomater 6(7) (2010) 2494-500.
[153] W. Lee, J.C. Debasitis, V.K. Lee, J.H. Lee, K. Fischer, K. Edminster, J.K. Park, S.S. Yoo, Multi-layered culture of human skin fibroblasts and keratinocytes through three-dimensional freeform fabrication, Biomaterials 30(8) (2009) 1587-95.
[154] X. Cui, T. Boland, Human microvasculature fabrication using thermal inkjet printing technology, Biomaterials 30(31) (2009) 6221-7.
[155] J. Malda, J. Visser, F.P. Melchels, T. Jungst, W.E. Hennink, W.J. Dhert, J. Groll, D.W. Hutmacher, 25th anniversary article: Engineering hydrogels for biofabrication, Adv Mater 25(36) (2013) 5011-28.
[156] B. Duan, L.A. Hockaday, K.H. Kang, J.T. Butcher, 3D bioprinting of heterogeneous aortic valve conduits with alginate/gelatin hydrogels, J Biomed Mater Res A 101(5) (2013) 1255-64.
[157] R. Chang, J. Nam, W. Sun, Effects of dispensing pressure and nozzle diameter on cell survival from solid freeform fabrication–based direct cell writing, Tissue Engineering Part A 14(1) (2008) 41-48.
[158] L.A. Hockaday, K.H. Kang, N.W. Colangelo, P.Y. Cheung, B. Duan, E. Malone, J. Wu, L.N. Girardi, L.J. Bonassar, H. Lipson, C.C. Chu, J.T. Butcher, Rapid 3D printing of anatomically accurate and mechanically heterogeneous aortic valve hydrogel scaffolds, Biofabrication 4(3) (2012) 1758-5082.
[159] N. Gjorevski, N. Sachs, A. Manfrin, S. Giger, M.E. Bragina, P. Ordóñez-Morán, H. Clevers, M.P. Lutolf, Designer matrices for intestinal stem cell and organoid culture, Nature 539(7630) (2016) 560-564.
[160] N. Sachs, Y. Tsukamoto, P. Kujala, P.J. Peters, H. Clevers, Intestinal epithelial organoids fuse to form self-organizing tubes in floating collagen gels, Development 144(6) (2017) 1107-1112.
[161] L.E. Jamieson, D.J. Harrison, C.J. Campbell, Chemical analysis of multicellular tumour spheroids, Analyst 140(12) (2015) 3910-3920.
[162] M. Quaranta, S.M. Borisov, I. Klimant, Indicators for optical oxygen sensors, Bioanalytical Reviews 4(2) (2012) 115-157.
[163] M.Y. Berezin, S. Achilefu, Fluorescence Lifetime Measurements and Biological Imaging, Chemical Reviews 110(5) (2010) 2641-2684.
[164] J. Swoger, F. Pampaloni, E.H. Stelzer, Light-sheet-based fluorescence microscopy for three-dimensional imaging of biological samples, Cold Spring Harb Protoc 1(1) (2014) 1-8.

[165] F. Helmchen, W. Denk, Deep tissue two-photon microscopy, Nat Methods 2(12) (2005) 932-40.
[166] R.K.P. Benninger, D.W. Piston, Two-Photon Excitation Microscopy for the Study of Living Cells and Tissues, Current Protocols in Cell Biology, John Wiley & Sons, Inc.2001.
[167] A. Hopt, E. Neher, Highly nonlinear photodamage in two-photon fluorescence microscopy, Biophysical Journal 80(4) (2001) 2029-2036.
[168] A. Ustione, D.W. Piston, A simple introduction to multiphoton microscopy, Journal of Microscopy 243(3) (2011) 221-226.
[169] G.H. Patterson, D.W. Piston, Photobleaching in two-photon excitation microscopy, Biophysical Journal 78(4) (2000) 2159-2162.
[170] J. Huisken, J. Swoger, F. Del Bene, J. Wittbrodt, E.H.K. Stelzer, Optical Sectioning Deep Inside Live Embryos by Selective Plane Illumination Microscopy, Science 305(5686) (2004) 1007-1009.
[171] P.A. Santi, Light Sheet Fluorescence Microscopy, Journal of Histochemistry & Cytochemistry 59(2) (2011) 129-138.
[172] F. Cella Zanacchi, Z. Lavagnino, M. Perrone Donnorso, A. Del Bue, L. Furia, M. Faretta, A. Diaspro, Live-cell 3D super-resolution imaging in thick biological samples, Nat Meth 8(12) (2011) 1047-1049.
[173] B. Patra, Y.S. Peng, C.C. Peng, W.H. Liao, Y.A. Chen, K.H. Lin, Y.C. Tung, C.H. Lee, Migration and vascular lumen formation of endothelial cells in cancer cell spheroids of various sizes, Biomicrofluidics 8(5) (2014).
[174] V. Marx, Microscopy: OpenSPIM 2.0, Nat Meth 13(12) (2016) 979-982.
[175] S.W. Hell, Far-Field Optical Nanoscopy, Science 316(5828) (2007) 1153-1158.
[176] L.M. Hirvonen, K. Wicker, O. Mandula, R. Heintzmann, Structured illumination microscopy of a living cell, European Biophysics Journal 38(6) (2009) 807-812.
[177] M.G.L. Gustafsson, L. Shao, P.M. Carlton, C.J.R. Wang, I.N. Golubovskaya, W.Z. Cande, D.A. Agard, J.W. Sedat, Three-Dimensional Resolution Doubling in Wide-Field Fluorescence Microscopy by Structured Illumination, Biophysical Journal 94(12) (2008) 4957-4970.
[178] M.J. Rust, M. Bates, X. Zhuang, Sub-diffraction-limit imaging by stochastic optical reconstruction microscopy (STORM), Nat Meth 3(10) (2006) 793-796.
[179] S. van de Linde, A. Loschberger, T. Klein, M. Heidbreder, S. Wolter, M. Heilemann, M. Sauer, Direct stochastic optical reconstruction microscopy with standard fluorescent probes, Nat. Protocols 6(7) (2011) 991-1009.
[180] S.T. Hess, T.P.K. Girirajan, M.D. Mason, Ultra-High Resolution Imaging by Fluorescence Photoactivation Localization Microscopy, Biophysical Journal 91(11) (2006) 4258-4272.
[181] T.A. Klar, S. Jakobs, M. Dyba, A. Egner, S.W. Hell, Fluorescence microscopy with diffraction resolution barrier broken by stimulated emission, Proceedings of the National Academy of Sciences of the United States of America 97(15) (2000) 8206-8210.
[182] Kevin T. Takasaki, Jun B. Ding, Bernardo L. Sabatini, Live-Cell Superresolution Imaging by Pulsed STED Two-Photon Excitation Microscopy, Biophysical Journal 104(4) (2013) 770-777.
[183] E.A. Specht, E. Braselmann, A.E. Palmer, A Critical and Comparative Review of Fluorescent Tools for Live Cell Imaging, Annual Review of Physiology (0) (2016).
[184] T. Niehorster, A. Loschberger, I. Gregor, B. Kramer, H.-J. Rahn, M. Patting, F. Koberling, J. Enderlein, M. Sauer, Multi-target spectrally resolved fluorescence lifetime imaging microscopy, Nat Meth 13(3) (2016) 257-262.
[185] L. Giordano, V.V. Shvadchak, J.A. Fauerbach, E.A. Jares-Erijman, T.M. Jovin, Highly Solvatochromic 7-Aryl-3-hydroxychromones, The Journal of Physical Chemistry Letters 3(8) (2012) 1011-1016.
[186] V.I. Shcheslavskiy, A. Neubauer, R. Bukowiecki, F. Dinter, W. Becker, Combined fluorescence and phosphorescence lifetime imaging, Applied Physics Letters 108(9) (2016) 091111.
[187] D.B. Papkovsky, R.I. Dmitriev, Biological detection by optical oxygen sensing, Chemical Society Reviews 42(22) (2013) 8700-8732.
[188] L.M. Hirvonen, M. Fisher-Levine, K. Suhling, A. Nomerotski, Photon counting phosphorescence lifetime imaging with TimepixCam, Review of Scientific Instruments 88(1) (2017) 013104.
[189] W. Becker, Fluorescence lifetime imaging--techniques and applications, J Microsc 247(2) (2012) 119-36.

[190] D.S. Bilan, V.V. Belousov, New tools for redox biology: From imaging to manipulation, Free Radical Biology and Medicine 109 (2017) 167-188.
[191] K. Apel, H. Hirt, REACTIVE OXYGEN SPECIES: Metabolism, Oxidative Stress, and Signal Transduction, Annual Review of Plant Biology 55(1) (2004) 373-399.
[192] D.M. Chudakov, S. Lukyanov, K.A. Lukyanov, Fluorescent proteins as a toolkit for in vivo imaging, Trends in Biotechnology 23(12) (2005) 605-613.
[193] A.S. Mishin, V.V. Belousov, K.M. Solntsev, K.A. Lukyanov, Novel uses of fluorescent proteins, Current opinion in chemical biology 27 (2015) 1-9.
[194] O.S. Wolfbeis, An overview of nanoparticles commonly used in fluorescent bioimaging, Chem Soc Rev 44(14) (2015) 4743-68.
[195] R. Nothdurft, P. Sarder, S. Bloch, J. Culver, S. Achilefu, Fluorescence lifetime imaging microscopy using near-infrared contrast agents, Journal of Microscopy 247(2) (2012) 202-207.
[196] R.I. Dmitriev, A.V. Kondrashina, K. Koren, I. Klimant, A.V. Zhdanov, J.M. Pakan, K.W. McDermott, D.B. Papkovsky, Small molecule phosphorescent probes for O 2 imaging in 3D tissue models, Biomaterials Science 2(6) (2014) 853-866.
[197] N. O'Donnell, R.I. Dmitriev, Three-dimensional tissue models and available probes for multi-parametric live cell microscopy: a brief overview, Multi-Parametric Live Cell Microscopy of 3D Tissue Models, Springer2017, pp. 49-67.
[198] N. Ma, M.A. Digman, L. Malacrida, E. Gratton, Measurements of absolute concentrations of NADH in cells using the phasor FLIM method, Biomedical Optics Express 7(7) (2016) 2441-2452.
[199] T.S. Blacker, M.R. Duchen, Investigating mitochondrial redox state using NADH and NADPH autofluorescence, Free Radical Biology and Medicine 100 (2016) 53-65.
[200] T.M. Cannon, A.T. Shah, M.C. Skala, Autofluorescence imaging captures heterogeneous drug response differences between 2D and 3D breast cancer cultures, Biomedical Optics Express 8(3) (2017) 1911-1925.
[201] R. Mongeon, V. Venkatachalam, G. Yellen, Cytosolic NADH-NAD(+) Redox Visualized in Brain Slices by Two-Photon Fluorescence Lifetime Biosensor Imaging, Antioxid Redox Signal 25(10) (2016) 553-63.
[202] K.C. Wagener, B. Kolbrink, K. Dietrich, K.M. Kizina, L.S. Terwitte, B. Kempkes, G. Bao, M. Müller, Redox Indicator Mice Stably Expressing Genetically Encoded Neuronal roGFP: Versatile Tools to Decipher Subcellular Redox Dynamics in Neuropathophysiology, Antioxidants & Redox Signaling 25(1) (2016) 41-58.
[203] R.I. Dmitriev, D.B. Papkovsky, Intracellular probes for imaging oxygen concentration: how good are they?, Methods and Applications in Fluorescence 3(3) (2015) 034001.
[204] R.I. Dmitriev, I.A. Okkelman, T. Foley, D.B. Papkovsky, Live cell microscopy of intestinal organoid oxygenation, The FASEB Journal 31(1 Supplement) (2017) 590.1.
[205] A.V. Zhdanov, I.A. Okkelman, A.V. Golubeva, B. Doerr, N.P. Hyland, S. Melgar, F. Shanahan, J.F. Cryan, D.B. Papkovsky, Quantitative analysis of mucosal oxygenation using ex vivo imaging of healthy and inflamed mammalian colon tissue, Cellular and Molecular Life Sciences 74(1) (2017) 141-151.
[206] A.V. Zhdanov, A.V. Golubeva, I.A. Okkelman, J.F. Cryan, D.B. Papkovsky, Imaging of oxygen gradients in giant umbrella cells: an ex vivo PLIM study, American Journal of Physiology - Cell Physiology 309(7) (2015) C501-C509.
[207] R.I. Dmitriev, D.B. Papkovsky, Multi-parametric O2 Imaging in Three-Dimensional Neural Cell Models with the Phosphorescent Probes, in: L. Lossi, A. Merighi (Eds.), Neuronal Cell Death: Methods and Protocols, Springer New York, New York, NY, 2015, pp. 55-71.
[208] A.V. Zhdanov, I.A. Okkelman, F.W.J. Collins, S. Melgar, D.B. Papkovsky, A novel effect of DMOG on cell metabolism: direct inhibition of mitochondrial function precedes HIF target gene expression, Biochimica et Biophysica Acta (BBA) - Bioenergetics 1847(10) (2015) 1254-1266.
[209] E. Roussakis, Z. Li, A.J. Nichols, C.L. Evans, Oxygen-Sensing Methods in Biomedicine from the Macroscale to the Microscale, Angewandte Chemie International Edition 54(29) (2015) 8340-8362.
[210] G. Yazgan, R.I. Dmitriev, V. Tyagi, J. Jenkins, G.-M. Rotaru, M. Rottmar, R.M. Rossi, C. Toncelli, D.B. Papkovsky, K. Maniura-Weber, G. Fortunato, Steering surface topographies of electrospun fibers: understanding the mechanisms, Scientific Reports 7(1) (2017) 158.

[211] J. Jenkins, S.M. Borisov, D.B. Papkovsky, R.I. Dmitriev, Sulforhodamine nanothermometer for multi-parametric FLIM imaging, Analytical Chemistry (2016).
[212] S. Poëa-Guyon, H. Pasquier, F. Mérola, N. Morel, M. Erard, The enhanced cyan fluorescent protein: a sensitive pH sensor for fluorescence lifetime imaging, Analytical and bioanalytical chemistry 405(12) (2013) 3983-3987.
[213] M. Tantama, Y.P. Hung, G. Yellen, Imaging Intracellular pH in Live Cells with a Genetically-Encoded Red Fluorescent Protein Sensor, Journal of the American Chemical Society 133(26) (2011) 10034-10037.
[214] D. Aigner, R. Dmitriev, S. Borisov, D. Papkovsky, I. Klimant, pH-sensitive perylene bisimide probes for live cell fluorescence lifetime imaging, Journal of Materials Chemistry B 2(39) (2014) 6792-6801.
[215] C. Hille, M. Berg, L. Bressel, D. Munzke, P. Primus, H.-G. Löhmannsröben, C. Dosche, Time-domain fluorescence lifetime imaging for intracellular pH sensing in living tissues, Analytical and Bioanalytical Chemistry 391(5) (2008) 1871.
[216] K.V. Kuchibhotla, C.R. Lattarulo, B.T. Hyman, B.J. Bacskai, Synchronous Hyperactivity and Intercellular Calcium Waves in Astrocytes in Alzheimer Mice, Science 323(5918) (2009) 1211-1215.
[217] C.D. Wilms, H. Schmidt, J. Eilers, Quantitative two-photon Ca2+ imaging via fluorescence lifetime analysis, Cell Calcium 40(1) (2006) 73-79.
[218] C.D. Wilms, J. Eilers, Photo-physical properties of Ca2+-indicator dyes suitable for two-photon fluorescence-lifetime recordings, Journal of Microscopy 225(3) (2007) 209-213.
[219] J.L. Rinnenthal, C. Börnchen, H. Radbruch, V. Andresen, A. Mossakowski, V. Siffrin, T. Seelemann, H. Spiecker, I. Moll, J. Herz, A.E. Hauser, F. Zipp, M.J. Behne, R. Niesner, Parallelized TCSPC for Dynamic Intravital Fluorescence Lifetime Imaging: Quantifying Neuronal Dysfunction in Neuroinflammation, PLoS One 8(4) (2013) e60100.
[220] N. Heim, O. Garaschuk, M.W. Friedrich, M. Mank, R.I. Milos, Y. Kovalchuk, A. Konnerth, O. Griesbeck, Improved calcium imaging in transgenic mice expressing a troponin C-based biosensor, Nat Meth 4(2) (2007) 127-129.
[221] T. Sotelo-Hitschfeld, M.I. Niemeyer, P. Mächler, I. Ruminot, R. Lerchundi, M.T. Wyss, J. Stobart, I. Fernández-Moncada, R. Valdebenito, P. Garrido-Gerter, Y. Contreras-Baeza, B.L. Schneider, P. Aebischer, S. Lengacher, A. San Martín, J. Le Douce, G. Bonvento, P.J. Magistretti, F.V. Sepúlveda, B. Weber, L.F. Barros, Channel-Mediated Lactate Release by K⁺-Stimulated Astrocytes, The Journal of Neuroscience 35(10) (2015) 4168.
[222] A. San Martín, S. Ceballo, I. Ruminot, R. Lerchundi, W.B. Frommer, L.F. Barros, A Genetically Encoded FRET Lactate Sensor and Its Use To Detect the Warburg Effect in Single Cancer Cells, PLoS One 8(2) (2013) e57712.
[223] L.E. Shimolina, M.A. Izquierdo, I. López-Duarte, J.A. Bull, M.V. Shirmanova, L.G. Klapshina, E.V. Zagaynova, M.K. Kuimova, Imaging tumor microscopic viscosity in vivo using molecular rotors, Scientific Reports 7 (2017) 41097.
[224] B.J. Müller, A.V. Zhdanov, S.M. Borisov, T. Foley, I.A. Okkelman, V. Tsytsarev, Q. Tang, R.S. Erzurumlu, Y. Chen, H. Zhang, C. Toncelli, I. Klimant, D.B. Papkovsky, R.I. Dmitriev, Nanoparticle-Based Fluoroionophore for Analysis of Potassium Ion Dynamics in 3D Tissue Models and In Vivo, Advanced Functional Materials 28(9) (2018) 1704598.
[225] M.D. Brand, D.G. Nicholls, Assessing mitochondrial dysfunction in cells, Biochemical Journal 435(2) (2011) 297-312.
[226] K.A. Foster, F. Galeffi, F.J. Gerich, D.A. Turner, M. Müller, Optical and pharmacological tools to investigate the role of mitochondria during oxidative stress and neurodegeneration, Progress in neurobiology 79(3) (2006) 136-171.
[227] A.E. Nel, L. Mädler, D. Velegol, T. Xia, E.M. Hoek, P. Somasundaran, F. Klaessig, V. Castranova, M. Thompson, Understanding biophysicochemical interactions at the nano–bio interface, Nature materials 8(7) (2009) 543.
[228] B.B. Lowell, B.M. Spiegelman, Towards a molecular understanding of adaptive thermogenesis, Nature 404(6778) (2000) 652-660.
[229] N.C. Bal, S.K. Maurya, D.H. Sopariwala, S.K. Sahoo, S.C. Gupta, S.A. Shaikh, M. Pant, L.A. Rowland, E. Bombardier, S.A. Goonasekera, A.R. Tupling, J.D. Molkentin, M. Periasamy, Sarcolipin

is a newly identified regulator of muscle-based thermogenesis in mammals, Nat Med 18(10) (2012) 1575-9.
[230] A. Fedorenko, P.V. Lishko, Y. Kirichok, Mechanism of fatty-acid-dependent UCP1 uncoupling in brown fat mitochondria, Cell 151(2) (2012) 400-13.
[231] H. Zhou, M. Sharma, O. Berezin, D. Zuckerman, M.Y. Berezin, Nanothermometry: From Microscopy to Thermal Treatments, Chemphyschem 17(1) (2016) 27-36.
[232] E.A. Repasky, S.S. Evans, M.W. Dewhirst, Temperature matters! And why it should matter to tumor immunologists, Cancer Immunol Res 1(4) (2013) 210-6.
[233] J. Jenkins, D.B. Papkovsky, R.I. Dmitriev, The Ca2+/Mn2+-transporting SPCA2 pump is regulated by oxygen and cell density in colon cancer cells, Biochemical Journal 473(16) (2016) 2507-2518.
[234] R.I. Dmitriev, S.M. Borisov, J. Jenkins, D.B. Papkovsky, Multi-parametric imaging of tumor spheroids with ultra-bright and tunable nanoparticle O2 probes, 2015, pp. 932806-932806-8.
[235] D.S. Bilan, L. Pase, L. Joosen, A.Y. Gorokhovatsky, Y.G. Ermakova, T.W.J. Gadella, C. Grabher, C. Schultz, S. Lukyanov, V.V. Belousov, HyPer-3: A Genetically Encoded H2O2 Probe with Improved Performance for Ratiometric and Fluorescence Lifetime Imaging, ACS Chemical Biology 8(3) (2013) 535-542.
[236] E.P. Melo, C. Lopes, P. Gollwitzer, S. Lortz, S. Lenzen, I. Mehmeti, C.F. Kaminski, D. Ron, E. Avezov, TriPer, an optical probe tuned to the endoplasmic reticulum tracks changes in luminal H2O2, BMC Biology 15(1) (2017) 24.
[237] G. Lukinavičius, C. Blaukopf, E. Pershagen, A. Schena, L. Reymond, E. Derivery, M. Gonzalez-Gaitan, E. D'Este, S.W. Hell, D.W. Gerlich, SiR-Hoechst is a far-red DNA stain for live-cell nanoscopy, Nature communications 6 (2015).
[238] R. Heim, D.C. Prasher, R.Y. Tsien, Wavelength mutations and posttranslational autoxidation of green fluorescent protein, Proceedings of the National Academy of Sciences 91(26) (1994) 12501-12504.
[239] R. Heim, A.B. Cubitt, R.Y. Tsien, Improved green fluorescence, Nature 373 (1995) 663.
[240] B.P. Cormack, R.H. Valdivia, S. Falkow, FACS-optimized mutants of the green fluorescent protein (GFP), Gene 173(1) (1996) 33-38.
[241] R.M. Wachter, M.-A. Elsliger, K. Kallio, G.T. Hanson, S.J. Remington, Structural basis of spectral shifts in the yellow-emission variants of green fluorescent protein, Structure 6(10) (1998) 1267-1277.
[242] R. Heim, R.Y. Tsien, Engineering green fluorescent protein for improved brightness, longer wavelengths and fluorescence resonance energy transfer, Current Biology 6(2) (1996) 178-182.
[243] R.E. Campbell, O. Tour, A.E. Palmer, P.A. Steinbach, G.S. Baird, D.A. Zacharias, R.Y. Tsien, A monomeric red fluorescent protein, Proceedings of the National Academy of Sciences 99(12) (2002) 7877-7882.
[244] B.J. Bevis, B.S. Glick, Rapidly maturing variants of the Discosoma red fluorescent protein (DsRed), Nat Biotechnol 20(1) (2002) 83-7.
[245] E.A. Rodriguez, G.N. Tran, L.A. Gross, J.L. Crisp, X. Shu, J.Y. Lin, R.Y. Tsien, A far-red fluorescent protein evolved from a cyanobacterial phycobiliprotein, Nature methods 13(9) (2016) 763-769.
[246] A. Kumagai, R. Ando, H. Miyatake, P. Greimel, T. Kobayashi, Y. Hirabayashi, T. Shimogori, A. Miyawaki, A bilirubin-inducible fluorescent protein from eel muscle, Cell 153(7) (2013) 1602-1611.
[247] X. Shu, V. Lev-Ram, T.J. Deerinck, Y. Qi, E.B. Ramko, M.W. Davidson, Y. Jin, M.H. Ellisman, R.Y. Tsien, A Genetically Encoded Tag for Correlated Light and Electron Microscopy of Intact Cells, Tissues, and Organisms, PLoS Biology 9(4) (2011) e1001041.
[248] V.V. Belousov, A.F. Fradkov, K.A. Lukyanov, D.B. Staroverov, K.S. Shakhbazov, A.V. Terskikh, S. Lukyanov, Genetically encoded fluorescent indicator for intracellular hydrogen peroxide, Nat Methods 3(4) (2006) 281-6.
[249] D. Poburko, J. Santo-Domingo, N. Demaurex, Dynamic Regulation of the Mitochondrial Proton Gradient during Cytosolic Calcium Elevations, The Journal of Biological Chemistry 286(13) (2011) 11672-11684.

[250] K.E. Luker, P. Pata, Shemiakina, II, A. Pereverzeva, A.C. Stacer, D.S. Shcherbo, V.Z. Pletnev, M. Skolnaja, K.A. Lukyanov, G.D. Luker, I. Pata, D.M. Chudakov, Comparative study reveals better far-red fluorescent protein for whole body imaging, Scientific Reports 5 (2015) 10332.
[251] D. Shcherbo, C.S. Murphy, G.V. Ermakova, E.A. Solovieva, T.V. Chepurnykh, A.S. Shcheglov, V.V. Verkhusha, V.Z. Pletnev, K.L. Hazelwood, P.M. Roche, S. Lukyanov, A.G. Zaraisky, M.W. Davidson, D.M. Chudakov, Far-red fluorescent tags for protein imaging in living tissues, Biochem J 418(3) (2009) 567-74.
[252] D.S. Bindels, L. Haarbosch, L. van Weeren, M. Postma, K.E. Wiese, M. Mastop, S. Aumonier, G. Gotthard, A. Royant, M.A. Hink, T.W.J. Gadella Jr, mScarlet: a bright monomeric red fluorescent protein for cellular imaging, Nature methods 14 (2016) 53.
[253] X. Shu, A. Royant, M.Z. Lin, T.A. Aguilera, V. Lev-Ram, P.A. Steinbach, R.Y. Tsien, Mammalian expression of infrared fluorescent proteins engineered from a bacterial phytochrome, Science (New York, N.Y.) 324(5928) (2009) 804-807.
[254] G.S. Filonov, K.D. Piatkevich, L.-M. Ting, J. Zhang, K. Kim, V.V. Verkhusha, Bright and stable near-infrared fluorescent protein for in vivo imaging, Nature biotechnology 29 (2011) 757.
[255] D. Yu, W.C. Gustafson, C. Han, C. Lafaye, M. Noirclerc-Savoye, W.P. Ge, D.A. Thayer, H. Huang, T.B. Kornberg, A. Royant, L.Y. Jan, Y.N. Jan, W.A. Weiss, X. Shu, An improved monomeric infrared fluorescent protein for neuronal and tumour brain imaging, Nat Commun 5(3626) (2014).
[256] D.M. Shcherbakova, V.V. Verkhusha, Near-infrared fluorescent proteins for multicolor in vivo imaging, Nature methods 10 (2013) 751.
[257] D.M. Shcherbakova, M. Baloban, A.V. Emelyanov, M. Brenowitz, P. Guo, V.V. Verkhusha, Bright monomeric near-infrared fluorescent proteins as tags and biosensors for multiscale imaging, Nat Commun 7(12405) (2016).
[258] A.A. Shemetov, O.S. Oliinyk, V.V. Verkhusha, How to Increase Brightness of Near-Infrared Fluorescent Proteins in Mammalian Cells, Cell chemical biology 24(6) (2017) 758-766.e3.
[259] J. Chu, R.D. Haynes, S.Y. Corbel, P. Li, E. Gonzalez-Gonzalez, J.S. Burg, N.J. Ataie, A.J. Lam, P.J. Cranfill, M.A. Baird, M.W. Davidson, H.L. Ng, K.C. Garcia, C.H. Contag, K. Shen, H.M. Blau, M.Z. Lin, Non-invasive intravital imaging of cellular differentiation with a bright red-excitable fluorescent protein, Nat Methods 11(5) (2014) 572-8.
[260] Shemiakina, II, G.V. Ermakova, P.J. Cranfill, M.A. Baird, R.A. Evans, E.A. Souslova, D.B. Staroverov, A.Y. Gorokhovatsky, E.V. Putintseva, T.V. Gorodnicheva, T.V. Chepurnykh, L. Strukova, S. Lukyanov, A.G. Zaraisky, M.W. Davidson, D.M. Chudakov, D. Shcherbo, A monomeric red fluorescent protein with low cytotoxicity, Nat Commun 3(1204) (2012).
[261] F. Pennacchietti, E.O. Serebrovskaya, A.R. Faro, I.I. Shemyakina, N.G. Bozhanova, A.A. Kotlobay, N.G. Gurskaya, A. Bodén, J. Dreier, D.M. Chudakov, K.A. Lukyanov, V.V. Verkhusha, A.S. Mishin, I. Testa, Fast reversibly photoswitching red fluorescent proteins for live-cell RESOLFT nanoscopy, Nature methods 15(8) (2018) 601-604.
[262] A.C. Stiel, M. Andresen, H. Bock, M. Hilbert, J. Schilde, A. Schönle, C. Eggeling, A. Egner, S.W. Hell, S. Jakobs, Generation of Monomeric Reversibly Switchable Red Fluorescent Proteins for Far-Field Fluorescence Nanoscopy, Biophysical Journal 95(6) (2008) 2989-2997.
[263] S. Pletnev, F.V. Subach, Z. Dauter, A. Wlodawer, V.V. Verkhusha, A Structural Basis for Reversible Photoswitching of Absorbance Spectra in Red Fluorescent Protein rsTagRFP, Journal of Molecular Biology 417(3) (2012) 144-151.
[264] F.V. Subach, L. Zhang, T.W.J. Gadella, N.G. Gurskaya, K.A. Lukyanov, V.V. Verkhusha, Red fluorescent protein with reversibly photoswitchable absorbance for photochromic FRET, Chemistry & biology 17(7) (2010) 745-755.
[265] N.C. Shaner, R.E. Campbell, P.A. Steinbach, B.N. Giepmans, A.E. Palmer, R.Y. Tsien, Improved monomeric red, orange and yellow fluorescent proteins derived from Discosoma sp. red fluorescent protein, Nat Biotechnol. 2004 Dec;22(12):1567-72. doi: 10.1038/nbt1037. Epub 2004 Nov 21.
[266] B.T. Bajar, E.S. Wang, A.J. Lam, B.B. Kim, C.L. Jacobs, E.S. Howe, M.W. Davidson, M.Z. Lin, J. Chu, Improving brightness and photostability of green and red fluorescent proteins for live cell imaging and FRET reporting, Scientific Reports 6 (2016) 20889.
[267] N.C. Shaner, M.Z. Lin, M.R. McKeown, P.A. Steinbach, K.L. Hazelwood, M.W. Davidson, R.Y. Tsien, Improving the photostability of bright monomeric orange and red fluorescent proteins, Nature methods 5 (2008) 545.

[268] A. Miyawaki, J. Llopis, R. Heim, J.M. McCaffery, J.A. Adams, M. Ikura, R.Y. Tsien, Fluorescent indicators for Ca2+based on green fluorescent proteins and calmodulin, Nature 388 (1997) 882.
[269] T. Nagai, K. Ibata, E.S. Park, M. Kubota, K. Mikoshiba, A. Miyawaki, A variant of yellow fluorescent protein with fast and efficient maturation for cell-biological applications, Nat Biotechnol 20(1) (2002) 87-90.
[270] O. Griesbeck, G.S. Baird, R.E. Campbell, D.A. Zacharias, R.Y. Tsien, Reducing the environmental sensitivity of yellow fluorescent protein. Mechanism and applications, J Biol Chem 276(31) (2001) 29188-94.
[271] N.C. Shaner, G.G. Lambert, A. Chammas, Y. Ni, P.J. Cranfill, M.A. Baird, B.R. Sell, J.R. Allen, R.N. Day, M. Israelsson, A bright monomeric green fluorescent protein derived from Branchiostoma lanceolatum, Nature methods 10(5) (2013) 407.
[272] S. Habuchi, R. Ando, P. Dedecker, W. Verheijen, H. Mizuno, A. Miyawaki, J. Hofkens, Reversible single-molecule photoswitching in the GFP-like fluorescent protein Dronpa, Proceedings of the National Academy of Sciences of the United States of America 102(27) (2005) 9511-9516.
[273] D.A. Zacharias, J.D. Violin, A.C. Newton, R.Y. Tsien, Partitioning of Lipid-Modified Monomeric GFPs into Membrane Microdomains of Live Cells, Science 296(5569) (2002) 913-916.
[274] J. Goedhart, D. von Stetten, M. Noirclerc-Savoye, M. Lelimousin, L. Joosen, M.A. Hink, L. van Weeren, T.W. Gadella, Jr., A. Royant, Structure-guided evolution of cyan fluorescent proteins towards a quantum yield of 93%, Nat Commun 3(751) (2012).
[275] M. Mastop, D.S. Bindels, N.C. Shaner, M. Postma, T.W.J. Gadella, Jr., J. Goedhart, Characterization of a spectrally diverse set of fluorescent proteins as FRET acceptors for mTurquoise2, Sci Rep 7(1) (2017) 017-12212.
[276] H.W. Ai, N.C. Shaner, Z. Cheng, R.Y. Tsien, R.E. Campbell, Exploration of new chromophore structures leads to the identification of improved blue fluorescent proteins, Biochemistry 46(20) (2007) 5904-10.
[277] O.M. Subach, P.J. Cranfill, M.W. Davidson, V.V. Verkhusha, An enhanced monomeric blue fluorescent protein with the high chemical stability of the chromophore, PLoS One 6(12) (2011) 8.
[278] P.J. Cranfill, B.R. Sell, M.A. Baird, J.R. Allen, Z. Lavagnino, H.M. de Gruiter, G.-J. Kremers, M.W. Davidson, A. Ustione, D.W. Piston, Quantitative Assessment of Fluorescent Proteins, Nature methods 13(7) (2016) 557-562.
[279] J.K. Heppert, D.J. Dickinson, A.M. Pani, C.D. Higgins, A. Steward, J. Ahringer, J.R. Kuhn, B. Goldstein, Comparative assessment of fluorescent proteins for in vivo imaging in an animal model system, Molecular Biology of the Cell 27(22) (2016) 3385-3394.
[280] R.I. Ghauharali, G.J. Brakenhoff, Fluorescence photobleaching-based image standardization for fluorescence microscopy, J Microsc 198(Pt 2) (2000) 88-100.
[281] C. Scharnagl, R. Raupp-Kossmann, S.F. Fischer, Molecular Basis for pH Sensitivity and Proton Transfer in Green Fluorescent Protein: Protonation and Conformational Substates from Electrostatic Calculations, Biophysical Journal 77(4) (1999) 1839-1857.
[282] O. Griesbeck, G.S. Baird, R.E. Campbell, D.A. Zacharias, R.Y. Tsien, Reducing the environmental sensitivity of yellow fluorescent protein: mechanism and applications, Journal of Biological Chemistry (2001).
[283] A. Germond, H. Fujita, T. Ichimura, T.M. Watanabe, Design and development of genetically encoded fluorescent sensors to monitor intracellular chemical and physical parameters, Biophysical Reviews 8(2) (2016) 121-138.
[284] P.J. Macdonald, Y. Chen, J.D. Mueller, Chromophore maturation and fluorescence fluctuation spectroscopy of fluorescent proteins in a cell-free expression system, Analytical Biochemistry 421(1) (2012) 291-298.
[285] R. Heim, D.C. Prasher, R.Y. Tsien, Wavelength mutations and posttranslational autoxidation of green fluorescent protein, Proceedings of the National Academy of Sciences 91(26) (1994) 12501.
[286] R. Erapaneedi, V.V. Belousov, M. Schäfers, F. Kiefer, A novel family of fluorescent hypoxia sensors reveal strong heterogeneity in tumor hypoxia at the cellular level, The EMBO Journal 35(1) (2016) 102-113.
[287] L.M. Costantini, M. Fossati, M. Francolini, E.L. Snapp, Assessing the Tendency of Fluorescent Proteins to Oligomerize under Physiologic Conditions, Traffic (Copenhagen, Denmark) 13(5) (2012) 643-649.

[288] T. Forster, Energiewanderung und fluoreszenz, Naturwissenschaften 33(6) (1946) 166-175.
[289] E.A. Jares-Erijman, T.M. Jovin, FRET imaging, Nature biotechnology 21(11) (2003) 1387.
[290] R.B. Sekar, A. Periasamy, Fluorescence resonance energy transfer (FRET) microscopy imaging of live cell protein localizations, The Journal of Cell Biology 160(5) (2003) 629-633.
[291] K. Truong, M. Ikura, The use of FRET imaging microscopy to detect protein-protein interactions and protein conformational changes in vivo, Curr Opin Struct Biol 11(5) (2001) 573-8.
[292] G.J. Kremers, J. Goedhart, E.B. van Munster, T.W. Gadella, Jr., Cyan and yellow super fluorescent proteins with improved brightness, protein folding, and FRET Forster radius, Biochemistry 45(21) (2006) 6570-80.
[293] K. Truong, A. Sawano, H. Mizuno, H. Hama, K.I. Tong, T.K. Mal, A. Miyawaki, M. Ikura, FRET-based in vivo Ca2+ imaging by a new calmodulin-GFP fusion molecule, Nature Structural Biology 8 (2001) 1069.
[294] M.A. Del Pozo, W.B. Kiosses, N.B. Alderson, N. Meller, K.M. Hahn, M.A. Schwartz, Integrins regulate GTP-Rac localized effector interactions through dissociation of Rho-GDI, Nature Cell Biology 4 (2002) 232.
[295] T. Laviv, B.B. Kim, J. Chu, A.J. Lam, M.Z. Lin, R. Yasuda, Simultaneous dual-color fluorescence lifetime imaging with novel red-shifted fluorescent proteins, Nature methods 13(12) (2016) 989.
[296] P. Weber, S. Schickinger, M. Wagner, B. Angres, T. Bruns, H. Schneckenburger, Monitoring of apoptosis in 3D cell cultures by FRET and light sheet fluorescence microscopy, International journal of molecular sciences 16(3) (2015) 5375-5385.
[297] K.A. Lukyanov, D.M. Chudakov, S. Lukyanov, V.V. Verkhusha, Photoactivatable fluorescent proteins, Nature Reviews Molecular Cell Biology 6 (2005) 885.
[298] K. Nienhaus, G.U. Nienhaus, Photoswitchable Fluorescent Proteins: Do Not Always Look on the Bright Side, ACS Nano 10(10) (2016) 9104-9108.
[299] S. Gayda, K. Nienhaus, G.U. Nienhaus, Mechanistic insights into reversible photoactivation in proteins of the GFP family, Biophys J 103(12) (2012) 2521-31.
[300] M. Andresen, A.C. Stiel, S. Trowitzsch, G. Weber, C. Eggeling, M.C. Wahl, S.W. Hell, S. Jakobs, Structural basis for reversible photoswitching in Dronpa, Proc Natl Acad Sci U S A 104(32) (2007) 13005-9.
[301] D.M. Chudakov, S. Lukyanov, K.A. Lukyanov, Tracking intracellular protein movements using photoswitchable fluorescent proteins PS-CFP2 and Dendra2, Nature Protocols 2 (2007) 2024.
[302] L.A. Masullo, A. Bodén, F. Pennacchietti, G. Coceano, M. Ratz, I. Testa, Enhanced photon collection enables four dimensional fluorescence nanoscopy of living systems, Nature Communications 9(1) (2018) 3281.
[303] J. López-Sagaseta, E. Malito, R. Rappuoli, M.J. Bottomley, Self-assembling protein nanoparticles in the design of vaccines, Computational and Structural Biotechnology Journal 14 (2016) 58-68.
[304] N.F. Steinmetz, Viral nanoparticles as platforms for next-generation therapeutics and imaging devices, Nanomedicine 6(5) (2010) 634-41.
[305] J.D. Perlmutter, M.F. Hagan, Mechanisms of virus assembly, Annual review of physical chemistry 66 (2015) 217-239.
[306] F. Carmona, M. Poli, M. Bertuzzi, A. Gianoncelli, F. Gangemi, P. Arosio, Study of ferritin self-assembly and heteropolymer formation by the use of Fluorescence Resonance Energy Transfer (FRET) technology, Biochimica et biophysica acta. General subjects 1861(3) (2017) 522-532.
[307] T. Douglas, M. Young, Viruses: making friends with old foes, Science 312(5775) (2006) 873-5.
[308] D.L. Caspar, A. Klug, Physical principles in the construction of regular viruses, Cold Spring Harb Symp Quant Biol 27 (1962) 1-24.
[309] B.V.V. Prasad, M.F. Schmid, Principles of Virus Structural Organization, Advances in experimental medicine and biology 726 (2012) 17-47.
[310] F.M. Brunel, J.D. Lewis, G. Destito, N.F. Steinmetz, M. Manchester, H. Stuhlmann, P.E. Dawson, Hydrazone Ligation Strategy to Assemble Multifunctional Viral Nanoparticles for Cell Imaging and Tumor Targeting, Nano Letters 10(3) (2010) 1093-1097.
[311] I. Barwal, R. Kumar, S. Kateriya, A.K. Dinda, S.C. Yadav, Targeted delivery system for cancer cells consist of multiple ligands conjugated genetically modified CCMV capsid on doxorubicin GNPs complex, Scientific Reports 6 (2016) 37096.

[312] I.L. Aanei, A.M. ElSohly, M.E. Farkas, C. Netirojjanakul, M. Regan, S. Taylor Murphy, J.P. O'Neil, Y. Seo, M.B. Francis, Biodistribution of Antibody-MS2 Viral Capsid Conjugates in Breast Cancer Models, Molecular Pharmaceutics 13(11) (2016) 3764-3772.
[313] J.-K. Rhee, M. Hovlid, J.D. Fiedler, S.D. Brown, F. Manzenrieder, H. Kitagishi, C. Nycholat, J.C. Paulson, M.G. Finn, Colorful Virus-like Particles: Fluorescent Protein Packaging by the Qβ Capsid, Biomacromolecules 12(11) (2011) 3977-3981.
[314] R.I. Dmitriev, N. O'Donnell, D.B. Papkovsky, Metallochelate Coupling of Phosphorescent Pt-Porphyrins to Peptides, Proteins, and Self-Assembling Protein Nanoparticles, Bioconjugate chemistry 27(2) (2016) 439-445.
[315] F.M. Brunel, J.D. Lewis, G. Destito, N.F. Steinmetz, M. Manchester, H. Stuhlmann, P.E. Dawson, Hydrazone ligation strategy to assemble multifunctional viral nanoparticles for cell imaging and tumor targeting, Nano Lett 10(3) (2010) 1093-7.
[316] A. Servid, P. Jordan, A. O'Neil, P. Prevelige, T. Douglas, Location of the Bacteriophage P22 Coat Protein C-terminus Provides Opportunities for the Design of Capsid Based Materials, Biomacromolecules 14(9) (2013) 10.1021/bm400796c.
[317] G. Hermanson, Tags and probes, Bioconjugate Techniques (1996) 297-416.
[318] P. Anand, A. O'Neil, E. Lin, T. Douglas, M. Holford, Tailored delivery of analgesic ziconotide across a blood brain barrier model using viral nanocontainers, Scientific Reports 5 (2015) 12497.
[319] C.R. Behrens, J.M. Hooker, A.C. Obermeyer, D.W. Romanini, E.M. Katz, M.B. Francis, Rapid Chemoselective Bioconjugation Through the Oxidative Coupling of Anilines and Aminophenols, Journal of the American Chemical Society 133(41) (2011) 16398-16401.
[320] W.F. Rurup, F. Verbij, M.S.T. Koay, C. Blum, V. Subramaniam, J.J.L.M. Cornelissen, Predicting the Loading of Virus-Like Particles with Fluorescent Proteins, Biomacromolecules 15(2) (2014) 558-563.
[321] I.J. Minten, L.J.A. Hendriks, R.J.M. Nolte, J.J.L.M. Cornelissen, Controlled Encapsulation of Multiple Proteins in Virus Capsids, Journal of the American Chemical Society 131(49) (2009) 17771-17773.
[322] I. Yildiz, K.L. Lee, K. Chen, S. Shukla, N.F. Steinmetz, Infusion of imaging and therapeutic molecules into the plant virus-based carrier cowpea mosaic virus: cargo-loading and delivery, J Control Release 172(2) (2013) 568-78.
[323] T. Douglas, E. Strable, D. Willits, A. Aitouchen, M. Libera, M. Young, Protein engineering of a viral cage for constrained nanomaterials synthesis, Advanced Materials 14(6) (2002) 415-418.
[324] C.R. Kaiser, M.L. Flenniken, E. Gillitzer, A.L. Harmsen, A.G. Harmsen, M.A. Jutila, T. Douglas, M.J. Young, Biodistribution studies of protein cage nanoparticles demonstrate broad tissue distribution and rapid clearance in vivo, Int J Nanomedicine 2(4) (2007) 715-33.
[325] H. Jaganathan, B. Godin, Biocompatibility assessment of Si-based nano- and micro-particles, Adv Drug Deliv Rev 64(15) (2012) 1800-19.
[326] S. Shukla, A.L. Ablack, A.M. Wen, K.L. Lee, J.D. Lewis, N.F. Steinmetz, Increased tumor homing and tissue penetration of the filamentous plant viral nanoparticle Potato virus X, Mol Pharm 10(1) (2013) 33-42.
[327] M.A. Bruckman, L.N. Randolph, A. VanMeter, S. Hern, A.J. Shoffstall, R.E. Taurog, N.F. Steinmetz, Biodistribution, pharmacokinetics, and blood compatibility of native and PEGylated tobacco mosaic virus nano-rods and-spheres in mice, Virology 449 (2014) 163-173.
[328] M. Carrillo-Tripp, C.M. Shepherd, I.A. Borelli, S. Venkataraman, G. Lander, P. Natarajan, J.E. Johnson, C.L. Brooks, V.S. Reddy, VIPERdb(2): an enhanced and web API enabled relational database for structural virology, Nucleic Acids Research 37(Database issue) (2009) D436-D442.
[329] A. Niehl, F. Appaix, S. Boscá, B. van der Sanden, J.-F. Nicoud, F. Bolze, M. Heinlein, Fluorescent Tobacco mosaic virus-Derived Bio-Nanoparticles for Intravital Two-Photon Imaging, Frontiers in Plant Science 6(1244) (2016).
[330] P.L. Chariou, K.L. Lee, A.M. Wen, N.M. Gulati, P.L. Stewart, N.F. Steinmetz, Detection and Imaging of Aggressive Cancer Cells Using an Epidermal Growth Factor Receptor (EGFR)-Targeted Filamentous Plant Virus-Based Nanoparticle, Bioconjugate chemistry 26(2) (2015) 262-269.
[331] K.L. Lee, S. Shukla, M. Wu, N.R. Ayat, C.E. El Sanadi, A.M. Wen, J.F. Edelbrock, J.K. Pokorski, U. Commandeur, G.R. Dubyak, N.F. Steinmetz, Stealth filaments: Polymer chain length and

conformation affect the in vivo fate of PEGylated potato virus X, Acta Biomaterialia 19 (2015) 166-179.
[332] S. Shukla, C. Dickmeis, A. Nagarajan, R. Fischer, U. Commandeur, N. Steinmetz, Molecular farming of fluorescent virus-based nanoparticles for optical imaging in plants, human cells and mouse models, Biomaterials science 2(5) (2014) 784-797.
[333] E.W. Kovacs, J.M. Hooker, D.W. Romanini, P.G. Holder, K.E. Berry, M.B. Francis, Dual-Surface-Modified Bacteriophage MS2 as an Ideal Scaffold for a Viral Capsid-Based Drug Delivery System, Bioconjugate chemistry 18(4) (2007) 1140-1147.
[334] C.E. Ashley, E.C. Carnes, G.K. Phillips, P.N. Durfee, M.D. Buley, C.A. Lino, D.P. Padilla, B. Phillips, M.B. Carter, C.L. Willman, C.J. Brinker, J.d.C. Caldeira, B. Chackerian, W. Wharton, D.S. Peabody, Cell-Specific Delivery of Diverse Cargos by Bacteriophage MS2 Virus-like Particles, ACS nano 5(7) (2011) 5729-5745.
[335] M.E. Farkas, I.L. Aanei, C.R. Behrens, G.J. Tong, S.T. Murphy, J.P. O'Neil, M.B. Francis, PET Imaging and Biodistribution of Chemically Modified Bacteriophage MS2, Molecular Pharmaceutics 10(1) (2013) 69-76.
[336] J.K. Pokorski, M.L. Hovlid, M. Finn, Cell targeting with hybrid Qβ virus-like particles displaying epidermal growth factor, ChemBioChem 12(16) (2011) 2441-2447.
[337] D.E. Prasuhn, P. Singh, E. Strable, S. Brown, M. Manchester, M.G. Finn, Plasma Clearance of Bacteriophage Qβ Particles as a Function of Surface Charge, Journal of the American Chemical Society 130(4) (2008) 1328-1334.
[338] C.R. Kaiser, M.L. Flenniken, E. Gillitzer, A.L. Harmsen, A.G. Harmsen, M.A. Jutila, T. Douglas, M.J. Young, Biodistribution studies of protein cage nanoparticles demonstrate broad tissue distribution and rapid clearance in vivo, International journal of nanomedicine 2(4) (2007) 715.
[339] P. Singh, D. Prasuhn, R.M. Yeh, G. Destito, C.S. Rae, K. Osborn, M. Finn, M. Manchester, Bio-distribution, toxicity and pathology of cowpea mosaic virus nanoparticles in vivo, Journal of controlled release 120(1-2) (2007) 41-50.
[340] L.O. Liepold, J. Revis, M. Allen, L. Oltrogge, M. Young, T. Douglas, Structural transitions in Cowpea chlorotic mottle virus (CCMV), Physical biology 2(4) (2005) S166.
[341] J.G. Millán, M. Brasch, E. Anaya-Plaza, A. de la Escosura, A.H. Velders, D.N. Reinhoudt, T. Torres, M.S.T. Koay, J.J.L.M. Cornelissen, Self-assembly triggered by self-assembly: Optically active, paramagnetic micelles encapsulated in protein cage nanoparticles, Journal of Inorganic Biochemistry 136 (2014) 140-146.
[342] I.J. Minten, V.I. Claessen, K. Blank, A.E. Rowan, R.J. Nolte, J.J. Cornelissen, Catalytic capsids: the art of confinement, Chemical science 2(2) (2011) 358-362.
[343] I.J. Minten, R.J. Nolte, J.J. Cornelissen, Complex assembly behavior during the encapsulation of green fluorescent protein analogs in virus derived protein capsules, Macromolecular bioscience 10(5) (2010) 539-545.
[344] M.B. van Eldijk, J.C.-Y. Wang, I.J. Minten, C. Li, A. Zlotnick, R.J. Nolte, J.J. Cornelissen, J.C. van Hest, Designing two self-assembly mechanisms into one viral capsid protein, Journal of the American Chemical Society 134(45) (2012) 18506-18509.
[345] M.B. van Eldijk, C.L. McGann, K.L. Kiick, J.C.M. van Hest, Elastomeric polypeptides, Topics in current chemistry 310 (2012) 71-116.
[346] M.B. van Eldijk, L. Schoonen, J.J. Cornelissen, R.J. Nolte, J. van Hest, Metal Ion-Induced Self-Assembly of a Multi-Responsive Block Copolypeptide into Well-Defined Nanocapsules, Small 12(18) (2016) 2476-2483.
[347] K.J. Koudelka, G. Destito, E.M. Plummer, S.A. Trauger, G. Siuzdak, M. Manchester, Endothelial targeting of cowpea mosaic virus (CPMV) via surface vimentin, PLoS Pathog 5(5) (2009) 1.
[348] N.F. Steinmetz, C.-F. Cho, A. Ablack, J.D. Lewis, M. Manchester, Cowpea mosaic virus nanoparticles target surface vimentin on cancer cells, Nanomedicine 6(2) (2011) 351-364.
[349] M.J. Gonzalez, E.M. Plummer, C.S. Rae, M. Manchester, Interaction of Cowpea mosaic virus (CPMV) nanoparticles with antigen presenting cells in vitro and in vivo, PLoS One 4(11) (2009) 0007981.
[350] I. Yildiz, K.L. Lee, K. Chen, S. Shukla, N.F. Steinmetz, Infusion of imaging and therapeutic molecules into the plant virus-based carrier cowpea mosaic virus: Cargo-loading and delivery, Journal of controlled release 172(2) (2013) 568-578.

[351] J.D. Lewis, G. Destito, A. Zijlstra, M.J. Gonzalez, J.P. Quigley, M. Manchester, H. Stuhlmann, Viral nanoparticles as tools for intravital vascular imaging, Nature Medicine 12 (2006) 354.
[352] L.P. Shriver, K.J. Koudelka, M. Manchester, Viral nanoparticles associate with regions of inflammation and blood brain barrier disruption during CNS infection, Journal of Neuroimmunology 211(1) (2009) 66-72.
[353] C.S. Rae, I. Wei Khor, Q. Wang, G. Destito, M.J. Gonzalez, P. Singh, D.M. Thomas, M.N. Estrada, E. Powell, M.G. Finn, M. Manchester, Systemic trafficking of plant virus nanoparticles in mice via the oral route, Virology 343(2) (2005) 224-235.
[354] K.S. Raja, Q. Wang, M.J. Gonzalez, M. Manchester, J.E. Johnson, M.G. Finn, Hybrid Virus−Polymer Materials. 1. Synthesis and Properties of PEG-Decorated Cowpea Mosaic Virus, Biomacromolecules 4(3) (2003) 472-476.
[355] T. Stylianopoulos, M.-Z. Poh, N. Insin, M.G. Bawendi, D. Fukumura, L.L. Munn, R.K. Jain, Diffusion of particles in the extracellular matrix: the effect of repulsive electrostatic interactions, Biophysical journal 99(5) (2010) 1342-1349.
[356] R. Gref, M. Lück, P. Quellec, M. Marchand, E. Dellacherie, S. Harnisch, T. Blunk, R.H. Müller, 'Stealth' corona-core nanoparticles surface modified by polyethylene glycol (PEG): influences of the corona (PEG chain length and surface density) and of the core composition on phagocytic uptake and plasma protein adsorption, Colloids and Surfaces B: Biointerfaces 18(3) (2000) 301-313.
[357] S. Schöttler, G. Becker, S. Winzen, T. Steinbach, K. Mohr, K. Landfester, V. Mailänder, F.R. Wurm, Protein adsorption is required for stealth effect of poly(ethylene glycol)- and poly(phosphoester)-coated nanocarriers, Nature Nanotechnology 11 (2016) 372.
[358] T. Ishida, H. Kiwada, Accelerated blood clearance (ABC) phenomenon upon repeated injection of PEGylated liposomes, International Journal of Pharmaceutics 354(1) (2008) 56-62.
[359] L. Xu, T.J. Anchordoquy, Effect of Cholesterol Nanodomains on the Targeting of Lipid-Based Gene Delivery in Cultured Cells, Molecular Pharmaceutics 7(4) (2010) 1311-1317.
[360] P. Yingyuad, M. Mével, C. Prata, C. Kontogiorgis, M. Thanou, A.D. Miller, Enzyme-triggered PEGylated siRNA-nanoparticles for controlled release of siRNA, Journal of RNAi and Gene Silencing : An International Journal of RNA and Gene Targeting Research 10 (2014) 490-499.
[361] M. Meyer, E. Wagner, pH-responsive shielding of non-viral gene vectors, Expert opinion on drug delivery 3(5) (2006) 563-571.
[362] J.D. Byrne, T. Betancourt, L. Brannon-Peppas, Active targeting schemes for nanoparticle systems in cancer therapeutics, Advanced drug delivery reviews 60(15) (2008) 1615-1626.
[363] C.-F. Cho, S. Shukla, E.J. Simpson, N.F. Steinmetz, L.G. Luyt, J.D. Lewis, Molecular targeted viral nanoparticles as tools for imaging cancer, Virus Hybrids as Nanomaterials, Springer2014, pp. 211-230.
[364] P. Arosio, F. Carmona, R. Gozzelino, F. Maccarinelli, M. Poli, The importance of eukaryotic ferritins in iron handling and cytoprotection, Biochem J 472(1) (2015) 1-15.
[365] M. Rivera, Bacterioferritin: Structure, Dynamics, and Protein–Protein Interactions at Play in Iron Storage and Mobilization, Accounts of Chemical Research 50(2) (2017) 331-340.
[366] J.F. Briat, C. Duc, K. Ravet, F. Gaymard, Ferritins and iron storage in plants, Biochim Biophys Acta 8 (2010) 806-14.
[367] P.M. Harrison, P. Arosio, The ferritins: molecular properties, iron storage function and cellular regulation, Biochimica et Biophysica Acta (BBA) - Bioenergetics 1275(3) (1996) 161-203.
[368] P.D. Hempstead, S.J. Yewdall, A.R. Fernie, D.M. Lawson, P.J. Artymiuk, D.W. Rice, G.C. Ford, P.M. Harrison, Comparison of the three-dimensional structures of recombinant human H and horse L ferritins at high resolution11Edited by R. Huber, Journal of Molecular Biology 268(2) (1997) 424-448.
[369] T.T. Chen, L. Li, D.H. Chung, C.D. Allen, S.V. Torti, F.M. Torti, J.G. Cyster, C.Y. Chen, F.M. Brodsky, E.C. Niemi, M.C. Nakamura, W.E. Seaman, M.R. Daws, TIM-2 is expressed on B cells and in liver and kidney and is a receptor for H-ferritin endocytosis, J Exp Med 202(7) (2005) 955-65.
[370] J. Han, W.E. Seaman, X. Di, W. Wang, M. Willingham, F.M. Torti, S.V. Torti, Iron Uptake Mediated by Binding of H-Ferritin to the TIM-2 Receptor in Mouse Cells, PLOS ONE 6(8) (2011) e23800.
[371] D. Moss, L.W. Powell, J.W. Halliday, S. Fargion, M.D. Cappellini, A.L. Fracanzani, S. Levi, P. Arosio, Functional roles of the ferritin receptors of human liver, hepatoma, lymphoid and erythroid cells, Journal of Inorganic Biochemistry 47(1) (1992) 219-227.

[372] P.C. Adams, L.W. Powell, J.W. Halliday, Isolation of a human hepatic ferritin receptor, Hepatology 8(4) (1988) 719-721.
[373] M. Takami, K. Mizumoto, I. Kasuya, K. Kino, H.H. Sussman, H. Tsunoo, Human placental ferritin receptor, Biochimica et Biophysica Acta (BBA) - General Subjects 884(1) (1986) 31-38.
[374] S. Hulet, S. Powers, J. Connor, Distribution of transferrin and ferritin binding in normal and multiple sclerotic human brains, Journal of the neurological sciences 165(1) (1999) 48-55.
[375] Q. Liao, P. Kong, J. Gao, F. Li, Z. Qian, Expression of ferritin receptor in placental microvilli membrane in pregnant women with different iron status at mid-term gestation, European journal of clinical nutrition 55(8) (2001) 651.
[376] L. Li, C.J. Fang, J.C. Ryan, E.C. Niemi, J.A. Lebron, P.J. Bjorkman, H. Arase, F.M. Torti, S.V. Torti, M.C. Nakamura, W.E. Seaman, Binding and uptake of H-ferritin are mediated by human transferrin receptor-1, Proc Natl Acad Sci U S A 107(8) (2010) 3505-10.
[377] A. Calzolari, I. Oliviero, S. Deaglio, G. Mariani, M. Biffoni, N.M. Sposi, F. Malavasi, C. Peschle, U. Testa, Transferrin receptor 2 is frequently expressed in human cancer cell lines, Blood Cells Mol Dis 39(1) (2007) 82-91.
[378] H. Kawabata, Transferrin and transferrin receptors update, Free radical biology & medicine 133 (2019) 46-54.
[379] J.Y. Li, N. Paragas, R.M. Ned, A. Qiu, M. Viltard, T. Leete, I.R. Drexler, X. Chen, S. Sanna-Cherchi, F. Mohammed, D. Williams, C.S. Lin, K.M. Schmidt-Ott, N.C. Andrews, J. Barasch, Scara5 Is a Ferritin Receptor Mediating Non-Transferrin Iron Delivery, Developmental Cell 16(1) (2009) 35-46.
[380] F. Wang, Y. Li, Y. Shen, A. Wang, S. Wang, T. Xie, The Functions and Applications of RGD in Tumor Therapy and Tissue Engineering, International Journal of Molecular Sciences 14(7) (2013) 13447-13462.
[381] X. Lin, J. Xie, G. Niu, F. Zhang, H. Gao, M. Yang, Q. Quan, M.A. Aronova, G. Zhang, S. Lee, R. Leapman, X. Chen, Chimeric ferritin nanocages for multiple function loading and multimodal imaging, Nano Lett 11(2) (2011) 814-9.
[382] M. Kanekiyo, C.-J. Wei, H.M. Yassine, P.M. McTamney, J.C. Boyington, J.R.R. Whittle, S.S. Rao, W.-P. Kong, L. Wang, G.J. Nabel, Self-assembling influenza nanoparticle vaccines elicit broadly neutralizing H1N1 antibodies, Nature 499 (2013) 102.
[383] B.-R. Lee, H.K. Ko, J.H. Ryu, K.Y. Ahn, Y.-H. Lee, S.J. Oh, J.H. Na, T.W. Kim, Y. Byun, I.C. Kwon, K. Kim, J. Lee, Engineered Human Ferritin Nanoparticles for Direct Delivery of Tumor Antigens to Lymph Node and Cancer Immunotherapy, Scientific Reports 6 (2016) 35182.
[384] Z. Zhen, W. Tang, H. Chen, X. Lin, T. Todd, G. Wang, T. Cowger, X. Chen, J. Xie, RGD-Modified Apoferritin Nanoparticles for Efficient Drug Delivery to Tumors, ACS Nano 7(6) (2013) 4830-4837.
[385] M. Uchida, M. Terashima, C.H. Cunningham, Y. Suzuki, D.A. Willits, A.F. Willis, P.C. Yang, P.S. Tsao, M.V. McConnell, M.J. Young, A human ferritin iron oxide nano-composite magnetic resonance contrast agent, Magnetic Resonance in Medicine: An Official Journal of the International Society for Magnetic Resonance in Medicine 60(5) (2008) 1073-1081.
[386] X. Lin, J. Xie, G. Niu, F. Zhang, H. Gao, M. Yang, Q. Quan, M.A. Aronova, G. Zhang, S. Lee, R. Leapman, X. Chen, Chimeric Ferritin Nanocages for Multiple Function Loading and Multimodal Imaging, Nano Letters 11(2) (2011) 814-819.
[387] M. Terashima, M. Uchida, H. Kosuge, P.S. Tsao, M.J. Young, S.M. Conolly, T. Douglas, M.V. McConnell, Human Ferritin Cages for Imaging Vascular Macrophages, Biomaterials 32(5) (2011) 1430-1437.
[388] M. Liang, K. Fan, M. Zhou, D. Duan, J. Zheng, D. Yang, J. Feng, X. Yan, H-ferritin–nanocaged doxorubicin nanoparticles specifically target and kill tumors with a single-dose injection, Proceedings of the National Academy of Sciences 111(41) (2014) 14900-14905.
[389] S. Sakamoto, H. Kawabata, T. Masuda, T. Uchiyama, C. Mizumoto, K. Ohmori, H.P. Koeffler, N. Kadowaki, A. Takaori-Kondo, H-Ferritin Is Preferentially Incorporated by Human Erythroid Cells through Transferrin Receptor 1 in a Threshold-Dependent Manner, PLoS One 10(10) (2015).
[390] B. Fernandez, N. Galvez, P. Sanchez, R. Cuesta, R. Bermejo, J.M. Dominguez-Vera, Fluorescence resonance energy transfer in ferritin labeled with multiple fluorescent dyes, J Biol Inorg Chem 13(3) (2008) 349-55.

[391] Y.J. Kang, H.J. Yang, S. Jeon, Y.S. Kang, Y. Do, S.Y. Hong, S. Kang, Polyvalent display of monosaccharides on ferritin protein cage nanoparticles for the recognition and binding of cell-surface lectins, Macromol Biosci 14(5) (2014) 619-25.
[392] L. Vannucci, E. Falvo, M. Fornara, P. Di Micco, O. Benada, J. Krizan, J. Svoboda, K. Hulikova-Capkova, V. Morea, A. Boffi, P. Ceci, Selective targeting of melanoma by PEG-masked protein-based multifunctional nanoparticles, International Journal of Nanomedicine 7 (2012) 1489-1509.
[393] A. Ruiz, Y. Hernández, C. Cabal, E. González, S. Veintemillas-Verdaguer, E. Martínez, M.P. Morales, Biodistribution and pharmacokinetics of uniform magnetite nanoparticles chemically modified with polyethylene glycol, Nanoscale 5(23) (2013) 11400-11408.
[394] A. Luzzago, G. Cesareni, Isolation of point mutations that affect the folding of the H chain of human ferritin in E.coli, The EMBO Journal 8(2) (1989) 569-576.
[395] Z. Zhen, W. Tang, H. Chen, X. Lin, T. Todd, G. Wang, T. Cowger, X. Chen, J. Xie, RGD-modified apoferritin nanoparticles for efficient drug delivery to tumors, ACS Nano 7(6) (2013) 4830-7.
[396] A. Ma-Ham, H. Wu, J. Wang, X. Kang, Y. Zhang, Y. Lin, Apoferritin-based nanomedicine platform for drug delivery: equilibrium binding study of daunomycin with DNA, Journal of Materials Chemistry 21(24) (2011) 8700-8708.
[397] G. Ferraro, S. Ciambellotti, L. Messori, A. Merlino, Cisplatin Binding Sites in Human H-Chain Ferritin, Inorganic Chemistry 56(15) (2017) 9064-9070.
[398] X. Lin, J. Xie, L. Zhu, S. Lee, G. Niu, Y. Ma, K. Kim, X. Chen, Hybrid Ferritin Nanoparticles as Activatable Probes for Tumor Imaging, Angewandte Chemie International Edition 50(7) (2011) 1569-1572.
[399] T. Kitagawa, H. Kosuge, M. Uchida, M.M. Dua, Y. Iida, R.L. Dalman, T. Douglas, M.V. McConnell, RGD-Conjugated Human Ferritin Nanoparticles for Imaging Vascular Inflammation and Angiogenesis in Experimental Carotid and Aortic Disease, Molecular imaging and biology : MIB : the official publication of the Academy of Molecular Imaging 14(3) (2012) 315-324.
[400] S. Geninatti Crich, M. Cadenazzi, S. Lanzardo, L. Conti, R. Ruiu, D. Alberti, F. Cavallo, J.C. Cutrin, S. Aime, Targeting ferritin receptors for the selective delivery of imaging and therapeutic agents to breast cancer cells, Nanoscale 7(15) (2015) 6527-33.
[401] E. Falvo, E. Tremante, R. Fraioli, C. Leonetti, C. Zamparelli, A. Boffi, V. Morea, P. Ceci, P. Giacomini, Antibody–drug conjugates: targeting melanoma with cisplatin encapsulated in protein-cage nanoparticles based on human ferritin, Nanoscale 5(24) (2013) 12278-12285.
[402] H.M. Yassine, J.C. Boyington, P.M. McTamney, C.-J. Wei, M. Kanekiyo, W.-P. Kong, J.R. Gallagher, L. Wang, Y. Zhang, M.G. Joyce, D. Lingwood, S.M. Moin, H. Andersen, Y. Okuno, S.S. Rao, A.K. Harris, P.D. Kwong, J.R. Mascola, G.J. Nabel, B.S. Graham, Hemagglutinin-stem nanoparticles generate heterosubtypic influenza protection, Nature Medicine 21 (2015) 1065.
[403] Q. Yang, S.K. Lai, Anti-PEG immunity: emergence, characteristics, and unaddressed questions, Wiley interdisciplinary reviews. Nanomedicine and nanobiotechnology 7(5) (2015) 655-677.
[404] R.I. Dmitriev, S.M. Borisov, H. Dussmann, S. Sun, B.J. Muller, J. Prehn, V.P. Baklaushev, I. Klimant, D.B. Papkovsky, Versatile Conjugated Polymer Nanoparticles for High-Resolution O2 Imaging in Cells and 3D Tissue Models, ACS Nano 9(5) (2015) 5275-88.
[405] D. Langevin, E. Raspaud, S. Mariot, A. Knyazev, A. Stocco, A. Salonen, A. Luch, A. Haase, B. Trouiller, C. Relier, O. Lozano, S. Thomas, A. Salvati, K. Dawson, Towards reproducible measurement of nanoparticle size using dynamic light scattering: Important controls and considerations, NanoImpact 10 (2018) 161-167.
[406] G.L. Semenza, Life with Oxygen, Science 318(5847) (2007) 62-64.
[407] M.C. Simon, B. Keith, The role of oxygen availability in embryonic development and stem cell function, Nature Reviews Molecular Cell Biology 9 (2008) 285.
[408] M. Erecińska, I.A. Silver, Tissue oxygen tension and brain sensitivity to hypoxia, Respiration Physiology 128(3) (2001) 263-276.
[409] J. Brunelle, N. Chandel, Oxygen deprivation induced cell death: an update, Apoptosis 7(6) (2002) 475-482.
[410] A.C. Kulkarni, P. Kuppusamy, N. Parinandi, Oxygen, the lead actor in the pathophysiologic drama: enactment of the trinity of normoxia, hypoxia, and hyperoxia in disease and therapy, Antioxidants & redox signaling 9(10) (2007) 1717-1730.

[411] E. Maltepe, O.D. Saugstad, Oxygen in Health and Disease: Regulation of Oxygen Homeostasis-Clinical Implications, Pediatric Research 65 (2009) 261.
[412] G.L. Semenza, Oxygen homeostasis, Wiley Interdisciplinary Reviews: Systems Biology and Medicine 2(3) (2010) 336-361.
[413] R.B. Elmes, Bioreductive fluorescent imaging agents: applications to tumour hypoxia, Chemical Communications 52(58) (2016) 8935-8956.
[414] A. Melvin, S. Rocha, Chromatin as an oxygen sensor and active player in the hypoxia response, Cellular Signalling 24(1) (2012) 35-43.
[415] B. Jankovic, C. Aquino-Parsons, J. Raleigh, E. Stanbridge, R. Durand, thE, J. Banath, S. MacPhail, P. Olive, Comparison between pimonidazole binding, oxygen electrode measurements, and expression of endogenous hypoxia markers in cancer of the uterine cervix, Cytometry Part B: Clinical Cytometry: The Journal of the International Society for Analytical Cytology 70(2) (2006) 45-55.
[416] T.W.L. Scheeren, P. Schober, L.A. Schwarte, Monitoring tissue oxygenation by near infrared spectroscopy (NIRS): background and current applications, Journal of Clinical Monitoring and Computing 26(4) (2012) 279-287.
[417] B. Gallez, C. Baudelet, B.F. Jordan, Assessment of tumor oxygenation by electron paramagnetic resonance: principles and applications, NMR in Biomedicine 17(5) (2004) 240-262.
[418] J.-H. Lee, T.-S. Lim, Y. Seo, P.L. Bishop, I. Papautsky, Needle-type dissolved oxygen microelectrode array sensors for in situ measurements, Sensors and Actuators B: Chemical 128(1) (2007) 179-185.
[419] R.I. Dmitriev, D.B. Papkovsky, Optical probes and techniques for O2 measurement in live cells and tissue, Cellular and Molecular Life Sciences 69(12) (2012) 2025-2039.
[420] E.R. Carraway, J.N. Demas, B.A. DeGraff, J.R. Bacon, Photophysics and photochemistry of oxygen sensors based on luminescent transition-metal complexes, Analytical Chemistry 63(4) (1991) 337-342.
[421] A.L. Medina-Castillo, J.F. Fernandez-Sanchez, C. Klein, M.K. Nazeeruddin, A. Segura-Carretero, A. Fernandez-Gutierrez, M. Graetzel, U.E. Spichiger-Keller, Engineering of efficient phosphorescent iridium cationic complex for developing oxygen-sensitive polymeric and nanostructured films, Analyst 132(9) (2007) 929-36.
[422] T.C. O'Riordan, A.V. Zhdanov, G.V. Ponomarev, D.B. Papkovsky, Analysis of Intracellular Oxygen and Metabolic Responses of Mammalian Cells by Time-Resolved Fluorometry, Analytical Chemistry 79(24) (2007) 9414-9419.
[423] R.I. Dmitriev, A.V. Zhdanov, G. Jasionek, D.B. Papkovsky, Assessment of Cellular Oxygen Gradients with a Panel of Phosphorescent Oxygen-Sensitive Probes, Analytical Chemistry 84(6) (2012) 2930-2938.
[424] E. Vives, P. Brodin, B. Lebleu, A truncated HIV-1 Tat protein basic domain rapidly translocates through the plasma membrane and accumulates in the cell nucleus, Journal of Biological Chemistry 272(25) (1997) 16010-16017.
[425] R.I. Dmitriev, A.V. Zhdanov, G.V. Ponomarev, D.V. Yashunski, D.B. Papkovsky, Intracellular oxygen-sensitive phosphorescent probes based on cell-penetrating peptides, Analytical Biochemistry 398(1) (2010) 24-33.
[426] K. Sadler, K.D. Eom, J.L. Yang, Y. Dimitrova, J.P. Tam, Translocating proline-rich peptides from the antimicrobial peptide bactenecin 7, Biochemistry 41(48) (2002) 14150-7.
[427] R.I. Dmitriev, H.M. Ropiak, D.V. Yashunsky, G.V. Ponomarev, A.V. Zhdanov, D.B. Papkovsky, Bactenecin 7 peptide fragment as a tool for intracellular delivery of a phosphorescent oxygen sensor, The FEBS journal 277(22) (2010) 4651-4661.
[428] A. Fercher, S.M. Borisov, A.V. Zhdanov, I. Klimant, D.B. Papkovsky, Intracellular O2 sensing probe based on cell-penetrating phosphorescent nanoparticles, ACS Nano 5(7) (2011) 5499-5508.
[429] R.I. Dmitriev, A.V. Zhdanov, Y.M. Nolan, D.B. Papkovsky, Imaging of neurosphere oxygenation with phosphorescent probes, Biomaterials 34(37) (2013) 9307-9317.
[430] R.I. Dmitriev, S.M. Borisov, A.V. Kondrashina, J.M. Pakan, U. Anilkumar, J.H. Prehn, A.V. Zhdanov, K.W. McDermott, I. Klimant, D.B. Papkovsky, Imaging oxygen in neural cell and tissue models by means of anionic cell-permeable phosphorescent nanoparticles, Cellular and Molecular Life Sciences 72(2) (2015) 367-381.

[431] H. Xiang, L. Zhou, Y. Feng, J. Cheng, D. Wu, X. Zhou, Tunable Fluorescent/Phosphorescent Platinum(II) Porphyrin–Fluorene Copolymers for Ratiometric Dual Emissive Oxygen Sensing, Inorganic Chemistry 51(9) (2012) 5208-5212.
[432] E. Snapp, Design and Use of Fluorescent Fusion Proteins in Cell Biology, Current protocols in cell biology / editorial board, Juan S. Bonifacino ... [et al.] CHAPTER (2005) Unit-21.4.
[433] T. Chishima, Y. Miyagi, X. Wang, H. Yamaoka, H. Shimada, A. Moossa, R.M. Hoffman, Cancer invasion and micrometastasis visualized in live tissue by green fluorescent protein expression, Cancer research 57(10) (1997) 2042-2047.
[434] D. Shcherbo, C.S. Murphy, G.V. Ermakova, E.A. Solovieva, T.V. Chepurnykh, A.S. Shcheglov, V.V. Verkhusha, V.Z. Pletnev, K.L. Hazelwood, P.M. Roche, Far-red fluorescent tags for protein imaging in living tissues, Biochemical Journal 418(3) (2009) 567-574.
[435] N.C. Shaner, G.G. Lambert, A. Chammas, Y. Ni, P.J. Cranfill, M.A. Baird, B.R. Sell, J.R. Allen, R.N. Day, M. Israelsson, M.W. Davidson, J. Wang, A bright monomeric green fluorescent protein derived from Branchiostoma lanceolatum, Nature methods 10(5) (2013) 407-409.
[436] S. Schmidt, I. Tavernaro, C. Cavelius, E. Weber, A. Kümper, C. Schmitz, J. Fleddermann, A. Kraegeloh, Silica Nanoparticles for Intracellular Protein Delivery: a Novel Synthesis Approach Using Green Fluorescent Protein, Nanoscale Research Letters 12 (2017) 545.
[437] A. Kapur, F. Aldeek, X. Ji, M. Safi, W. Wang, A. Del Cid, O. Steinbock, H. Mattoussi, Self-Assembled Gold Nanoparticle–Fluorescent Protein Conjugates as Platforms for Sensing Thiolate Compounds via Modulation of Energy Transfer Quenching, Bioconjugate Chemistry 28(2) (2017) 678-687.
[438] C. You, J. Piehler, Multivalent chelators for spatially and temporally controlled protein functionalization, Anal Bioanal Chem 406(14) (2014) 3345-57.
[439] A.N. Kapanidis, Y.W. Ebright, R.H. Ebright, Site-specific incorporation of fluorescent probes into protein: hexahistidine-tag-mediated fluorescent labeling with (Ni(2+):nitrilotriacetic Acid (n)-fluorochrome conjugates, J Am Chem Soc 123(48) (2001) 12123-5.
[440] C.T. Hauser, R.Y. Tsien, A hexahistidine-Zn²⁺-dye label reveals STIM1 surface exposure, Proceedings of the National Academy of Sciences 104(10) (2007) 3693-3697.
[441] Y.-T. Lai, Y.-Y. Chang, L. Hu, Y. Yang, A. Chao, Z.-Y. Du, J.A. Tanner, M.-L. Chye, C. Qian, K.-M. Ng, H. Li, H. Sun, Rapid labeling of intracellular His-tagged proteins in living cells, Proceedings of the National Academy of Sciences of the United States of America 112(10) (2015) 2948-2953.
[442] R. Wieneke, N. Labòria, M. Rajan, A. Kollmannsperger, F. Natale, M.C. Cardoso, R. Tampé, Live-Cell Targeting of His-Tagged Proteins by Multivalent N-Nitrilotriacetic Acid Carrier Complexes, Journal of the American Chemical Society 136(40) (2014) 13975-13978.
[443] M.B. van Eldijk, J.C.Y. Wang, I.J. Minten, C. Li, A. Zlotnick, R.J.M. Nolte, J.J.L.M. Cornelissen, J.C.M. van Hest, Designing Two Self-Assembly Mechanisms into One Viral Capsid Protein, Journal of the American Chemical Society 134(45) (2012) 18506-18509.
[444] D. Kroger, M. Liley, W. Schiweck, A. Skerra, H. Vogel, Immobilization of histidine-tagged proteins on gold surfaces using chelator thioalkanes, Biosensors & bioelectronics 14(2) (1999) 155-61.
[445] D.M. Lawson, P.J. Artymiuk, S.J. Yewdall, J.M. Smith, J.C. Livingstone, A. Treffry, A. Luzzago, S. Levi, P. Arosio, G. Cesareni, et al., Solving the structure of human H ferritin by genetically engineering intermolecular crystal contacts, Nature 349(6309) (1991) 541-4.
[446] G. Gilliland, H.M. Berman, H. Weissig, I.N. Shindyalov, J. Westbrook, P.E. Bourne, T.N. Bhat, Z. Feng, The Protein Data Bank, Nucleic Acids Research 28(1) (2000) 235-242.
[447] T. Kitagawa, H. Kosuge, M. Uchida, M.M. Dua, Y. Iida, R.L. Dalman, T. Douglas, M.V. McConnell, RGD-conjugated human ferritin nanoparticles for imaging vascular inflammation and angiogenesis in experimental carotid and aortic disease, Mol Imaging Biol 14(3) (2012) 315-24.
[448] F.B. Loiselle, J.R. Casey, Measurement of Intracellular pH, Methods Mol Biol 637 (2010) 311-31.
[449] P. Swietach, R.D. Vaughan-Jones, A.L. Harris, A. Hulikova, The chemistry, physiology and pathology of pH in cancer, Philosophical Transactions of the Royal Society B: Biological Sciences 369(1638) (2014) 20130099.
[450] H. Zhao, Y. Cai, Z. Yang, D. He, B. Shen, Acidosis leads to neurological disorders through overexciting cortical pyramidal neurons, Biochem Biophys Res Commun 415(2) (2011) 224-8.

[451] C.-H. Wu, Y.-H. Kuo, R.-L. Hong, H.-C. Wu, α-Enolase–binding peptide enhances drug delivery efficiency and therapeutic efficacy against colorectal cancer, Science Translational Medicine 7(290) (2015) 290ra91-290ra91.
[452] E. Falvo, E. Tremante, R. Fraioli, C. Leonetti, C. Zamparelli, A. Boffi, V. Morea, P. Ceci, P. Giacomini, Antibody-drug conjugates: targeting melanoma with cisplatin encapsulated in protein-cage nanoparticles based on human ferritin, Nanoscale 5(24) (2013) 12278-85.
[453] X.T. Ji, L. Huang, H.Q. Huang, Construction of nanometer cisplatin core-ferritin (NCC-F) and proteomic analysis of gastric cancer cell apoptosis induced with cisplatin released from the NCC-F, J Proteomics 75(11) (2012) 3145-57.
[454] S.-E. Kim, K.-Y. Ahn, J.-S. Park, K.R. Kim, K.E. Lee, S.-S. Han, J. Lee, Fluorescent Ferritin Nanoparticles and Application to the Aptamer Sensor, Analytical Chemistry 83(15) (2011) 5834-5843.
[455] L. Zang, H. Zhao, J. Hua, F. Qin, Y. Zheng, Z. Zhang, W. Cao, The effect of imidazole on the enhancement of gadolinium-porphyrin phosphorescence at room temperature, Dalton transactions (Cambridge, England : 2003) 45(42) (2016) 16889-16895.
[456] L.I. Selby, C.M. Cortez-Jugo, G.K. Such, A.P.R. Johnston, Nanoescapology: progress toward understanding the endosomal escape of polymeric nanoparticles, Wiley Interdisciplinary Reviews: Nanomedicine and Nanobiotechnology 9(5) (2017) e1452.
[457] K. Najjar, A. Erazo-Oliveras, J.-P. Pellois, Delivery of proteins, peptides or cell-impermeable small molecules into live cells by incubation with the endosomolytic reagent dfTAT, Journal of visualized experiments : JoVE (103) (2015) 10.3791/53175.
[458] J.C. Salerno, V.M. Ngwa, S.J. Nowak, C.A. Chrestensen, A.N. Healey, J.L. McMurry, Novel cell-penetrating peptide-adaptors effect intracellular delivery and endosomal escape of protein cargos, J Cell Sci 129(5) (2016) 893-7.
[459] T. Consolati, J.M. Bolivar, Z. Petrasek, J. Berenguer, A. Hidalgo, J.M. Guisán, B. Nidetzky, Bio-based, internally pH sensitive materials: immobilized yellow fluorescent protein as optical sensor for spatiotemporal mapping of pH inside porous matrices, ACS applied materials & interfaces (2018).
[460] J.R. Gershlak, S. Hernandez, G. Fontana, L.R. Perreault, K.J. Hansen, S.A. Larson, B.Y. Binder, D.M. Dolivo, T. Yang, T. Dominko, Crossing kingdoms: Using decellularized plants as perfusable tissue engineering scaffolds, Biomaterials 125 (2017) 13-22.
[461] G. Fontana, J. Gershlak, M. Adamski, J.S. Lee, S. Matsumoto, H.D. Le, B. Binder, J. Wirth, G. Gaudette, W.L. Murphy, Biofunctionalized Plants as Diverse Biomaterials for Human Cell Culture, Advanced Healthcare Materials 6(8) (2017).
[462] V. Lombard, H. Golaconda Ramulu, E. Drula, P.M. Coutinho, B. Henrissat, The carbohydrate-active enzymes database (CAZy) in 2013, Nucleic Acids Res 42(Database issue) (2014) 21.
[463] P. Tomme, A. Boraston, B. McLean, J. Kormos, A.L. Creagh, K. Sturch, N.R. Gilkes, C.A. Haynes, R.A.J. Warren, D.G. Kilburn, Characterization and affinity applications of cellulose-binding domains, Journal of Chromatography B: Biomedical Sciences and Applications 715(1) (1998) 283-296.
[464] N. Din, I.J. Forsythe, L.D. Burtnick, N.R. Gilkes, R.C. Miller, R.A.J. Warren, D.G. Kilburn, The cellulose-binding domain of endoglucanase A (CenA) from Cellulomonas fimi: evidence for the involvement of tryptophan residues in binding, Molecular microbiology 11(4) (1994) 747-755.
[465] Y. Wang, R. Kim, D.B. Gunasekara, M.I. Reed, M. DiSalvo, D.L. Nguyen, S.J. Bultman, C.E. Sims, S.T. Magness, N.L. Allbritton, Formation of human colonic crypt array by application of chemical gradients across a shaped epithelial monolayer, Cellular and Molecular Gastroenterology and Hepatology 5(2) (2018) 113-130.
[466] A.A. Appel, M.A. Anastasio, J.C. Larson, E.M. Brey, Imaging challenges in biomaterials and tissue engineering, Biomaterials 34(28) (2013) 6615-6630.
[467] L. Teodori, A. Crupi, A. Costa, A. Diaspro, S. Melzer, A. Tarnok, Three-dimensional imaging technologies: a priority for the advancement of tissue engineering and a challenge for the imaging community, Journal of biophotonics 10(1) (2017) 24-45.
[468] S.W. Lane, D.A. Williams, F.M. Watt, Modulating the stem cell niche for tissue regeneration, Nature biotechnology 32(8) (2014) 795.
[469] A. Zhdanov, C. Favre, L. O'Flaherty, J. Adam, R. O'Connor, P. Pollard, D. Papkovsky, Comparative bioenergetic assessment of transformed cells using a cell energy budget platform, Integrative Biology 3(11) (2011) 1135-1142.

[470] D.A. Ferrick, A. Neilson, C. Beeson, Advances in measuring cellular bioenergetics using extracellular flux, Drug discovery today 13(5) (2008) 268-274.
[471] K.K. Kaysinger, W.K. Ramp, Extracellular pH modulates the activity of cultured human osteoblasts, Journal of cellular biochemistry 68(1) (1998) 83-89.
[472] K. Lee, E.A. Silva, D.J. Mooney, Growth factor delivery-based tissue engineering: general approaches and a review of recent developments, Journal of the Royal Society Interface 8(55) (2011) 153-170.
[473] M.H. Wu, J.P. Urban, Z.F. Cui, Z. Cui, X. Xu, Effect of extracellular pH on matrix synthesis by chondrocytes in 3D agarose gel, Biotechnology progress 23(2) (2007) 430-434.
[474] M.-A. Elsliger, R.M. Wachter, G.T. Hanson, K. Kallio, S.J. Remington, Structural and Spectral Response of Green Fluorescent Protein Variants to Changes in pH, Biochemistry 38(17) (1999) 5296-5301.
[475] E.M. Brown, R.J. MacLeod, Extracellular calcium sensing and extracellular calcium signaling, Physiological reviews 81(1) (2001) 239-297.
[476] A.V. Zhdanov, M.W. Ward, C.T. Taylor, E.A. Souslova, D.M. Chudakov, J.H.M. Prehn, D.B. Papkovsky, Extracellular calcium depletion transiently elevates oxygen consumption in neurosecretory PC12 cells through activation of mitochondrial Na+/Ca2+ exchange, Biochimica et Biophysica Acta (BBA) - Bioenergetics 1797(9) (2010) 1627-1637.
[477] G.R. Monteith, N. Prevarskaya, S.J. Roberts-Thomson, The calcium–cancer signalling nexus, Nature Reviews Cancer 17 (2017) 367.
[478] Y.N. Tallini, M. Ohkura, B.-R. Choi, G. Ji, K. Imoto, R. Doran, J. Lee, P. Plan, J. Wilson, H.-B. Xin, A. Sanbe, J. Gulick, J. Mathai, J. Robbins, G. Salama, J. Nakai, M.I. Kotlikoff, Imaging cellular signals in the heart in vivo: Cardiac expression of the high-signal Ca(2+) indicator GCaMP2, Proceedings of the National Academy of Sciences of the United States of America 103(12) (2006) 4753-4758.
[479] Q. Wang, B. Shui, M.I. Kotlikoff, H. Sondermann, Structural Basis for Calcium Sensing by GCaMP2, Structure 16(12) (2008) 1817-1827.
[480] L. Tian, S.A. Hires, T. Mao, D. Huber, M.E. Chiappe, S.H. Chalasani, L. Petreanu, J. Akerboom, S.A. McKinney, E.R. Schreiter, C.I. Bargmann, V. Jayaraman, K. Svoboda, L.L. Looger, Imaging neural activity in worms, flies and mice with improved GCaMP calcium indicators, Nat Methods 6(12) (2009) 875-81.
[481] T.-W. Chen, T.J. Wardill, Y. Sun, S.R. Pulver, S.L. Renninger, A. Baohan, E.R. Schreiter, R.A. Kerr, M.B. Orger, V. Jayaraman, L.L. Looger, K. Svoboda, D.S. Kim, Ultra-sensitive fluorescent proteins for imaging neuronal activity, Nature 499(7458) (2013) 295-300.
[482] J. Akerboom, N. Carreras Calderón, L. Tian, S. Wabnig, M. Prigge, J. Tolö, A. Gordus, M.B. Orger, K.E. Severi, J.J. Macklin, R. Patel, S.R. Pulver, T.J. Wardill, E. Fischer, C. Schüler, T.-W. Chen, K.S. Sarkisyan, J.S. Marvin, C.I. Bargmann, D.S. Kim, S. Kügler, L. Lagnado, P. Hegemann, A. Gottschalk, E.R. Schreiter, L.L. Looger, Genetically encoded calcium indicators for multi-color neural activity imaging and combination with optogenetics, Frontiers in Molecular Neuroscience 6 (2013) 2.
[483] M. Mank, D.F. Reiff, N. Heim, M.W. Friedrich, A. Borst, O. Griesbeck, A FRET-Based Calcium Biosensor with Fast Signal Kinetics and High Fluorescence Change, Biophysical journal 90(5) (2006) 1790-1796.
[484] M. Mank, A.F. Santos, S. Direnberger, T.D. Mrsic-Flogel, S.B. Hofer, V. Stein, T. Hendel, D.F. Reiff, C. Levelt, A. Borst, T. Bonhoeffer, M. Hübener, O. Griesbeck, A genetically encoded calcium indicator for chronic in vivo two-photon imaging, Nature Methods 5 (2008) 805.
[485] C.D. Wilms, M. Häusser, Twitching towards the ideal calcium sensor, Nature Methods 11 (2014) 139.
[486] P. Sarder, D. Maji, S. Achilefu, Molecular probes for fluorescence lifetime imaging, Bioconjugate chemistry 26(6) (2015) 963-974.
[487] M. Tantama, Y.P. Hung, G. Yellen, Imaging intracellular pH in live cells with a genetically encoded red fluorescent protein sensor, Journal of the American Chemical Society 133(26) (2011) 10034-10037.
[488] H.J. Lin, P. Herman, J.R. Lakowicz, Fluorescence lifetime-resolved pH imaging of living cells, Cytometry Part A 52(2) (2003) 77-89.

[489] T. Gensch, D. Kaschuba, Fluorescent genetically encoded calcium indicators and their in vivo application, Fluorescent Proteins II, Springer2011, pp. 125-161.
[490] B. Sauer, Q. Tian, P. Lipp, L. Kaestner, Confocal FLIM of genetically encoded FRET sensors for quantitative Ca2+ imaging, Cold Spring Harbor Protocols 2014(12) (2014) pdb. prot077040.
[491] J.L. Rinnenthal, C. Börnchen, H. Radbruch, V. Andresen, A. Mossakowski, V. Siffrin, T. Seelemann, H. Spiecker, I. Moll, J. Herz, Parallelized TCSPC for dynamic intravital fluorescence lifetime imaging: quantifying neuronal dysfunction in neuroinflammation, PLoS One 8(4) (2013) e60100.
[492] Y.N. Tallini, M. Ohkura, B.-R. Choi, G. Ji, K. Imoto, R. Doran, J. Lee, P. Plan, J. Wilson, H.-B. Xin, Imaging cellular signals in the heart in vivo: Cardiac expression of the high-signal Ca2+ indicator GCaMP2, Proceedings of the National Academy of Sciences of the United States of America 103(12) (2006) 4753-4758.
[493] J. Nakai, M. Ohkura, K. Imoto, A high signal-to-noise Ca2+ probe composed of a single green fluorescent protein, Nature biotechnology 19(2) (2001) 137-141.
[494] N. O'Donnell, I.A. Okkelman, P. Timashev, T.I. Gromovykh, D.B. Papkovsky, R.I. Dmitriev, Cellulose-based scaffolds for fluorescence lifetime imaging-assisted tissue engineering, Acta biomaterialia (2018).
[495] S. Hestrin, M. Schramm, Synthesis of cellulose by Acetobacter xylinum. 2. Preparation of freeze-dried cells capable of polymerizing glucose to cellulose, Biochemical Journal 58(2) (1954) 345.
[496] J. Akerboom, J.D.V. Rivera, M.M.R. Guilbe, E.C.A. Malavé, H.H. Hernandez, L. Tian, S.A. Hires, J.S. Marvin, L.L. Looger, E.R. Schreiter, Crystal structures of the GCaMP calcium sensor reveal the mechanism of fluorescence signal change and aid rational design, Journal of biological chemistry 284(10) (2009) 6455-6464.
[497] D.L. Nelson, A.L. Lehninger, M.M. Cox, Lehninger principles of biochemistry, Macmillan2008.
[498] H.J. Sung, W. Ma, P.-y. Wang, J. Hynes, T.C. O'riordan, C.A. Combs, J.P. McCoy Jr, F. Bunz, J.-G. Kang, P.M. Hwang, Mitochondrial respiration protects against oxygen-associated DNA damage, Nature communications 1 (2010) 5.
[499] S. Kwok, C. Lee, S.A. Sánchez, T.L. Hazlett, E. Gratton, Y. Hayashi, Genetically encoded probe for fluorescence lifetime imaging of CaMKII activity, Biochemical and biophysical research communications 369(2) (2008) 519-525.
[500] R. Laine, D.W. Stuckey, H. Manning, S.C. Warren, G. Kennedy, D. Carling, C. Dunsby, A. Sardini, P.M.W. French, Fluorescence Lifetime Readouts of Troponin-C-Based Calcium FRET Sensors: A Quantitative Comparison of CFP and mTFP1 as Donor Fluorophores, PLoS One 7(11) (2012) e49200.
[501] M.M. Malinen, L.K. Kanninen, A. Corlu, H.M. Isoniemi, Y.R. Lou, M.L. Yliperttula, A.O. Urtti, Differentiation of liver progenitor cell line to functional organotypic cultures in 3D nanofibrillar cellulose and hyaluronan-gelatin hydrogels, Biomaterials 35(19) (2014) 5110-21.
[502] B. Rinner, G. Gandolfi, K. Meditz, M.-T. Frisch, K. Wagner, A. Ciarrocchi, F. Torricelli, R. Koivuniemi, J. Niklander, B. Liegl-Atzwanger, B. Lohberger, E. Heitzer, N. Ghaffari-Tabrizi-Wizsy, D. Zweytick, I. Zalaudek, MUG-Mel2, a novel highly pigmented and well characterized NRAS mutated human melanoma cell line, Scientific Reports 7(1) (2017) 2098.
[503] I. Azoidis, J. Metcalfe, J. Reynolds, S. Keeton, S.S. Hakki, J. Sheard, D. Widera, Three-dimensional cell culture of human mesenchymal stem cells in nanofibrillar cellulose hydrogels, MRS Communications 7(3) (2017) 458-465.
[504] W. Czaja, D. Kyryliouk, C.A. DePaula, D.D. Buechter, Oxidation of γ-irradiated microbial cellulose results in bioresorbable, highly conformable biomaterial, Journal of Applied Polymer Science 131(6) (2014).
[505] J. Andersson, H. Stenhamre, H. Bäckdahl, P. Gatenholm, Behavior of human chondrocytes in engineered porous bacterial cellulose scaffolds, Journal of Biomedical Materials Research Part A 94A(4) (2010) 1124-1132.
[506] C. Weber, S. Reinhardt, K. Eghbalzadeh, M. Wacker, M. Guschlbauer, A. Maul, A. Sterner-Kock, T. Wahlers, J. Wippermann, M. Scherner, Patency and in vivo compatibility of bacterial nanocellulose grafts as small-diameter vascular substitute, Journal of Vascular Surgery.
[507] J.S. Lee, J.S. Lee, W.L. Murphy, Modular Peptides Promote Human Mesenchymal Stem Cell Differentiation on Biomaterial Surfaces, Acta Biomaterialia 6(1) (2010) 21-28.

Acknowledgments

I would like to first thank Science Foundation Ireland for their funding of this project and my PhD education. Thank you to UCC Biochemistry and Cell Biology department and staff for their brilliant support over the past four years.

I would like to express my upmost gratitude and thanks to my supervisor and mentor, Dr. Ruslan Dmitriev for giving me the opportunity to carry out my PhD studies under his supervision. For all his support, friendship and training during my time at UCC, helping me to grow not just as a scientist, but as a person.

Thank you to my second supervisor Prof. Dmitri Papkovsky for welcoming me into his lab group and for all his advice and mentoring during my time at UCC.

I would like to thank all the members of our lab, past and present who provided much needed distractions, motivation, and advice in both the good and bad times, as well as creating a fun, friendly atmosphere: Irina, Alex, PanPan, Sophia, Selina, Caroline, Alicia, Patrycja and James.

My friends and former housemates Angela and Conor (my fellow PhD colleague) for all their support over the past two years and helping to make home for me in Cork.

Finally, I would like to thank my Family for all their support. To my Mother, for all the countless words of encouragement when things didn't go according to plan, for teaching me to never give up and perhaps more importantly when to enjoy life. To my Grandmother for her example of strength, and for all her support and encouragement given throughout my life, not just during my PhD. To my Brother for his support and reading countless numbers of drafts of abstracts and papers. To my partner Shannon for all her emotional support and encouragement especially over the last year in helping me to succeed in this difficult task.

And finally, to my Grandfather, for all the lessons you taught me, and for everything you ever did for me. I am sorry you didn't get to see me finish, but this is for you. I know you would be proud.